DOI: 10.2478/sspjce-2024-0001

Investigation of the Effect of Dilation Angle of Soil on the Performance of Grouted Tieback Under Axial Static Load by Analytical Approach

Feriel Mekki[1,2]

[1]Department of Architecture, Faculty of Earth Science, University of Badj Mokhtar, P.B.N°:12, Sidi Amar, Annaba, 23000, Algeria
[2]Laboratory of Soils and Hydraulic, University of Badj Mokhtar, P.B.N°:12, Sidi Amar, Annaba, 23000, Algeria
e-mail: feriel.mekki@univ-annaba.dz

Abstract
Studies on how non-associated flow rules affect the performance of grouted tieback using the upper bound of limit analysis theory are relatively rare. In this paper, the expression of the collapse load of a single, inclined, rough grouted tieback subjected to axial static load placed in a frictional soil was determined by constructing a failure mechanism by combining a non-associated flow rule in the upper bound limit analysis technique and the linear Mohr-Coulomb yield criterion. The effects of variation of dilation angle, the soil friction angle, the grouted tieback's angle of inclination, the bonded length, and the diameter of bonded length on the ultimate load were investigated. The results obtained from the present study clearly indicated that the dilation angle, the soil friction angle, the grouted tieback's angle of inclination, and the bonded length all significantly affect the collapse load but the bonded length's diameter has no effect on the critical load.

Keywords: axial static load, bonded length, diameter of bonded length, dilation angle, performance of grouted tieback

1 Introduction

Grouted tiebacks are tension members broadly used in different civil engineering practices as a soil reinforcement technique either temporarily or permanently because their application is an efficient, attractive, and economical design solution. These devices are used to control the deformation, and the displacement of engineered structures and to improve the bearing capacity of the soil. Grouted tiebacks are able to transfer the applied tensile load from the structure to the surrounding ground at greater depth through the friction mobilized at their interfaces.

These structural elements can be installed in an inclined position or vertically depending on the load orientation or the type of structure requiring support. The determination of the performance of grouted tiebacks is very important in the design and the dimensioning of these tension members.

However, their performance is not easily determined because it is affected by several parameters including the properties of the surrounding soil, the installation technique, the orientation of the grouted tiebacks, their diameter, and their length, the method of interaction between the surrounding soil and grouted tiebacks.

Numerous studies have been conducted by various researchers to compute the static uplift capacity of grouted tiebacks placed in frictional soils; the majority of past research has been based on empiricism . Some scholars [1, 2] proposed an expression to estimate the skin friction along the bonded length of grouted tiebacks. Other authors [3, 4, 5] suggested a formulation to calculate the critical load of grouted tieback. In addition, the failure mechanism was developed theoretically using the upper bound of limit analysis and linear Mohr-Coulomb failure criterion by [6, 7, 9, 12] to investigate the collapse load of single vertical grouted tieback under uplift tensile force and they considered the influence of the length of grouted tieback and the friction angle of the soil on the ultimate load. The researchers [11] also evaluated the ultimate pullout capacity which is expressed according to the bearing capacity factor of a single inclined grouted tieback subjected to axial static loading based on the kinematic approach of limit analysis and the linear Mohr-Coulomb yield criterion. They identified the effect of the angle of slope, the inclination of grouted tieback and the friction angle of the soil on the non-dimensional factor.
The authors [13] compare the performance of inclined and vertical grouted tiebacks subjected to axial static loading placed in three sandy soils using the upper bound limit analysis method to investigate the variation of the bonded length and the diameter of the bonded length on the ultimate pullout capacity. Several researchers have used this theorem extensively to come up with solid solutions to a variety of geotechnical engineering problems [14, 15, 16, 17, 18].

However, the existing studies are based on the associated flow rule to determine the performance of grouted tieback under axial static loading using the upper bound theorem of limit analysis; the dilatancy impact was not taken into account in any investigation.

The objective of the study described in this work is:
- To incorporate the non-associated flow rule in the upper bound theorem of limit analysis and also to find the influence of dilation angle (ψ) on the pullout capacity of single, inclined, rough grouted tieback subjected to axial static load placed in frictional soil .
- To examine the variation of limit load with changes in the dilation angle, the soil friction angle, the grouted tieback's angle of inclination, the bonded length and the diameter of bonded length.

2 Problem Definition and Principal Hypotheses

The upper bound limit analysis approach combined with linear Mohr-Coulomb failure criterion must contain the non-associated flow rule in order to examine the impact of the dilation angle (ψ) on the collapse load of inclined , single rough grouted tieback subjected to axial static load (F) placed in sloping ground (homogeneous , isotropic , dry , frictional soil medium which is defined through its unit weight (γ) and friction angle (φ)) ; the sloping surface and the grouted tieback are inclined respectively at an angle (μ) and (λ) with the horizontal plane. The grouted

tieback's interaction with the surrounding soil mass is expected to have a higher friction angle (δ) than the soil itself (φ) [19].

3 Including the Non-Associated Flow Rule in the Formulation of Upper Bound of Limit Analysis

According to the plasticity theory, if the dilation angle (ψ) is not equal to the friction angle (φ), the frictional material obeys a non-associated flow rule; (η) represents the dilative coefficient which is expressed according to the Equations (1); the dilative coefficient of frictional material can range in value from 0 to 1. The material follows the associated flow rule when the dilation angle (ψ) and friction angle (φ) are the same; however, this rule was unable to predict the plastic behavior of soil. Consequently, non-associated plasticity must be employed.

$$\eta = \frac{\Psi}{\varphi} \tag{1}$$

The researchers [20] proposed the following expressions to take dilation into consideration:

$$\eta = \frac{cos(\varphi).cos\,(\Psi)}{1 - sin(\varphi).sin\,(\Psi)} \tag{2}$$

$$\tan(\varphi^*) = \tan(\varphi).\frac{cos(\varphi).cos\,(\Psi)}{1 - sin(\varphi).sin\,(\Psi)} \tag{3}$$

$$c^* = \mathrm{c}.\frac{cos(\varphi).cos\,(\Psi)}{1 - sin(\varphi).sin\,(\Psi)} \tag{4}$$

where the modified cohesion and modified friction angle are denoted by (c^*) and (φ^*) respectively. Equations (3) and (4) are used in the current work to introduce a non-associated flow rule in the upper bound approach of limit analysis for examining the impact of dilation angle on the ultimate load of grouted tiebacks.

4 Determination of the Failure Mechanism

According to the specifications of the upper bound theorem of limit analysis, a failure mechanism is constructed in which the soil is subjected to the linear Mohr-Coulomb failure criterion and non-associated flow rule as indicated in Figure 1. This mechanism permitted the calculation of the critical load in the case of axial static loading. The collapse mechanism is composed of a triangular rigid block (*AMN*) which is defined with the kinematic variable (β); where (*OM*) is the total length of the grouted tieback, (*AM*) and, (*NM*) are the linear rupture surfaces.

It is believed that the triangular wedge (*AMN*) moves with velocity (V_1), making an angle (Ψ) with the linear rupture surfaces (*AM*), and (*NM*). The grouted tieback is assumed to move with velocities (V_0) and (V_{01}) which is the relative velocity at the soil-grouted tieback interface. The direction of the relative velocity (V_{01}) between the triangles (*AMO*) and (*OMN*) is at an angle (Ψ) with the contact surface.

At the ultimate failure state, it is supposed that the grouted tieback and the triangular rigid block (*AMN*) having weight (W_{AMN}) move with the velocity (V_0) in the inclined direction as a single rigid unit. Following the velocity hodograph, all the velocities can be represented in terms of (V_0), as indicated in Figure 2 below.

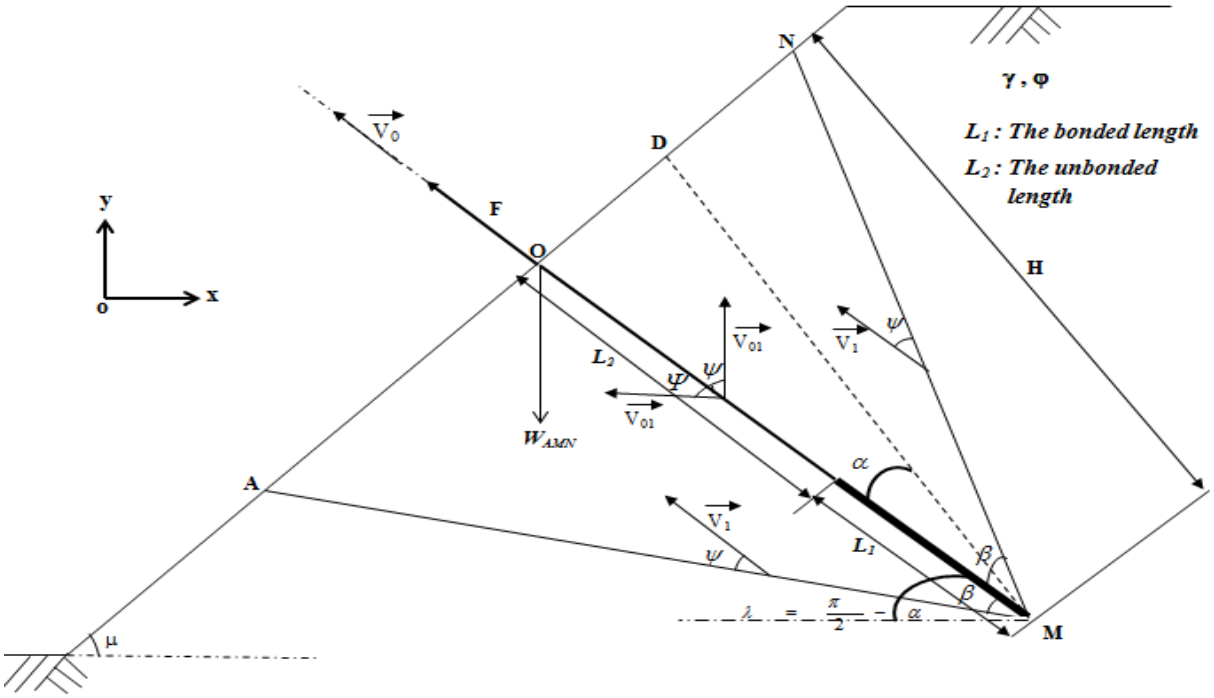

Figure 1: Failure mechanism at ultimate load for rough inclined grouted tieback in frictional soil under axial static loading according to non-associated flow rule and linear Mohr-Coulomb yield criterion

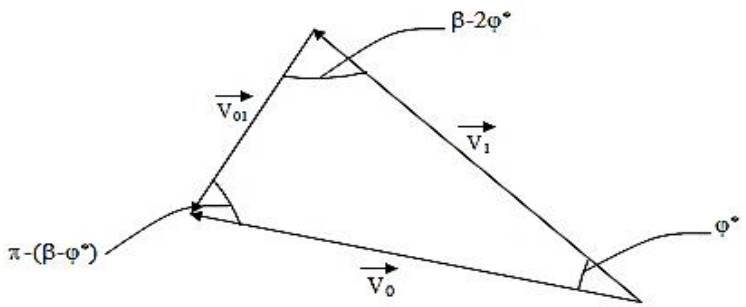

Figure 2: Velocity hodograph

4.1 Problem Formulation

The current study will suggest a number of formulations predicated on the upper bound theorem of limit analysis to determine the collapse load of an inclined , single rough grouted tieback subjected to axial static load (*F*) placed in sloping ground (frictional soil). Based on the geometric relationships of the kinematically admissible velocity hodograph, as illustrated in Figure 2 above; the following expressions of the velocities can be derived:

The velocity of the block:

$$V_0 = \frac{V_0.sin(\beta - \varphi^*)}{sin(\beta - 2\varphi^*)} \tag{5}$$

The relative velocity:

$$V_{01} = \frac{V_0.sin(\varphi^*)}{sin(\beta - 2\varphi^*)} \tag{6}$$

The internal energy dissipation rate owing to the soil cohesion (E_1) and the internal energy dissipation rate of the interface soil-grouted tieback (E_2) are added together to form the overall internal energy dissipation rate:

$$E_1 = \frac{c^*.\pi.H^2.V_0.sin(2\beta).sin(\beta - \varphi^*).cos(\varphi^*)}{2.sin(\beta - 2\varphi^*).\cos(\beta - \alpha).\cos(\alpha + \beta).\sin(\beta - 2\varphi^*)} \tag{7}$$

$$\alpha = \frac{\pi}{2} - \lambda \tag{8}$$

where (λ) is the grouted tieback's inclination.

$$E_2 = \frac{c^*.\pi.d.L_1.V_0.sin(\varphi^*).cos(\varphi^*)}{sin(\beta - 2\varphi^*)} \tag{9}$$

$$E_{Total} = E_1 + E_2 \tag{10}$$

$$E_{Total} = \frac{c^*.\pi.H^2.V_0.sin(2\beta).sin(\beta - \varphi^*).cos(\varphi^*)}{2.sin(\beta - 2\varphi^*).\cos(\beta - \alpha).\cos(\alpha + \beta).\sin(\beta - 2\varphi^*)} + \frac{c^*.\pi.d.L_1.V_0.sin(\varphi^*).cos(\varphi^*)}{sin(\beta - 2\varphi^*)} \tag{11}$$

The rigid block's weight can be expressed mathematically as follows:

$$W_{AMN} = \frac{\pi.\gamma.L.H^2.\tan(\beta).[tan(\beta - \alpha) + tan(\alpha + \beta)]}{6} \tag{12}$$

where (*L*) is the grouted tieback's total length.

The following expression can be used to calculate the work done by the external force:

$$T = F.V_0 \tag{13}$$

The expression for computing the work of the gravitational force is provided below:

$$T_{AMN} = W_{AMN}.V_1.\cos(\pi - \alpha) \tag{14}$$

By equating the rate of work performed by external forces to the rate of internal energy dissipation, the value of the limit load (F) is obtained:

$$F = \frac{c^*.\pi.H^2.sin(2\beta).sin(\beta-\varphi^*).cos(\varphi^*)}{2.sin(\beta-2\varphi^*).\cos(\beta-\alpha).\cos(\alpha+\beta).\sin(\beta-2\varphi^*)} + \frac{\frac{c^*.\pi.d.L_1.sin(\varphi^*).cos(\varphi^*)}{sin(\beta-2\varphi^*)} + \pi.\gamma.L.H^2.\tan(\beta).[tan(\beta-\alpha)+tan(\alpha+\beta)].\sin(\beta-\varphi^*).\cos(\pi-\alpha)}{6.sin(\beta-2\varphi^*)} \tag{15}$$

The internal energy dissipation rate through the friction of granular soil is equal to zero for a rough grouted tieback ($\delta > \varphi$), hence the expression of the collapse load (F) can be written as:

$$F = \frac{\pi.\gamma.L.H^2.\tan(\beta).[tan(\beta-\alpha)+tan(\alpha+\beta)].\sin(\beta-\varphi^*).\cos(\pi-\alpha)}{6.sin(\beta-2\varphi^*)} \tag{16}$$

5 Results and Discussion

Using MATHCAD software, the current study's optimizations were carried out. The following sets of parameters' results were computed: The range of the soil's angle of friction (φ) was 30°-40° with an interval of 2°, the dilation angle (ψ) was equal to {0, 0.25φ, 0.5φ, 0.75φ, φ}, the angle of inclination of grouted tieback (λ) took on three different values {10°, 15°, 20°}, the bonded length (L_{bonded}) was varied from 6 m to 10 m with an interval of 2 m and three values were considered of the diameter of bonded length ($d_{bonded\ length}$): {0.20 m, 0.25 m, 0.30 m}. Knowing that the angle of inclination of the sloping surface; the soil's unit weight and the unbonded length of grouted tieback are respectively as follows: (μ = 45°, γ = 20 kN/m^3, $L_{unbonded}$ = 14 m); they were kept constant.

5.1 The Effect of Combination of Non-Associated Flow Rule With the Soil Friction Angle and the Grouted Tieback's Angle of Inclination

The variation of limit load (F) using different dilative coefficient values (η) for changes in soil friction angle (φ) and the grouted tieback's angle of inclination of (λ) are demonstrated in (Figures 3, 4, and 5). The figures show that as the dilative coefficient (η), the friction angle of

the soil (φ), and the angle of inclination of grouted tieback (λ) increase, the collapse load (F) increases as well.

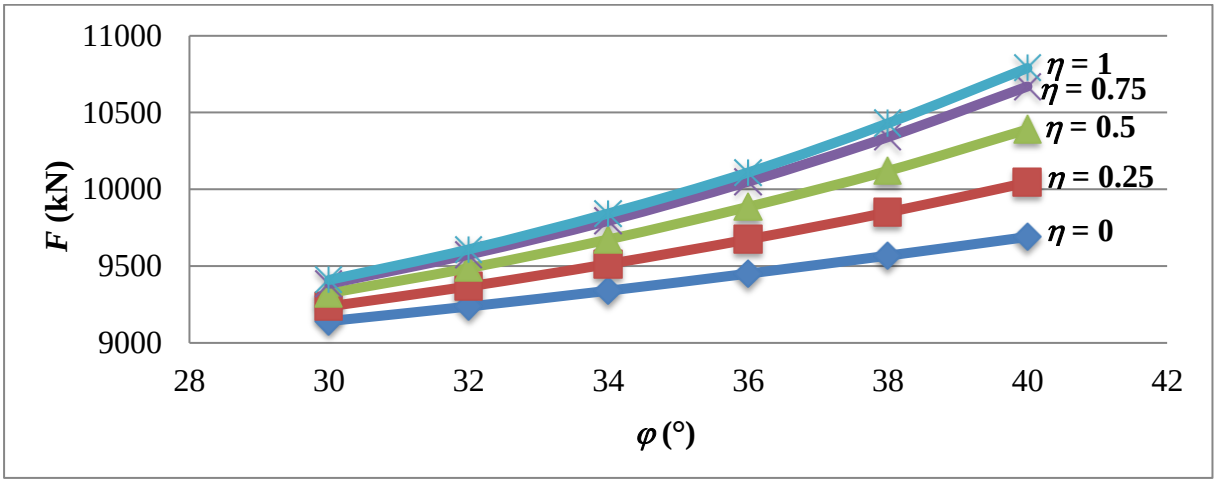

Figure 3: The variation of ultimate load with (φ) and (η) for (λ = 10°)

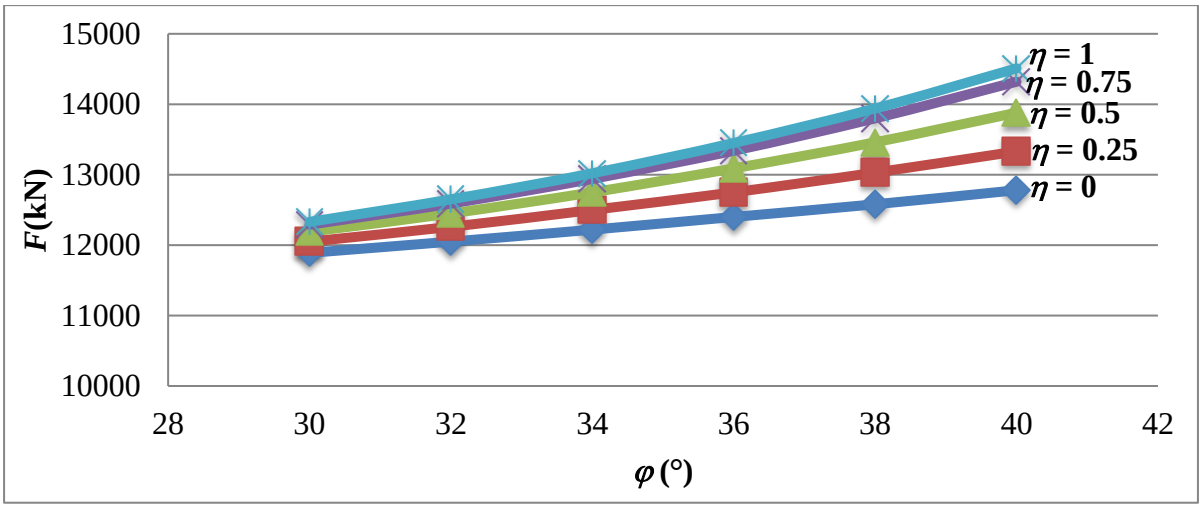

Figure 4: The variation of ultimate load with (φ) and (η) for (λ = 15°)

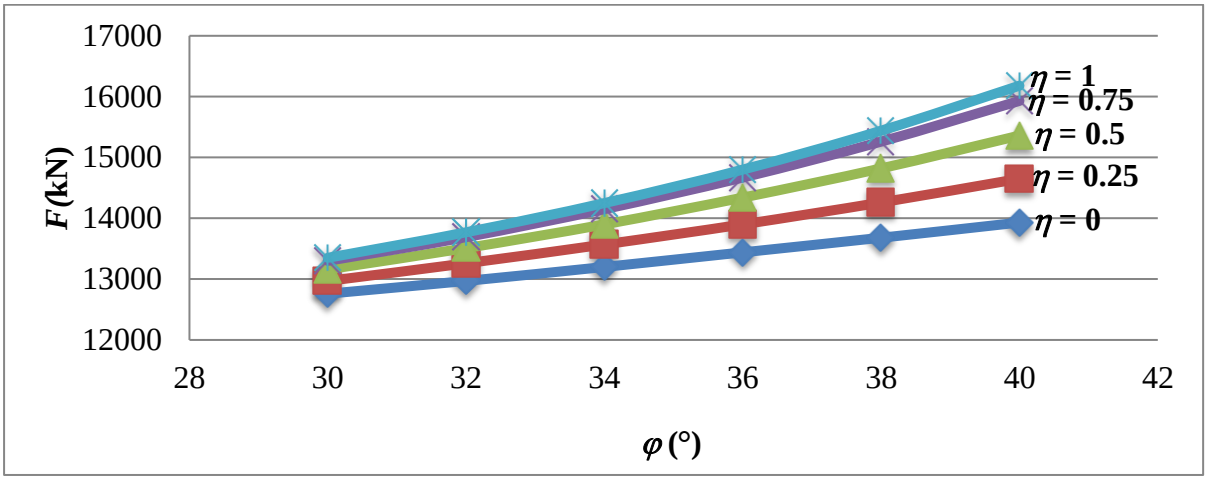

Figure 5: The variation of ultimate load with (φ) and (η) for (λ = 20°)

5.2 The Effect of Combination of Non-Associated Flow Rule With the Soil Friction Angle and the Bonded Length

In this section, a parametric analysis is done to determine how the non-associated flow rule, the soil friction angle (φ), and the bonded length (L_{bonded}) affect the grouted tieback's limit load (F). (Figures 6, 7 and 8) present a variation on critical load (F) against the friction angle of the soil (φ) under different dilative coefficients (η) and different bonded lengths (L_{bonded}). It can be found that the non-associated flow rule, the soil friction angle (φ), and the bonded length (L_{bonded}) have a significant effect on the ultimate load (F).

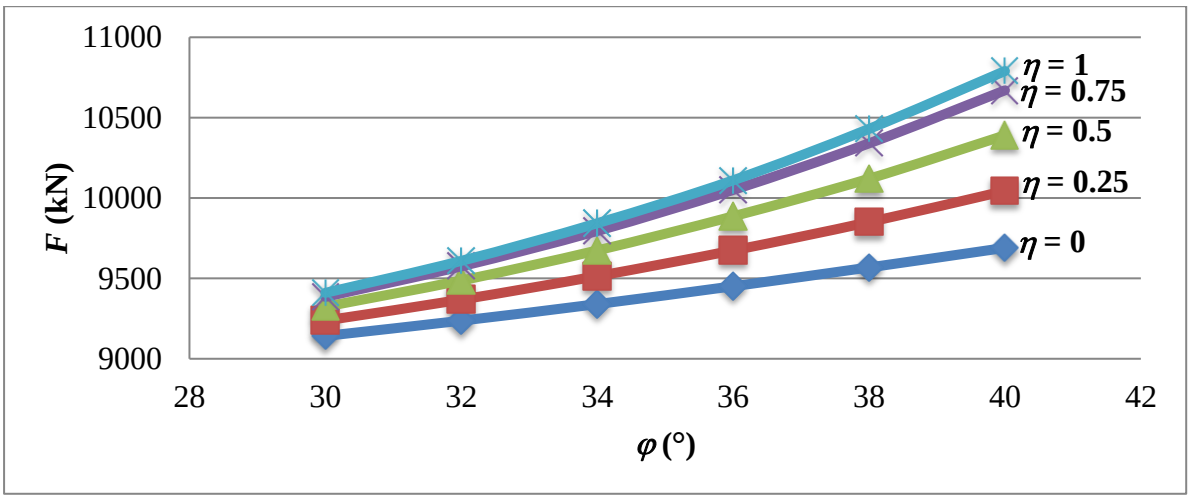

Figure 6: The variation of ultimate load with (φ) and (η) for (L_{bonded} = 6 m)

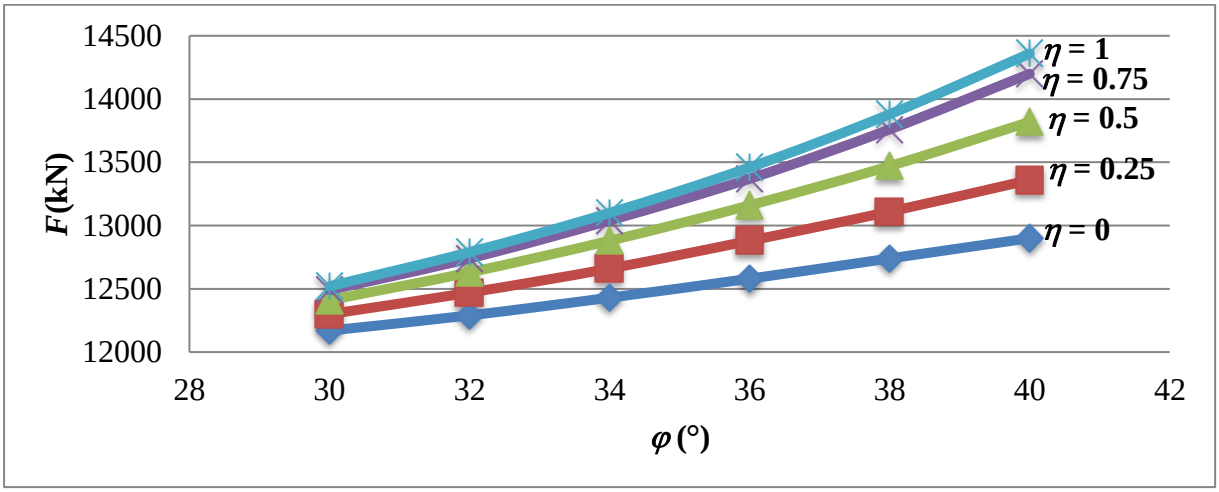

Figure 7: The variation of ultimate load with (φ) and (η) for (L_{bonded} = 8 m)

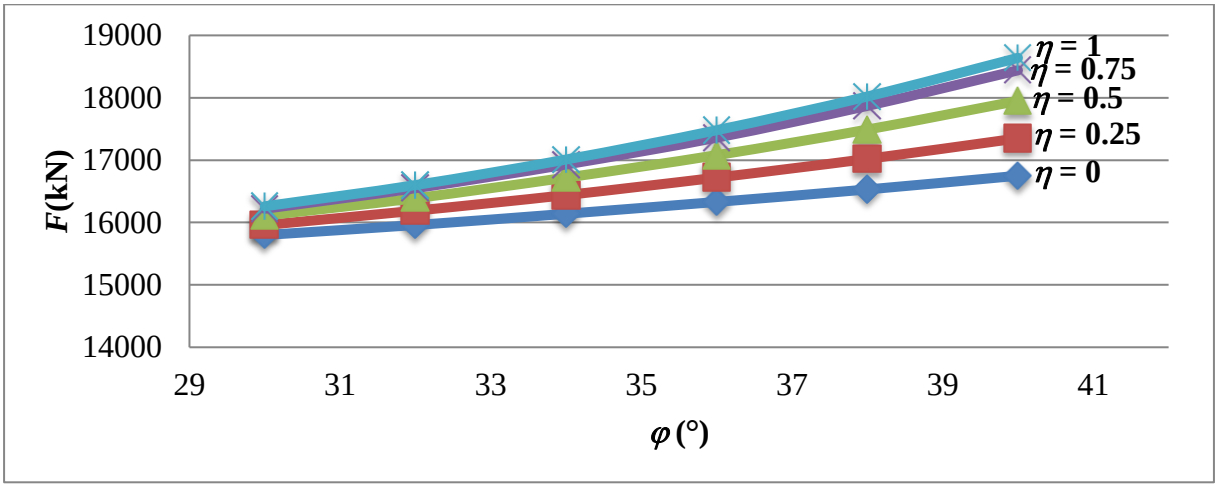

Figure 8: The variation of ultimate load with (φ) and (η) for (L_{bonded} = 10 m)

5.3 The Effect of Combination of Non-Associated Flow Rule With the Soil Friction Angle and the Bonded Length's Diameter

The influence of the non-associated flow rule and the bonded length's diameter of ($d_{bonded\ length}$) with different angles of friction of the soil (φ) on the ultimate load (F) are presented in (Figures 9, 10, and 11). The collapse load (F) is shown to increase with increasing soil angle of friction (φ), dilative coefficient (η), and maintain constant with increasing diameter of bonded length ($d_{bonded\ length}$).

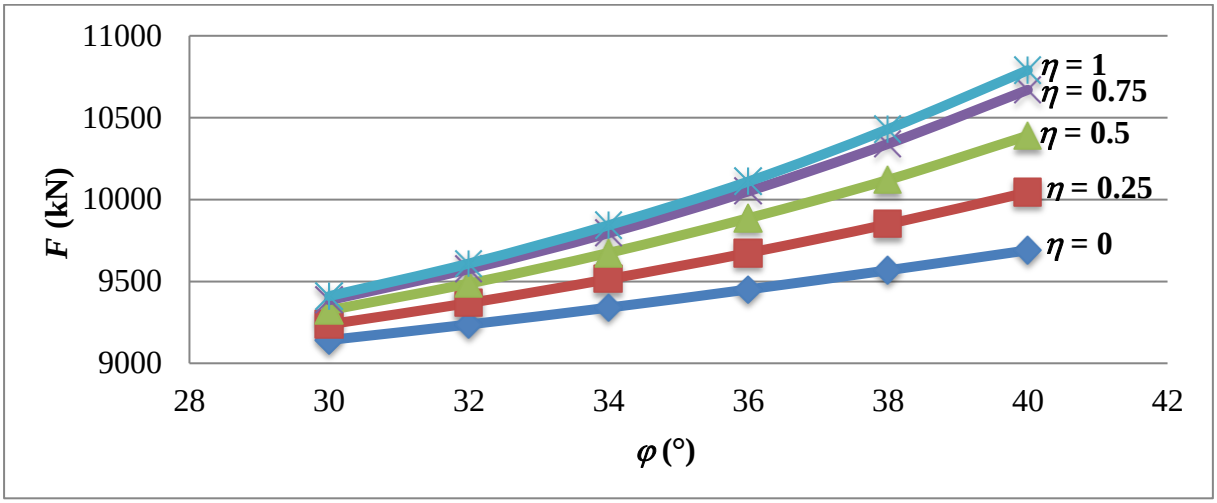

Figure 9: The variation of ultimate load with (φ) and (η) for ($d_{bonded\ length}$ = 0.20m)

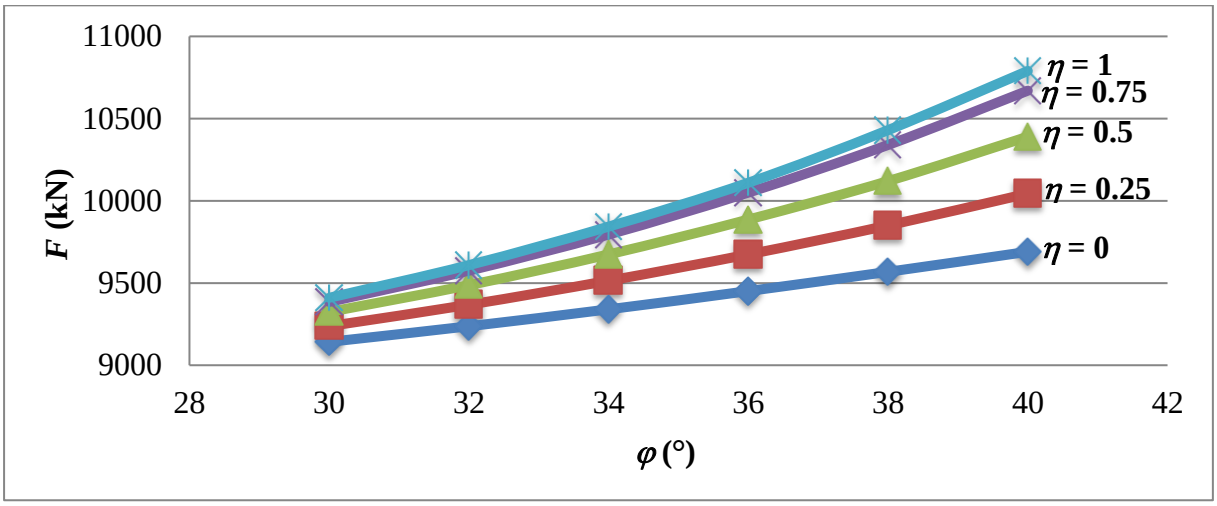

Figure 10: The variation of ultimate load with (φ) and (η) for ($d_{bonded\ length}$ = 0.25m)

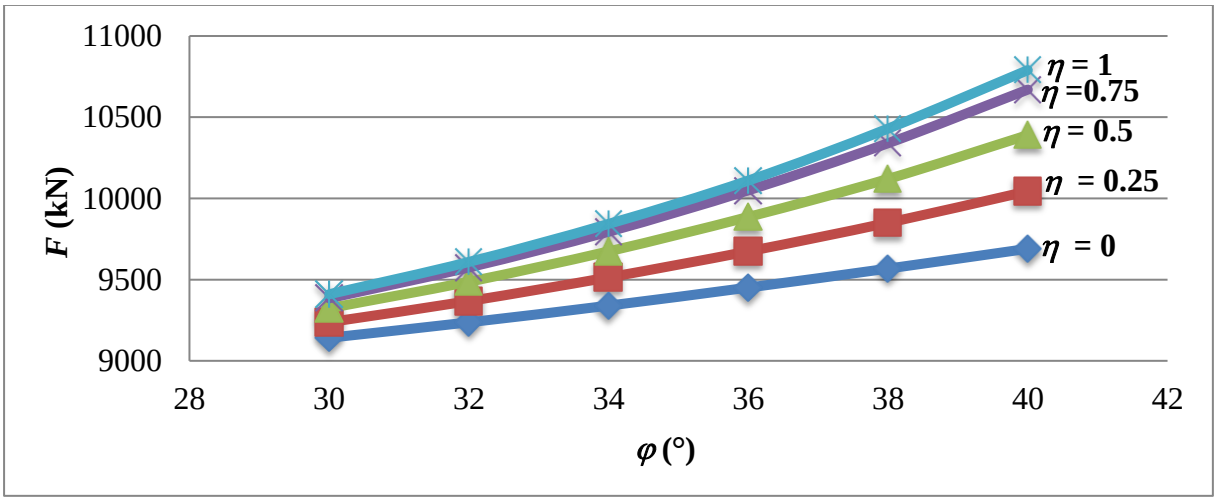

Figure 11: The variation of ultimate load with (φ) and (η) for ($d_{bonded\ length}$ = 0.30m)

6 Conclusion

A series of formulations using the upper bound theorem was utilized to determine the collapse load of a single, inclined rough grouted tieback under axial static loading placed in cohesionless soil. Effects of dilation angle, soil friction angle, grouted tieback's angle of inclination, the bonded length, and the diameter of bonded length were considered in this study. The main conclusions are recapitulated as follows:
- When employing the non-associated flow rule the collapse load (F) of grouted tieback is lower than when using the associated flow rule;

- The ultimate load (F) increases substantially with the increase in the dilation angle (ψ). Therefore, the dilatancy of geotechnical materials should be taken into account while designing the grouted tiebacks.

- Also, the soil angle of friction (φ), the grouted tieback's inclination (λ), and the bonded length (L_{bonded}) affect significantly the collapse load but the stability of grouted tieback is unaffected by the bonded length's diameter ($d_{bonded\ length}$).

References

[1] Hawkes, J. M., Evans R. H. (1951). Bond stresses in reinforced concrete columns and beams. *Structural Engineering, 29*(12), 323-327.

[2] Phillips, S.H.E. (1970).*Factors affecting design of anchorages in rock,* Cementation Research Report R48/70, cementation research Ltd., London.

[3] Littlejohn, G.S. (1970). Soil anchors. In the Conference on Ground Engineering. I.C.E, pp.33-34, London, England.

[4] Kramer, H. (1978). Determination of the carrying capacity of ground anchors with the correlation and regression analysis. *Revue Française de Géotechnique*, *3*, 76-81.

[5] Hanna, T.H. (1982).*Foundations in tension-ground anchors,* 1st Ed., Berkshire, England: Trans Tech Publications.

[6] Mekki, F., Meksaouine, M. & Guenfoud, M. (2009). Theoretical study of the behaviour of anchors in homogeneous soil. *International Review on Modelling and Simulations, 2*(2), 221- 226.

[7] Mekki, F., Meksaouine, M. & Guenfoud, M. (2011). Etude théorique du comportement des tirants d'ancrages dans un sol pulvérulent. *Synthèse: Revue des Sciences et de la Technologie*, *23*, 22-30.

[8] Rong, J. Z., Jun, J.Z., Pei, Y.L., Juan, Z. & Shun, Y. (2012). A method for predicting mechanical behavior of HPJG-Anchors part I: Mechanical characteristics and load transfer models. *Computer and Geotechnics*, 45, 62-73. DOI:10.1016/j.compgeo.2012.05.004

[9] Mekki, F. (2015).*Etude théorique du comportement des tirants d'ancrages*, Deutschland, Allemagne : Editions Universitaires Européennes.

[10] Yang, Z., Chen, J., Zhang, H., Zhao, X. &Li, H. (2018). Analytical calculation on the load displacement curve of grouted soil anchor. *Journal of Engineering Science and Technology Review*, *11* (3), 31- 41. DOI:10.25103/jestr.113.05

[11] Mekki, F., Meksaouine, M. (2019). Application of the theory of limit analysis for the study of ground anchor in homogeneous soil. *Selected Scientific Papers. Journal of Civil Engineering*, *14*(2), 73-86. DOI: 10.1515/sspjce-2019-0019

[12] Mekki, F., Meksaouine, M. (2020). Theoretical study of behaviour of ground anchor in frictional soil by the use of the kinematic approach of limit analysis. In Makul, N. (Ed.), *Recent Advances in Science and Technology Research*, 7, 1st Ed., pp.44-55, West Bengal, India: Book Publisher International.

[13] Mekki, F., (2022).Comparison between the performance of vertical and inclined grouted soil anchors in sandy soils under static axial load. *Algerian Journal of Research and Technology, 6*(2)1-8.

[14] Nguyen-Thoi, T., Phung-Van, P., Nguyen-Thoi, M.H. & Dang-Trung, H. (2015). An upper-bound limit analysis of mindlin plates using CS-DSG3 method and second-order cone programming. *Journal of Computational and Applied Mathematics*, *281*, 32-48.DOI:10.1016/J.CAM.2014.12.006

[15] Pan, Q., Dias, D. (2017). Upper-bound analysis on the face stability of non-circular tunnel. *Tunnelling and Underground Space Technology, 62*, 96-102.DOI :10.1016/j.tust.2016.11.010

[16] Chiozzi, A., Milani, G., Grillanda, M. & Tralli, A. (2018). A fast and general upper-bound limit analysis approach for out-of-plane loaded masonry walls. *Meccanica*, *53*, 1875-1898. DOI : 10.1007/s11012-017-0637-x

[17] Lyu, C., Zeng, Z. (2019).Upper bound limit analysis of unsymmetrical progressive collapse of shallow tunnels in inclined rock stratum. *Computers and Geotechnics*,*116*,103199.DOI:10.1016/j.compgeo.2019.103199

[18] Alhajj Chehade, H., Dias, D., Sadek, M., Jenck, O. & Hage Chehade, F. (2020). Upper bound seismic limit analysis of geosynthetic-reinforced unsaturated soil walls. *Geotextiles and Geomembrane*s, *48*(4), 419-430. DOI : 10.1016/j.geotexmem.2020.02.001

[19] Chen, W.F. (1975). *Limit Analysis and Soil Plasticity*, 1st Ed., Amsterdam, New York: Elsevier.

[20] Drescher, A., Detournay, E. (1993). Limit load in translational failure mechanisms for associative and non-associative materials. *Géotechnique, 43*(3), 443–456. DOI :10.1080/geot.1993.43.3.443

DOI: 10.2478/sspjce-2024-0002

Viscoelastic and Thermal Characterization of a Composite Material Based on Unsaturated Polyester Resin Reinforced with Perlite

Ouided Dehas[1*], Yasmina Biskri[1], Mohammed Benzerara[2], Laidi Babouri[1], Acheref Cherifi[3]

[1]Higher Normal School of Technological Education, Azzaba, Skikda, Algeria.
[2]Materials, Geomaterials and Environment Laboratory (LMGE), Department of Civil Engineering, Badji Mokhtar- Annaba university, P. O. Box 12, 23000 Annaba, Algeria.
[3]Research center in industrial technologies, additive manufacturing research unit, Industry zone A15, Setif 19000, Algeria.
[*]e-mail: dehasouided@gmail.com

Abstract
In this work, it was proposed to replace the conventional reinforcement of the unsaturated polyester resin by a mineral, from a siliceous volcanic rock of volcanic nature, perlite. UPR/perlite composites with different proportions of phase components (from 1% to 5% of powder mass part). We used unsaturated polyester resin (UPR) as well as the hardener cobalt octoate and treated and untreated perlite of different dimensions (greater than 60µm, and less than 60µm). The composites were prepared by the contact molding process. The composite plates are hardened for 24 hours at room temperature then placed in an oven for 15 hours at 50°C to undergo post-curing. The composites obtained were subjected to different characterization techniques, namely rheological tests (dynamic mechanical analysis (DMA)), thermal tests (differential calorimetric analysis (DSC)) and Thermogravimetric analysis (ATG) and structural characterization by Fourier transform infrared (FTIR). The DMA measurements showed that the UPR/perlite composites with untreated filler presented conservation modules higher than that of the resin without perlite for the rates of 3% and 4%, while for the composites with treated filler, that at 3% of perlite shown the highest modulus along the glassy zone. Also, the glass transition temperature of the UPR resin was not affected by the addition of perlite. The decrease in intensity at mid-height of the tan δ peaks allowed deducing the existence of a fairly strong UPR/perlite interface. DSC thermograms showed that the exothermic peak is shifted to higher temperatures, due to a delay in the curing reaction caused by the presence of the perlite particles. This study concluded that the perlite enhances the properties of composites.

Keywords: unsaturated polyester resin, perlite, composites, DMA, Tg.

1 Introduction

In recent years, polymers have been the subject of increasing interest from manufacturers. The aim was to achieve the production and marketing of new materials with improved thermomechanical properties. Currently, polymer materials offer ease of processing and are therefore widely used in all industrial sectors. Their intrinsic properties being, however,

relatively weak, it is necessary to improve those using adjuvants (coloring, fillers, reinforcements, unfolding, etc.) The evolution of polymer materials has involved the development of composites with an organic matrix reinforced by small particles (e.g. talc, fiberglass, wood chips, calcium carbonate, etc.), also called filler. The introduction of filler makes it possible to improve the mechanical and physical properties of the matrix (polymer) [1].

Polymer composite materials are multiphase materials used for their physicochemical, mechanical and electrical properties, etc. However, when designing the object, we often realize that the properties of the polymer alone are insufficient. Indeed, modern technology requires materials that combine rigidity, mechanical resistance, high toughness and great lightness. No simple material can combine all these physical characteristics at the same time; this is why, for a number of years, we have been seeking to obtain materials combining different properties, "composite materials".

Composites have often played a role as a substitute for metallic and ceramic materials, due to their lightness, ease of execution and good properties. In fact, the respective qualities of the associated constituents complement each other to form a material with improved mechanical, thermal, electrical and/or physicochemical performances. The progress of composite materials having one or more of these particular properties generally rejoins to a specified need. It is thus possible to create heterogeneous materials allowing, for example, to reduce the mass of a part, while improving its mechanical properties, thanks to the combination of a fibrous reinforcement and an organic resin.

The adaptability of this material makes it an incontestable asset which explains its increasingly widespread use, particularly in the transport industry (air, maritime and rail), sports and leisure, and the construction industry [2].

Recently, nanocomposites with UPR matrix and particle reinforcements have been an exciting area of research due to the significant improvements in all the properties among these nanomaterials we can cite epoxy resin/perlite [3-9], These composites have been widely Used in industrial applications such as marine, automotive, pipeline systems and construction industrial due to their low cost, high chemical resistance and good workability.

Several studies in which fibrous reinforcements have been incorporated into thermosets and particularly into polyester resin can be found in the literature [10-35] Indeed, among fiber-reinforced polyester materials, glass fiber composites are the most general due to their favorable mechanical and economic characteristics [10]. However, a disadvantage constituted by the lack of affinity between the matrix and the reinforcement generates a transition to fragile mechanical behavior and can inflict limitations on many applications.

For this reason, research on fiber-reinforced thermosetting polymers generally focus on characterizing interface behavior, adaptation of the interface [11-15] as well as on the effects of the fiber-matrix interface and on the mechanical properties of composite materials [12] Organosilanes are the most widely used coupling agents for improving the interfacial adhesion of fiber glass reinforced materials. Their efficacy depends, among other things, on the nature and pretreatment of the substrate, the type of silane used and the process [19-21]. In addition to glass fibers, thermosets have also been reinforced with other types of fibers. A study of the influence of interfacial shear strength on various mechanical strength properties of a carbon fiber-reinforced epoxy composite showed that the strengths with notable shear stresses could be significantly improved by a more effective interface [22].

Currently, there is great interest in incorporating plant fibers into polymers in order to develop low-density biocomposites. Similarly, several natural fibers such as sisal, jute and the Alfa have been studied as reinforcement in UPR composites [25-29]. Recently, nanocomposites with an unsaturated polyester matrix and mineral filler have been a new area of research due to the acceptable performance on all properties among these nanomaterials we can cite polyester resin / montmorillonite (MMT) [36-38], UPR /clay [39].
In this work, we proposed to replace the classic reinforcement of unsaturated polyester resin with an ore, coming from a siliceous rock of volcanic nature, perlite. This filler has the particular characteristic, relative to ores already incorporated into polymers, of containing a very large proportion of pores which can allow it to exfoliate under certain conditions, and to show a large specific surface area. Access of the liquid resin to the pores of the filler could make it possible to develop sufficient interactions to obtain new composites with acceptable performance, which constitutes the essential objective of our study.

2 Experimental

2.1 Materials

2.1.1 Unsaturated polyester resin

Isophthalic unsaturated polyester resin provided by the company Maghreb Pipe of M'sila (Algeria) specialized in the manufacture of polyester resin laminate and fiber glass was used in this study. It is a product marketed by the company Exon Mobil Chemical in the form of a low viscosity mixture of 373 mPa.S at 25°C. The mechanical and physical characteristics of this resin are given in Table 1.

Table 1: Mechanical and Physical characteristics of resin

Characteristics	Unit	Value
Tensile strength	MPa	40-60
Barcol hardness	-	40-45
Flexural strength	MPa	80-100
Application method	-	Manual application
Density	kg/dm^3	1.09 -1.11
Curing time	min	45-60

2.1.2 Hardener

It is a substance which increases the speed of a chemical reaction without being consumed and without modifying the final position of the thermodynamic equilibrium of this reaction. The dosage to be respected for this catalyst is 1.5-2% by mass. Raw molecular formula of catalyst ‘’ methyl ethyl ketone peroxide (MEKP)”: $C_8H_{18}O_6$

Table 2: Characteristics of MEKP catalyst

Chemical formula	$C_8H_{18}O_6$
Molecular weight	210.22 g/mol
Density at 20°C	1.14 g/cm^3

Active oxygen	9.0-9.2 (% mass)
Storage temperature	25°C max
Color	Clear
Storage	6 months

2.1.3 Perlite

In the initial state, perlite looks like sand containing water. It is a natural siliceous volcanic rock. It is expanded industrially by a heat treatment which expands it by 4 to 20 times its volume and forms small porous grains showing tiny cavities. It is very light and friable; it is a natural and ecological mineral insulator, non-polluting and non-toxic for humans. The perlite used in this work was supplied to us in this expanded form and comes from Tlemcen-Maghnia, Algeria. The general characteristics of perlite are grouped in Table 3.

Table 3: Physical characteristics of perlite

Characteristics	Unit	Value
Color	-	White
Shine	%	84
Refractive index	-	1.47
Specific gravity	g/cm^3	2.34
Density	Kg/m^3	70

2.2 Preparation of UPR/Perlite composites

2.2.1 Sifting perlite

Before preparing the composites, the perlite was sifted using sieves with different mesh sizes, in order to separate two fractions of ores with the following grain sizes: between 80 µm and 60 µm (Perlite >60 µm) and less than 60µm (Perlite <60 µm).

2.2.2 Silane treatment

In the literature, chemical treatment with (3-aminopropyl) triethoxysilane, also known as silane (Figure 1) is often used on fibers of mineral and plant origin.

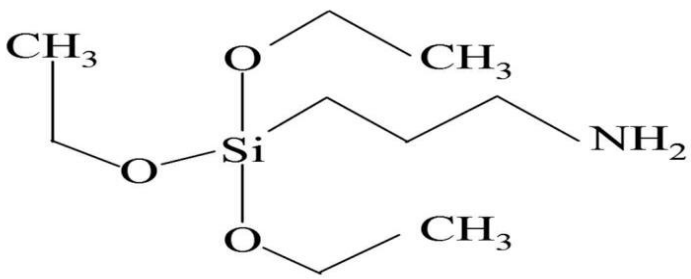

Figure 1: Chemical formula of (3-aminopropyl) triethoxysilane

Silinization is one of the chemical treatments which aim to facilitate adhesion between the fillers and the polymer matrix. The procedure adopted for chemical treatments with silane is as follows: firstly, the charge submits to gasification. Thus, an ethanol/water solution (60/40, v/v) was prepared; the pH was adjusted between 4 and 4.5 by adding a drop of glacial acetic acid. Then, silane (3% by mass) was added. Hydrolysis of the prepared solution was carried out for 2 h at room temperature. Finally, perlite was added, and the suspension was kept for 3 h at 70°C. Then, before extrusion, the load is pre-dried at 105°C for 24 hours in order to eliminate the absorbed humidity and ethanol, and thus avoid the formation of agglomerates. A single concentration of silane was chosen and fixed [40]. The manufacturing process of composite materials influences the properties of the finished product; so, this is a very important step. Indeed, depending on the desired performance of the composite, the conditions and implementation parameters were determined. The production process used in this work is contact molding, frequently used for shaping thermosetting matrix mixtures. The accelerated unsaturated polyester resin is mixed randomly and gently in a container. Perlite, of both particle sizes, untreated and surface treated and steamed at 60°C for 24 hours, is added at the following rates 1, 2, 3, 4 and 5%. Finally, to have good curing of the polyester resin a concentration of about 1.5 % of methyl ethyl ketone peroxide (MEKP) is added. The different mixtures, thus prepared, are poured onto a Teflon sheet on which the wooden mold is placed. The plates of the three types of composites are hardened for 24 hours at room temperature then placed in an oven for 15 hours at 50°C to undergo post-curing (Figure 2).

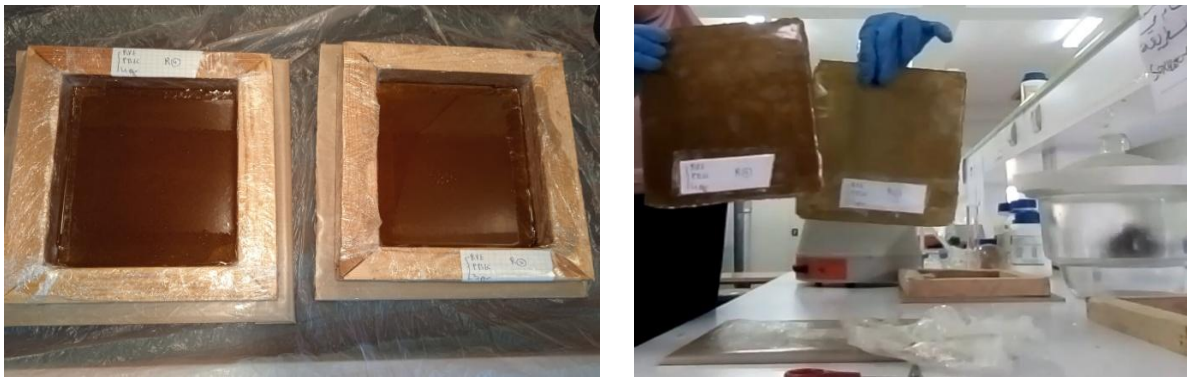

Figure 2: UPR/perlite composites preparation steps

3 Experimental techniques

3.1.1 Structural analysis by FTIR spectroscopy

The structural study by infrared spectrophotometry aims to highlight the existence of interactions between the matrix and the incorporated reinforcements. The perlite ore was analyzed in the form of pellets prepared according to the following compositions: 3% perlite and 97% potassium bromide (KBr) (scan number: 10). The FTIR spectra of the polyester resin and composites were obtained on very thin films (scan number: 5). The infrared spectra were recorded using a Perkin Elmer type spectrophotometer over a wave number range spanning from 4000 to 500 cm^{-1}, using a resolution equal to 2 cm^{-1}.

3.1.2 Dynamic Mechanical Thermal Analysis

The viscoelastic properties of pure UPR resin and UPR/perlite composite materials were studied in dynamical mechanical thermal analyzer DMAQ-800TA (TA instruments, New Castle, DE). The tests were carried out at a frequency of 1 Hz, amplitude of 10 µm, a heating rate of 5°C/min and over a temperature range ranging from -50 to 180°C. The tests were performed using rectangular samples with dimensions of (35x10x4) mm^3. All experiments were carried out under nitrogen atmosphere (flow: 50 mL/min).

3.1.3 Differential Scanning Calorimetry (DSC)

The DSC study was carried out using a TA Q-100 apparatus (TA instruments, New Castle, DE). Samples weighing between 5 and 10 mg was placed in a sealed aluminum pan, then placed in the oven where they submit to the following three-step program: heating from 25 to 250°C at a heating rate of 10°C / min, then they were maintained at 250°C for 2 min followed by cooling down to 25°C. Afterwards, a second DSC heating run was carried out from 25 up to 25°C at a heating rate of 10°C /min. All experiments were carried out under nitrogen atmosphere (flow rate: 50 mL/min).

3.1.4 Thermal Gravimetric Analysis (TGA)

Thermal Gravimetric Analysis (TGA) is a thermal analysis technique for measuring the quantity and rate of change in mass of a sample as a function of temperature and time. It makes it possible to evaluate the loss of mass or phase variations when the material decomposes, dehydrates or oxidizes. The TGA of the composites was carried out in Q-500 TA instrument (TA Instruments, New Castle, DE). An inert gas sweep is provided in the balance compartment with a flow rate of 100 mL/min, in order to protect the mechanism carrying out the weighing from any risk of oxidation. In this study, the measurements were carried out using a temperature sweep ranging from ambient to 600°C, at a heating rate of 10°C/min.

4 Results and discussion

4.1.1 Characterization of UPR, perlite and UPR/perlite composites by IRTF

The FTIR spectrum of the unsaturated polyester resin, represented by Figure 3, shows a large mass characteristic of the elongation vibrations of the hydroxyl groups between 3600 and 3200 cm^{-1}. The elongation vibrations of aromatic CH are observed between 3090 and 3000 cm^{-1}, while those of aliphatic CH are detected between 2990 and 2850 cm^{-1}, approximately. On the other hand, a strong band is observed around 1720 cm^{-1}. This is a characteristic of the carbonyl group of polyester while the vibration bands of the aromatic cycle are identified around 1600, 1504 and 1470 cm^{-1}. The region between 1400 and 1000 cm^{-1} is particularly complex because it is rich in bands and contains the deformation vibration of the C-O bond of polyester [41].

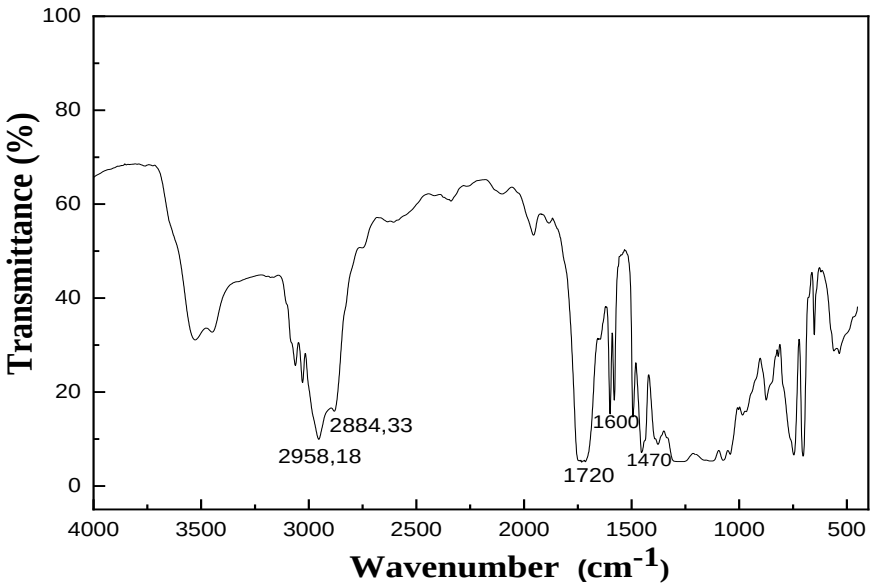

Figure 3: FTIR spectra of unsaturated polyester resin (UPR)

The FTIR spectra given in (Figure 4) characterizes untreated and treated perlite by silane. The spectrum of untreated perlite shows a broad absorption band, situated between 3600 and 3000

cm^{-1} and attributed to the valence vibrations of hydroxyl groups. Furthermore, the band observed at 1637 cm^{-1} is characteristic of the vibration of the H-O-H bond of water adsorbed on the surface of the ore. The intense band detected between 1400 and 800 cm^{-1} and centered around 1046 cm^{-1} is attributed to the vibration of the Si-O bond of the Si-O-Si group, while the one located at 797 cm^{-1} corresponds to the vibrations of deformation of the Si-O bond of the Si-O-Al group [42-43].

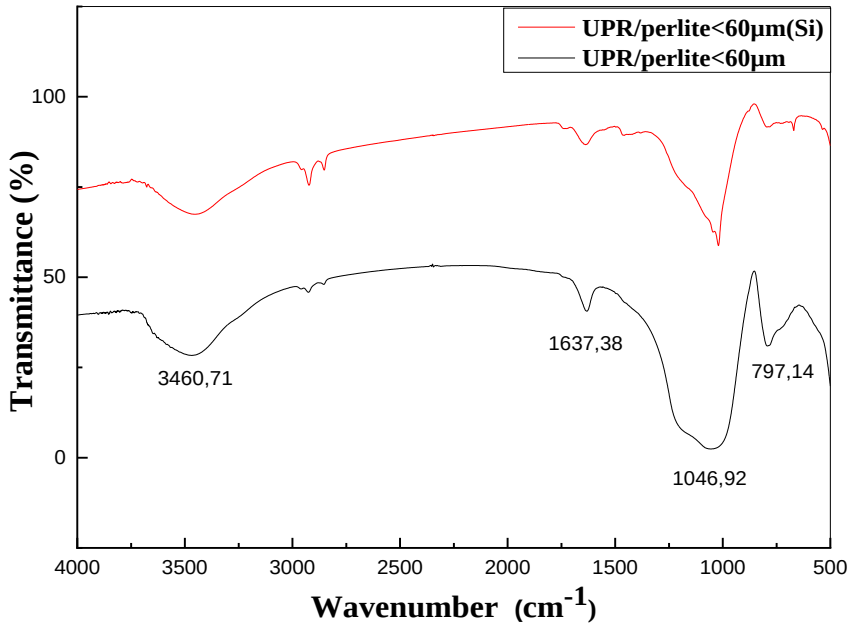

Figure 4: FTIR spectra of entreated perlite and perlite treated by silane

After treatment, we notice that the spectrum of the perlite treated with the silane coupling agent is partially different from that of the untreated perlite and this is explained by:
The surface treatment should lead to the appearance of a new bond relating the silicon atoms of the treating agent to the hydroxyls of the filler, which results in the formation of a Si-O bridge between the two components. But, if the vibration frequency of this last bond coincides with that of the Si-O bond already existing in the structure of the perlite, it becomes difficult to comment on the result of the treatment.
Furthermore, the FTIR spectrum of the UPR/perlite composite >60µm at 3pcr, given in (Figure 5), is perfectly similar to that of UPR. We note, however, a rather remarkable intensification of the band characteristic of the valence vibrations of the hydroxyl groups, which appears in this spectrum in the form of a fairly broad mass, denoting a greater concentration of the OH groups in the composite, following the incorporation of the load.

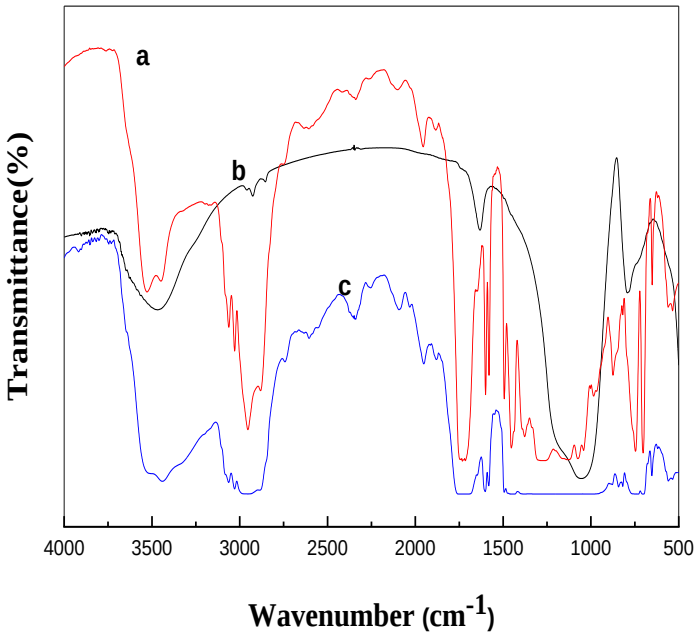

Figure 5: FTIR spectra of: (a) UPR, (b) untreated pearlite and (c) UPR/perlite composite >60µm at 3%

4.1.2 Viscoelastic properties of UPR/perlite composites

4.1.2.1 Effect of rate of filler

The variations in the conservation module E' of the UPR resin and the UPR/perlite composites<60µm formulated from the untreated mineral charge are given in (Figure 6). The thermograms show a similar appearance including, firstly, the glassy domain extending until the occurrence of the glass transition, identified thanks to the strong reduction in the modulus, then the region characteristic of rubber behavior where the materials present constant modules. In the glassy domain where the storage modulus does not vary with increasing temperature, we found that after the addition of perlite, the modulus increases with the loading rate. This increase is very evident for the loading rates of 3 and 4% which, apparently, contribute to a notable increase in the stiffness of the composites. So, more the rate increases, more the modulus is higher. Approaching the glass transition, the conservation module of composites drops sharply due to the increase in flexibility of composites. Beyond the glass transition zone, the modulus E' of the composites reaches very low values because of their rubbery behavior and does not vary with the increase in temperature and perlite content. The result concluded from this study funds the fact that the addition of 3-4% perlite improves the properties of UPR resin.

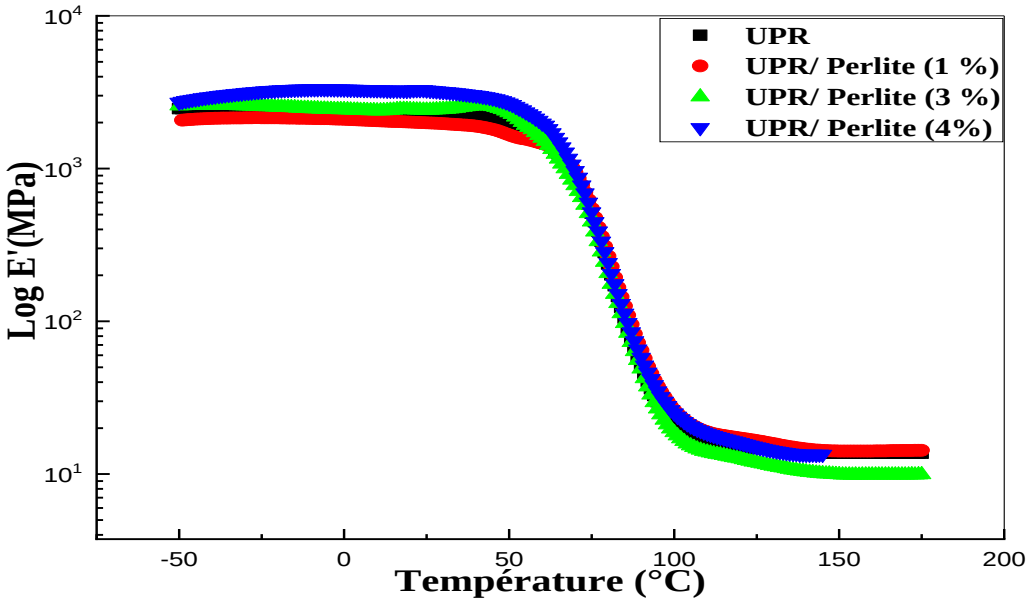

Figure 6: Variations in the conservation module E' of UPR resin and UPR/perlite composites <60µm as a function of temperature and the rate of untreated perlite

The study of the variations in the glass transition temperature of the resin after the incorporation of the perlite is carried out by monitoring the variations of the loss factor tan δ as a function of the temperature and the loading rate as expressed in the (Figure 7**)**. The variations in tan δ show, essentially, a main structural relaxation due to the UPR resin whose Tg, being around 91°C, does not seem to be affected by the addition of perlite. A minor structural relaxation is also detected around 60°C and is also observed during variations in the storage modulus E', for perlite rates of 3 and 4%. By analogy with the UPR/PET fiber composites [44], the demonstration of such a transition suggests the formation of an interface resulting from the favorable interactions between the perlite and the UPR resin. However, due to the lack of affinity between the mineral perlite and the organic resin, it is quite possible that the interactions are of a mechanical nature, resulting from the platelet or flake shape of the perlite, which allows it to anchor in the matrix.

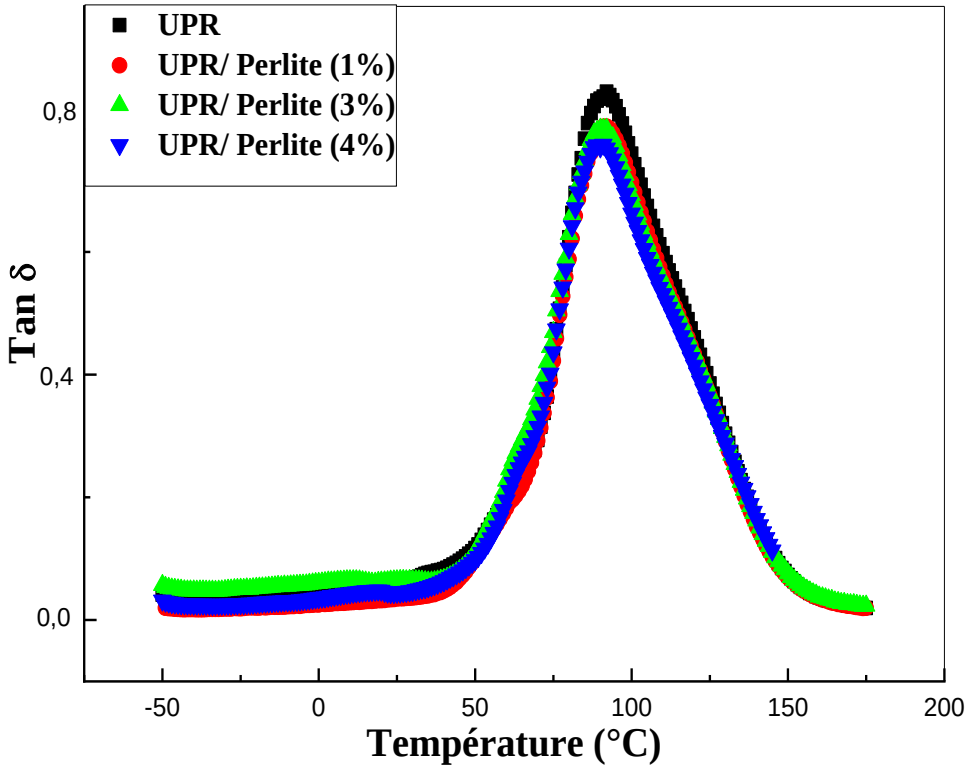

Figure 7: Variations in the factor of loss tan δ of UPR resin and UPR/perlite composites <60µm as a function of temperature and the rate of untreated perlite

Morote-Martinez et al. [39], Pothan et al. [45] et Aziz et al. [46], proposed that the interactions between a reinforcement and a matrix can be evaluated from the values of the maximum of tan δ. Similarly, Martınez-Hernandez et al. [47] et Keusch et al. [48] stated that the intensity of the tan δ peak is inversely proportional to the interface resistance. Furthermore, the width at half maximum of the tan δ peak indicates the volume of the interface [46]. According to the values shown in Table 4, we found that compared to the UPR resin, the values of the tan δ peak maxima of the composites decrease slightly with the addition of perlite. This supports the existence of interactions between these two components and/or the increase in the degree of crosslinking of the UPR resin in the presence of perlite. Furthermore, the increase in the value of the width at half height of the tan δ peak when the concentration of the filler is 4% is equal with the development of a wider interface between the perlite and the UPR resin. This suggests that at this rate, optimal dispersion of the load is achieved and thus supports the results of the mechanical tests.

Table 4 : Tg values, from height to maximum and the width at half maximum of the tan δ peak of UPR and untreated UPR/perlite <60µm composites

Composites	Tg (°C)	Maximum height	Width at half height (cm)
UPR	91	0.86	1.4
UPR/ Perlite (1%)	90	0.80	1.4
UPR/Perlite (3%)	90	0.80	1.4
UPR/Perlite (4%)	91	0.77	1.6

4.1.2.2 Effect of perlite surface treatment

The effect of the surface treatment of perlite with silane on variations in the conservation module E' of the UPR/perlite <60µm composites is shown in (Figure 8). In the vitreous domain, the modulus E' of the composites with the rates of filler of 1 and 3% is not affected at all by the silane treatment, but shows an improvement, relative to the composites with untreated filler after the Tg of the UPR resin. Furthermore, the modulus E' decreases notably for the composite with 4% perlite, and this along the vitreous and rubbery domains. This seems to suggest that the best dispersion is obtained for low concentrations of perlite whose composites show a higher modulus in the vitreous domain. The decrease in modulus in the case of the 4% composite could probably be due to the agglomeration of the filler which distortions the effect of the surface treatment. As for untreated perlite composites, variations in E' show a second minor structural relaxation occurring around 55°C and which affirms to the formation of an intermediate structure which has its own viscoelastic characteristics, different from those of the matrix.

The results of E' are supported by (Figure 9) giving the variations of tan δ as a function of the temperature and the rate of perlite treated and the values of the parameters reported in Table 5. Indeed, we notice that the Tg of the resin UPR is not affected by the treatment and the maximum height of the tan δ peak decreases slightly with the increase in the rate of filler, which confirms the existence of interactions between the UPR resin and the perlite. Furthermore, the volume of the interface decreases with the increase in the treated perlite rate up to 4%, which confirms the formation of charge aggregates when the perlite rate ranges this concentration.

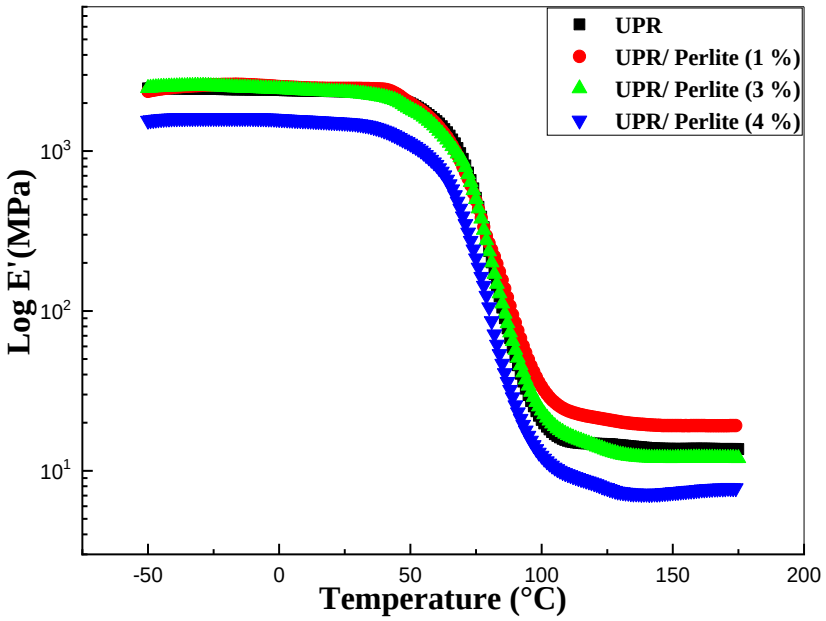

Figure 8: Variations in the conservation module E' of UPR resin and UPR/perlite composites <60µm treated with silane as a function of temperature

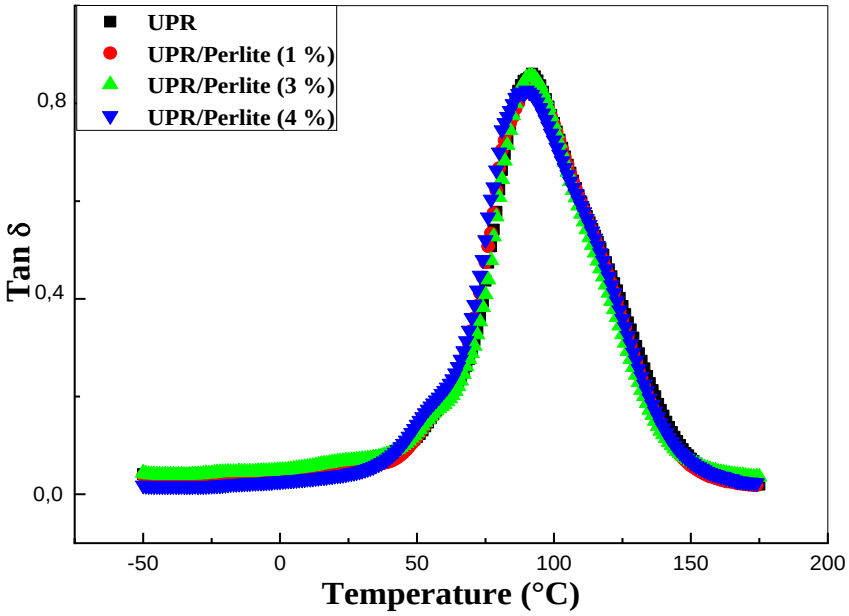

Figure 9: Variations in the factor of loss tan δ of UPR resin and UPR/perlite composites <60µm treated with silane as a function of temperature

Table 5: Tg values, from height to maximum and the width at half maximum of the tan δ peak of UPR and silane-treated UPR/perlite <60µm composites

Composites	Tg (°C)	Maximum height	Width at half height (cm)
UPR	91	0.86	1.4
UPR/Perlite (1%)	91	0.83	1.4
UPR/Perlite (3%)	91	0.85	1.4
UPR/Perlite (4%)	91	0.82	1.3

4.1.3 Thermal properties of UPR/perlite composites

4.1.3.1 Study of post-curing and glass transition processes

The DSC analysis was carried out in order to highlight the influence of the perlite ore particles on the curing behavior of the polyester resin, and to evaluate the evolution of the thermal characteristics of the UPR/perlite composites as a function of the rate of filler and surface treatment. The thermograms representing the first heating cycles of the UPR/perlite composites are given in (Figure 10). They present, first, the glass transition temperature of the UPR matrix, then an exothermic peak corresponding to the post-curing process whose temperature maximum and area closely depend on the rate of perlite contained in the composite. Furthermore, the thermograms of the second heating cycle reveal only the Tg of the UPR resin, without any exothermic peak, which suggests the total hardening of the matrix, as illustrated in (Figure 11).

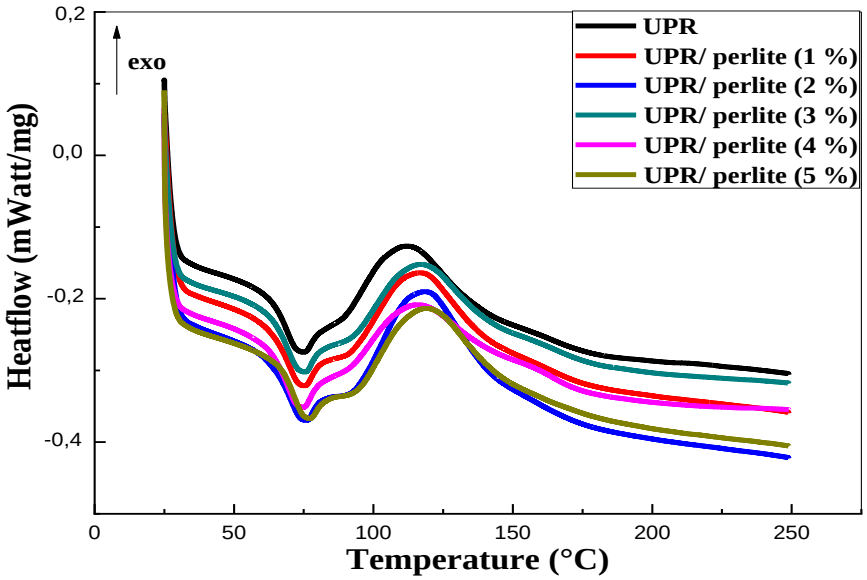

Figure 10: DSC thermograms of UPR resin and UPR/perlite composites <60µm treated with silane (first heating cycles)

Table 6 brings together the values of the maximum temperature of the exothermic peaks and the enthalpy of the post-curing reaction for the pure resin and the UPR/perlite composites. Relative to pure resin, the addition of perlite resulted in a slight delay in the matrix curing

reaction, shifting the exothermic peak to higher temperatures (3 and 4% specifically), as is shown in (Figure 8). Furthermore, the enthalpy of the reaction decreased for concentrations of 3, 4 and 5%, but increased for rates of 1.2% perlite. Same results were noticed by Chieruzzi et al [37] who noted that the addition of clay nanoparticles causes a delay in the curing process and affects the final crosslinking rate of the resin. For 1 and 2% composites, the increase in post-curing temperature and enthalpy reflects slow hardening due to low reactivity of the UPR resin following the addition of perlite. Furthermore, the composites reinforced with 3 and 4% perlite exhibit a reduction in the enthalpy of the reaction and an increase in the temperature at the maximum of the exothermic peak which expresses a great ability of the resin to harden because of the good dispersion of perlite within the matrix. For the composite containing a concentration of 5% perlite, the increase in the reaction enthalpy and the slight decrease in the exothermic peak temperature, compared to the previous composites, reflect a low ability of the UPR resin to harden.

Table 6: Post-curing temperature and enthalpy values evaluated from the thermograms of the first heating cycle of the UPR resin and the UPR/perlite <60μm composites treated with the silane

Composites	$T_{post\text{-}Curing}$ (°C)	$\Delta H_{post\text{-}curing}$ (J/g)
UPR	112	21
UPR/Perlite (1%)	118	26
UPR/Perlite (2%)	118	25
UPR/Perlite (3%)	120	14
UPR/Perlite (4%)	119	11
UPR/Perlite (5%)	117	19

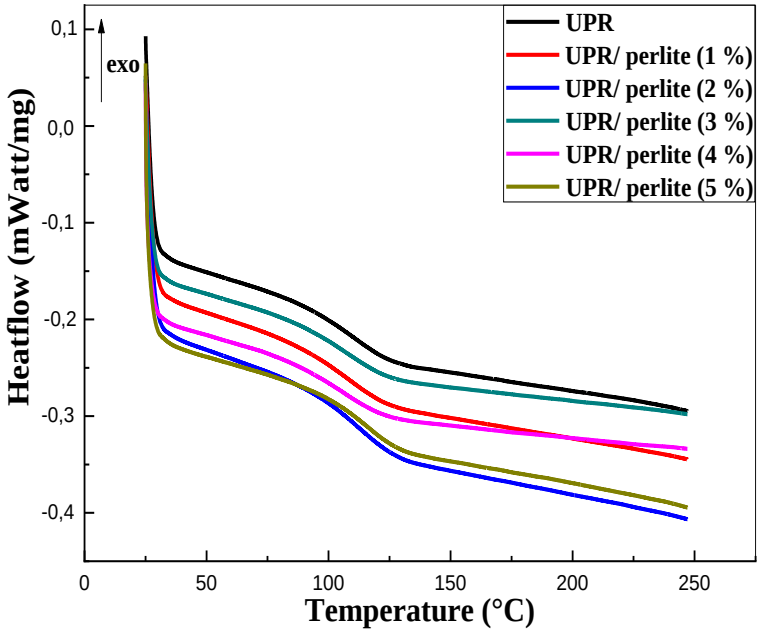

Figure 11: DSC thermograms of UPR resin and UPR/perlite composites <60µm treated with silane (second heating cycles)

The Tg values of the UPR resin in the composites with perlite filler are determined from the thermograms of the second heating cycle and reported in Table 7. Due to the absence of affinity between perlite and UPR, small variations are observed on the Tg of the UPR matrix. This means that in the presence of perlite, the kinetics of the crosslinking reaction of the UPR matrix is considerably disturbed, as was concluded from the thermograms of the first heating cycles; however the total rate of the reaction or the degree crosslinking is only slightly influenced by the presence of the filler and its concentration. Thus, the variations noted in the Tg values can only be attributed to variations in the degrees of crosslinking of the UPR resin in the presence of perlite.

Table 7: Tg values of pure UPR resin and UPR/perlite <60µm composites treated with silane, evaluated from the thermograms of the second heating cycle

Composites	T_g (°C)
UPR	91
UPR/Perlite (1%)	91
UPR/Perlite (2%)	92
UPR/Perlite (3%)	91
UPR/Perlite (4%)	91
UPR/Perlite (5%)	92

4.1.4 Study of the thermal stability of UPR/perlite composites

Figures 12 and 13 represent, respectively, the TG and DTG curves of the matrix and the UPR/perlite composites. Similar to UPR resin, the composites show single-step decomposition.

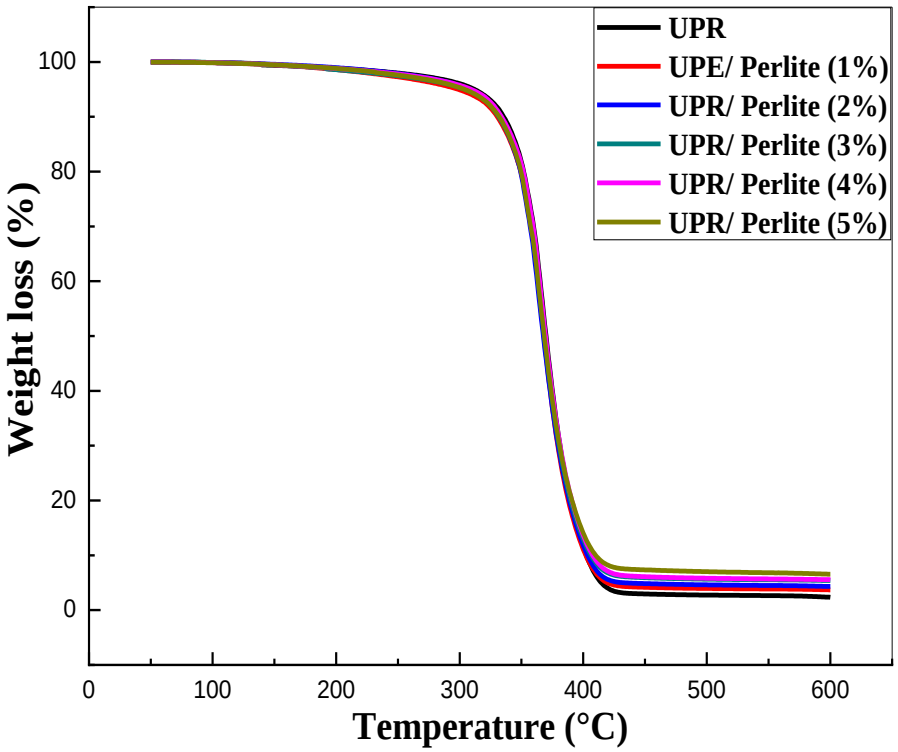

Figure 12: TG thermograms of UPR resin and UPR/perlite composites<60 μm treated with silane

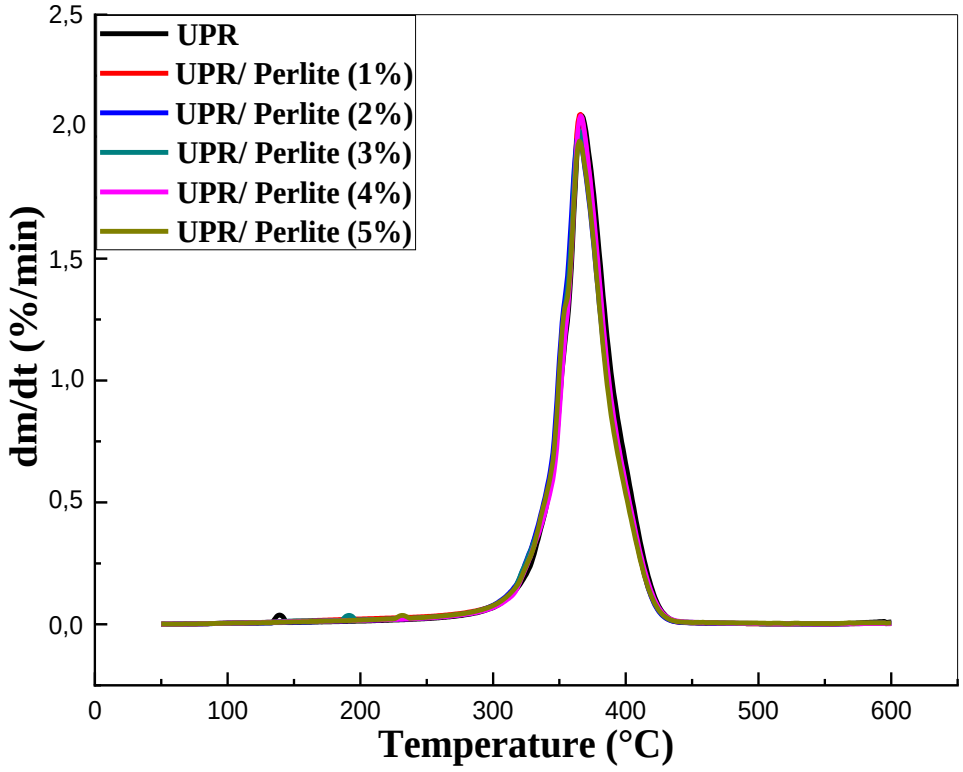

Figure 13: DTG thermograms of UPR resin and UPR/perlite composites<60 µm treated with silane

UPR/perlite composites have thermal stability close to that of pure resin. The values of the degradation parameters, estimated from the TG and DTG curves, are assembled in Table 8. The start of decomposition temperature increases significantly after the addition of perlite, unlike the maximum and end of decomposition temperatures which vary slightly, as shown in Figures 14 and 15.

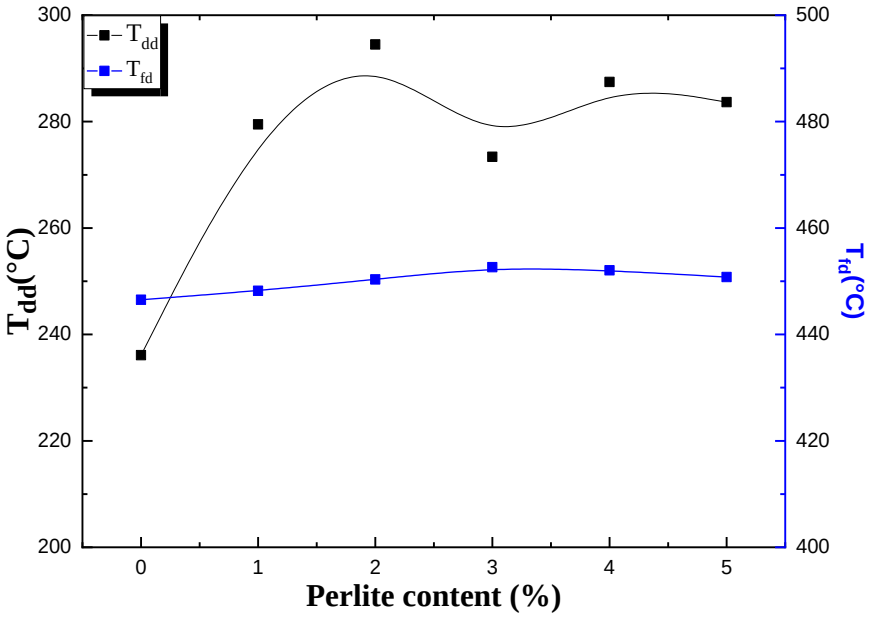

Figure 14: Variations in the start and end temperatures of decomposition of the UPR resin in the UPR/perlite composites <60 µm treated with silane as a function of the rate of charge

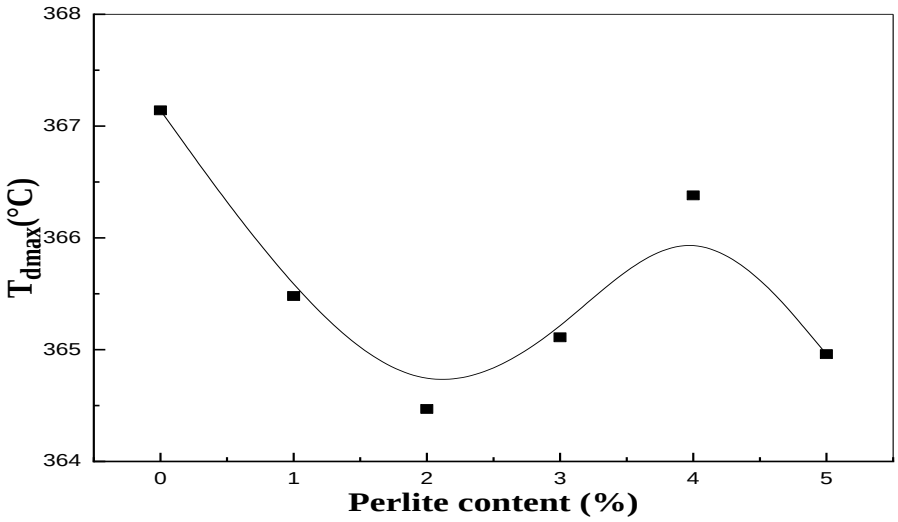

Figure 15: Variations in the maximum decomposition temperature of the UPR resin in the UPR/perlite composites <60 µm treated with the silane as a function of the rate of charge

Table 8: Values of decomposition parameters of UPR resin in UPR/perlite composites <60 µm treated with silane

Rate of filler (%) / Parameter	0	1	2	3	4	5
T_{dd} (°C)	236	279	295	273	287	284
T_{fd} (°C)	447	448	450	453	452	451
T_{dmax} (°C)	367	365	364	365	366	365
V_d (% min)	2,10	2,09	1,99	2,02	2,08	1,98
Loss of mass at T_{dmax} (%)	56	54	55	53	57	60
m_{res} (%)	3	3	4	6	6	7

5 Conclusion

The characterization of the UPR/perlite composites as a function of the rate of filler, the particle size and their surface treatment by the silane coupling agent made it possible to attract certain conclusions. Thus, the infrared analysis did not make it possible to highlight interactions between the filler and the resin, even after the surface treatment with silane, but a slightly remarkable intensification of the band characteristic of the vibrations of the hydroxyl groups was observed.

The filler (perlite) used in this study has the particular characteristic, relatively to minerals already incorporated in the polymers, contain very important pores that can allow it to exfoliate under certain conditions, and show a high specific surface. The access of the liquid resin at the pores of the filler might help develop sufficient interaction to obtain new composites with acceptable performance, which is the main objective of our work.

DMA measurements showed that the filler platelets are well inserted into the matrix and contribute to the mechanical strength of the composites, and this is because "the conservation moduli are higher than that of the resin for rates of 3 and 4% " and we also have " the decrease in the intensity at mid-height of the tan δ peaks made it possible to deduce the existence of a fairly strong UPR/perlite interface" which improves the properties of these composites. Another thermal analysis confirmed that the incorporation of this mineral does not affect the thermal stability of the polyester resin. DSC thermograms showed that the exothermic peak is removed to higher temperatures, due to a delay in the curing reaction caused by the presence of the perlite particles. so we can say that the performances of this material are improved and we have a resistant and at the same time light composite material and also the quality/price ratio increases (economic side). The substitution of traditional fibers such as glass, carbon fibers, etc. Due to the mineral fillers, perlite is interesting from an economic and environmental point of view. We were interested in valorizing this local mineral filler, perlite. Several aspects of this work deserve to be developed subsequently.

These include preparing composite materials with particle sizes less than 60µm; Use other chemical treatment of this filler to increase adhesion and specific surface area, Production of hybrid composites with PET mats and particle reinforcement. Perlite-reinforced unsaturated polyester resin (UPR) composites have been widely used in industrial applications such as marine, automotive, pipeline systems and construction industries due to their low cost, high chemical resistance and good workability.

References

[1] Kadri A., Chouabia N. (2020). Elaboration et caractérisation d'une matrice de PEHD/SiO_2 Mémoire de master, université 08 Mai 45 Guelma-Algérie.

[2] Godara, S.S., Abhishek, Y., Bharat, G., & Rana, R S. (2021). Review on history and characterization of polymer composite materials. Materials Today: Proceedings,44, 2674-277.https://doi.org/10.1016/j.matpr.2020.12.680.

[3] Henghua, Z., Qianbin, D., Juetian, L., & Jiabang, W. (2023). Modified sodium acetate trihydrate/expanded perlite composite phase change material encapsulated by epoxy resin for Radiant floor heating. Journal of Energy Storage,65.

[4] Aneta, K., Wojciech, K., Jacek, G., & Robert, S. (2018). Ablative test of composites with epoxy resin and expanded perlite. Composite Structures, 202, 978-987. https://doi.org/10.1016/j.compstruct.2018.05.018.

[5] AnilSelmi,K.,Gulnare,A.,Mustafa,K.., Suheyla, K., Mura,t I.,& Mehmet G .(2024).Implementat ion of the PECVD process to produce a novel range of filler-polymer-coated perlites for use in epoxy composites. Journal of Industrial and Engineering Chemistry ,133.379-393. https://doi.org/10.1016/j.jiec.2023.12.009.

[6] Mehmet, N K., & Meral, O. (2023). Effect of expanded perlite addition on the thermal conductivity and mechanical properties of bio-composites with hemp-filled. Journal of Building Engineering**,** 71 ,106515, https://doi.org/10.1016/j.jobe.2023.106515.

[7] Wojciech, K., Damian, D., Wojciech, Ż., & Robert, G. (2018). Effect of composition on ablative properties of epoxy composites modified with expanded perlite. Composite Structures , 183, 654-662. https://doi.org/10.1016/j.compstruct.2017.08.047.

[8] Mohamad, A., & Ahmet, E. (2018). Effect of perlite particle contents on delamination toughness of S-glass fiber reinforced epoxy matrix composites. Composites Part B: Engineering , 141,182-190. https://doi.org/10.1016/j.compositesb.2017.12.059.

[9] Md, A., & Ho, S K. (2017). Prediction and evaluation of density and volume fractions for the novel perlite composite affected by internal structure formation. Construction and Building Materials,141,201-215. https://doi.org/10.1016/j.conbuildmat.2017.03.015.

[10] Chandrakanta, M., Chitta,R D. & Smitismita,B.(2021).Influence of moisture absorption on Mechanical properties of kenaf/glass reinforced polyester hybrid composite. Materials Today: Proceeding,38,2596-2600. DOI. https://doi.org/10.1016/j.matpr.2020.08.100.

[11] Aji,t D.,Kelkar,Ram M.,Ronnie,B., & Sachin,S.(2010).Effect of nanoparticles and nano fibers On Mode I fracture toughnesss of fiber glass reinforced polymeric matrix composites. Materials Science and Engineering B, 168,85-89.

[12] Xuyao, Z, Weiguo, L., Li-Hua, S., Ying, L., & Jianxiang, W. (2024). Micromechanics-based modeling of temperature-dependent effective moduli of fiber reinforced polymer composites with interfacial debonding. Composites: Part A, 180.108049. https://doi.org/10.1016/j.compositesa.2024.108049.

[13] Cuixia, W., Longwei G., Yangyang,X., Chao, Z., Xinxin, S.,Chuanwen, X., Gang, Z., Haibo, J., Peng, Z., Hongyuan, F., Zhuwei, P. & Xiaoguang .(2024). Flexural performance and damage evolution of multiple fiberglass-reinforced UV-CIPP composite materials-- A view from mechanics and energy release. Journal of Materials Research and Technology, 29, 3317–3339. https://doi.org/10.1016/j.jmrt.2024.02.051.

[14] Kutlay, S., Mehmet, S., Yoldas, S., Gökhan, E., Ümit, H. & Seckin, E. (2012). Surface treatments of jute fabric: The influence of surface characteristics on jute fabrics and mechanical properties of jute/polyester composites. Industrial Crops and Products, 35, 22–30. https://doi.org/10.1016/j.indcrop.2011.05.020.

[15] Seshaiah,T., Ravikiran, Ch., Narayanan, K., Bridjesh, P. & Seshibe, M,(2024).Experimental and numerical analysis of the Microstructure and mechanical properties of unidirectional glass fiber reinforced epoxy composites. Composite Structures, 331 .117887. https://doi.org/10.1016/j.compstruct.2024.117887.

[16] Mahima, H., Mohaimenul, I., Pavel, Ch., Rafi, U., & Adib, B. (2024). A comparative study on the influence of MWCNT, GO, and Al (OH)3 gel matrix modification on hierarchical structured composite reinforced with needle-punched jute fiber and glass fiber. Results in Engineering,21. 101671. https://doi.org/10.1016/j.rineng.2023.101671.

[17] Pouya, R., Faramarz, A., Mohammad, F., & Mohammad hossein, S. (2019). Effect of styrene-butadiene rubber and fumed silica nano-filler on the microstructure and mechanical properties of glass fiber reinforced unsaturated polyester resin. Composites Part B,173. 106803. https://doi.org/10.1016/j.compositesb.2019.05.014.

[18] Jiaxin, Ch., Yu,I H., Taka, A ., & Hiroshi, U.(2023). Surface modification of carbon-fiber-reinforced plastic by using photo-activated chlorine dioxide radicals as pretreatment of electroless plating. Surfaces and Interfaces, 37, 102644,https://doi.org/10.1016/j.surfin.2023.102644.

[19] Adib Bin, R., Mahima, H., Mohaimenul, I. & Rafi, U. (2024). Nanotechnology-enhanced fiber-reinforced polymer composites: Recent advancements on processing techniques and applications. Heliyon, 10. Issue 2 .e 24692.https://doi.org/10.1016/j.heliyon.2024.e24692.

[20] Sanjeev, K., Robb, W., Ranganathan, P., Yedla, SB., Kalukanimuttam, M. & Kiran, P. (2003). Sample preparation techniques for nano -mechanical characterization of glass fiber reinforced polyester matrix composites. Composites Part A: Applied Science and Manufacturing,34,53-65.

[21] Kabir, M., Wang, H. & Lau, F. (2012). Chemical treatments on plant-based natural fibre reinforced polymer composites. Composites Part B: Engineering, 43,Issue 7,2883-2892.https://doi.org/10.1016/j.compositesb.2012.04.053.

[22] Sundeep., Kanthi, L., Manikandan, N., Akash,P. & Joby,J.(2023).Study of mechanical properties of pineapple leaf fiber and E-glass fiber reinforced hybrid epoxymatrix composite materials .Materials Today: Proceedings.

[23] Abdul,K.,P Venkat,R.,Snehith,K. & Tanya,B.(2023).Influence of the stacking on mechanical and physical properties of jute/banana natural fiber reinforced polymer matrix composite. Materials Today: Proceedings https://doi.org/10.1016/j.matpr.2023.11.017.

[24] Caroline, A., Baillie., John, E., Castle.,Michael,G. & Bader.(1993).The influence of chemistry on the adhesion at the interface of carbon /epoxy composites. Composites Science and Technology.48,97-102.https://doi.org/10.1016/0266-3538(93)90124-Y.

[25] Anand, H., Govardhan, G., Madan,K. & Vinay,L.(2023).Influence of surface treatment on mechanical properties of Roystorea-regia/banana fiber reinforced hybrid polyester composites. M Materials Today: Proceedings,24.

[26] Kriti, Sh., Devnani, L. (2022). Recent advancement in sisal fiber reinforced polymer Composites. Materials Today: Proceedings, 65,3893-3901. https://doi.org/10.1016/j.matpr.2022.07.185.

[27] Asrar, R., Rajiv, K., Prasanna, K. & Mural . (2023). Natural fiber reinforced polymer composites: A comprehensive review of Tribo-Mechanical properties. Tribology International ,189.108978. https://doi.org/10.1016/j.triboint.2023.108978.

[28] Tejas,R. ,Sandeep.G & Inderdeep,S.(2024). Microwave-assisted alkali treatment of sisal fiber for fabricating composite as non-structural building materials. Construction and Building Materials,411.134651. https://doi.org/10.1016/j.conbuildmat.2023.134651.

[29] Bismarck, A., Mohanty, A., Aranberri-Askargorta,I S., Czapla. ,Misra ,M., Hinrichsen, G., & al .(2001). Surface characterization of natural fibres: surface properties and the water up-take behavior of modified sisal and coir fibres. Green Chem, 3,100-107.

[30] Bhanu,K.,Goriparthi, K.N.S.,Suman. & Nalluri,M R.(2012).Effect of fiber surface treatments on mechanical and abrasive wear performance of polylactide /jute composites. Composites Part A: Applied Science and Manufacturing,43,1800-1808. https://doi.org/10.1016/j.compositesa.2012.05.007.

[31] Arif Mahmud, Md., Nafis, A., Ferdausee, R A., Ayub, N Kh., Masudur, R.& Nasrin J. (2023). Coir fiber as thermal insulator and its performance as reinforcing material in biocomposite production. Heliyon, 9,e 15597.https://doi.org/10.1016/j.heliyon.2023.e15597

[32] Ezeh, M E., Agu, C. & Peter. (2022). Application of selected chemical modification agents on banana fibre for enhanced composite production. Cleaner Materials, 5,100131. https://doi.org/10.1016/j.clema.2022.100131.

[33] Mohit, H., Rangappa, S., Laongdaw T.,Suchart, S.,Abeer, N. & Abdullah, M.(2023).Banana /coir biofibers and carbon /innegra fabrics and BN/MWCNT nanoparticles reinforced UV resistant polester hybrid composites. Construction and Building Materials, 392.

[34] Subrata, D.,Angela, D.,La, R., Stergios, G., & Sotirios, G.(2023).Effect of accelerated weathering on the performance of natural fibre reinforced recyclable polymer composites and comparison with conventional composites. Composites PartC, 12.100378. https://doi.org/10.1016/j.jcomc.2023.100378.

[35]] Karla, G.,Minna, H., & Karin, O.(2024). Mechanical recycling of epoxy composites reinforced with short-cut aramid fibers: Surface functionalization – The missing piece of the puzzle. Polymer, 295.126747. https://doi.org/10.1016/j.polymer.2024.126747.

[36] Weikang, L., Yitian, Z., Grant, E., Qiang, G., Tianzhen, Ch., Shuning, S., Michael, H., Darren, M., Lisbeth, G., Mingyuan, L., & Han, H. (2024). Mechanical properties and scratch recovery of nanoclay/polyester composite coatings for pre-coated metal (PCM) sheets. Composites Part B, 273,111217. https://doi.org/10.1016/j.compositesb.2024.111217.

[37] Chieruzzi, M., Miliozzi, A. & Kenny, J. (2013). Effects of the nanoparticles on the thermal expansion and nanoparticlesties of unsaturated polyester/clay nanocomposites. Composites: Part A,45.44-48 https://doi.org/10.1016/j.compositesa.2012.09.016.

[38] Suh, D- J., Lim, Y –T. & Park,O .(2000).The property and formation mechanism of unsaturated polyester–layered silicate nanocomposite depending on the fabrication methods . Polymer, 41.8557-8563. https://doi.org/10.1016/S0032-3861(00)00216-0.

[39] Morote-Martınez, V., Torregrosa-Coque, R. & MiguelMartı´n-Martı´nez, J. (2011). Addition of unmodified nanoclay to improve the performance of unsaturated polyester resin coating on natural stone. International Journal of Adhesion & Adhesives, 31,154-163. https://doi.org/10.1016/j.ijadhadh.2010.12.001.

[40] Gharbi, A., Hassen, R. B & Boufi ,S.(2014).Composite materials from unsaturated polyester resin and olive nuts residue: the effect of silane treatment. Industrial Crops and Products, 62, 491-498. https://doi.org/10.1016/j.indcrop.2014.09.012.

[41] Dehas,W.(2017). Elaboration et caractérisation des composites à base de résines insaturées et de renforts d'origine minérales et organiques. thése de doctorat, université Ferhat abbassétif -1- Algérie .

[42] Guessoum, M., Nekkaa, S., Fenouillot-Rimlinger, F. & Haddaoui, N. (2012). Effects of kaolin surface treatments on the thermomechanical properties and on the degradation of polypropylene. International Journal of Polymer Science, 9.

[43] Majouli, A., Alami Younssi, S., Tahiri S., Albizane, A., Loukili, H. & Belhaj, M. (2011). Characterization of flat membrane support elaborated from local Moroccan perlite. Desalination, 277,.61-66. https://doi.org/10.1016/j.desal.2011.04.003.

[44] Dehas, W.,Guessoum, M.,Douibi, A., José Antonio, & J.,José Miguel Martin ,M.(2016).Thermal, mechanical, and viscoelastic properties of recycled poly(ethylene terephthalate) fiber-reinforced unsaturated polyester composites. Polymer composite. DOI 10.1002/pc.24119.

[45] Pothan, L-A, Oommen, Z. & Thomas, S. (2003). Dynamic mechanical analysis of banana fiber reinforced polyester composites. Composites Science and Technology, 63,283-293. https://doi.org/10.1016/S0266-3538(02)00254-3.

[46] Aziz, P., Sharifah, H., Martin Ansell,J., Simon Clarke, & Simon Panteny ,R.(2005).Modified polyester resins for natural fibre composites. Composites Science and Technology, 65.525-535.

[47] Martınez-Hernandez, A-L., Velasco-Santos, C., de-Icaza M. & Castano, V-M. (2007). Composites from chicken feathers quill and recycled polypropylene. Composites. Part B, 38, 405.

[48] Keusch,S. & Haessler R.(1999). Determination of mechanical properties of Al_2O_3, Mg $(OH)_2$ and sic filled E-glass/ epoxy composites. Composites. Part A, 30,997.

DOI: 10.2478/sspjce-2024-0003

Transient Flow in Pressurized Pipes: A Comparative Study of Five Resolution Methods

Abdelouaheb Toumi[1,2*], Fateh Sekiou[3,4], Fateh Afoufou[4,5]

[1]Laboratory of Civil Engineering and Hydraulics (LGCH), University of Guelma 8th May 1945, Guelma, Algeria.
[2]Department of Civil Engineering and Hydraulics (DGCH), University of Guelma 8th May 1945, Guelma, Algeria.
[3]Department of hydraulic, University of Oum El Bouaghi, Oum El Bouaghi, Algeria, sekiou.fateh@univ-oeb.dz
[4]Department of hydraulic, University of Batna 2, Batna, Algeria, f.afoufou@univ-batna2.dz
[5]LARHYSS Laboratory, Mohamed Khider University, Biskra, Algeria
*e-mail: toumi.abdelouaheb@univ-guelma.dz

Abstract

This article solves, models, and simulates, by five different methods, the system of partial differential equations of hyperbolic type governing the transient flow in the case of a gravity pipe supplied from a reservoir and equipped with a valve at its extremity. To make this work smoother and more attractive when calculating hydraulic parameters in transient flow, we took into consideration the two valve closing laws most commonly used in practice and in case of fast and slow closing. The reliability and safety of operation of the pressure pipeline system (PPS) depends on protection systems against the harmful effects of transient flow. To be able to place the most suitable protection device where it is needed, we must use numerical methods to model and simulate such processes. To this end, we applied five methods to solve the transient flow equations and subsequently search for the method giving results with practical credibility. The results obtained show that the methods of MarcCormak and Alternative lead, in fast and slow closures, to very close values by giving more logical graphic representations to the phenomenon generated. The Lax-Friedrichs method can join them but with another appearance of the representation of pressures, and the method of characteristics neglects certain parameters such as the inclination of the pipe while the Richtmayer method should be avoided in its current form because of the error gap between it and the other methods, and the graphical representation of the results obtained, like the pressure over time, which does not give a logical interpretation of the phenomenon produced.

Keywords: hyperbolic transient flow equations; resolution methods, most suitable method, pressurized pipes.

1 Introduction

In the networks of hydraulic systems, transient flows appear when the initial conditions of the permanent flow are disturbed, for example, in the case of the slow or fast closing of a valve. However, what is disturbing of these flows is the gigantic, in a lapse of time, of their parameters where their values exceed the tolerance. Several studies have been carried out on this subject of research such as Maurice Gariel's study on the optimization of closing law of distributor in

order to reduce the water hammer and so codify the practical rules for calculating the maximum water hammer, and along a penstock supplying a turbine. Hayashi and Eansfoed's study of the sudden opening or closing of the valve downstream of a pipe [1], later Thirriot (1967) studied approximate methods for calculating water hammer in relatively long pipes [2]. Steeter et al (1983) and also Almeida and Koelle (1992) discuss the type of scheme that update when friction is dominant [3,4].

Zhang et al., (2018) studied unsteady flow friction model in coiled tubing [5] using an implicit finite difference method conducted by Twyman (2018) [6]. Trabelsi and Triki (2019) performed a dual control technique for mitigating water-hammer phenomenon in pressurized steel-piping systems [7]. Assessment of inline technique-based water hammer control strategy in water supply systems was highlighted by Ben Iffa and Triki (2019) and (Azhari et al., (2019) numerically analyzed the transient pressures in geothermal wells with water hammer during injection fall-off test [8,9]. Norazlina S. and Norsarahaida A. (2015) analyzed 6 types of valve closure laws: instantaneous (m=0), linear (m=1), concave (m=0.05), concave (m=0.5), convex (m=5) and convex (m=50), they clearly show the change in pressure wave profile and amplitude from one law to the other and notes that the instantaneous and convex closure law results in minimum and maximum pressure respectively [10]. Recently Zhao et al (2020) show that the flow rate and, in particular, the valve closing speed strongly affect the increase in water hammer pressure, the higher the flow rate and valve closing speed, the greater the increase in water hammer pressure [11]. Rahul and Arun (2020), who conducted experimental and numerical investigations of water hammer analysis in pipeline with two different materials and their combined configuration had been described [12]. In addition, Aliabadi et al., (2020) studied the frequency response of water hammer with fluid-structure interaction in a viscoelastic pipe [13]. In Mery et al., (2021) study, water hammer mitigation was carried out by air vessel and by pass forward configuration [14]. While Kandil et al., (2021) performed a study dealing with the effect of pipe materials properties on the water hammers by considering the fluid-structure interaction, frictionless model [15]. In addition, (Khalideh et al., 2021) investigated the influence of dimensions and material of the pipes on the water hammer effect in microbial fuel cells waste water treatment plants [16]. Sławomir (2021) applied the shock response spectrum method to severity assessment of water hammer loads [17]. Toumi and Remini (2021) solved the Saint Venant equations for cases of double and triple effect pumping stations [18]. Liu (2021) investigated the sensitivity of six main parameters that affect the transient flow rate, the results show that the flow rate and Young's modulus are positively correlated with the maximum pressure, while the pipe diameter, valve closing time and wall thickness are negatively correlated, he further states that the flow rate, diameter and valve closing time are the key parameters that affect the model simulation hammer [19].

Han et al (2022) showed that extending the valve closing time can effectively reduce the maximum water hammer pressure and that pressure vibration were affected by the closing law, the faster the valve closing speed in the closing early stage, the greater the water hammer pressure [20]. Cao et al (2022) notes that in both case of fast closing and slow closing situations, the optimized nonlinear valve closure presents different shapes this permit to guiding valve real-time control, as well as providing a reference for valve design for the purpose of wave surge [21].

This paper is devoted to the study of the transient flow of the hydraulic in gravity buried pipe, which consists of a cast iron pipe, specially optimize law and time closing valve. To achieve

this objective, the calculation of water hammer will be based on the five numerical methods to calculate the hydraulic parameters in transient flow.

The search for the best calculation method among the five methods used requires numerous, meticulous, precise, repetitive and worrying calculations and demands extreme attention to the results obtained. In order to show how to carefully obtain this method, it is appropriate to show the general procedure to be followed through a case study.

2 Mathematical model

The equations can faithfully describe the phenomena of transient flow in hydraulic adduction pipeline are the basic hyperbolic equations demonstrated successively from the continuity equations and dynamics [3,18]:

$$\begin{cases} \rho \frac{\partial u}{\partial x} + \frac{1}{a^2}\left(\frac{\partial P}{\partial t} + u\frac{\partial P}{\partial x}\right) = 0 \\ \frac{\partial u}{\partial t} + u\frac{\partial u}{\partial x} + \frac{1}{\rho}\frac{\partial P}{\partial x} = -g(\sin(\alpha) + j) \end{cases} \quad (1)$$

Where, a: wave velocity (m/s);
P: pressure (Pa);
ρ: density of the liquid, for water $\rho = 10^3 kg / m^3$;
u: velocity in the x direction (m/s);
g: acceleration due to gravity (m / s^2);
α: pipe inclination angle;
j: unit pressure drop.
These two equations express the variation of two parameters, namely velocity and pressure over time, t, in the direction of flow, x [22,23].To know the values of these two parameters at any time and in any place of a water supply pipeline, we used five methods to solve the mathematical model represented by the two previous partial differential equations. And since most of the data are given by flow and manometric pressure, we had to convert the two previous equations to these two parameters.

3 Transformation of the transient flow equations

The transformation of equations for transient flow in pressure pipes, written as a function of velocity and pressure (see system of equations 1), to equations written as a function of piezometric head and flow rate without neglecting the terms $u(\partial u/\partial x)$ and $u(\partial P/\partial x)$ in front of the terms $\partial u/\partial t$ and $\partial P/\partial t$ and the pipe may have an inclination with respect to the horizontal plane, i.e. $\sin(\alpha)\neq 0$, must use the following mathematical expressions and introduce them into the system equations number 1.

$$\frac{\partial P}{\partial t} = \frac{\partial(\rho g(H-Z)}{\partial t} = \rho g\left(\frac{\partial H}{\partial t} - \frac{\partial Z}{\partial t}\right) \quad (2)$$

Where : H and Z are successively the manometric head and the geodesic level.

$$\frac{\partial P}{\partial x} = \frac{\partial(\rho g(H-Z)}{\partial x} = \rho g\left(\frac{\partial H}{\partial x} - \frac{\partial Z}{\partial x}\right) \tag{3}$$

$$u\frac{\partial P}{\partial x} = \frac{Q}{S}\frac{\partial P}{\partial x} = \rho g\frac{Q}{S}\left(\frac{\partial H}{\partial x} - \frac{\partial Z}{\partial x}\right) \tag{4}$$

Where :S and Q are successively the pipe cross section and the flow rate.

$$\frac{\partial u}{\partial t} = \frac{1}{S}\frac{\partial Q}{\partial t} \tag{5}$$

$$u.\frac{\partial u}{\partial x} = \frac{Q}{S}\frac{\partial u}{\partial x} = \frac{Q}{S}\frac{1}{S}\frac{\partial Q}{\partial x} = \frac{Q}{S^2}\frac{\partial Q}{\partial x} \tag{6}$$

$$\frac{\partial u}{\partial x} = \frac{1}{S}\frac{\partial Q}{\partial x} \tag{7}$$

$$\begin{cases} a\left(\frac{1}{S}\frac{\partial Q}{\partial x}\right) + \frac{1}{\rho\, a}\left(\rho g\left(\frac{\partial H}{\partial t} - \frac{\partial Z}{\partial t}\right) + \rho g\frac{Q}{S}\left(\frac{\partial H}{\partial x} - \frac{\partial Z}{\partial x}\right)\right) = 0 \\ \quad \frac{1}{S}\frac{\partial Q}{\partial t} + \frac{Q}{S^2}\frac{\partial Q}{\partial x} + \frac{1}{\rho}\left(\rho g\left(\frac{\partial H}{\partial x} - \frac{\partial Z}{\partial x}\right)\right) = -g(\sin(\alpha) + j) \end{cases} \tag{8}$$

$$\begin{cases} \left(\frac{a}{S}\frac{\partial Q}{\partial x}\right) + \frac{g}{a}\left(\left(\frac{\partial H}{\partial t} - \frac{\partial Z}{\partial t}\right) + \frac{Q}{S}\left(\frac{\partial H}{\partial x} - \frac{\partial Z}{\partial x}\right)\right) = 0 \\ \quad \frac{1}{S}\frac{\partial Q}{\partial t} + \frac{Q}{S^2}\frac{\partial Q}{\partial x} + g\left(\left(\frac{\partial H}{\partial x} - \frac{\partial Z}{\partial x}\right)\right) = -g(\sin(\alpha) + j) \end{cases} \tag{9}$$

Multiply the first equation by a/g and the second by S, we get:

$$\begin{cases} \left(\frac{a^2}{gS}\frac{\partial Q}{\partial x}\right) + \left(\frac{\partial H}{\partial t} - \frac{\partial Z}{\partial t}\right) + \frac{Q}{S}\left(\frac{\partial H}{\partial x} - \frac{\partial Z}{\partial x}\right) = 0 \\ \quad \frac{\partial Q}{\partial t} + \frac{Q}{S}\frac{\partial Q}{\partial x} + gS\left(\frac{\partial H}{\partial x} - \frac{\partial Z}{\partial x}\right) = -gS(\sin(\alpha) + j) \end{cases} \tag{10}$$

$$\begin{cases} \frac{\partial H}{\partial t} = \frac{Q}{S}\frac{\partial Z}{\partial x} - \left(\frac{a^2}{gS}\frac{\partial Q}{\partial x}\right) - \frac{Q}{S}\frac{\partial H}{\partial x} + \frac{\partial Z}{\partial t} \\ \frac{\partial Q}{\partial t} = -\frac{Q}{S}\frac{\partial Q}{\partial x} - gS\left(\frac{\partial H}{\partial x} - \frac{\partial Z}{\partial x}\right) - gS(\sin(\alpha) + j) \end{cases} \tag{11}$$

$\partial Z/\partial t=0$

$$\begin{cases} \frac{\partial H}{\partial t} = \frac{Q}{S}\frac{\partial Z}{\partial x} - \frac{a^2}{gS}\frac{\partial Q}{\partial x} - \frac{Q}{S}\frac{\partial H}{\partial x} \\ \frac{\partial Q}{\partial t} = -\frac{Q}{S}\frac{\partial Q}{\partial x} - gS\frac{\partial H}{\partial x} + gS\frac{\partial Z}{\partial x} - gS\sin(\alpha) - gSj \end{cases} \tag{12}$$

$\partial Z/\partial X=\sin(\alpha)$

$$\begin{cases} \frac{\partial H}{\partial t} = \frac{Q}{S}\sin(\alpha) - \frac{a^2}{gS}\frac{\partial Q}{\partial x} - \frac{Q}{S}\frac{\partial H}{\partial x} \\ \frac{\partial Q}{\partial t} = -\frac{Q}{S}\frac{\partial Q}{\partial x} - gS\frac{\partial H}{\partial x} - gSj \end{cases} \tag{13}$$

These two equations express the change in head and flow rate over time in the direction of flow. This transformation was carried out since in real cases, the data is available in heights and flows and all intermediate parameters are calculated by similar units.

4 Materials and methods

4.1 Solution methods

4.1.1 Method Of Characteristics

The application of the MOC on the system of equations number 1 gives the following algebraic expressions [19]:

$$CP = H(i) + RQ(i) - T_1.((Q(i+1).|Q(i)|)) \tag{14}$$

$$CM = H(i+2) - RQ(i+2) + T_1.((Q(i+1).|Q(i+2)|)) \tag{15}$$

$$H(i+1) = (CP + CM)/2 \tag{16}$$

$$Q(i+1) = \big(CP - H(i+1)\big)/R \tag{17}$$

These algebraic equations make it possible to calculate the flow rate and the manometric head in transient flow.

4.1.2 Lax-Friedrichs method

The Lax-Friedrichs method is used in this article to solve the transient flow equations mentioned in system number (13).This method makes it possible to transform the equations of the system number (13) into algebraic equations, easy to process numerically. Applying this scheme gives the following system of equations:

$$\begin{cases} H_i^{k+1} = (H_{i+1}^k + H_{i-1}^k)/2 + C_1 - C_2\left(Q_{i+1}^k - Q_{i-1}^k\right) - C_3\left(H_{i+1}^k - H_{i-1}^k\right) \\ Q_i^{k+1} = (Q_{i+1}^k + Q_{i-1}^k)/2 - d_1(Q_{i+1}^k - Q_{i-1}^k) - d_2(H_{i+1}^k - H_{i-1}^k) - d_3\overline{Q}_i|\overline{Q}_i| \end{cases} \tag{17}$$

With :

$$C_1 = \frac{\overline{Q}_i \Delta t_i \sin(\alpha)}{S}; C_2 = \frac{a^2 \Delta t}{2gS\Delta x};\ C_3 = \frac{\overline{Q}_i \Delta t}{2S\Delta x}$$

$$d_1 = \frac{\Delta t}{2\Delta x}\frac{\overline{Q}_i}{S}; d_2 = \frac{\Delta t g S}{2\Delta x};\ d_3 = \Delta t \frac{\lambda}{2dS}$$

$$\overline{Q}_i = \frac{1}{2}\left(Q_{i+1}^k + Q_{i-1}^k\right) \tag{19}$$

Δt: time step; Δx: space step; S: cross-section of the pipe; d: pipe diameter; λ: coefficient of friction; i: space index; k: time index.

4.1.3 Richtmayer method

This method is composed of two steps, one of prediction and the other of correction. The first step in the Richtmyer two-step Lax–Wendroff method calculates values for f(H(x, t)) and f(Q(x, t)) at half time steps, $t_{n+1/2}$ and half grid points, $x_{i+1/2}$. In the second step values at t_{n+1} are calculated using the data for t_n and $t_{n+1/2}$.

a. Predictor step

Application of the Richtmayer method for the first step on the system of equation number 13 gives the following expressions:

$$\begin{cases} H_{i1}^{k+1} = (H_{i+1}^{k} + H_{i}^{k})/2 + C_1 - C_2\left(Q_{i+1}^{k} - Q_{i}^{k}\right) - C_3\left(H_{i+1}^{k} - H_{i}^{k}\right) \\ H_{i2}^{k+1} = (H_{i}^{k} + H_{i-1}^{k})/2 + C_1 - C_2\left(Q_{i}^{k} - Q_{i-1}^{k}\right) - C_3\left(H_{i}^{k} - H_{i-1}^{k}\right) \\ Q_{i1}^{k+1} = (Q_{i+1}^{k} + Q_{i}^{k})/2 - d_1\left(Q_{i+1}^{k} - Q_{i}^{k}\right) - d_2\left(H_{i+1}^{k} - H_{i}^{k}\right) - d_3(\overline{Q}_i|\overline{Q}_i|) \\ Q_{i2}^{k+1} = (Q_{i}^{k} + Q_{i-1}^{k})/2 - d_1\left(Q_{i}^{k} - Q_{i-1}^{k}\right) - d_2\left(H_{i}^{k} - H_{i-1}^{k}\right) - d_3(\overline{Q}_i|\overline{Q}_i|) \end{cases} \quad (20)$$

With :

$$C_1 = \frac{\overline{Q}_i \Delta t_i \sin(\alpha)}{S};\ C_2 = \frac{a^2 \Delta t}{2gS\Delta x}; C_3 = \frac{\overline{Q}_i \Delta t}{2S\Delta x}$$

$$d_1 = \frac{\Delta t}{2\Delta x}\frac{\overline{Q}_i}{S}; d_2 = \frac{\Delta t g S}{2\Delta x};\ d_3 = \Delta t \frac{\lambda}{2dS}$$

$$\overline{Q}_i = \frac{1}{2}(Q_{i+1}^{n} + Q_{i-1}^{n})$$

b. Corrector step

Applying the second step, gives the following expressions:

$$\begin{cases} H_{i}^{k+1} = H_{i}^{k} + C_{11} - C_{22}\left(Q_{i1}^{k} - Q_{i2}^{k}\right) - C_{33}\left(H_{i1}^{k} - H_{i2}^{k}\right) \\ Q_{i1}^{k+1} = Q_{i}^{k} - d_{11}\left(Q_{i1}^{k} - Q_{i2}^{k}\right) - d_{22}\left(H_{i1}^{k} - H_{i2}^{k}\right) - d_{33}(\overline{Q}_i|\overline{Q}_i|) \end{cases} \quad (21)$$

With:

$$C_{11} = C1; C_{22} = 2C_2; C_{33} = 2C_3$$
$$d_{11} = 2d_1; d_{22} = 2d_2; d_{33} = d_3$$

4.1.4 MacCormak method

The MacCormack method is a widely used discretization scheme for the numerical solution of hyperbolic partial differential equations. This second-order finite difference method was introduced by Robert W. MacCormack in 1969 [24]. The MacCormack method is elegant and easy to understand and program [25].

a. Predictor step

In the predictor step, the provisional values of H and Q at time level (t+Δt) are estimated as follows:

$$\begin{cases} H_i^* = H_i^k + C_1 - C_2\left(Q_{i+1}^k - Q_i^k\right) - C_3\left(H_{i+1}^k - H_i^k\right) \\ Q_i^* = Q_i^k - d_1\left(Q_{i+1}^k - Q_i^k\right) - d_2\left(H_{i+1}^k - H_i^k\right) - d_3\overline{Q}_i|\overline{Q}_i| \end{cases} \quad (22)$$

With:

$$C_1 = \frac{\overline{Q}_i \Delta t_i \sin(\alpha)}{S}; C_2 = \frac{a^2 \Delta t}{gS\Delta x}; C_3 = \frac{\overline{Q}_i \Delta t}{S\Delta x}$$
$$d_1 = \frac{\Delta t}{\Delta x}\frac{\overline{Q}_i}{S}; d_2 = \frac{\Delta t g S}{\Delta x}; d_3 = \Delta t \frac{\lambda}{2dS}$$

b. Corrector step

In the corrector step, the predicted values H and Q are corrected according to the follow equations :

$$\begin{cases} H_i^{k+1} = (H_i^k + H_i^*)/2 + C11 - C22\left(Q_i^k - Q_{i-1}^k\right) - C33\left(H_i^k - H_{i-1}^k\right) \\ Q_i^{k+1} = (Q_i^k + Q_i^*)/2 - d11\left(Q_i^k - Q_{i-1}^k\right) - d22\left(H_i^k - H_{i-1}^k\right) - d33\overline{Q}_i|\overline{Q}_i| \end{cases} \quad (23)$$

With:

$$C_{11} = \frac{\Delta t \overline{Q}_i}{S}\sin(\alpha); C_{22} = \frac{\Delta t a^2}{2gS\Delta x}; C_{33} = \frac{\Delta t \overline{Q}_i}{S2\Delta x}$$
$$d_{11} = \frac{\Delta t \overline{Q}_i}{2\Delta x S}; d_{22} = \frac{\Delta t g S}{2\Delta x}; d_{33} = \frac{\Delta t \lambda}{2dS}$$

4.1.5 Alternative method

Like the methods of Richtmayer and MarcCormak, the alternative method consists of two steps, the first for the prediction and the second for the correction.

a. Predictor step

$$\begin{cases} H_{i1}^{k+1} = H_i^k + C_1 - C_2\left(Q_i^k - Q_{i-1}^k\right) - C_3\left(H_i^k - H_{i-1}^k\right) \\ Q_{i1}^{k+1} = Q_i^k - d_1\left(Q_i^k - Q_{i-1}^k\right) - d_2\left(H_i^k - H_{i-1}^k\right) - d_3\overline{Q}_i|\overline{Q}_i| \end{cases} \quad (24)$$

With:

$$C_1 = \frac{\overline{Q}_i \Delta t_i \sin(\alpha)}{S}; C_2 = \frac{a^2 \Delta t}{gS\Delta x}; C_3 = \frac{\overline{Q}_i \Delta t}{S\Delta x}$$
$$d_1 = \frac{\Delta t}{\Delta x}\frac{\overline{Q}_i}{S}; d_2 = \frac{\Delta t g S}{\Delta x}; d_3 = \Delta t \frac{\lambda}{2dS}$$

b. Corrector step

$$\begin{cases} H_{i1}^{k+1} = \frac{1}{2}\left(H_i^k + H_{i1}^{k+1}\right) + C_{11} - C_{22}\left(Q_{i+1}^{k+1} - Q_i^{k+1}\right) - C_{33}\left(H_{i+1}^{k+1} - H_i^{k+1}\right) \\ Q_{i1}^{k+1} = \frac{1}{2}\left(Q_i^k + Q_{i1}^{k+1}\right) - d_1\left(Q_{i+1}^{k+1} - Q_i^{k+1}\right) - d_2\left(H_{i+1}^{k+1} - H_i^{k+1}\right) - d_3\overline{Q}_i|\overline{Q}_i| \end{cases} \quad (25)$$

With:

$$C_{11} = C_1 = \frac{\overline{Q}_i \Delta t_i \sin(\alpha)}{S}; C_{22} = C_2/2 = \frac{a^2 \Delta t}{2gS\Delta x}; C_{33} = C_3/2 = \frac{\overline{Q}_i \Delta t}{2S\Delta x}$$

$$d_{11} = d_1/2 = \frac{\Delta t}{2\Delta x}\frac{\overline{Q}_i}{S};\ d_{22} = d_2/2 = \frac{\Delta t g S}{2\Delta x};\ d_{33} = d_3 = \Delta t\frac{\lambda}{2dS}$$

4.2 Problem statement and boundary conditions

4.2.1 Problem statement

To give concrete form to the mathematical model obtained and put into practice the five resolution methods, the RPV (Reservoir - Pipeline - Valve) system is adopted: it consists of a large reservoir at the upstream end of the inclined pipeline and a valve at the downstream end discharging to the atmosphere. A reservoir (R) equipped with an overflow at an altitude of 200 m, supplies a flow of 350 l/s via a gravity pipe (P) of length equal to 1000 m and inclined at 10°. The motorized valve with controlled closure is located at the other end of the pipe, at an altitude of 50 m. The transient flow is generated by fast and/or slow valve closing time. The schematic shape of the problem is shown in Fig 1.

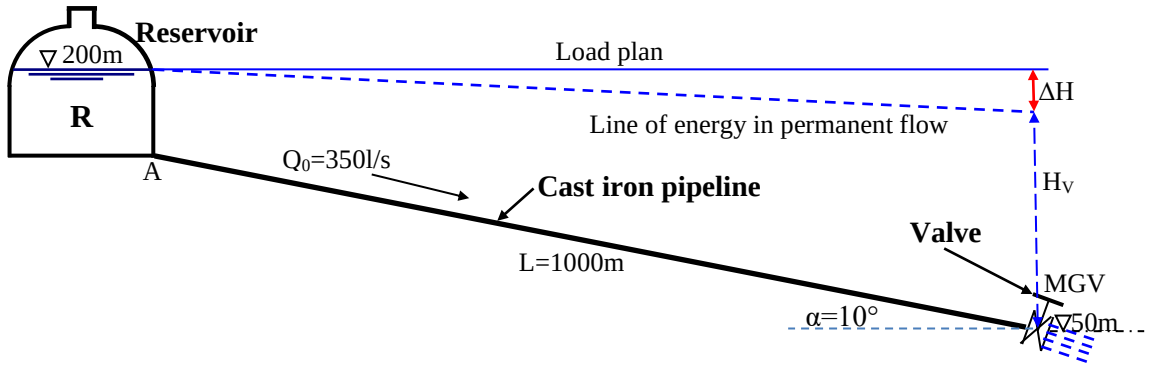

Figure 1: Schematic of the reservoir-pipe-valve system

4.2.2 Boundary conditions and stability criterion

When applying the MOC, Lax–Friedrichs, Richtmayer, MacCormak and Alternative methods, they appear, at the limits (on the left and on the right), undefined variables in the domain of interest, this section has highlighted how we get rid of -us definitely.

a. At the outlet of the reservoir

The manometric head at the level of the first node (inlet of the pipe) is equal to the manometric height of the water in the reservoir H(1)=Hr, while the flow rate is obtained by applying the characteristic equations on the left and its expression is written as follows.

$$CN = H(2) - Q(2)(R - T.|Q(2)|) \quad (26)$$

H(2) and Q(2) are quantities calculated at time (t) so:

$$Q(1) = (H_R - CN)/R \quad (27)$$

With:

$$T=B.(x(i+2)-x(i+1))=B.\Delta x \quad (28)$$

$$B = \frac{\lambda}{2.g.d.S^2} \quad (29)$$

And

$$R = \frac{a}{g.S} \tag{30}$$

Where: the parameter R represents the flow resistance effect and the elements of this parameter are: a: wave velocity (m/s); S: pipe cross section in (m^2).

b. At the valve

In the case of instantaneous closing (valve closing time equals zero) Q(n)=0, the manometric head at node number N is written as follows:

$$H(n) = CP \tag{31}$$

With:

$$CP = H(n-1) + Q(n-1)(R - T.|Q(n-1)|) \tag{32}$$

In the case where closing is controlled, the flow at the valve follows, over time, a function depending on the chosen closing law, and the flow, in this case, is written as a function of Q0, Δt, Ct and m by the following expression [10,26].

$$Q_n^{k+1} = \left(1 - \left(\frac{i\Delta t}{Ct}\right)^m\right) Q_n^k \tag{33}$$

Where,
m : exponent determining the valve closing law;
Δt: time step;
k: time index;
Ct: the total valve closing time;
Q^K and Q^{K+1} are successively the flow rates at times t and t+Δt.
Figure hereafter shows the envelope curves of the possible laws for closing a valve in a hydraulic system.

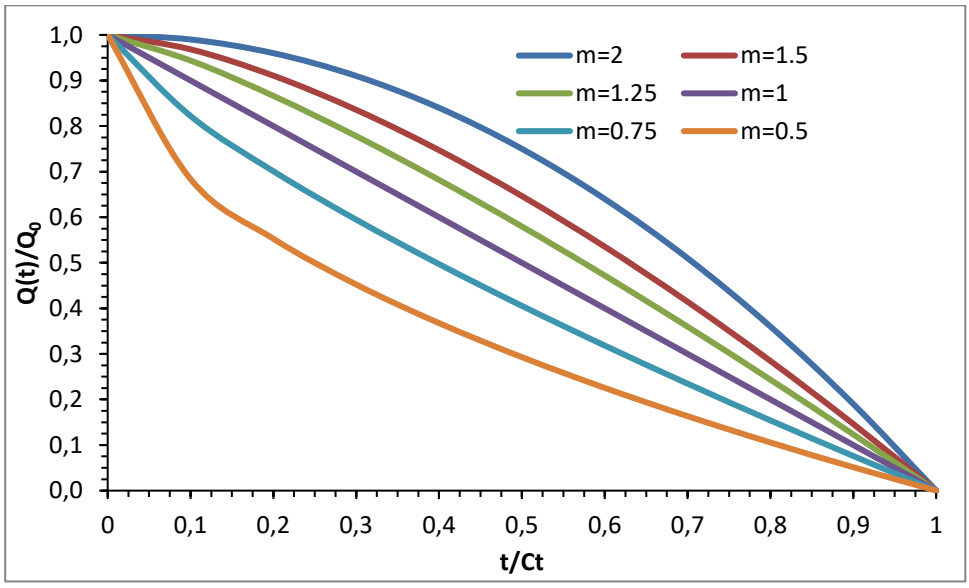

Figure 2: Closing functions corresponding to different values of exponent m

The exponent m, of the expression of Q at node n, generates the infinity of functions of Q and consequently the search for the optimal value of this exponent turns out to be a major priority for an optimal management.
In this case, the manometric head at the valve is calculated by the following relationship:

$$H(n) = CP - R.Q(n) \quad (34)$$

With:

$$CP = H(n-1) + Q(n-1)(R - T.|Q(n-1)|) \quad (35)$$

The stability criterion of the Lax method must ensure the stability of the finite difference method and the method of characteristics (MOC), which allows us to write the following expression:

$$\Delta x \geq a.\Delta t \quad (36)$$

Where, a: wave velocity in (m/s); Δt: time step; Δx: space step; N: number of discretization nodes; L: length of the pipe [6, 27, 28].
The flowchart in Figure 3 gives the schematic representation of the solution to the transient flow problem in pressurized pipelines.

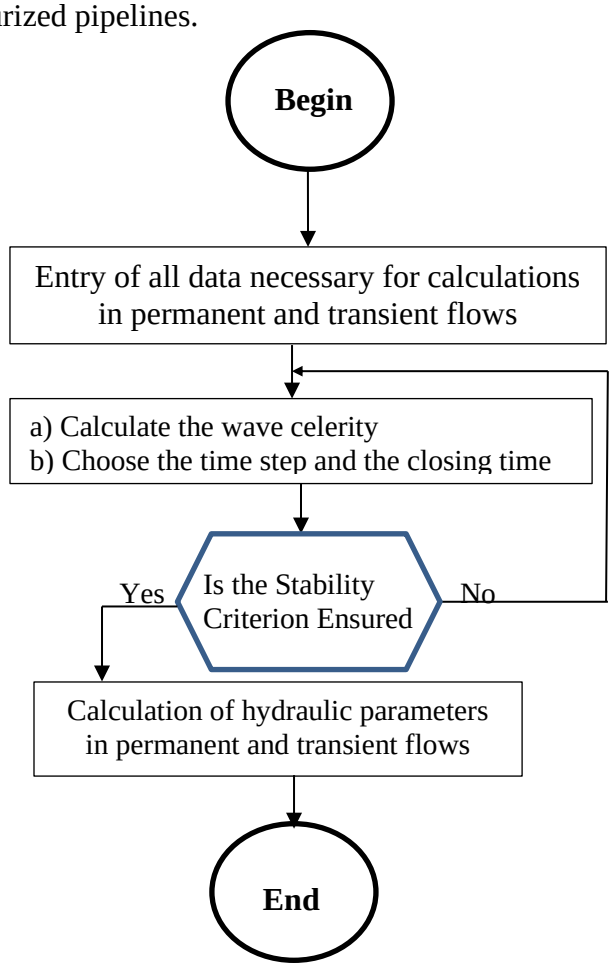

Figure 3: Flowchart for calculating hydraulic parameters in transient state

The execution of this algorithm requires knowledge of the characteristics of the materials used, the reservoir, the volume flow transported by the pipe and the liquid. All the latter characteristics are represented in table 1.

Table 1: Information regarding the proposed problem and used methods

Kind of materials	Cast iron
Elasticity modulus in Pascal	$E_{FC}=1.03.\ 10^{11}$
Pipe Poisson's ratio	$\nu_m= 0.26$
Coefficient of vertical friction between the backfill and the walls of the trench	$\mu'=0.50$
Rankine's coefficient	K=0.33
Soil density (KN/m^3)	γ=19000
Height of embankment above pipe (H) in (m)	1.0 m
Trench width (B_d) in (m)	1.10 m
exterior diameter (B_C)in (mm)	d_{ext}=635
internal diameter in (mm)	d_{int}=600
Pipe thickness e_1 in (mm)	e_1=17.5
Pipe roughness ε in (mm)	ε=0.03
Pipe length (m)	L=1000
Pipe inclination	10°
Pipe pressure rating in (bar)	42
Fluid elasticity modulus	Kw = $2.07.10^9$ Pa
Fluid temperature	15°C
Kinematic viscosity	$1.1445.\ 10^{-6}$ (m^2/s)
Density of the liquid	$\rho = 10^3$kg/m^3
Reservoir overflow level in (m)	200
Flow leaving the reservoir in (l/s)	350
Initial rapid valve closure time	0,01 t_4 seconds
Final rapid valve closure time	0,5 t_4 (t_4 return period)
Initial slow valve closure time	0,51 t_4
Final slow valve closure time	10 t_4
MOC, Lax-Friedrichs, Richtmayer, MacCormak and Alternative	one-dimensional

5 Results and Discussion

To begin transient calculations, the resolution method has to use the results obtained under steady-state conditions. The results are shown in Table 2.
Instantaneous closure (zero closure time) generates an oscillatory phenomenon of overpressure and underpressure with a return period of 4L/a Dupont A., (1979), which has harmful effects on the pipe and its appurtenances at the same time. Although practically unfeasible due to its zero delay, this type of closure must be avoided if the hydraulic system is not to be jeopardized[29]. In addition, it generates high pressures which, at certain points in the hydraulic system, exceed the resistance of the pipe. Whereas rapid closing, with a closing time of between

0 and 0.5 t_4 (where t4 is the return period) Dupont A., (1979), generates high pressure values which can also damage the hydraulic system [29]. Closing is said to be slow if the valve's closing time is greater than the shock wave's forward and return times $t > 0.5t_4$ [29]. Manual closing is not mandatory. Indeed, technological advances have led to the emergence of motorized valves that close and open according to the control signal. This opportunity generates laws linking flow and control signal, such as linear, concave and convex laws. From the first operation at $t=t_0$ (t_0 is the equilibrium time) until the valve is completely closed, and after a certain time after closure, what will be the values of the flow parameters at all the nodal points in the pipe. The answer to this question is part of what follows.

Table 2: Simulation result in steady state

Average flow velocity V in (m/s)	1.2378
Reynolds number Re	648933.500
coefficient of friction Lambda	$1.334596\ 10^{-2}$
Load loss in (m)	1.9109
Number of discretization points N	892
Duration of the return period t_4 in (seconds)	3.564
The value of R=a/gS in (s/m^2)	404.632507
Water hammer value Vdh in (m)	141.621384
Pipe resistance RC in (s^2/m^5)	15.599385
The space step Δx in(m)	1.1223
the time step Δt in (s)	0.001
Resistance of the discretization element RDE in (s^2/m^5)	$1.75.10^{-2}$
Manometric head in (m)	198.089081
Manometric pressure in (m.w.c)	148.089081
Pressure in (bar)	14.527

5.1 Case of rapid valve closing

To determine the effect of rapid closure on overpressure values for linear and quadratic laws, we simulated valve pressure for times ranging from 0.01 t_4 to 0.5 t_4 with a time step of 0.01 t_4(i.e. 50 valve closing times tested).Figures 4 and 5 show successively for linear and quadratic valve closing laws, the evolution of the overpressure as a function of time at the valve for the five closing methods tested.

These graphic representations lead to different physical interpretations of the phenomenon. Indeed, the Richtmayer method records the largest value of pressure at the start of the calculation and this value decreases linearly over time. The MOC shows that during this interval, the pressure increases proportionally during the time of the wave's outward and return journey. The Lax method records arising pressure which is characterized by the appearance of two lines of different slopes. The high slope line (lower) is linked to the direction of the wave from the valve to the reservoir (from t_0=0.01 to t_1=L/a) and the lows lope line (upper) is linked to the return of the wave from the tank to the valve (from t_1=L/a to t_2=2L/a). The graphs of the MacCormak and Alternative methods are both characterized by the appearance of two straight lines, the first rising specific to the time of the wave from the valve to the reservoir (from t_0=0.01 to t_1=L/a) and the second descending specific to the return time of the wave from the tank to the valve (from t_1=L/a to t_2=2L/a).

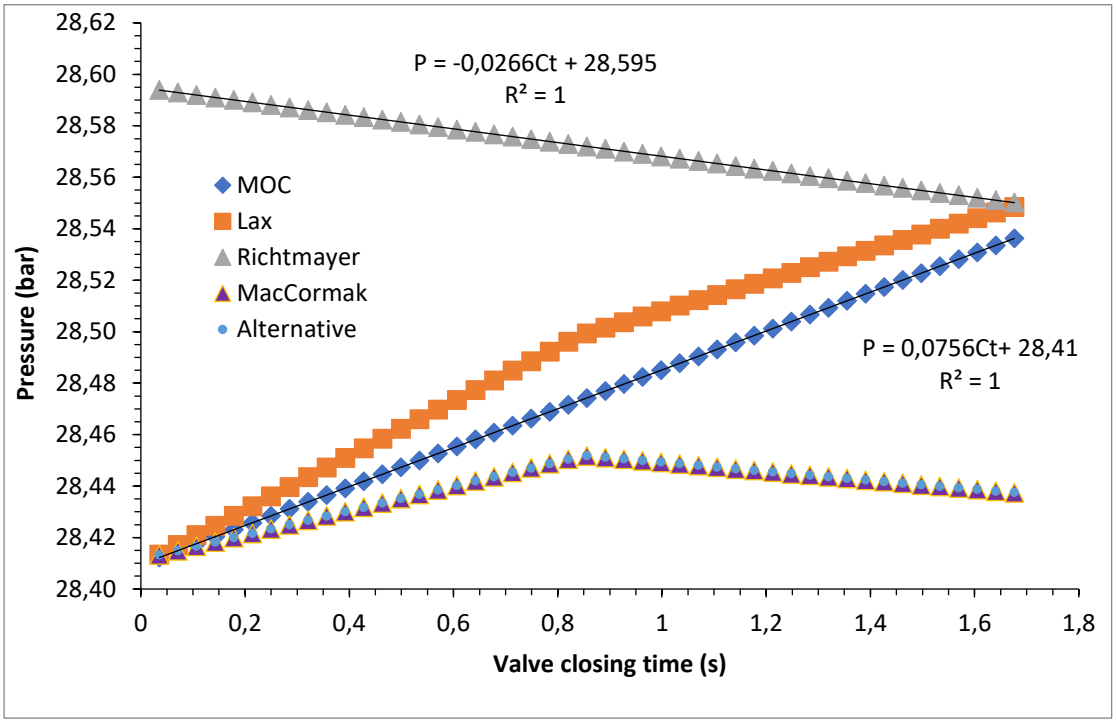

Figure 4: Variation of pressure for linear closing law as a function of time closing valve for the cast iron pipeline

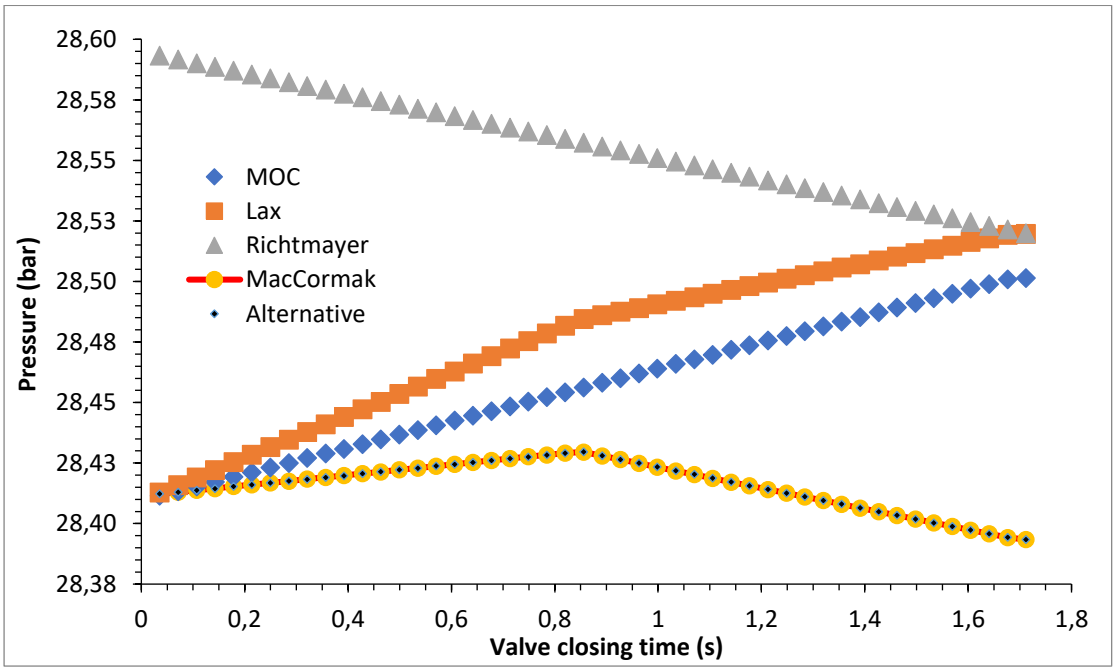

Figure 5: Variation of pressure for quadratic closing law as a function of time closing valve for the Cast iron pipeline

5.2 Case of slow valve closing

This section is focused on the search, for different valve closing times t ranging from 0.01 t_4 seconds to 10 t_4 seconds (i.e. 950 valve closing times tested), with a step size of Δt=0.001s, for the for linear and quadratic closing laws generating the overpressure and the underpressure. Figures 6, 7, 8 and 9 show respectively the variation over time (t equal to 10 t_4) of the overpressure and depression at the valve for a slow closing time equal to twice the return period (2 t_4) for the valve closing laws linear and quadratic.

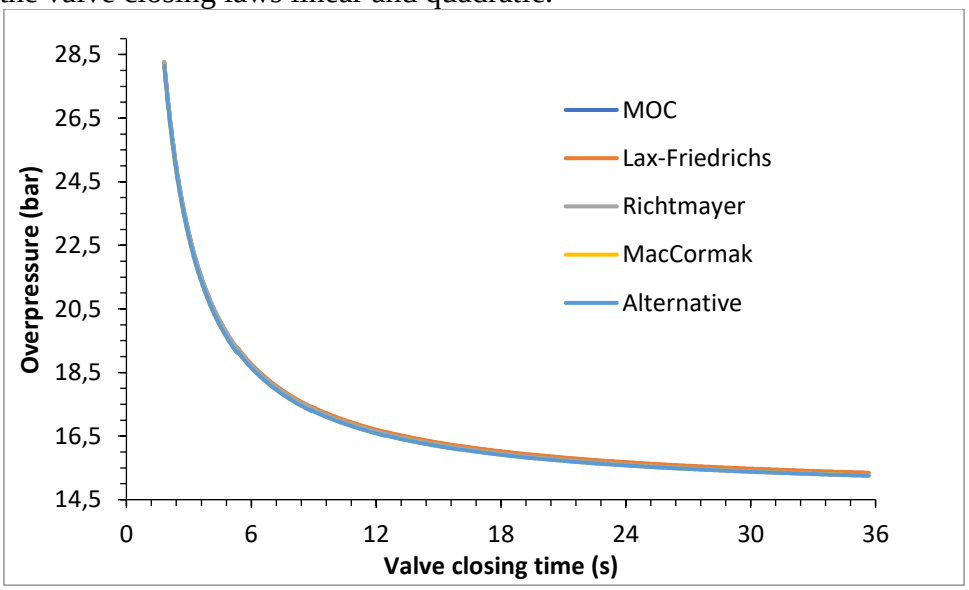

Figure 6: Variation of overpressure for linear closing laws (m=1) as a function of time closing valve for the cast iron pipeline

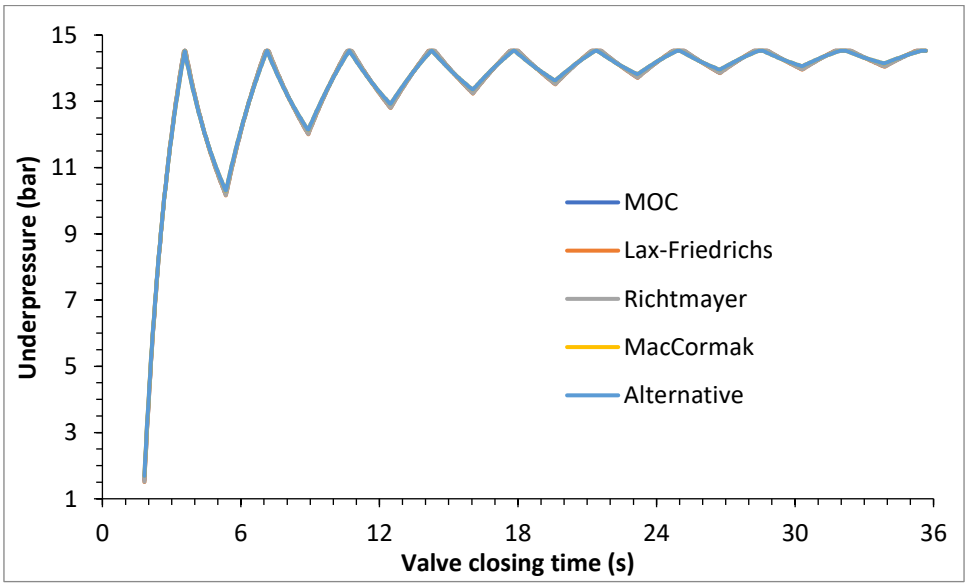

Figure 7: Variation of underpressure for linear closing laws (m=1) as a function of time closing valve for the cast iron pipeline

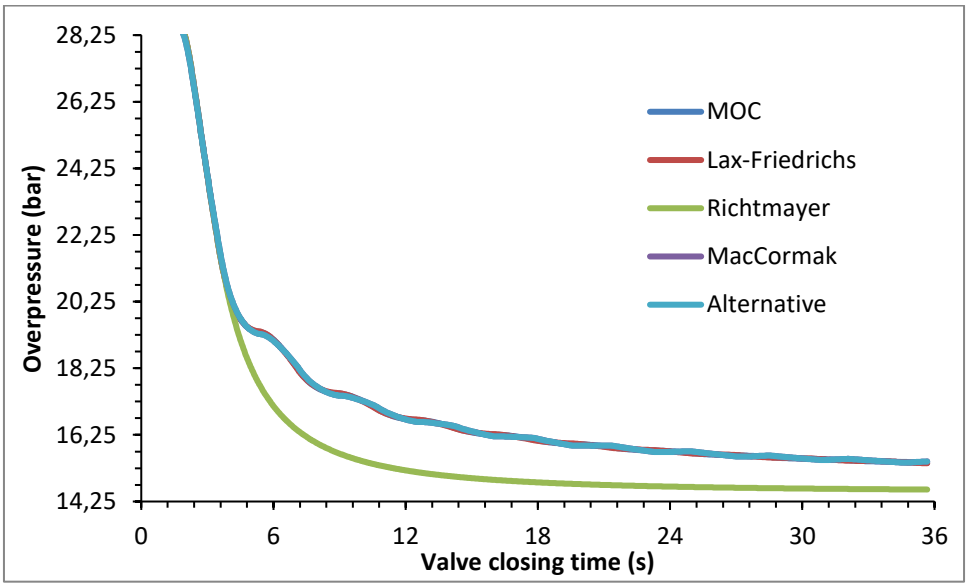

Figure 8: Variation of overpressure for quadratic closing laws (m=2) as a function of time closing valve for the cast iron pipeline

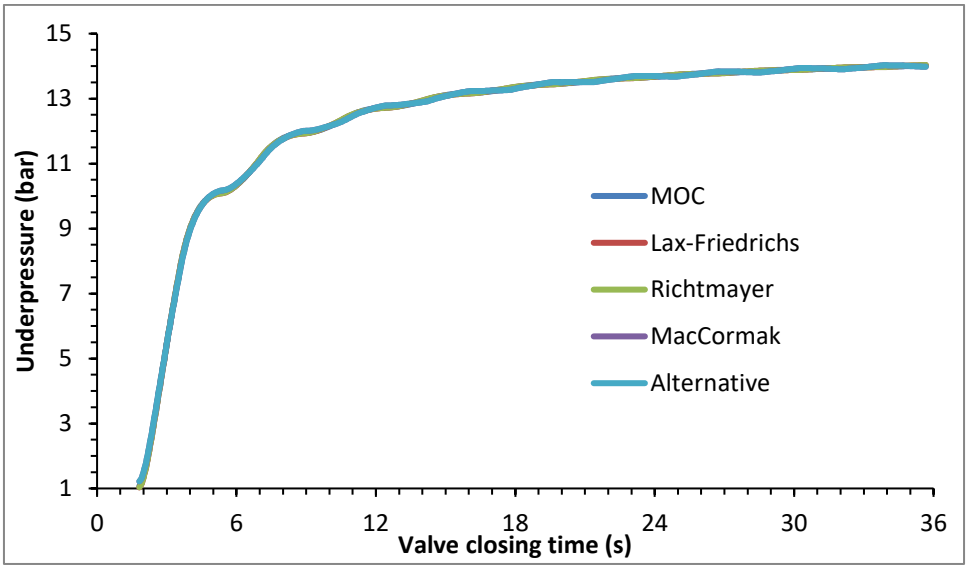

Figure 9: Variation of underpressure for quadratic closing laws (m=2) as a function of time closing valve for the cast iron pipeline

When the valve closing law takes a linear form, the five methods give overpressure and depression curves which converge almost in the same way to stabilize at the permanent state values. While the quadratic law of closing the valve shows that the Richtmayer method, in the case of calculating the overpressure, gives beyond a time approximately equal to t=4.20 seconds a curve distinct from the others while the curves of depression almost coincide.

6 Conclusion

In this paper, five methods have been used to solve the system of hyperbolic equations in partial derivatives governing transient flow in hydraulic systems under pressure. The search for a reliable method, giving reasonable results with a logical interpretation of the physical phenome nongenerated, requires the application of these five techniques. A transient flow is reproduced by the linear and quadratic closing of a valve placed in a simple hydraulic system composed of a reservoir, a pipe, and a valve.
The application of the five methods to the cases of fast and slow closures shows that the two methods of MarcCormak and Alternative lead, in fast and slow closures, to very close values by giving graphic representations allowing more logical interpretations of the phenomenon physics generated. The Lax-Friedrichs method can also be considered useful but with another appearance of the representation of the pressures and another philosophy of the interpretation of the results obtained. The method of characteristics neglects certain parameters like the inclination of the pipe but it remains useful at the limits to make start other methods while the Richtmayer method should be avoided in its current form given the error gap between it and the other methods and the unique appearance that it gives to the graphic representation of the variation of the overpressure over time.

References

[1] Hayashi T., Eansfoad G. (1960). Sudden opening or closing of an outlet valve on a pipeline, revue la Houille Blanche. N° 6, pp. 657-673.

[2] Thirriot C. (1967). Méthodes approchées de calcul des coups de bélier dans des conduits relativement longues, La Houille Blanche. N°2, pp. 179–192.

[3] Streeter V. L., Wylie E. B. (1983). Fluid Mechanics, 206 pages. Eds. McGraw-Hill, Ryerson Ann Arbor. Michigan 48106 U.S.A.

[4] Almeida A., Koelle E. (1992). Fluid Transients in Pipe Networks, *Computational Mechanics Publications and Elsevier Applied Science*. 564 pages

[5] Wenping Z., Huaizhong S, Gensheng li, Xianzhi S. (2018), Fluid hammer analysis with unsteady flow friction model in coiled tubing drilling, *Journal of Petroleum Science and Engineering PII*: S0920-4105(18)30274-2, DOI: 10.1016/j.petrol.2018.03.088

[6] Twyman J. (2018). Interpolation schemes for valve closure modelling, *Ingeniare: Revista Chilena de Ingenieria*. N°26, pp. 252–263.

[7] Trabelsi M., Triki A. (2019), Dual control technique for mitigating water-hammer phenomenon in pressurized steel-piping systems, International, *Journal of Pressure Vessels and Piping* N°172, pp. 397–413.

[8] BenIffa R., Triki A. (2019), Assessment of inline technique-based water hammer control strategy in water supply systems, Journal of Water Supply: *Research and Technology-Aqua*. Vol 68, Issue 7, pp. 562–572.

[9] Aazhari S. Adiputro, Sadiq J. Zarrouk, Richard J. Clarke, Virginie Harcouët-Menou, STIJN Bos (2020), Geothermal wellswith water hammer during injection fall-off test: Numerical pressure transient analysis, Geothermics, Vol 87, pp. 1-12.

https://doi.org/10.1016/j.geothermics.2020.101838

[10] SUBANI N., NORSARAHAIDA A. (2015). Analysis of water hammer with different closing valve laws on transient flow of hydrogen-natural gas mixture, *Abstract and Applied Analysis*. Volume, Article ID 510675, 12 pages.

[11] Li Zhao,Yusi Yang, Tong Wang, Wensheng Han, Rongchu Wu,Pengli Wang,Qiaoning Wang, and Liang Zhou(2020), An Experimental Study on the Water Hammer with Cavity Collapse under Multiple Interruptions, *Water* 2020, *12*(9), 2566;

https://doi.org/10.3390/w12092566

[12] Rahul K. G., Arun K. (2020), Experimental and numerical investigations of water hammer analysis in pipeline with two different materials and their combined configuration, *International Journal of Pressure Vessels and Piping*, Vol.188, 104219, pp.1-11.

[13] Aliabadi H. K., Ahmadi A., Keramat A.R. (2020),Frequency response of water hammer with fluid-structure interaction in a viscoelastic pipe, *Mechanical Systems and Signal Processing*, Vol 144, pp.1-19. https://doi.org/10.1016/j.ymssp.2020.106848

[14] Mery H. O., Hassan J. M., Ekaid A. L. (2021), Water Hammer Mitigation by Air Vessel and By pass Forward Configuration, IOP Conf. Series: *Materials Science and Engineering*, pp. 1-16. doi:10.1088/1757-899X/1094/1/012052

[15] Kandil M., Kamal A.M., El-Sayed T.A. (2021), Study the effect of pipe materials properties on the water hammer considering the fluid-structure interaction, frictionless model, *International Journal of Pressure Vessels and Piping*.

https://doi.org/10.1016/j.ijpvp.2021.104550.

[16] Khalideh Al. Bk. Al., La'Aly A. Al-S., Abeer Al-B., Alessa A., Amani Ly., EID Gul., Zhou H., Qing Y., Pietro B., Francesco F. (2021), Investigation of the influence of dimensions and material of the pipes on the water hammer effect in microbial fuel cells wastewater treatment plants, *Sustainable Energy Technologies and Assessments*, Vol 44, pp. 1-10.

[17] Sławomir H. (2021), Applied the shock response spectrum method to severity assessment of water hammer loads, *Mechanical Systems and Signal Processing*, Vol 157, , pp. 1-15.

[18] Toumi A., Remini B. (2022), Resolution of the Saint-Venant equations: a case of double and triple effect pumping stations, *Arabian Journal of Geosciences*, pp.1-23.

https://doi.org/10.1007/s12517-021-08269-8

[19] Jinhao Liu Jianhua Wu, Yusheng Zhang, Xinhao Wu (2021), Sensitivity Analysis of Hydraulic Transient Simulations Based on the MOC in the Gravity Flow, *Water* 2021, *13*(23), 3464; https://doi.org/10.3390/w13233464

[20] Yong Han, Weidong Shi, Hong Xu, Jiabin Wang, and Ling Zhou(2022), Effects of Closing Times and Laws on Water Hammer in a Ball Valve Pipeline, *Water* 2022, *14*(9), 1497 https://doi.org/10.3390/w14091497;

[21] Zheng Cao,Qi Xia,Xijian Guo,Lin Lu, and Jianqiang Deng(2022) A Novel Surge Damping Method for Hydraulic Transients with Operating Pump Using an Optimized Valve Control Strategy, *Water* 2022, *14*(10), 1576; https://doi.org/10.3390/w14101576

[22] Meunier M. (1980). Les coups de bélier et la protection des réseaux d'eau sous pression, in: *ENGREF*, Paris, 198 pages.

[23] Oouargh Y. (1971). Ecoulement forcé en hydraulique, Tome II, *Édition Paris*.

[24] MacCormack, R. W., The Effect of viscosity in hypervelocity impact cratering, *AIAA Paper*, 69-354 (1969).

[25] Anderson, J. D., Jr., Computational Fluid Dynamics: The Basics with Applications, *McGraw Hill* (1994)

[26] Provenzano P.G., Baroni F., Aguerre R. J. (2011). The closing function in the water hammer modeling, Latin American Applied Research. Vol. 41, pp. 43–47.

[27] Shamine L.F(2005) Two-step Lax–Friedrichs method, *Applied Mathematics Letters* 18 1134–1136

[28] Goldberg D. E., BENJAMIN W. E. (1983). Characteristics method using time-line interpolations, *Journal of Hydraulic Engineering*. N°109, pp. 670–683.

[29] Dupont A. (1979). Hydraulique urbaine, ouvrages de transport – Elévation et distribution des eaux. Tome 2. *Edition Eyrolles* Paris. 484 pages.

DOI: 10.2478/sspjce-2024-0004

Analysis of Load Eccentricity in Cold-Formed Steel RHS Columns under Compression Considering Geometric Imperfections

Elvira Hodovanets*, Vincent Kvocak

Technical University of Kosice, Slovakia
Faculty of Civil Engineering, Institute of Structural Engineering and Transportation Structures
*e-mail: elvira.hodovanets@tuke.sk

Abstract

This research investigates the impact of hinged and fixed boundary conditions on the behavior of cold-formed steel rectangular hollow section (RHS) columns under eccentric compression. Theoretical analysis and numerical experiments were conducted to study the effects of geometric imperfections and eccentric loading on deformation and failure mechanisms. The findings highlight the significant influence of boundary conditions and geometric imperfections on the columns' stability and load-bearing capacity. These results emphasize the need for careful consideration of these factors in the design and analysis of cold-formed steel structures.

Keywords: eccentricity, cold-formed steel, geometric imperfections, boundary conditions, load-bearing capacity

1 Introduction

The way a column is supported at its ends—whether it is hinged, fixed, or a combination of both—significantly affects its stability, load-bearing capacity, and overall deformation behavior under applied loads.

Hinged boundary conditions allow for rotations at the column ends, which can result in greater deflections and reduced stability compared to fixed conditions, where the ends are restrained from rotating. In practical applications, hinged supports are often used where connections permit some degree of rotational freedom. This can be advantageous in certain designs, but it also introduces complexities in predicting the column's behavior under loads, especially when eccentric loading is involved.

Fixed boundary conditions, on the other hand, provide higher stability as they restrict rotations at the ends of the column. This increased rigidity helps in maintaining the structural integrity and enhancing the load-bearing capacity. Columns with fixed supports are generally more stable and less prone to buckling under axial loads. However, the trade-off is the potential for higher internal stresses, which must be carefully managed in design.

The significance of boundary conditions becomes even more pronounced when dealing with slender columns. Slender columns, characterized by a high length-to-cross-sectional dimension ratio, are more susceptible to buckling. The type of boundary condition can drastically influence the critical load at which buckling occurs. For slender columns, even small eccentricities in loading can lead to significant bending moments, increasing the risk of instability. Therefore, accurately modeling and understanding

the effects of boundary conditions is crucial for the safe and efficient design of slender structural elements.
Extensive research has been conducted to explore the impact of boundary conditions on column stability. Numerical methods, such as those implemented in finite element software like ANSYS, have been instrumental in predicting the complex interactions between boundary conditions, load eccentricities, and geometric imperfections.

2 Theory of hinged and fixed boundary conditions

Boundary conditions significantly influence the behavior and ultimate bending strength of thin-walled structures. Previous studies [1] subjected columns to various boundary conditions, demonstrating their impact on ultimate bending strength. For instance, columns with fixed boundary conditions exhibited higher bending loads due to increased axial stiffness. Conversely, boundary conditions allowing rotations at the loaded end result in decreased ultimate bending strength due to increased deformability. In our study, two types of boundary conditions were examined: hinged and fixed supports. It was observed that the experimental results for columns with fixed supports exhibited a much closer agreement with theoretical predictions. Consequently, the primary focus of this paper is on columns with hinged boundary conditions. This choice was made because the hinged boundary conditions produced more complex and illustrative deformation patterns, which are essential for comprehensively understanding the effects of eccentric loading and geometric imperfections on local stability. This detailed focus on hinged conditions allows for a deeper investigation into the local buckling phenomena and their implications for structural design and analysis.
When a column is hinged at one end only, the boundary conditions at that end do not provide stiffness against bending moments. This causes greater deformations and bending due to the inability of the support to resist lateral forces from eccentric loading.
For columns two-side hinged, loading may cause buckling in the direction of the weaker axis, especially if there is an eccentricity of the load. In analyzing such columns, special attention should be given to longer, less rigid walls, which are more prone to local stability losses and offer less resistance to lateral bending.

3 Experimental studies

In our investigation, we selected short columns with dimensions of 160 mm by 100 mm and a length of 450 mm, constructed with a steel thickness of 2.74 mm, as the primary focus was to examine local resistance phenomena. The decision to utilize short columns was driven by the specific intent to isolate and analyze localized effects and behaviors under compressive loads, without the complexities introduced by global buckling that longer columns might exhibit.
The chosen cross-section dimensions were specifically selected to ensure the column could be classified as slender, falling into the Class 4 category according to Eurocode specifications.
It is recognized that for longer columns, the influence of eccentricity on global buckling would likely be more pronounced. Longer columns would introduce additional variables related to overall stability, making it challenging to isolate local effects [2].
The geometric accuracy of the column was verified using 3D scanning, and the results were integrated into numerical models for further analysis. Material testing revealed enhanced mechanical properties, including a yield strength of 314 MPa and a tensile strength of 460 MPa, exceeding the standard requirements for grade S235.
To test the column, two-sided hinged boundary conditions were employed (Figure 1), simulating realistic operational scenarios. Special attention was given to the influence of geometric imperfections,

such as small deviations from ideal shapes and sizes, which can affect the structure's strength and stability under load.

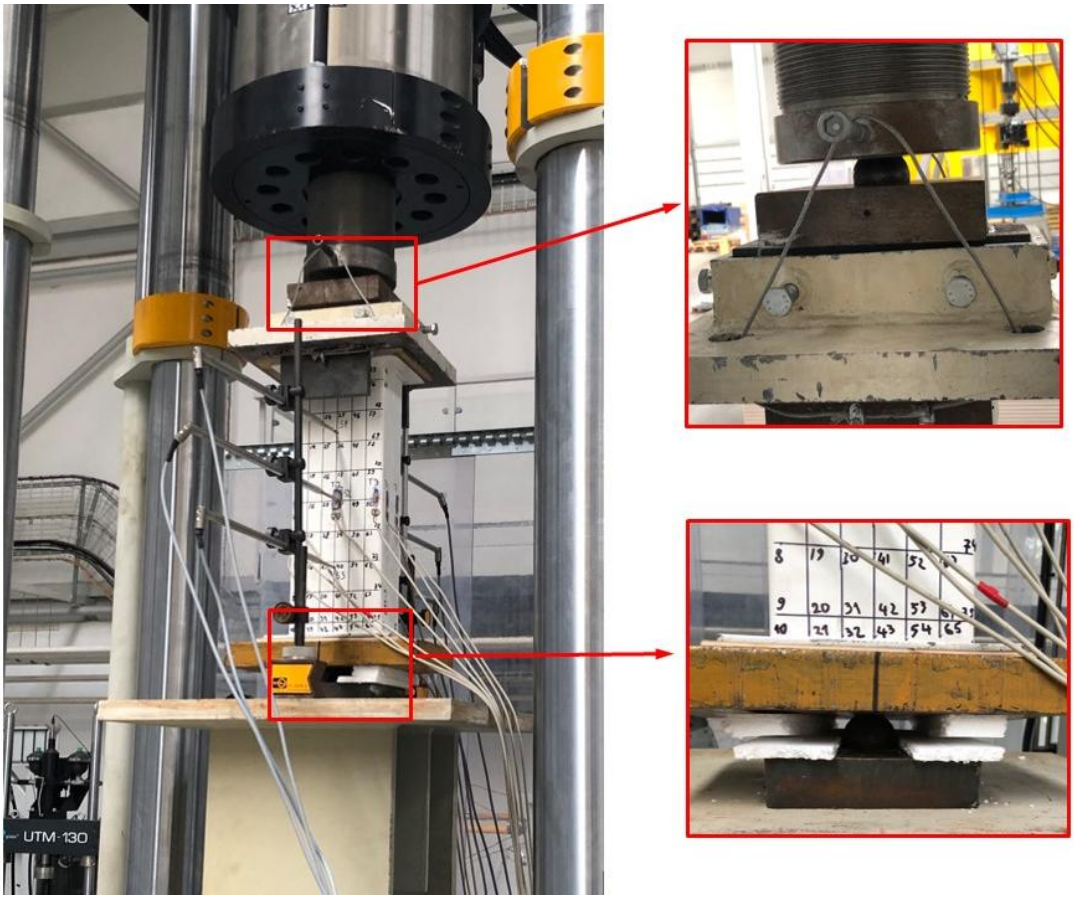

Figure 1: Two-sided hinged boundary conditions of research column

3.1 Measurement of Eccentricity

The measurement of eccentricity involved installing strain gauges around the column's circumference (Figure 2) to capture deformations during loading.
Strain gauges measured deformation at specific points, which was used to calculate stress. Using these stress values, the moments were determined, and from these, the eccentricity was calculated. This analysis helped understand the impact of eccentric loading on the column's behavior.
The strain gauge data revealed uneven stress distribution, indicating load eccentricity (Figure 3). This eccentricity can be attributed to factors such as material differences or varying thicknesses of the opposite wider walls of the column, as well as initial geometric imperfections.
Special attention was given to the top welded plate, which may have imperfections and may not be parallel to the column's base. When the load is applied, it initially transmits through these imperfections, causing the column to deviate towards the more protruding side, resulting in an uneven stress distribution around the perimeter. This can lead to local instability and a decrease in the column's overall load-bearing capacity.
Additionally, if the plates are not welded parallel, it can misalign the column under load. Consequently, the wall pressed by the plate may receive more stress, increasing eccentricity and complicating the calculation of the column's strength and stability [3-4].

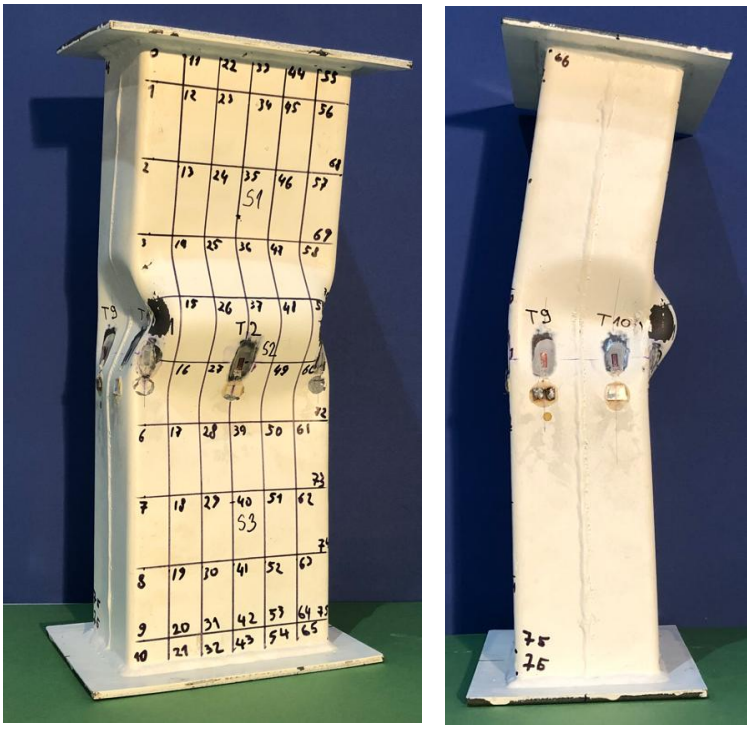

Figure 2: Deformation form from experiment

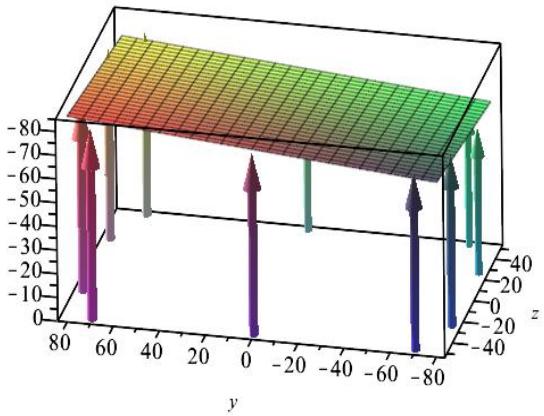

Figure 3: Stress distribution from experiment

4 Comparative analysis of numerical and experimental results

For a deeper analysis, we employed numerical modeling techniques, such as in ANSYS, to replicate the experimental conditions and test how accurately the numerical models predict the behavior of real structures. Our model included simulations incorporating geometric imperfections, boundary conditions, and nonlinear material properties to evaluate their effects on critical loads and deformation behavior.
The following tables present data on the influence of eccentricity on the critical force and total deformation of the RHS column, obtained through numerical simulation. Eccentricity values range from -30 mm to +30 mm, indicating the distance from the center of the column where the force was applied.

The tables highlight data for two different loading conditions: when the eccentricity is applied only from the top and when it is applied from both ends.

Table 1: Eccentricity applied only from the top.

Eccentricity [mm]	Force-numerical [kN]	Total Deformation [mm]	Type of Deformation	Force-numerical / Force-experiment
-30	251.59	13.45	4 (a)	0.859
-20	284.18	14.32	4 (a)	0.970
-10	324.49	15.22	4 (a)	1.108
-8	332.04	15.41	4 (a)	1.133
-6	342.92	15.41	4 (a)	1.170
-4	352.44	15.77	4 (a)	1.203
-2	360.83	15.96	4 (a)	1.232
-1	366.46	16.04	4 (a)	1.250
-0.75	367.40	12.84	4 (b)	1.254
-0.5	368.21	8.89	4 (c)	1.257
0	369.53	8.91	4 (c)	1.261
0.5	371.45	8.97	4 (d)	1.268
1	373.74	8.99	4 (d)	1.276
2	375.07	8.91	4 (e)	1.280
2.5	374.21	13.26	4 (f)	1.278
4	368.07	15.88	4 (g)	1.256
6	358.17	15.68	4 (g)	1.222
8	347.48	15.49	4 (g)	1.186
10	335.80	15.31	4 (g)	1.146
20	294.46	14.41	4 (g)	1.005
30	259.86	13.56	4 (g)	0.887

The following tables present data on the influence of eccentricity on the critical force and total deformation of the RHS column, obtained through numerical simulation. Eccentricity values range from -30 mm to +30 mm, indicating the distance from the center of the column where the force was applied. The tables highlight data for two different loading conditions: when the eccentricity is applied only from the top and when it is applied from both ends. This approach allows for a comparison of how unilateral and bilateral eccentricity affects the column's bearing capacity and deformation.

The experimental data showed an ultimate force of about 293 kN and a calculated eccentricity at the middle of the column of about 8 mm. When we compare these values with the numerical data in the tables, we observe that the force corresponding to an eccentricity of 10 mm matches closely with the experimental ultimate force. This suggests that using these calculations provides a reasonable approximation that can be compared with experimental results.

Table 2: Eccentricity applied from both top and bottom.

Eccentricity [mm]	Force-numerical [kN]	Total Deformation [mm]	Type of Deformation	Force-numerical / Force-experiment
-30	208.02	12.58	5 (a)	0.710
-20	244.17	13.61	5 (a)	0.833
-10	295.25	14.77	5 (a)	1.008
-8	308.41	15.02	5 (b)	1.053
-6	322.00	15.28	5 (b)	1.099
-4	337.56	15.43	5 (b)	1.153
-2	353.77	8.71	5 (c)	1.207
-1	361.81	8.81	5 (c)	1.235
-0.75	363.21	8.82	5 (c)	1.240
-0.5	366.40	8.86	5 (c)	1.250
0	369.53	8.91	5 (d)	1.261
0.5	374.01	8.97	5 (e)	1.276
1	374.70	8.83	5 (f)	1.279
2	367.58	8.71	5 (f)	1.255
2.5	368.36	12.81	5 (f)	1.258
4	350.87	14.48	5 (g)	1.198
6	335.13	14.57	5 (g)	1.144
8	320.58	14.33	5 (g)	1.094
10	306.27	14.09	5 (g)	1.045
20	252.25	13.02	5 (g)	0.861
30	214.30	12.07	5 (g)	0.731

Figures 4 and 5 depict the types of deformations occurring in a column under eccentric loading from the top only and from both top and bottom simultaneously.

Certain deformation characteristics correspond to each type of eccentricity. For example, Figures 4(a) and 5(a) show a column with an eccentricity of -30 mm, where the strain shape is symmetrical about the vertical axis but differs in stress form and distribution. In both cases, stress concentrations are noted in areas of greatest curvature.

By changing the boundary conditions from one-sided to two-sided, the stress distribution and deformation shape of the column change. For instance, in Figure 5(b) with an eccentricity of -8 mm from the top and bottom, deformation is concentrated in the middle part of the column and is smaller at the ends, compared to Figure 4(a) where such eccentricity is applied only on one side.

Special attention should be paid to Figure 5(g), which illustrates a significant change in column behavior at high positive and negative values of eccentricity. The deformation indicates a significant asymmetry in the column's response, suggesting a critical effect of load eccentricity on structural stability. This may be due to increased lateral bending and additional moments introduced into the system, especially noticeable with eccentricity.

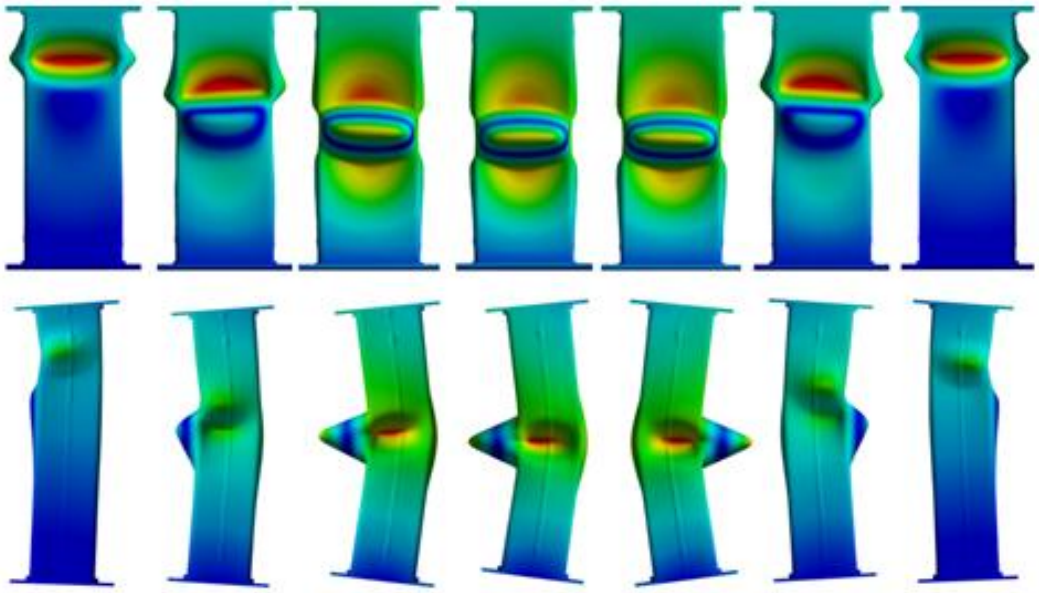

a) b) c) d) e) f) g)

Figure 4: Type of deformation with eccentricity at top

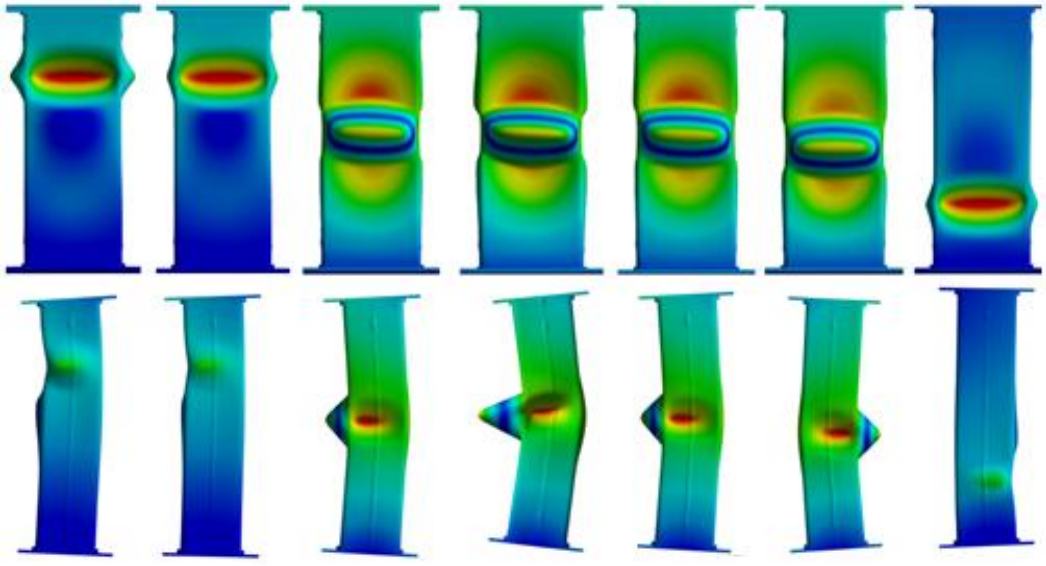

a) b) c) d) e) f) g)

Figure 5: Type of deformation with eccentricity at top and bottom

5 Conclusion

This study provides new insights into the behavior of cold-formed steel columns with a rectangular hollow section under eccentric compressive loading. The consideration of geometric imperfections and boundary conditions, as demonstrated by experimental and numerical models, significantly influences the magnitude of critical loads and the deformation character of the column. Analysis of the data revealed

that manufacturing and installation imperfections, such as wall thickness variations and non-parallelism of welded plates, lead to a reduction in load-bearing capacity and may cause unexpected forms of stability loss.
Moreover, it was found that geometric imperfections significantly change the internal stress distribution in the column, indicating the necessity to consider these parameters in design and analysis. The presented results of experiments and ANSYS modeling confirm that existing methods of calculating column strength may be insufficient if not all possible influences and imperfections are considered.
Additionally, the types of deformations identified at high eccentricity values indicate an asymmetric response of the column to loading, which may suggest a critical impact of load eccentricity on structural stability.

Acknowledgments

The paper has been supported by the projects: VEGA 1/0642/24" Analysis of FRP and Concrete Composite Structural Members "of the Scientific Grant Agency of the Ministry of Education, science, research and sport of the Slovak Republic.

References

[1] Sadovsky, Z., & Kriváček, J. (2018). Influence of boundary conditions and load eccentricity on strength of cold-formed lipped channel columns. *Thin-Walled Structures, 131*, 556-565. https://doi.org/10.1016/j.tws.2018.07.020

[2] Hodovanets, E., Ali, M. A., & Kvocak, V. (2023). Cold-formed closed profiles - Experimental program and theoretical analysis. *AIP Conference Proceedings, 2887(1),* 020065. https://doi.org/10.1063/5.0197568

[3] Hasanalı, M., Mojtabei, S. M., Hajirasouliha, I., & Clifton, G. C. (2023). More accurate design equations for cold-formed steel members subjected to combined axial compressive load and bending. *Thin-Walled Structures, 185,* 110588. https://doi.org/10.1016/j.tws.2023.110588

[4] Rozylo, P., & Debski, H. (2024). Stability and load carrying capacity of thin-walled composite columns with square cross-section under axial compression. *Composite Structures, 329,* 117795. https://doi.org/10.1016/j.compstruct.2024.117795

[5] Yun, X., Meng, X., & Gardner, L. (2022). Design of cold-formed steel SHS and RHS beam-columns considering the influence of steel grade. *Thin-Walled Structures, 171,* 108600. https://doi.org/10.1016/j.tws.2022.108600

DOI: 10.2478/sspjce-2024-0005

Assessment of a residential building in terms of carbon footprint and circular economy

Jana Budajova[1*], Silvia Vilcekova[2], Eva Kridlova Burdova[2] and Peter Mesaros[3]

Technical University of Kosice, Vysokoskolska 4, 042 00 Kosice, Slovakia
[1] Faculty of Civil Engineering, Institute of Architectural Engineering
[2] Faculty of Civil Engineering, Institute for Sustainable and Circular Construction
[3] Faculty of Civil Engineering, Institute of Technology, Economics and Management in Construction
*e-mail: jana.budajova@tuke.sk

Abstract

Built environment contributes significantly to social and economic development, but it is also resource intensive. It is therefore one of the main producers of emissions and carbon footprint. Choosing building designs with a long service life is the key to resolving environmental problems. In this paper, the life cycle of a residential building is evaluated to reduce the greenhouse gas emissions and costs associated with the construction, use and disposal of the building. Life Cycle Assessment and Life Cycle Costing methods were used to evaluate the environmental and financial impact of the residential building. The system boundaries were defined as "Cradle to Grave" and a lifetime of 60 years. The calculation showed that the building emitted 843 tons of CO_{2e}, or 19.8 kg CO_{2e}/m^2/year, and the life cycle costs were 2 026 €/m^2. Considering the phases considered, the energy consumption phase (B6) caused the highest CO_{2e} emissions, up to 50.1%.

Keywords: life cycle assessment, residential building, carbon footprint, circular economy, life cycle cost

1 Introduction

The construction sector and its related manufacturing supply chain emit greenhouse gases (GHG) due to misallocation of resources and misuse of energy. Sustainability has a wider definition and includes three aspects – environmental protection, social aspect, and economic security [1].
The circular economy is a model of production and consumption in which products and services are designed to enable sharing, reuse, repairability and recyclability. Unlike the linear economy, where resources are overused and unnecessary waste is created, in the circular economy scarce resources they use effectively, and the value of the products does not end up buried in a landfill. The circular economy tries to reflect natural processes where no waste is created. Waste is considered a resource that is returned to circulation, creating a closed cycle of materials, products, and components [2, 3]. Life cycle assessment (LCA) can support circular economy

(CE), which is already written into regulations and is becoming an important tool for environmental management in the construction industry [2]. It seeks to address issues the problems of energy consumption and carbon emissions, given the significant environmental burden created by the construction industry. Therefore, environmental assessments such as LCA have been developed for buildings [1]. Construction contributes around 35% of the total municipal waste disposed in landfills [4]. Due to growing concerns about resource use in building construction, energy consumption during building operation, end-of-life waste disposal and related environmental impacts. As a consequence of the global development of building construction, the operation, maintenance/renovation and decommissioning of buildings would place an even greater burden on the environment. Therefore, due to the increased emphasis on sustainability, the construction industry is a key target for reducing environmental impacts worldwide [5]. Carbon footprint has become an important concept against climate change and sustainability. It involves the calculation of the amount of greenhouse gases, especially carbon dioxide (CO_2), which are produced directly or indirectly by an individual, organization, event, or product. This concept helps us better understand the ecological impact of our activity and serves as a basis for the development of measures aimed at reducing emissions and a sustainable lifestyle [6, 7]. Greenhouse gas emission values are expressed as equivalents. Global warming potential (GWP) is expressed as CO_2 equivalent [8]. The assessment of a residential building in terms of carbon footprint and circular economy involves evaluating the environmental impact of the building's construction, operation, and eventual disposal, as well as considering how resources can be used more efficiently and sustainably throughout its lifecycle [9, 10]. The evaluation also includes costs that have been calculated for the entire cycle. This assessment aims to reduce greenhouse gas emissions, minimize waste generation, and promote the reuse and recycling of materials to create a more sustainable and environmentally friendly living space. Can a building be overpriced without negative environmental impacts? These are the questions we ask in this paper.

2 Materials and methods

The assessment of the life cycle of the residential building from the point of view of environmental and economic aspects was carried out in accordance with valid international standards. Based on these standards, the analysis consists of the goal and scope, inventory analyzes (the process of obtaining and gathering information about all inputs and outputs that are associated with a product or service during its life cycle), impact analyzes (evaluation and quantification of the environmental impacts associated with the product or by the service during their life cycle) and interpretation of the results.

2.1 Goal and Scope

To analyse the impact of the building on the environment for the "Cradle to Cradle" system boundary, the software OneClickLCA was used, which works in accordance with EN 15987+A2+AC, STN EN ISO 14040 and ISO 14044. In the software, materials were selected, their transport distances, operating energy, water consumption and quantification of their emissions. The effects on the environment were determined on the gross floor area of the building, which was converted to $1m^2$ for a lifetime of 50 years. Life cycle costs were also

quantified using the OneClickLCA software, which worked in accordance with the ISO 15686-5 standard according to the structure of the EN 16627 standard. The system boundaries of the life cycle according to the standardized phase marking A1 to D are shown in Figures 1 and 2.

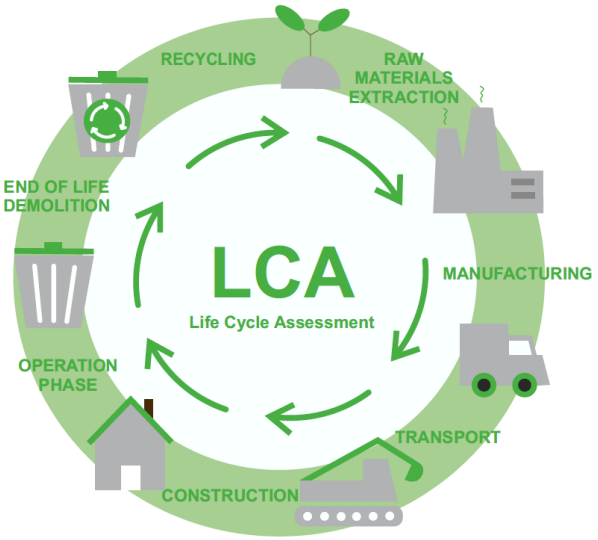

Figure 1: Life cycle assessment [Author]

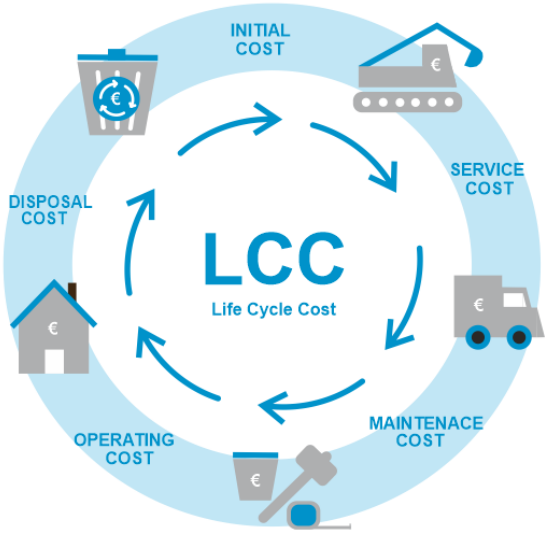

Figure 2: Life cycle cost [Author]

2.2 Life cycle inventory analysis

The selected residential building is located in Poprad. Poprad is one of the larger cities in Slovakia. It is in the north of Slovakia, near the High Tatras (figure 3). The gross floor area is 849.38 m^2 on four floors, which is a smaller apartment building in Slovakia. The residential building is part of a complex of four identical residential buildings (figure 4 and 5) and meets the thermal requirements for category A0 (zero building). The building has a brick load-bearing system made of clay bricks; the ceilings are made of reinforced concrete slabs 160 mm thick. The building is insulated with Greywall EPS (expanded polystyrene) insulation. It's important to consider the energy consumption values of the building, which are 42.4 kWh/m^2/a of electricity and 68.8 kWh/m^2. Calculating the carbon footprint of the residential building per 1m^2 of gross floor area over a 50-year period can provide valuable insights into its environmental impact. Analyzing and optimizing these values can help in implementing more sustainable practices and reducing carbon emissions.

Figure 3: Position of residential building [13]

Figure 4: Residential building

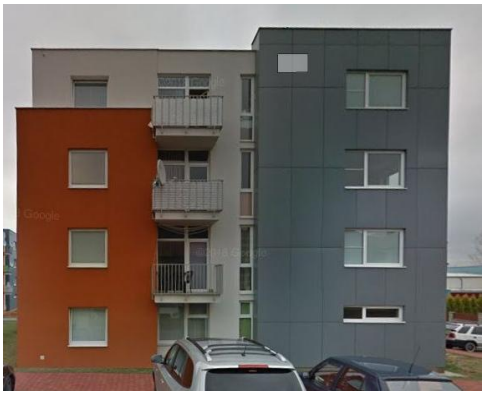

Figure 5: Residential building [14]

The materials used in the residential building, their amount and cost are shown in Figure 6.

Class	Quantity	Unit	€
Ready-mix concrete	338,044	m^3	51 295
Reinforcement steel (rebar)	32,272	ton	19 575
Brick	633,392	m^3	45 371
Aggregate (crushed gravel)	64,412	m^3	1 868
Formwork	99,755	m^2	2 604
Insulation, EPS, Rock wool, XPS	1 058,607	m^3	15 440
Waterproofing and vapor barrier	2 198,612	m^2	8 843
Plasters, mortars and paints	222 577,127	kg	70 786
Masonry lintel	90	m	1 046
Other structures	5 053,686	m^2	53 639

Figure 6: Total sum [Author]

2.3 Life cycle impact assessment

In the Life Cycle Impact Assessment (LCIA) step, all inventory data of the residential building were evaluated. The LCA approach allowed the assessment of many categories of environmental impacts. The main environmental impact indicators included in this study were shown in Figure 7. The residential building was also analyzed in terms of life cycle costs. Life cycle costing refers to the total cost of owning and maintaining a product or system throughout its lifetime. Nominal life cycle cost is the total cost including inflation or the time value of money, while discounted life cycle cost considers the time value of money by discounting future costs to present value. This helps in comparing costs over time and making informed decisions.

Impacts categories		**Unit**
Global Warming Potential total	GWP-Total	[kg CO_{2e}]
Global Warming Potential fossil	GWP-Fossil	[kg CO_{2e}]
Global Warming Potential biogenic	GWP-Bio	[kg $CO_{2e\ bio}$]
Global Warming Potential, LULUC	GWP-LULUC	[kg CO_{2e}]

Figure 7: Impact categories [Author]

3 Results and discussion

3.1 Life cycle assessment - Global warming potential

In the GWP-Total category, the largest share of CO_{2e} emissions is operational energy phase B6 of up to 50%, followed by the product phase with 20.9%, where used bricks, mortars, and screeds 25.5% and 18.1% have the most negative impact on the climate change (figure 8). The phase with the lowest share of CO_{2e} is the transport with share 1.2%. Consumptions of electricity and energy are the main contributors of CO_{2e}. In the GWP-Fossil (figure 9) category, the operational energy phase of B6 has the largest contribution to CO_{2e} emissions at 50.1%, followed by the product phase at 22.9%, where the largest negative impacts are from used coatings, paints, and lacquers at 25.2% and bricks at 20.8%. In the GWP-Bio (figure 10) category, the C3 and C4 phases cause 99.3% of the emissions. In the GWP-LULUC (land use and land use change) (figure 11) category, the product phase A1-A4 and B4-B5 have the largest contribution to CO_{2e} emissions up to 49% and 32.9% respectively.

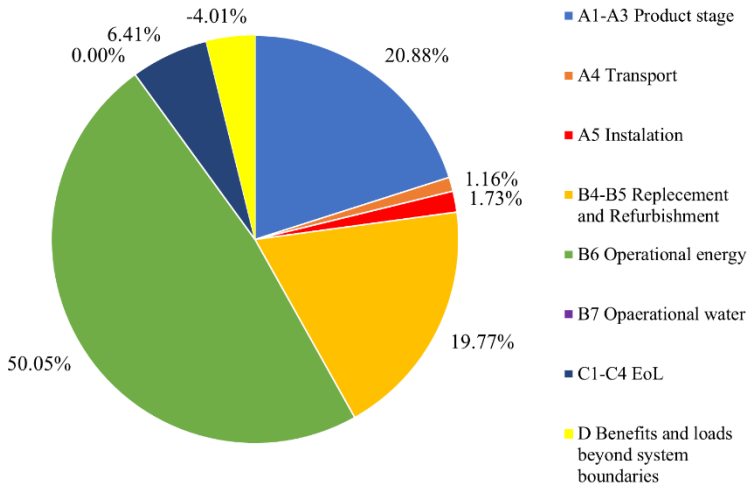

Figure 8: GWP-Total [Author]

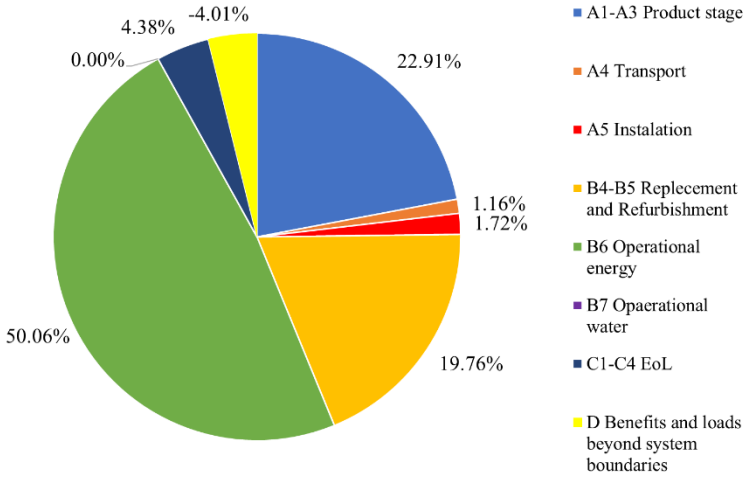

Figure 9: GWP-Fossil [Author]

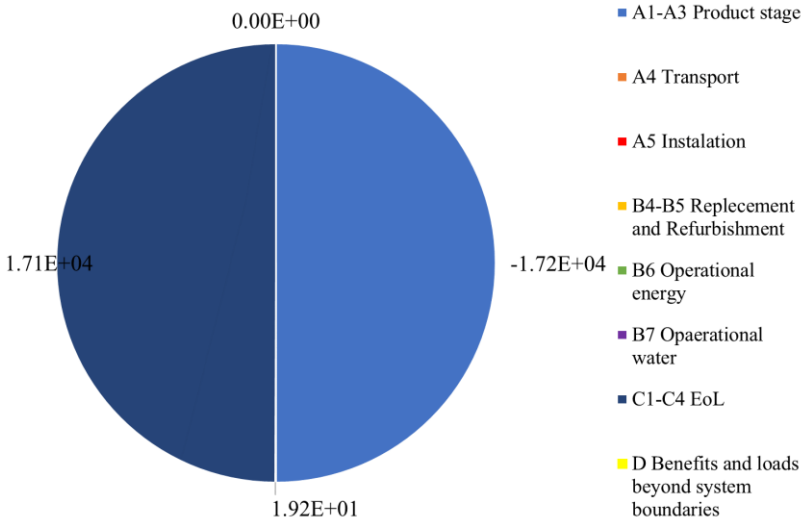

Figure 10: GWP-bio [kg CO_{2e} bio] [Author]

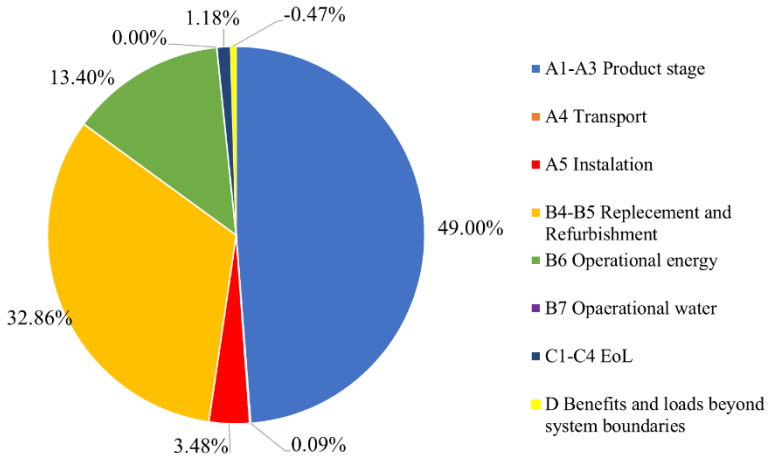

Figure 11: GWP-LULUC [Author]

The whole building comprehensively generated CO_{2e} emissions in the range of 843 tons of CO_{2e}. Converted to FU, it causes emissions of 19.8 kg CO_{2e}/m^2/year (figure 7). Stages that contribute the most to a carbon footprint, were the operational energy B6, product A1-A3 and recovery and renovation B4-B5. The energy consumption phase (B6) was represented by a 50.1% share, followed by the product phase (A1-A3) by a 20.88% share and recovery and renovation (B4-B5) by a 19.77% share. The least represented were transport (A4) and installation (A5) with a share of 1.16% and 1.73%, respectively.

3.2 Results of life cycle cost

From the calculation of life cycle costs, it emerged that the building had a nominal value of 1 720 881€. The total life cycle costs in terms of functional unit reached 2 026 EUR/m^2 (1 720 881 €/849.5 m^2) (see figure 12). Based on the context provided, the estimated distribution of life cycle costs reached, energy costs 14.7%, construction costs 67.3%, building maintenance costs 11.6%. These percentages represented the allocation of the life cycle budget to different cost categories. The EoL phase represents only a small amount of 1% (see figure 13).

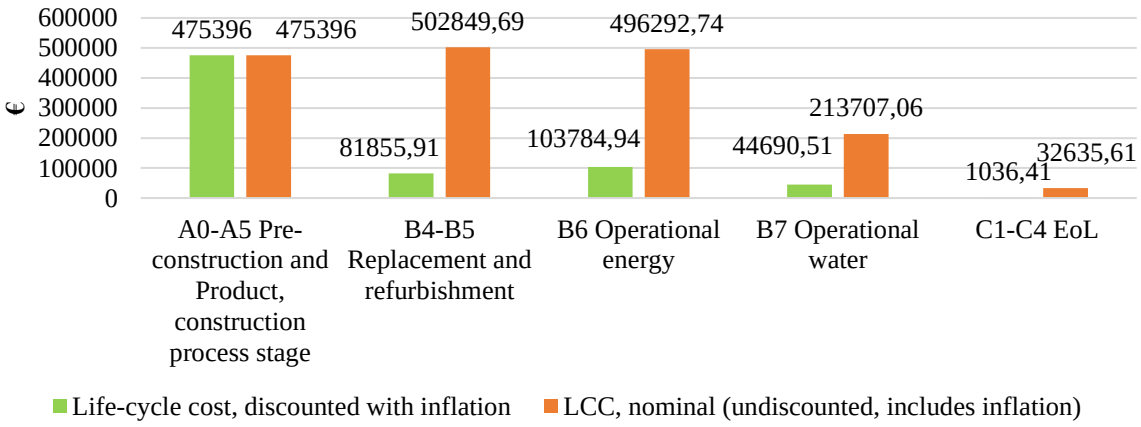

Figure 12: Life cycle stages

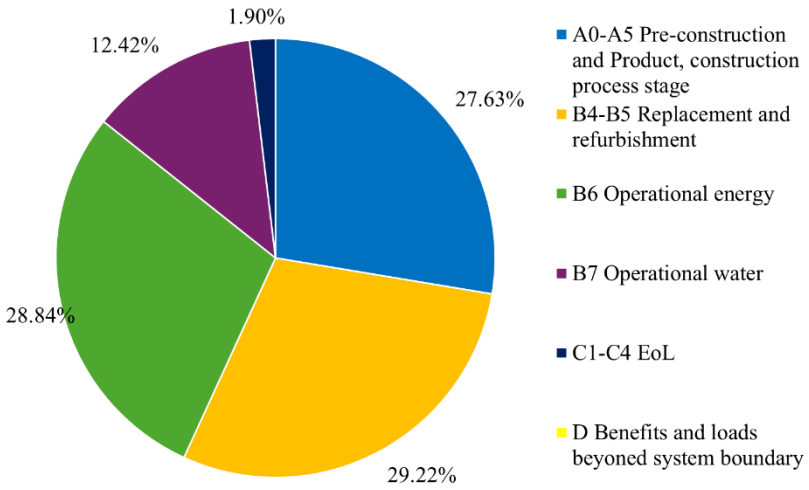

Figure 13: Life cycle cost stages [Author]

3.3 Discussion

Carbon footprint of the residential building is determined using by using LCA. The estimated useful life was calculated for a period of 50 years. The whole building generates CO_{2e} emissions in the range of 843 tons, which represents 19.8 kg CO_{2e}/m^2/year and 992 kg CO_{2e}/m^2. Compared to the study of residential buildings [11], which evaluates a 5-storey and 13-storey residential buildings from South-East Turkey, a building rated in Slovakia causes less CO_{2e} emissions. Emission ranges from 3 956 to 5 809 kg CO_{2e}/m^2. In comparison with this study, the energy consumption phase accounted for the largest greenhouse gas emissions. In this study, a different insulation material was used for the walls which may have caused higher emissions. The authors further state that by choosing the appropriate insulation material, a reduction in emissions can be achieved and this is confirmed in their study. In this study, the total life cycle costs are reached at USD 7.28 million, which is EUR 6.4 million for a five-story building and USD 1.72 million, which is 1.5 million € for a thirteen-story building over the proposed 50 lifetime. Among the most expensive (49-52%) materials and structures are concrete foundations, reinforced concrete slab. For the building investigated in this study, the total life cycle cost is 1.72 million € which is comparable with the mentioned study [11]. The study [12] examined a ten-storey building in Denmark. It has a total area of 7 000 m^2, the external wall is a sandwich construction with mineral wool, and the building uses an HVAC system with a heat pump and photovoltaic panels. The total LCC is 15.4 million €, per m^2 is 2 203 €/m^2.

4 Conclusion

The construction and maintenance of building structures involve energy-intensive processes throughout their life cycle, starting from the extraction of raw materials, product production, and even disposal. This highlights the importance of considering the environmental impact and energy consumption associated with the entire lifecycle of buildings. Energy-intensive processes consume large amounts of energy resources and produce significant emissions and waste. Absolutely, the environmental impact of construction includes various stages such as

material extraction, transportation, manufacturing, operation, maintenance, and end-of-life considerations. It's important to consider these factors to minimize the environmental footprint of construction projects. These phases also have significant economic costs. Assessing the environmental impact and life cycle costs of a residence as a challenging task and it is necessary to evaluate all elements and phases of the life cycle. Results of this study point out that operational energy contributes the most to the carbon footprint (50%) as well as the biggest costs also go to operational energy. The amount of CO_{2e} emissions is affected not only by the choice of materials but also by the total gross floor area. Future research will focus on conducting an in-depth analysis and comparison of the environmental and economic aspects of different buildings, which can help identify environmentally friendly measures and sustainable practices. This approach can lead to more informed decision-making in the construction industry and contribute to the creation of greener and more efficient buildings.

Acknowledgments

This study was financially supported by Grant Agency of Slovak Republic to support project No. VEGA 1/0057/24 and by the Slovak Research and Development Agency APVV-22-0576.

References

[1] Mhatre P., Gedam V., Unnikrishnan S. & Verma S. (2021). Circular economy in built environment–Literature review and theory development Journal of Building Engineering 35 101995.

[2] Joensuu T., Leino R., Heinonen J. & Saari A. (2021). Developing Buildings' Life Cycle Assessment in Circular Economy-Comparing methods for assessing carbon footprint of reusable components Sustainable Cities and Society 103499.

[3] Tunn, V. S., Bocken, N. M., van den Hende, E. A., & Schoormans, J. P. (2019). Business models for sustainable consumption in the circular economy: An expert study. Journal of cleaner production, 212, 324-333.

[4] Kamali M., Hewage K. & Sadiq R. (2019). Conventional versus modular construction methods: A comparative cradle-to-gate LCA for residential buildings Energy and Buildings 204 109479.

[5] Joensuu T., Leino R., Heinonen J. & Saari, A. (2021). Developing Buildings Life Cycle Assessment in Circular Economy-Comparing methods for assessing carbon footprint of reusable components Sustainable Cities and Society 103499.

[6] East A. J. (2008). September What is a carbon footprint? An overview of definitions and methodologies. In Vegetable industry carbon footprint scoping study - Discussion papers and workshop Horticulture Australia Limited.

[7] Števo S. (2008). Uhlíková stopa bývania v globalizovaných domoch TZB Haustechnik roč. 25 pp16-20.

[8] Amoo L. M. & Fagbenle R. L. (2020). Climate change in developing nations of the world In Applications of Heat, Mass and Fluid Boundary Layers (Woodhead Publishing) pp 437-71.

[9] Ghisellini, P., Ripa, M., & Ulgiati, S. (2018). Exploring environmental and economic costs and benefits of a circular economy approach to the construction and demolition sector. A literature review. Journal of Cleaner Production, 178, 618-643.

[10] Chau, C. K., Leung, T. M., & Ng, W. Y. (2015). A review on life cycle assessment, life cycle energy assessment and life cycle carbon emissions assessment on buildings. Applied energy, 143, 395-413.

[11] Atmaca A. (2016). Life-cycle assessment and cost analysis of residential buildings in South-East of Turkey: part 2—a case study The International Journal of Life Cycle Assessment 21 pp 925-942.

[12] Marszal, A. J., & Heiselberg, P. (2011). Life cycle cost analysis of a multi-storey residential Net Zero Energy Building in Denmark. *Energy*, 36(9), 5600-5609.

[13] Google Maps, Available online: 12.03.2024

https://www.google.sk/maps/place/LUNA+RESIDENCE+POPRAD+-+MATEJOVCE/@49.0788993,20.3278781,376m/data=!3m1!1e3!4m14!1m7!3m6!1s0x473e3bc5e38c4fb7:0x7af2e9cb4a896bdf!2sLUNA+RESIDENCE+POPRAD+-+MATEJOVCE!8m2!3d49.0794723!4d20.3194412!16s%2Fg%2F11txjd76ds!3m5!1s0x473e3bc5e38c4fb7:0x7af2e9cb4a896bdf!8m2!3d49.0794723!4d20.3194412!16s%2Fg%2F11txjd76ds?entry=ttu

[14] Google Maps, Street View, Available online: 12.03.2024

https://www.google.sk/maps/@49.079063,20.3286721,3a,60y,150.13h,87.15t/data=!3m6!1e1!3m4!1se3SmxDWDIsN0nAhY63-gmw!2e0!7i16384!8i8192?entry=ttu

DOI: 10.2478/sspjce-2024-0006

Study of Repairs and Various Post-Seismic Interventions Carried Out in Ancient Sites in Algeria

Said Benmehidi[1*], Abdelhak Bordjiba[2]

[1] Laboratory of Design and Modeling of Architectural and Urban Forms and Ambiances - LACOMOFA Biskra. Department of Architecture, Badji Mokhtar - Annaba University 12, P.O.Box, 23000 Annaba, Algeria.
[*]e-mail: said.benmehidi@univ-annaba.dz
[2] Laboratory of Design and Modeling of Architectural and Urban Forms and Ambiances - LACOMOFA Biskra. Department of Architecture, Badji Mokhtar - Annaba University 12, P.O.Box, 23000 Annaba, Algeria.
e-mail: abdelhak.bordjiba@univ-annaba.dz

Abstract

Centuries of accumulated experience in construction during ancient times led to considerable expertise. Roman builders, for example, honed their engineering and construction skills to a high degree, even factoring in considerations for seismic hazards. Through an examination of the vestiges of Roman civilization, one can discern various parallels between the structures found in Europe and those in Roman Africa, particularly in the methods employed for repairs labeled by scholars as post-seismic restoration. The investigation took place across multiple historic locations in Algeria, including Djemila, Timgad, and Lambèse, aiming to examine the possible correlation between previous renovations and seismic activity. This was achieved through visual examination and comparative analysis with findings from Italian sites such as Pompeii and Ostia.

Keywords: earthquake, antiquity, construction, ancient sites, construction techniques and materials.

1 Introduction

Algeria, situated in North Africa along the Mediterranean coast, has long been susceptible to earthquakes owing to its geographical location. Its proximity to the meeting point of tectonic plates, namely the African and Eurasian plates, akin to neighboring countries in the Mediterranean basin, has resulted in significant and devastating seismic occurrences. Despite advancements in understanding contemporary earthquakes, historical seismic events in Algeria remain relatively under-documented and less comprehended.

The northern part of Algeria, which harbors several ancient cities, is located in a region prone to earthquakes. Historical records from the Algerian seismic database indicate numerous seismic occurrences in the area, some of which were significant in magnitude (for instance, Algiers in 1365 and 1716, Djijel in 1856, El Asnam in 1980 with a magnitude of 7.3, Constantine in 1985 with a magnitude of 6.0, and Zemmouri in 2003 with a magnitude of 6.8).

Due to its reputation for seismic activity, Northern Algeria presents an intriguing case for study, especially with its array of ancient sites.

The enduring presence of ancient artifacts today is testament to their resilience against natural calamities. This endurance is not coincidental; rather, it undoubtedly stems from a deliberate approach or careful planning by the builders of that era.

In pursuit of this goal, we analyzed various instances and sought to juxtapose them with prior research, including works by GIULIANI [1], RUGGIERI [2], DESSALES [3], and TOMASSINI [4], all of which delineated typological classifications of disorders observed on archaeological sites.

2 Methods

Using a comparative method, we will explore the behavior of ancient builders towards earthquakes. The following study will primarily focus on comparing indices - regarded by researchers as post-seismic repairs - between ancient sites in Algeria and those in Italy.

3 Ancient Earthquakes and current Seismicity

Historically, Algeria is renowned for being a highly seismic area. Through Latin accounts, we have gleaned some indications regarding the destruction caused to buildings and the restoration efforts on the structures affected by earthquakes as early as the 1st century BCE and CE. According to FERDI & HARBI, scant information about earthquakes in Algeria during antiquity has been found in epigraphic and literary sources, such as the earthquakes of Lambaesis in 267 and Sitifis in 419 [5]. Examples include the one in Ad Maiores, now Negrine, in 267 CE, where, according to an inscription, an earthquake was believed to have caused the collapse of an arch overnight. Another earthquake was recorded on July 21, 365; according to LEPELLEY, it likely affected a significant portion of the Mediterranean, including possibly the Roman city of Cuicul (Djemila) [6], as well as the earthquake in Sitifis (present-day Sétif) in 419, mentioned by GUIDOBONI, referencing St. Augustine's Sermons [7].

Presently, the CRAAG (Centre de Recherche en Astronomie, Astrophysique et Géophysique) possesses substantial data regarding seismic occurrences in Algeria. As per the findings of this research institution, seismic activity in northern Algeria persists without interruption. The surveillance system registers around 50 tremors monthly, predominantly of low magnitude, and largely distant from urban areas, comprising nearly 90% of the recorded seismic events.

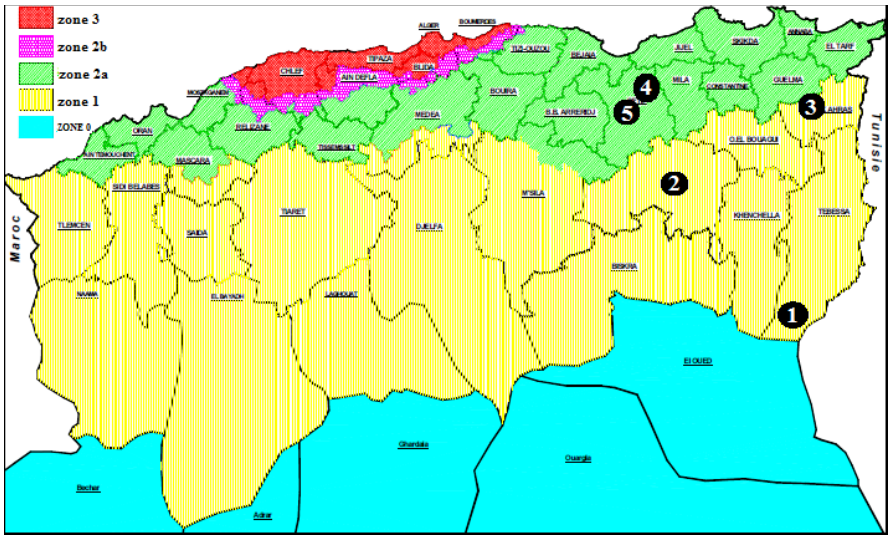

Figure 1: Distribution of ancient earthquakes on the seismic zoning map (source: CGS - RPA99 version 2003). Number 1: Negrine earthquake in 267, Number 2: Lambèse and Timgad earthquakes in 267, Number 3: Khemissa earthquake in 355, Number 4: Djemila earthquake in 365, Number 5: Sétif earthquake in 365.

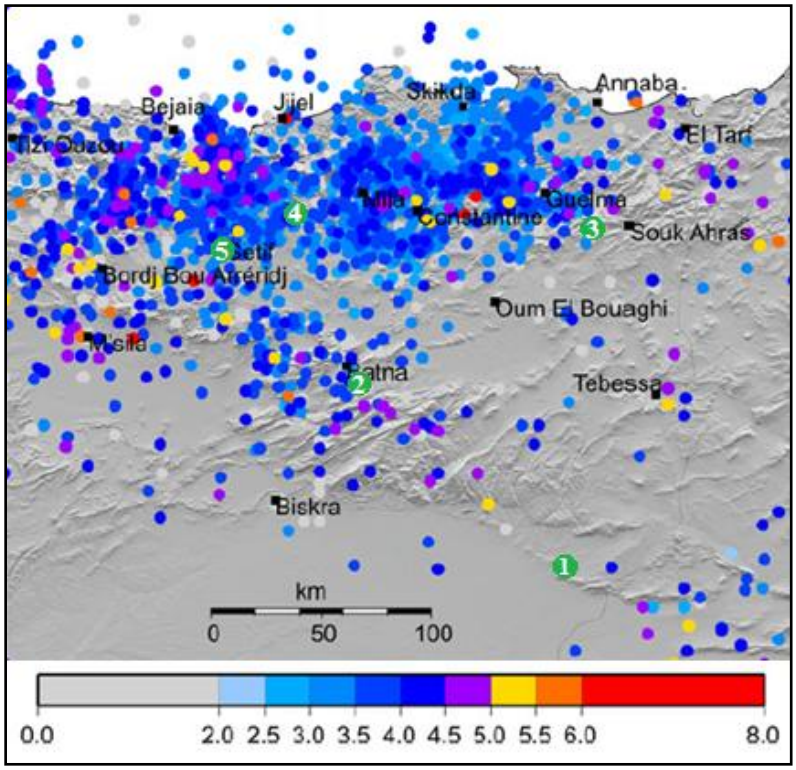

Figure 2: Ancient seismic activity distribution compared to recent seismic events and their magnitude (source: HARBI & AL.) [8]. Colored points represent recent earthquakes according to their magnitude. Number 1: Negrine earthquake in 267, Number 2: Lambèse and Timgad earthquakes in 267, Number 3: Khemissa earthquake in 355, Number 4: Djemila earthquake in 365, Number 5: Sétif earthquake in 365.

Table 1: Key earthquakes recorded from antiquity to the 20th century in eastern Algeria, particularly in the Sétif-Batna study area (reported by the author).

Seismic location	Date of the earthquake	Source of information
Ad Maiores	267	- BALLU [9]. - LEPELLEY [6]. - FERDI & HARBI [5]. - HARBI & AL. [10].
Lambaesis	267	- BALLU [11]. - LEPELLEY [12]. - FERDI & HARBI [5]. - HARBI & AL. [10].
Thamugadi	267	- BALLU [9]. - LEPELLEY [12, 6] - LAPORTE & DUPUIS [13].
Thubursicu Numidarum	355	- LEPELLEY [12, 6] - FERDI & HARBI [5].
Cuicul	365	- ALBERTINI [14]. - REBUFFAT [15].
Setifis	419	- GUIDOBONI [7]. - FERDI & HARBI [5]. - HARBI & AL. [10].
Lambaesis	October 13th, 1893	- HARBI & AL. [10].
Lambaesis	December 27th, 1893	- HARBI & AL. [10].
Setif Region	1850 – 1852 – 1855 – 1863 – 1867 – 1877 – 1875 – 1881 – 1885 – 1886 – 1887 – 1888 – 1889 – 1890 – 1893 – 1895 – 1898 – 1902 – 1909 – 1913 – 1930 – 1931 – 1938 – 1953 – 1963.	- HARBI & AL. [10].
Batna Region	1856 – 1858 – 1866 – 1869 – 1870 – 1875 – 1879 – 1882 – 1892 – 1893 – 1895 – 1898 – 1901 – 1904 – 1907 – 1911 – 1924 – 1925.	- HARBI & AL. [10].

4 Study area and earthquakes

Algeria's earthquake-prone regions predominantly lie adjacent to the Tell Atlas Mountains, encompassing locales like Kabylie and the Aurès mountains. We selected our study area due to its history of seismic events and the accessibility of pertinent indices central to our research focus. Figure 3 provides a depiction of earthquake occurrences within this study region.

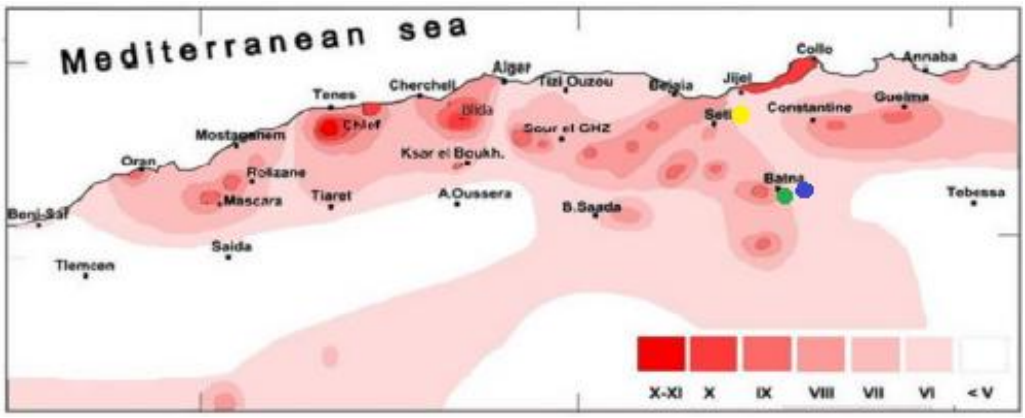

Figure 3: Localization of ancient sites - case study - on the map of macroseismic intensities in Northern Algeria (source: CRAAG 1999). Green point: Lambaesis, Blue point: Timgad, Yellow point: Djemila.

Algeria boasts a wealth of archaeological sites bearing witness to its ancient history. Among them, we will examine three sites:

• **Tazoult (Lambèse or Lambeisis):** A Roman city initially established as a military camp by the Third Legion of Augustus, located 10 kilometers from Batna.

• **Timgad (Thamugadi):** A well-preserved ancient Roman city situated in the province of Batna.

• **Djemila (Cuicul):** Another UNESCO World Heritage Site, a Roman archaeological site located in the province of Sétif.

Certainly, these ancient sites have been affected by several seismic events with varying magnitudes, as evidenced by Figures 2 and 3, as well as Table 1.

5 Antique sites - case studies - and work carried out over time

The well-maintained excavation reports serve as essential resources for analytically studying archaeological sites. They provide invaluable insights into the excavation and restoration efforts undertaken at different historical locations, enabling a deeper understanding of these endeavors.

5.1 Tazoult (Lambèse or Lambeisis)

Founded in 81 AD as the camp for the III Augustan Legion, Lambèse evolved into the principal city of the Numidia province under Septimius Severus, reigning from 198 to 208 AD. Though the excavation efforts have only partially revealed its remnants, Lambèse retains immense importance in the region's historical landscape. As documented by Albert BALLU, the primary focus of Lambèse's restoration work has centered on excavation endeavors and upkeep tasks, including the repair of wall coping stones damaged by weather in 1926 [16].

5.2 Timgad (Thamugadi)

Founded in 100 AD under Emperor Trajan and the III Augusta Legion, Timgad stands out for its remarkably intact ancient remnants. Spearheading the excavation and restoration initiatives at Timgad was Albert BALLU. His endeavors encompassed archaeological excavations to deepen insights into the city's history and layout, alongside restoration projects aimed at safeguarding and reviving existing architectural marvels. The primary goal was the stabilization of structures, occasionally involving partial reconstructions to recapture the site's initial allure [16].

5.3 Djemila (Cuicul)

The remnants of the former city of Cuicul, known today as Djemila, represent a settlement established by Emperor Nerva (96-98) for Roman veterans. Deserted in the 7th century, the city's remains were unearthed during the 19th century. Cuicul, akin to numerous other meticulously excavated urban centers, stands as an archaeological marvel, boasting remarkably preserved Roman architecture despite pockets of unexplored terrain.

Efforts to excavate and restore the significant historical site have been initiated to record, safeguard, and improve its condition. These endeavors play a vital role in comprehending the region's history. Key components of the excavation and restoration work at Djemila involve refurbishing dilapidated buildings and structures to halt their ongoing decay. This encompasses rebuilding walls, columns, and other architectural features [16].

Claude LEPELLEY argues that there is no explicit or implicit acknowledgment of the alleged widespread earthquake that supposedly occurred on July 21, 365. Optatus of Milevus, Augustine, and even Ammianus Marcellinus do not make any mention of it [6]. Similarly, despite the abundance of inscriptions in the epigraphic record, there is no reference to this event.

R. REBUFFAT examined signs of seismic events in Africa, drawing from findings in Cuicul, Numidia [15]. This researcher tended to associate the aftermath of this earthquake with the various demolitions, constructions, and repairs of structures witnessed across Africa in the approximately two decades following 365.

DRICI notes the presence of 76 epigraphic texts documenting construction or restoration efforts on municipal public monuments. These texts span the twenty-year period from the reign of Valentinian I starting in February 364 to the passing of Gratian in August 383 [17]. This suggests a significant surge in building endeavors during this era. Scholars posit that the emphasis on restoration (33 or 34 instances, as opposed to 15 or 16 new constructions) reflects the imperative to address the aftermath of the 365 earthquake, which left African cities in a state of disrepair.

Numidia emerged as the province primarily impacted by the surge of public construction projects from 364 to 367. It inaugurated 15 projects, indicative of its proactive approach towards revitalizing the monumental legacy of its urban centers.

6 Comparison of repairs and various post-seismic interventions carried out in ancient sites in Algeria with those in Italy

Throughout history, humans have attempted to distance themselves from the impact of earthquakes, often striving to erase their memory altogether. This explains the scarcity of information about ancient earthquakes in literary and epigraphic records, despite their likely occurrence. Unlike people, buildings retain the evidence of seismic activity and any efforts made by humans to mitigate its consequences, making them invaluable sources for understanding the history of earthquakes.

After the Pompeii earthquake of 62 AD, various mechanisms designed to counteract lateral forces had to be incorporated into repairs and reconstruction endeavors to enhance building resilience [4].

Pompeii's inhabitants prioritized the interconnection of structural components as the main strategy to mitigate the earthquake risk of their buildings [4]. A plethora of instances, spanning from minor fixes like patching small fissures to comprehensive constructions, underscore the utilization of technical mechanisms designed to unite different segments of the edifice.

Numerous integrated measures were implemented to preserve masonry coherence and prevent the need for excessive hammering between distinct masonry sections. These interventions involved utilizing modern materials intricately connected via recesses crafted within the preexisting wall.

Moreover, special attention is paid to the alignment of chainages at building corners, leading to a significant enhancement in the coordination between adjacent perpendicular panels [3].

Figure 4: Brick corner of a building in Timgad (source: Author 2023).

After the 62 earthquake, certain buildings saw improvements in their seismic resilience through reinforcement interventions. Additionally, in Pompeii, employing construction methods like brickwork might have contributed to the favorable performance of buildings [3].

Additionally, employing a brick structure, even if confined solely to the outer wall, enhances shear resistance. It demands more energy to collapse compared to a disorderly masonry with

identical constraints and geometric features, especially under seismic forces perpendicular to the panel.

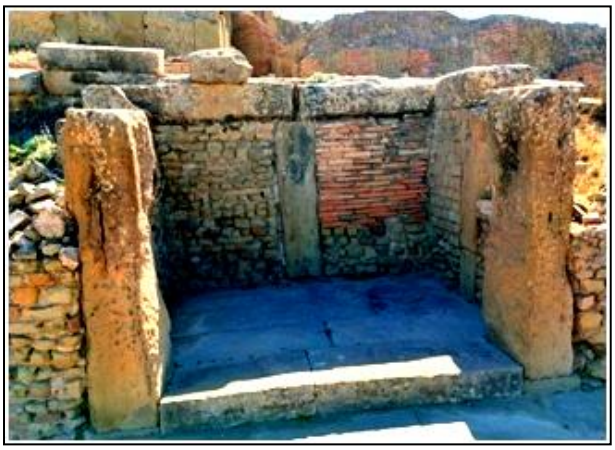

Figure 5: Example of brick usage in the repair of a wall in Timgad (source: Author 2023).

Following the 62 earthquake, additional evidence has surfaced regarding reinforcement measures. By examining the previously noted structural shortcomings, particularly the toppling of masonry, potential strategies emerged for Pompeians to lessen the seismic vulnerability of their buildings. Notably, various buttresses were constructed, featuring specific geometries and materials to enhance stability [4]. These buttresses ranged from modest masonry structures positioned against existing walls to more extensive interventions. It appears these efforts were aimed at counteracting the prevalent issue of wall overturning, exacerbated by the elongated spans of walls in public buildings lacking intermediate supports.

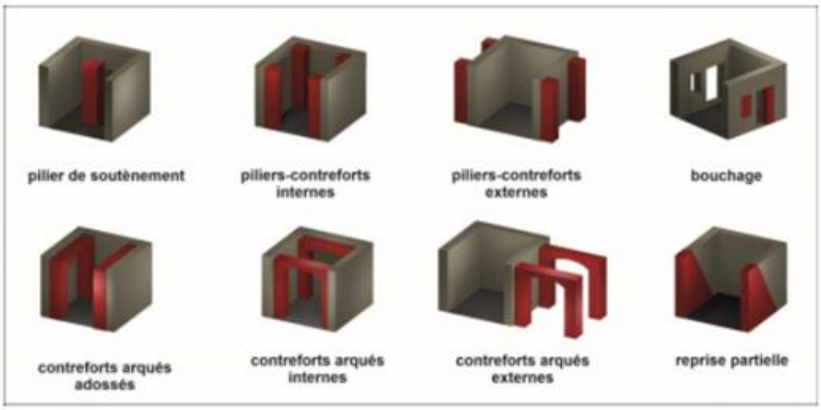

Figure 6: Schematic representation of the repair and reinforcement interventions identified in Ostia (source: TOMASSINI) [4].

Figure 7: Buttresses (source: Author 2023). Numbers 1 & 2: External buttress pillars at Timgad, Numbers 3 & 4: Reinforcement wall at Djemila.

One of the most common interventions found in various ancient sites is the blocking of openings, which can be seen as an acknowledgment that doors are vulnerable points (especially arches and keystones).

Figure 8: Blocking of openings at Djemila (source: Author 2023).

Additionally, intermediate pillars are incorporated to reinforce the arches. This reinforcement is primarily attributed to the occurrence of fallen vault keys, which are commonly regarded as the most dependable indication of earthquake damage [18]. When subjected to horizontal shaking without substantial vertical load, the vault keys tend to collapse, while the load typically maintains the cohesion of the masonry blocks through intense friction at their interfaces.

Figure 9: Support pillars at Djemila (source: Author 2023).

7 Results and conclusions

This contribution does not aim to claim that every structural intervention spotted in these historic sites can be solely attributed to an earthquake, as relying on a single piece of evidence is not definitive. Nevertheless, the multitude of correlations does raise the possibility for this hypothesis to merit further examination. Only through comprehensive and meticulous scrutiny of each building can we gain additional insights and determine whether alternative interpretations are viable.

Prudence is certainly warranted, but by comparing the restoration and various interventions carried out after earthquakes between ancient sites in Algeria (Djemila, Timgad, and Lambèse) and those in Italy (Pompeii and Ostia...), we can confirm:

- The hypothesis of the occurrence of one or multiple earthquakes in antiquity in Algeria.
- The reaction of builders of the time to adapt to earthquakes.
- The transmission of knowledge (non-punctuality), perhaps through the movement of builders.

Improving our comprehension of previous seismic events allows us to not only assess regional seismic hazards but also to reconstruct the historical records of specific locations.

References

[1] Giuliani C. F. (2011). Provvedimenti antisismici nell'antichità. *Journal of ancient topography. Volume* 21, 25-52.

[2] Ruggieri N. (2017). Seismic Vulnerability of The Ancient Pompeii Through the Evaluation of The 62 Ad Earthquake Effects. *International Journal of Architectural Heritage. Volume 11, N°4,* 490–500.

[3] Dessales H. (2020). Construction Et Culture Sismique À L'époque Romaine. *Ædificare, Revue Internationale D'histoire De La Construction. N°7,* 45-76.

[4] Tomassini P. (2021). Construire, Reparer, Consolider. *Melanges De L'école Française De Rome – Antiquite. Volume 133, N°2,* 427-455.

[5] Ferdi S & Harbi A. (2013). Roman Literary and Epigraphic Sources for The Study Of Historical Seismicity In Algeria Circa 42–420 Ad. *Journal Of Seismology. Volume 18, N°2,* 277-287.

[6] Lepelley C. (1984). L'afrique Du Nord Et Le Pretendu Seisme Universel Du 21 Juillet 365. *Melanges De L'ecole Française De Rome. Antiquite T. 96. N°1,* 463-491.

[7] Guidoboni E. (1994). Catalogue Of Ancient Earthquakes in The Mediterranean Area Up to the 10th Century. *Instituto Nazionale Di Geofisica Press. P 504.*

[8] Harbi A, Peresan A & Panza G. (2010). Seismicity Of Eastern Algeria: A Revised and Extended Earthquake Catalogue. *Natural Hazards. Volume 54,* 725–747.

[9] Ballu A. (1897). *The ruins of timgad (antique thamugadi).* Paris: Eds. Leroux.

[10] Harbi A, Sebaï A, Benmedjber M, Ousadou F, Rouchiche Y, Grigahcene A, Aïni D, Bourouis S, Maouche S & Ayadi A. (2015). The Algerian Homogenized Macroseismic Database (267–1989): A Deeper Insight into The Algerian Historical Seismicity. *Seismological Research Letters. Volume 86, N°6,* 1705-1716.

[11] Ballu A. (1893). Antique monuments of Algeria: Tébessa, Lambèse, Timgad. In Conference given at the Trocadéro palace, December 11. Paris: Len pod.

[12] Lepelley C. (1981). *Les cités de l'afrique romaine au bas-empire, tome II, Notices d'histoire municipale.* Paris : Études augustiniennes.

[13] Laporte J P & Dupuis X. (2009). De Negrines Maiores A Negrine. *Antiquites Africaines. Volume 45, N°1,* 51-102.

[14] Albertini E. (1943). Une Nouvelle Basilique Civile A Cuicul (Djemila). *Comptes Rendus Des Seances De L'academie Des Inscriptions Et Belles-Lettres. Volume 87, N°3,* 376-386.

[15] Rebuffat R. (1980). Cuicul Le 21 Juillet 365. *Antiquites Africaines. T. 15,* 309-328.

[16] Department of historic monuments of Algeria. (1927). *Report on the excavation and consolidation work carried out in 1926.* Alger: Jules Carbonel.

[17] Drici S. (2020). Seismes Durant L'antiquite: La Part Des Textes Et De L'archeosismologie. *Ikosim. N°9,* 45-56.

[18] Kamai R & Hatzor Y H. (2008). Numerical Analysis of Block Displacements in Ancient Masonry Structures: A New Method to Estimate Historic Ground Motions. *International Journal for Numerical and Analytical Methods in Geomechanics. Volume 32,* 1321-1340.

DOI: 10.2478/sspjce-2024-0007

Long-Term Accumulation with Latent Heat in Storage Tanks with Experimental Enhancement

Michal Gorás* **and František Vranay**

Technical University of Košice, Slovakia
Faculty of Civil Engineering, Institute of Architectural Engineering/ Building Services Department
*e-mail: michal.goras@tuke.sk

Abstract

Utilization of Thermal Tank Energy Storage Systems (TTES) for efficient storage and release of thermal energy. TTES systems are an integral part of energy infrastructures that enable the storage of surplus energy in the form of heat and its subsequent use as required. We focus on the study of the benefits and challenges associated with the implementation of TTES systems and analyze their impact on temperature stabilization, minimization of heat losses, and overall efficiency. We also discuss the flexible control of tank charging and discharging in TTES systems. Finally, we conclude by reviewing further research aimed at optimizing TTES systems to achieve sustainable and efficient use of thermal energy in the future.

Keywords: renewable energy, long term storage, latent heat, solar energy, PCM substances

1 Introduction

Thermal energy storage (TES) is a key technology in the energy sector that allows surplus energy, especially solar energy, to be stored in the form of heat for subsequent use when needed. One of the key elements of TES systems is phase change materials (PCMs), which are known for their ability to store latent heat. These materials, referred to as phase change materials (PCMs), could absorb or release significant amounts of heat during phase transitions between solid and liquid states.

In addition, the use of water as a medium for TES systems is discussed, representing one of the most common and efficient methods for storing and utilizing heat. Another objective is to provide an overview of the different applications of TES technologies and discuss their benefits in current energy systems.

2 Energy Storage

Thermal Energy Storage (TES) is a fundamental technology enabling the storage of surplus energy in the form of heat for subsequent utilization as needed, as well as Figure 1. TES systems operate based on principles of physical chemistry, where energy is stored or released due to phase changes in the material. One of the most significant aspects of TES is latent heat storage, where energy is absorbed or released during the transition of the material between solid and liquid states. This process allows for efficient storage of large amounts of energy with relatively minor temperature changes [1].

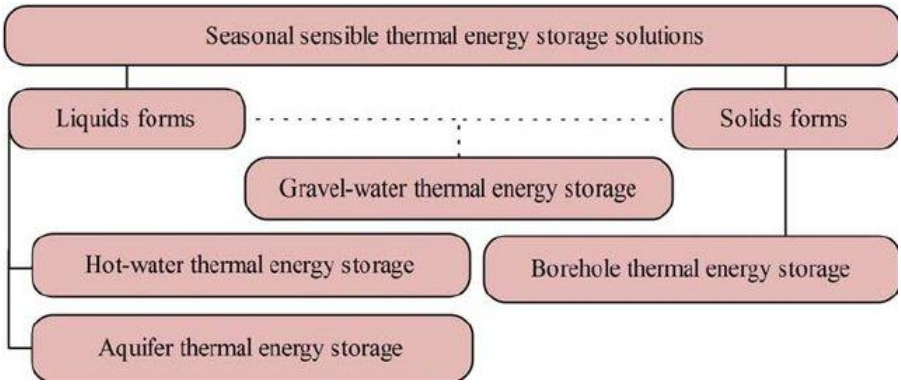

Figure 1: Various solutions for seasonal sensible thermal energy storage [2]

Phase Change Materials (PCM) are key components of TES systems. These materials have the capability to absorb or release significant amounts of heat during phase changes, making them ideal for energy storage. PCM materials are often utilized in the form of capsules or capsules placed in thermally insulated environments, enabling effective control of heat flow [3].

2.1 Pit thermal energy storage

Pit Thermal Energy Storage (PTES) is one form of TES technology utilized for storing surplus energy in the form of heat in underground spaces, as well as Figure 2. This system operates on the principle of a heat pump, where excess heat obtained from various sources (such as solar panels or geothermal heat pumps) is stored in underground environments, where it is retained until needed. When heat is required, it can be retrieved from the underground environment and utilized for heating buildings or other thermal processes [4].

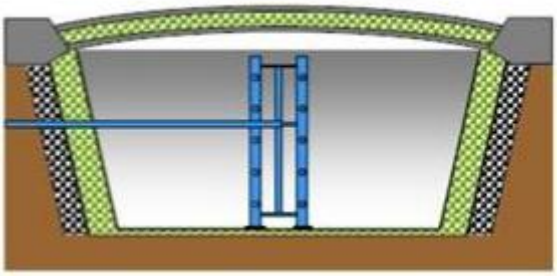

Figure 2: Pit thermal energy storage

PTES systems are popular due to their ability to efficiently store large amounts of energy with relatively low losses. These systems are also flexible and can be adapted to various needs and site conditions.

2.2 Tank theral energy storage

Tank Thermal Energy Storage (TTES) is another form of TES technology utilized for storing thermal energy in tanks, as well as Figure 3. TTES systems operate on the principle of heating water or another thermal medium to high temperatures and storing this heat in a thermally insulated tank. When heat is needed, it can be extracted from the tank and utilized for heating buildings, heating hot water, or other thermal processes [5].

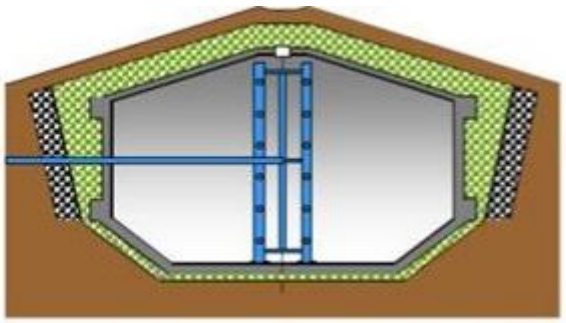

Figure 3: Tank thermal energy storage

One of the advantages of TTES systems is their ability to efficiently store thermal energy with minimal losses. These systems are also suitable for various applications, including industrial processes, solar thermal power plants, and building heating. TTES tanks can come in different sizes and shapes, allowing them to be tailored to specific needs and conditions.

2.3 The use of water as a medium for TES systems

Water is one of the most common and efficient mediums used in TES systems for storing and distributing thermal energy. It is readily available, cost-effective, and has a high thermal capacity, making it an ideal choice for many TES applications. Water is frequently utilized in various forms, including thermal tanks, hot water reservoirs, and other systems for heating and cooling buildings.

The advantages of using water as a medium for TES systems include its high thermal capacity, good thermal conductivity, easy availability, and environmental friendliness. Additionally, water is stable and non-flammable, reducing the risk of accidents and enhancing operational safety [6]. Despite its many advantages, the use of water also comes with some limitations, including the need for appropriate infrastructure for storage and distribution, as well as potential issues with freezing in colder conditions. However, with proper planning and technical solutions, water becomes an efficient and reliable medium for TES systems.

3 Measuring and optimizing TTES performance

Our storage tanks are powered by primary charging sources in the form of selectively heated collectors with an area of 225 m2. These collectors allow the overflow of warm glycol solution, transferring thermal energy into water. Subsequently, this heated water is stored in three thermal tanks with a capacity of 178 m3, as well as Figure 4. These tanks, made of special concrete and thermally insulated, are located beneath the building's surface.

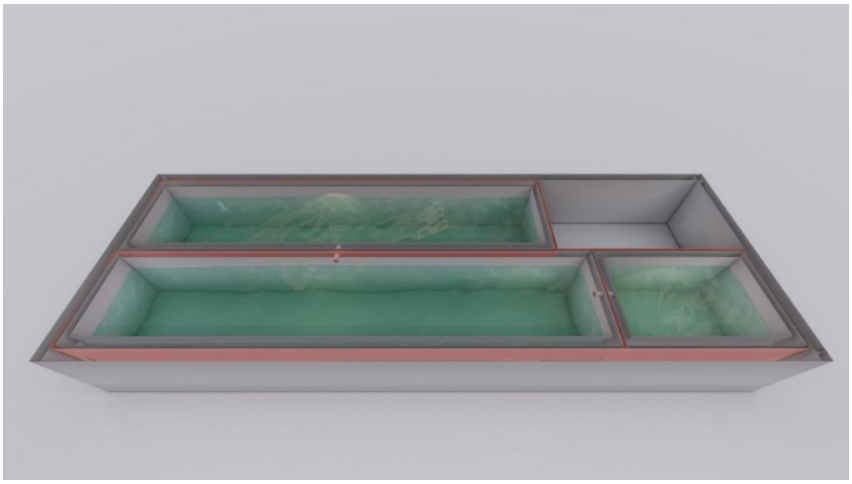

Figure 4: Heat energy storage in three different sizes.

The storage management system allows manual adjustment of charging and discharging according to current needs, necessitating switching between tanks based on seasonal changes, as well as Figure 5. An experimental building was constructed above the tanks to simulate seasonal conditions as accurately as possible.

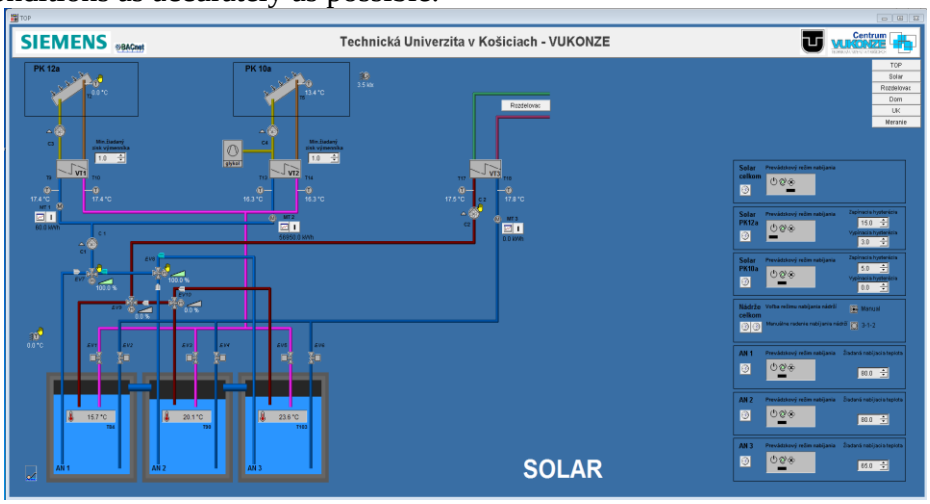

Figure 5: TTES control scheme

3.1 Measurement and Optimization of System Performance

We began by analyzing tank AN1 with a volume of 24 m3, which is the smallest thermal tank in our study. This tank exhibited significant thermal losses due to water evaporation from its surface. Measurements were conducted over a period of two years, as well as Figure 6.

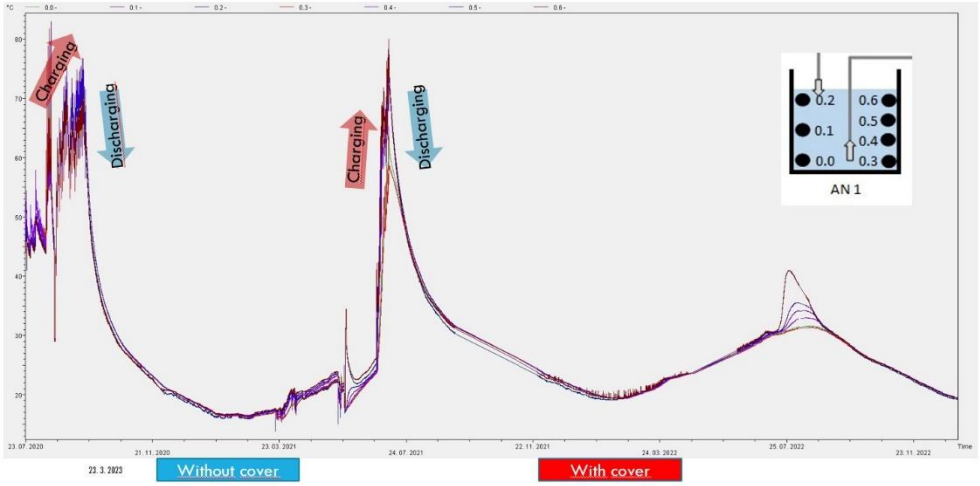

Figure 6: Temperature readings recorded over a two-year period within the AN1 tank.

During the first measurement period, significant thermal losses were observed due to water evaporation from the ground.

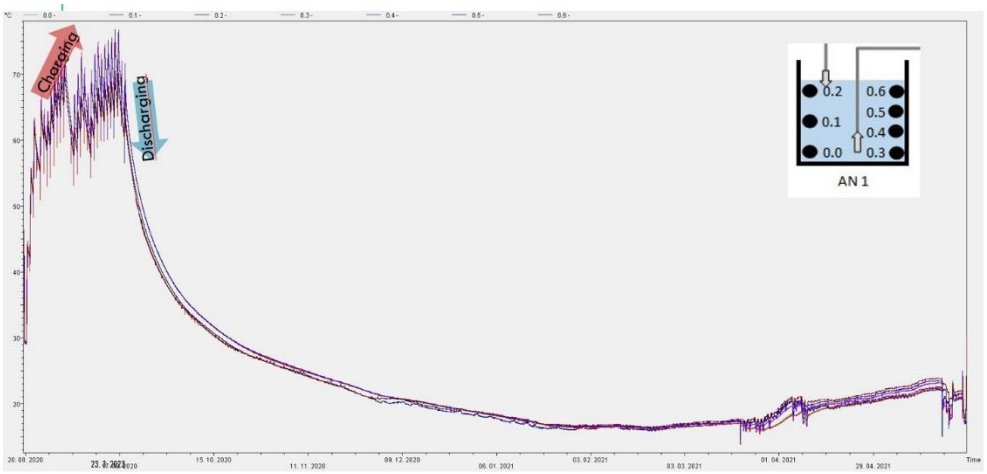

Figure 7: Temperature readings during the first year without any masking.

From the collected data, it is evident that the discharge rate exhibited a quadratic decline without energy consumption, as well as Figure 7.

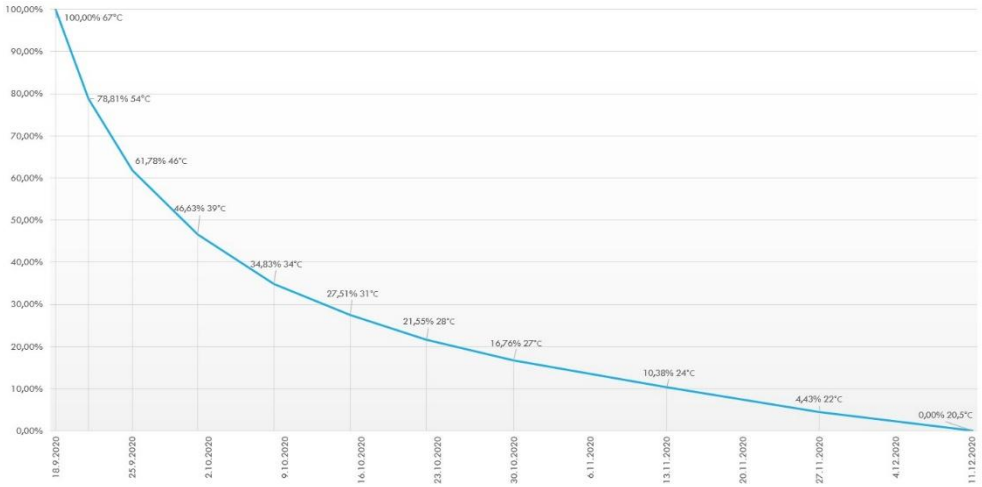

Figure 8: Graph of percentages without coverage

The graph shows a rapid temperature decrease from a maximum average temperature of 67°C to an initial charging temperature of 18°C over 85 days, as well as Figure 8. However, such rapid discharging does not represent an efficient use of energy. During the second measurement period, we applied a thermal insulation with a thickness of 20 mm to the tank's surface to minimize heat losses due to evaporation.

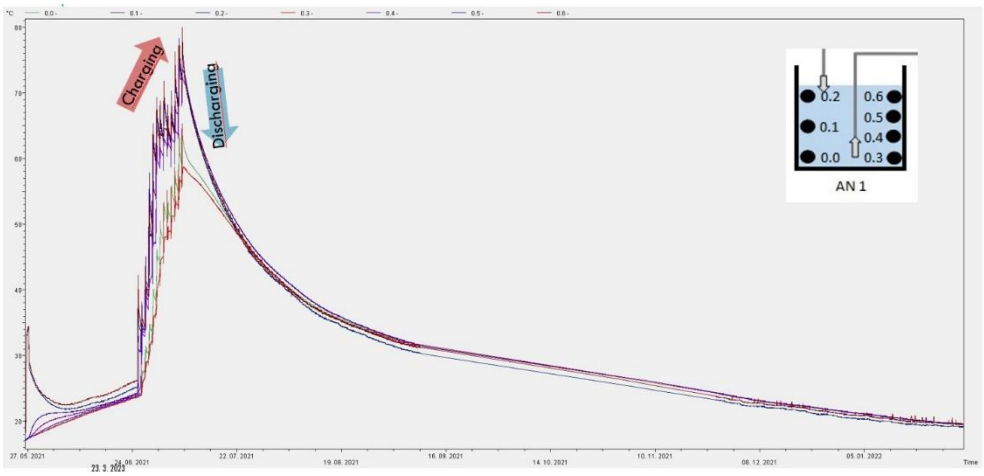

Figure 9: PTES system efficiency 39% in 2017

Regular temperature readings indicate a slower discharge rate compared to the previous period, transitioning from quadratic to linear at specific temperatures, as well as Figure 9.

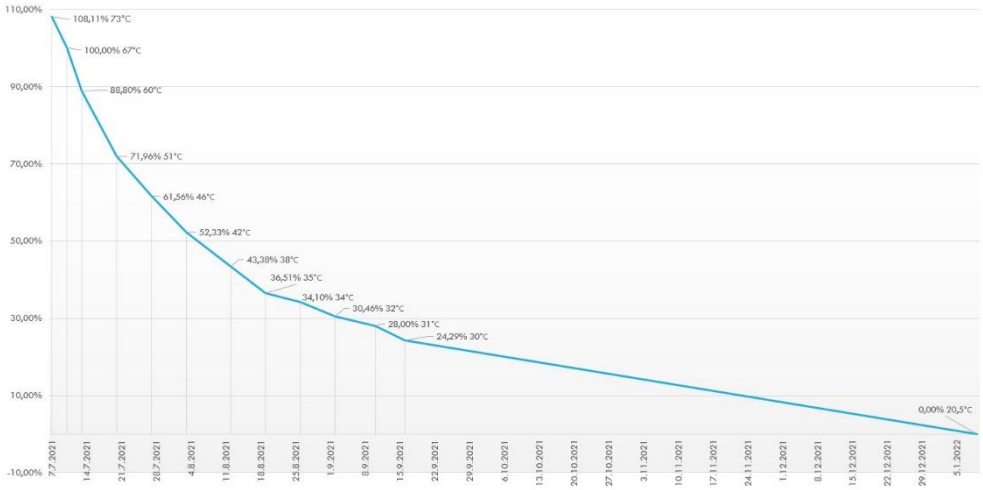

Figure 10: Presents a percentage graph with the coverage

Although we charged the tank up to a temperature of 73°C, for comparison purposes, we standardized it to 67°C. The thermal cover proved to be effective, as demonstrated by the temperature readings. For example, after 3 weeks of discharging, the temperature dropped from 34°C before covering to 46°C after covering, as well as Figure 10. It took 183 days for the tank to discharge back to its original temperature of 18°C.

4 Conclusion

We discuss the latest innovations in thermal energy storage (TES) and analyse the potential challenges and opportunities that lie ahead. We also consider the possible direction of development in this field and the impact that new technologies and societal trends may have on the future of TES.

Considerations for the use of phase change materials (PCMs) in our thermal energy storage in tanks (TTES) research open the door to improving the efficiency and performance of our system. PCM materials could absorb and release large amounts of heat during phase change, allowing for efficient thermal energy storage and release.

Incorporating PCM materials into TTES systems could lead to stabilization of tank temperatures and minimization of heat losses. In this way, we could optimize the use of thermal energy and increase the efficiency of our system, allowing us to better utilize the stored thermal energy for building heating and other thermal processes.

In addition, the use of PCM materials would allow more flexible management of the charging and discharging of the tanks according to actual needs and seasonal changes. This would allow us to use thermal energy more efficiently and improve the overall efficiency of our TTES system.

References

[1] *Geothermics*, Seama Koohi-Fayegh, Faculty of Engineering and Applied Science, University of Ontario Institute of Technology, 2000 Simcoe Street North, Oshawa, Ontario, L1H 7K4, Canada, 2015

[2] *Seasonal Sensible Thermal Energy Storage Solutions*, Lavinia Socaciu, Technical university of Cluj-Napoca, 2011

[3] *Applied Thermal Engineering*, Masih Alavy, Peimaneh Shirazi, Marc A. Rosen, Department of Mechanical and Manufacturing Engineering, Ontario Tech University, Oshawa, ON, L1G 0C5, Canada, 2024

[4] *Future Grid-Scale Energy Storage Solutions*, Maziar Dehghan, Mahsa Ghasemizadeh, Saeed Rahgozar, Abolfazl Pourrajabian, Ahmad Arabkoohsar, Department of Civil and Mechanical Engineering, Technical University of Denmark, Lyngby, Denmark, 2023

[5] *Saisonale Warmespeicher – Bauarten, Betriebsweise und Anwendungen. Chemie Ingenieur Technik*, Marx R, Nußbicker-Lux J, Bauer D, Heidemann W, Druck H., 2011

[6] *Stendorf Sorensen - Solar District Heating Trends and Possibilities*, D. Trier, F. Bava, C. Kok Skov, 2018

DOI: 10.2478/sspjce-2024-0008

Relationship between Porosity-Ultrasonic Pulse Velocity and Water Absorption of Concrete Containing Plastic and Rubber Waste by Full Factor Desing

Ameur Belmouhoub[1*], Assia Abdelouahed[1]

[1]University of 20 Août 1955-Skikda
Faculty of Technology, Department of Civil Engineering Laboratory LMGHU
*e-mail : a.belmouhoub@univ-skiksa.dz, a.abdelouahed@univ-skikda.dz

Abstract

Utilizing waste plastic and rubber in civil engineering is one of the most environmentally friendly and economically advantageous options. In this work, the aim was to study the relationship between porosity, ultrasonic pulse velocity, and water absorption using waste plastic and rubber in ordinary concrete and analyze the results with a program called JMP, where cement was replaced with rubber as a mass substitute in proportions of 2% and 4% and sand was replaced with plastic as a mass substitute in proportions of 2%, 4%, and 6%. The tests used were ultrasonic speed at 28 days, porosity, water absorption by total immersion, and sorptivity. The findings reveal that as the amount of rubber and plastic increases, the speed of ultrasonic decreases. Additionally, higher amounts of rubber and plastic lead to increased porosity, water absorption by total immersion, and sorptivity. The speed of ultrasonic pulses varies between 4065.04 m/s and 3838.90 m/s, porosity levels range from 11.63% to 13.44%, water absorption by total immersion falls between 5.40% and 6.16%, and sorptivity ranges from 9.93 g/m^2 to 13.99 g/m^2. Furthermore, the addition of rubber and plastic waste causes large voids and cracks to form inside the concrete structure. These voids and cracks can increase the porosity of the concrete, which raises the rate of water absorption and lowers the ultrasonic pulse velocity, according to scanning electron microscopy (SEM) data. After assessing the data, it was determined that the numerical simulations for various factors such as ultrasonic pulse velocity, porosity, water absorption by total immersion, and water absorption by capillary exhibited strong correlation, with calculated coefficients R^2 near 1.

Keywords: rubber, plastic, concrete, microstructure, factorial desing

1 Introduction

Plastic and rubber waste are major problems in today's world, with many negative effects on the environment [1]. The accumulation of rubber tires is on the rise [2] , as the number of tires used in the world each year has reached more than 13.5 million tons [3,4]. While the amount of plastic waste in the world is estimated at 300 million tons annually [5]. This waste takes a long time to decompose, causing damage to the environment and human health [6]. However, there are new opportunities to exploit this waste; particularly in the concrete sector. One strategy to enhance sustainability and minimise the use of natural resources is to include waste plastic and rubber in concrete [7, 8, 9, 10, 11, 12, 13]. This waste

can be processed into fine particles or granules and mixed with cement, granules, and water to form the concrete mix. Adding these wastes can improve the flexibility and thermal insulation capacity of concrete. Using concrete with plastic and rubber waste, also reduces the amount of waste sent to landfills or combustion, helping to preserve the environment. Senhadji et al. [14] used plastic PVC in concrete to replace the sand with rations of 30, 50, and 70% by volume, which led to a decrease in the ultrasonic pulse velocity at ages 28 and 90 with increasing the level of plastic PVC. Also, Akçaözoğlu et al. [15] used three types of plastic (PE, PP, and PVC) in proportions of 25%, 50%, and 75%. The results indicated that each time the percentage of this waste increased, the ultrasonic speed decreased. According to the authors, Saikia and Brito [16], the higher permeability of concrete with plastic aggregate is attributed to the expansion of porosity resulting from the loose connection between the cement paste and the plastic aggregate. Concrete with PET aggregate showed higher percolated porosity compared to concrete with PC aggregate at increased replacement levels (10%, 20%, and 50%). As well, it was also observed that water absorption rose as the plastic content increased. Concrete with 50% recycled plastic aggregates exhibited a significant increase in water absorption, approximately 117% higher than conventional concrete. The introduction of plastic aggregates heightened porosity in the concrete, resulting in a substantial shift in water absorption behavior. Colangelo et al. [17], found that the porosity of concrete rose by approximately 19.5%, 31.2%, and 40.1% when the substitution ratio increased to 10%, 20%, and 30%, respectively. Similarly, the water absorption also surged from 9.0% to 15.2% accordingly. This was attributed to the greater presence of trapped air stemming from the higher plastic aggregate content, leading to the formation of larger pores within the concrete structure. Coppola et al. [18] and Albano et al. [19] found that the higher water absorption for concrete contains waste plastic compared to control concrete. Kou et al. [20] used plastic PVC granules as a substitute for sand, finding that water absorption rose as the amount of plastic PVC increased. Senthil et al. [21] conducted a study in which varying proportions (0%, 10%, 20%, 30%, 40%, and 50%) of waste E-plastic electronic parts were used to substitute natural coarse aggregates by volume in concrete. The findings revealed that as the amount of E-plastic in the concrete increased, there was a corresponding increase in capillary water absorption compared to the control concrete. Chidiac and Mihaljevic [22] found that the capillary water absorption rate rose as the proportion of HDPE (high-density polyethylene) and LDPE (low-density polyethylene) plastics increased. On the other hand, Kumar and Dev [23] used rubber as a powder in proportions (0, 10, 15, 20, 25, and 30%) for the substitution of fine aggregates. They found that the ultrasonic velocity decreased as the percentage of rubber increased. Djebien et al. [24] observed that when the amount of tire rubber increased from 1% to 4%, the ultrasonic pulse velocity decreased by 1.10% and 10.11%, respectively. Si et al. [25] found the ultrasonic velocity with rubber waste ranges from 4006 m/s to 4037 m/s, which is lower than the 4308 m/s for ordinary concrete. The incorporation of rubber into concrete created voids in the concrete structure, causing increased diffusion time, which led to a decrease in ultrasonic velocity. This is also explained by the decrease in adhesion between the rubber tire rubber (RTR) and the cement paste, which leads to the occurrence of micro-cracks in the concrete, which in turn leads to raising its porosity and slow down the pulse velocity. Ramdani et al. [26] observed that the higher the rubber content in the concrete, the lower the pulse velocity. Khan and Khitab [27] findings indicate that higher rubber content leads to an increase in porosity. It was found that the crumb rubber acted as an air-entraining agent, boosting the porosity of the concrete. According to Turatsinze and Garros [28], the replacement of the natural aggregates with 25% rubber led to an increase in porosity of 30% compared to the control concrete. This increase is due to the increase in the percentage of air in the concrete. Gupta et al. [29] observed that the water absorption of concrete containing rubber increased with an increase in the percentage of rubber ash. The water absorption increased from 1.08% to 1.26% for concrete containing 0% and 20% of rubber ash, respectively, with the same w/c ratio at 28 days. Yilmaz and Degirmenci [30], and Ganjian et al. [31] observed an increase in the water absorption for all concrete containing waste rubber powder. According to Thomas et al. [32], rubberized concrete absorbs more water than ordinary concrete. Blessen et al. [33] conducted a study where they incorporated rubber powder in varying ratios (0 to 20%)

to replace fine aggregates in a mix. Their findings revealed that the sorptivity of the mix increased compared to the control mix, reaching a peak value of 0.7 mm with a 20% substitution.

Design of experiments JMP is a statistical tool used to design and assess experiments to test scientific theories. It also assists users in understanding the results and making well-informed decisions [34,35,36].

The aim of this study was to use waste plastic and rubber in concrete to study the relationship between porosity, ultrasonic pulse velocity, and water absorption. The results were analyzed using the JMP program, where sand was substituted for plastic in amounts of 2%, 4%, and 6%, and cement was substituted for rubber in amounts of 2% and 4%. Various findings from this study suggest that adding rubber and plastic to concrete increases its porosity, which raises water absorption and lowers ultrasonic velocity.

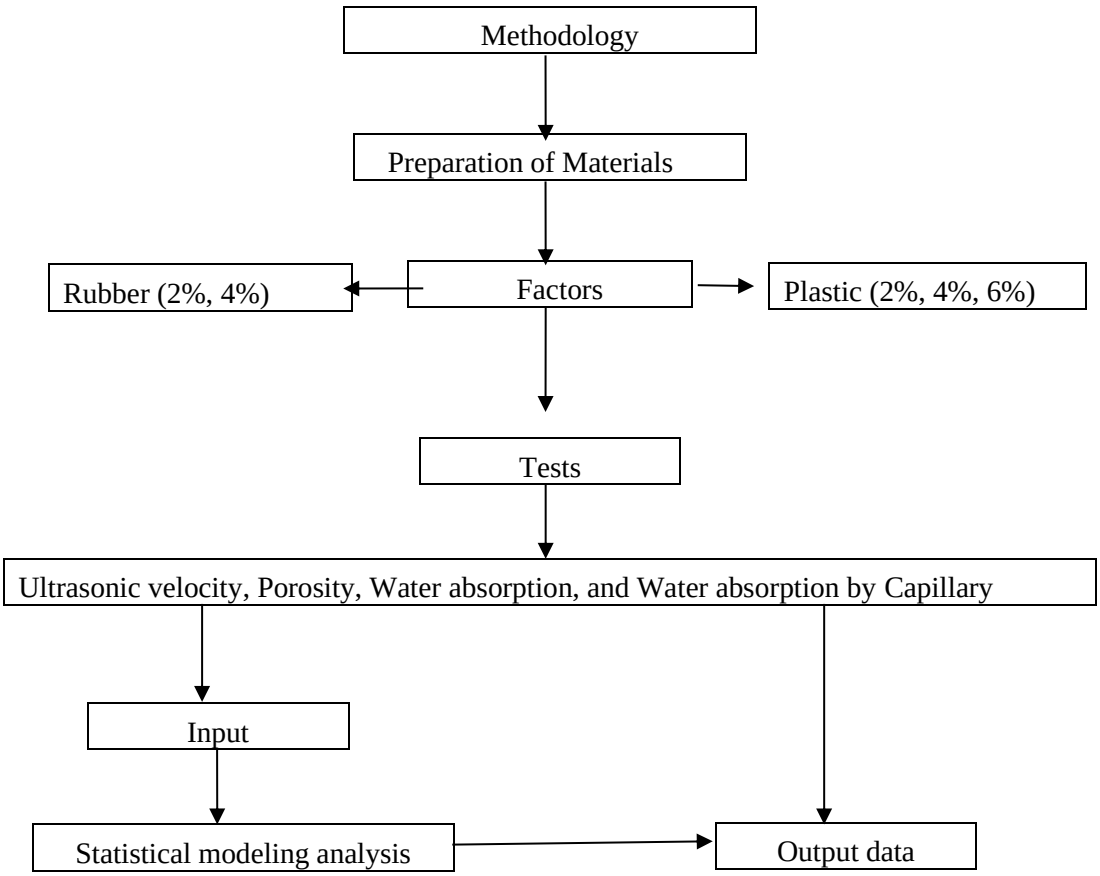

Figure 1: Flowchart illustrating the main stages of the research

2 Materials and methods

2.1 Materials

For this study, CRS CEMI-42.5 cement, brought from the Ain-Kebira (Setif) region of eastern Algeria, was employed. Its chemical and physical components are listed in Tables 1 and 2.

Table 1: Chemical composition of the cement

Designation	CaO	Al_2O_3	Fe_2O_3	SiO_2	MgO	Na_2O	K_2O	Cl	SO_3	C_3S	C_2S	C_3A	C_4AF
Content (%)	62.04	4.59	5.08	23.41	1.74	0.17	0.34	0.05	1.46	36.50	39.90	3.50	15.40

Table 2: Physical composition of the cement

Designation	**Value**
Apparent density (g/cm^3)	3.10
Absolute density (g/cm^3)	1.05
BSS (cm^2/g)	2800.20
Initial setting time (min	90
Final setting time (min)	260

Two different types of gravel were used: 3/8 and 8/15, and sand 0/3 was employed. The rubber waste utilized was in powder with a size of less than 0.08 mm, and it was treated for 20 minutes with 10% sodium hydroxide (NaOH). After that, it was given a water wash and dried in open air [23], as illustrated in Figure 2. In this study, plastic was also employed as fine aggregates, as depicted in Figure 2, with a diameter of 1 mm. Table 3 displays sand, gravel, rubber, and plastic physical and chemical characteristics.

Table 3: Characteristics of sand (0/3), gravel (3/8), gravel (8/15), and rubber

Characteristics	**Sand (0/3)**	**Gravel (3/8)**	**Gravel (8/15)**	**Rubber**	**Plastic**
Absolute density (g/cm^3)	2.55	2.66	2.66	0.94	1.67
Apparent density (g/cm^3)	1.62	1.36	1.42	0.34	0.33
Fineness modulus (%)	1.97	-	-	-	-
Sand equivalent (%)	81.61	-	-	-	-
Absorption (%)	2.5	0.99	0.99	-	-

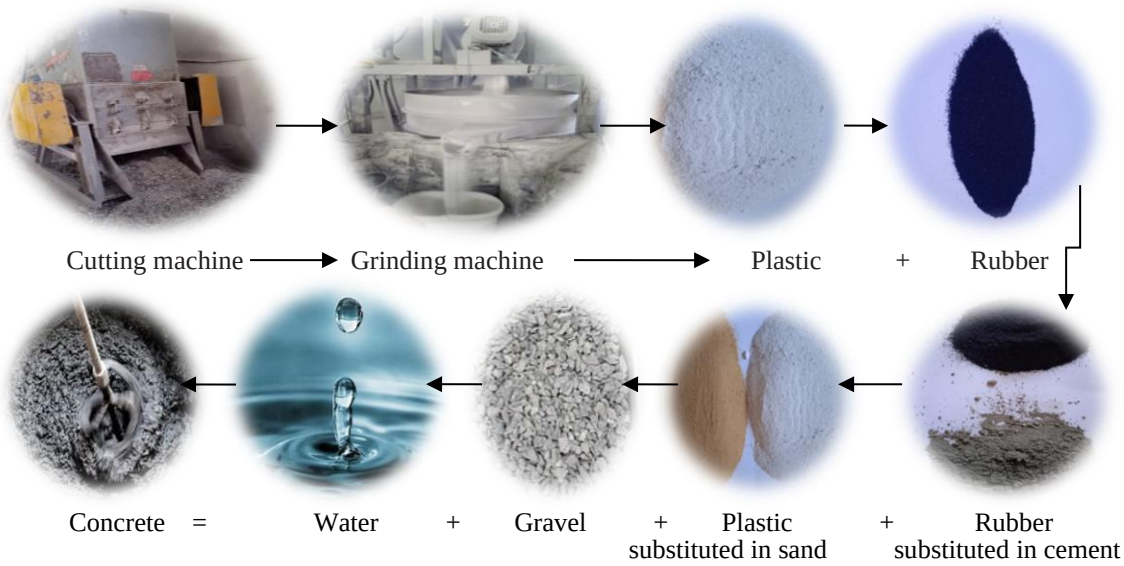

Figure 2: Flowchart showing the main stages of concrete manufacturing

Figure 3, shows the particle size curves for plastic, sand, gravel (3/8), and gravel (8/15). The particle size curves were created using the NF EN 933-1 standard.

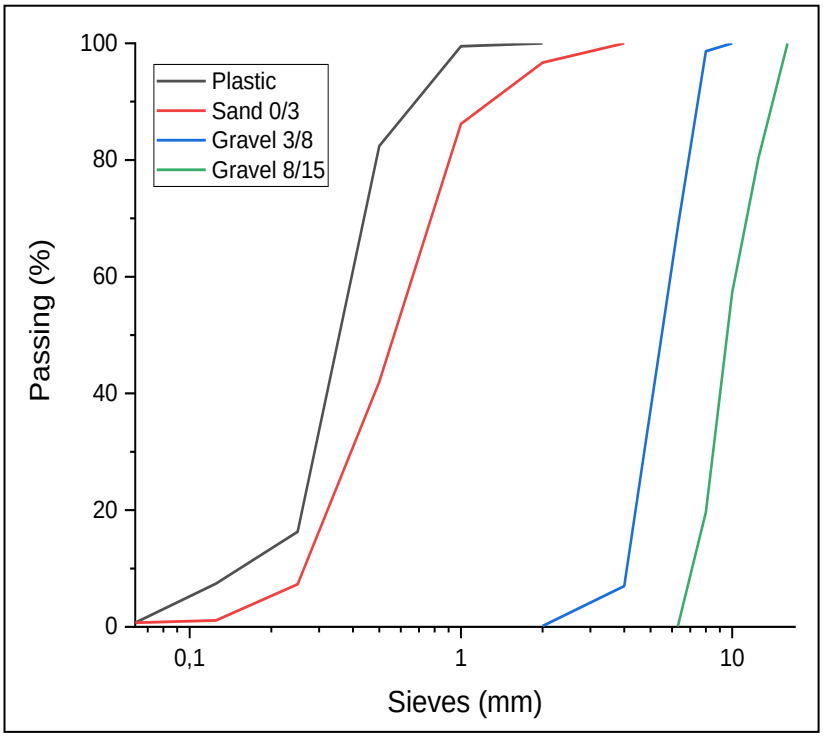

Figure 3: The particle size curve of the plastic, sand 0/3, gravel 3/8 and gravel 8/15

2.2 Experimental program

In this research, the Dreux-Gorisse method was utilized with a fixed water-to-cement ratio of 0.5. Cement was replaced with rubber at rates of 2% and 4%, while sand was replaced with plastic at ratios of 2%, 4%, and 6%. The preparation procedure began by sequentially adding gravel 8/15, gravel 3/8, sand, plastic aggregates, and rubber powder into the mixer. To ensure even distribution of rubber and plastic aggregates in the concrete elements, a dry mixing process was carried out for three minutes. Following this, cement was added to the mixture and further mixed for an additional minute. Water was then incorporated, and the components were mixed until homogeneous for two minutes. The specific compositions of the various mixtures being studied are outlined in Table 4. Subsequent to mixing, test samples were placed in molds at a temperature of 20 °C for 24 hours. After mixing, the specimens were taken out of the molds and stored in water until testing.

Table 4: The quantities of gravel, sand, cement, water, and rubber in one cubic meter

Mixes	**Gravel (8/15) (kg/m^3)**	**Gravel (3/8) (kg/m^3)**	**Sand (0/3) (kg/m^3)**	**Cement (kg/m^3)**	**Water (l/m^3)**	**Rubber (kg/m^3)**	**Plastic (kg/m^3)**
B0	689	219	741	400	209	0	0
B1	689	219	726.18	392	209	8	14.82
B2	689	219	711.36	392	209	8	29.64
B3	689	219	696.54	392	209	8	44.46
B4	689	219	726.18	384	209	16	14.82
B5	689	219	711.36	384	209	16	29.64
B6	689	219	696.54	384	209	16	44.46

Where:
B0: Ordinary concrete.
B1: Concrete containing 2% rubber and 2% plastic.
B2: Concrete containing 2% rubber and 4% plastic.
B3: Concrete containing 2% rubber and 6% plastic.
B4: Concrete containing 4% rubber and 2% plastic.
B5: Concrete containing 4% rubber and 4% plastic.
B6: Concrete containing 4% rubber and 6% plastic.

The dimensions of the molds used were 10 x 10 x 10 cm^3 for the test ultrasonic pulse velocity, porosity, and water absorption by total immersion, and 7 x 7 x 28 cm^3 for the test water absorption by capillary, as shown in Figure 4.

(a) (b) (c) (d)

Figure 4: Tests used in this study: (a) ultrasonic pulse velocity; (b) porosity; (c) water absorption by total immersion; (d) water absorption by capillary

Table 5: The tests used with standards

Tests	**Standards**
Ultrasonic pulse velocity	NF EN 12504-4
Porosity	NF EN 18-459
Water absorption by total immersion	NBN B 15-215:1989
Capillary water absorption	NF P 18-404

2.3 Mixture proportions

The current study aims to comprehend the distinct effects of plastic content and rubber on the characteristics of concrete. The relationship that the sum of factors produces is as follows:

$$Y=A_0+A_1A+A_2B+A_{12}AB \quad (1)$$

The expected response is denoted by (Y), while the model coefficients are represented by (A_0, A_1, and A_{12}).

3 Results and discussion

In this section, the relationship between porosity, ultrasonic pulse velocity, and water absorption using waste plastic and rubber in concrete is studied, and the results are analyzed using JMP software.

3.1 Relationship between porosity and ultrasonic pulse velocity at 28 days

After 28 days of curing, the relationship between the porosity and ultrasonic pulse velocity of concrete was determined by a linear regression equation created by analyzing test results using the software "Origin."

The relationship between pulse velocity and porosity is depicted in Figure 5.This response's equation is fc = -0.0089x +47.50. Porosity and ultrasonic pulse velocity have a strong association, with an R^2 = 0.90 correlation coefficient.

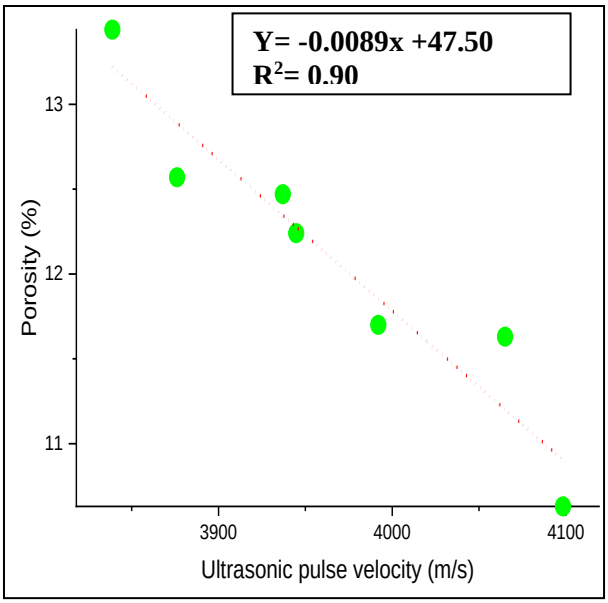

Figure 5: Intersection between porosity and pulse velocity

This suggests that porosity and ultrasonic pulse velocity are directly and linearly influenced by rubber and plastic powder. Additionally, expanding the pores raises the porosity, which lowers the ultrasonic pulse velocity. Consequently, the purpose of this connection is only to confirm that the experimental results obtained before modeling are correct.

3.2 Relationship between porosity and water absorption

Figure 6, shows the intersection between porosity and water absorption. The equation for this response is: fc = 1.41 x + 4.61.

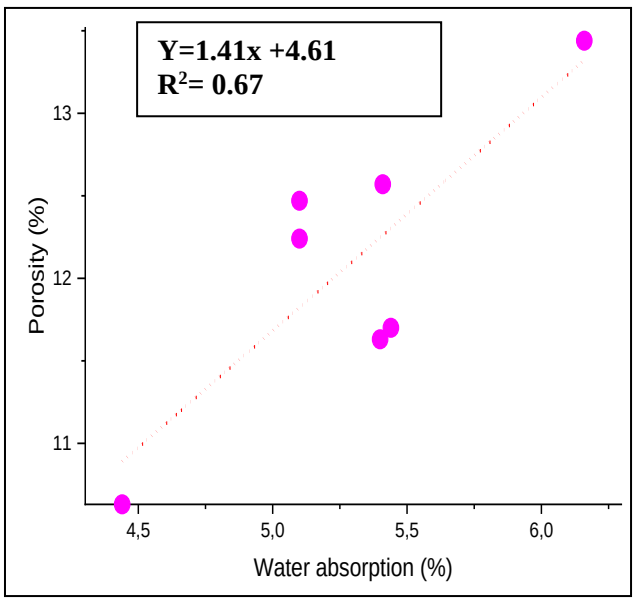

Figure 6: Intersection between porosity and water absorption

It shows an intermediate relationship between the results, with a correlation coefficient of R^2 equal to 0.67. Accordingly, 67% of the change in porosity is influenced by water absorption. The regression is positive, which indicates that increasing porosity causes an increase in water absorption. As the plastic and rubber aggregate content increases, the size of voids increases, resulting in a higher water absorption ratio.

3.3 Modeling of the mechanical response (UPV-PR-WA-WAC)

This section included the analysis of variance, summary of adjustments, and experimental results for ultrasonic pulse velocity, porosity, water absorption by total immersion, and water absorption by capillary.

3.3.1 Correlation: (UPV, PR, WA, and WAC)

There are six experiments total, with two levels for rubber and three for plastic presented in Table 6, and the summary of adjustments is presented in Table 7.
From Table 7, and Figure 7, the correlation coefficients ($R^2 > 0.9$) for ultrasonic pulse velocity, porosity, water absorption by total immersion, and water absorption by capillary. This demonstrates a strong correlation between the model records and the experimentally obtained responses.

Table 6: Experimental results

Mixes	**Rubber (%)**	**Plastic (%)**	**UPV (m/s)**	**PR (%)**	**WA (%)**	**WAC (g/m^2) at (24h)**
B1	2	2	4065.04	11.63	5.40	9.93
B2	2	4	3992.03	11.70	5.44	10.11
B3	2	6	3944.79	12.24	5.10	10.29
B4	4	2	3937.01	12.47	5.10	11.59
B5	4	4	3876.20	12.57	5.41	11.77
B6	4	6	3838.90	13.44	6.16	13.99

Table 7: Summary of adjustment

Tests	**UPV (m/s)**	**PR (%)**	**WA (%)**	**WAC (g/m^2)**
R^2	0,993	0,938	0.925	0.941
Adjusted R^2	0.984	0.846	0.812	0.853
Root of mean square error	10.069	0.260	0.167	0.588
Mean of response	3942.328	12.341	5.435	11.280

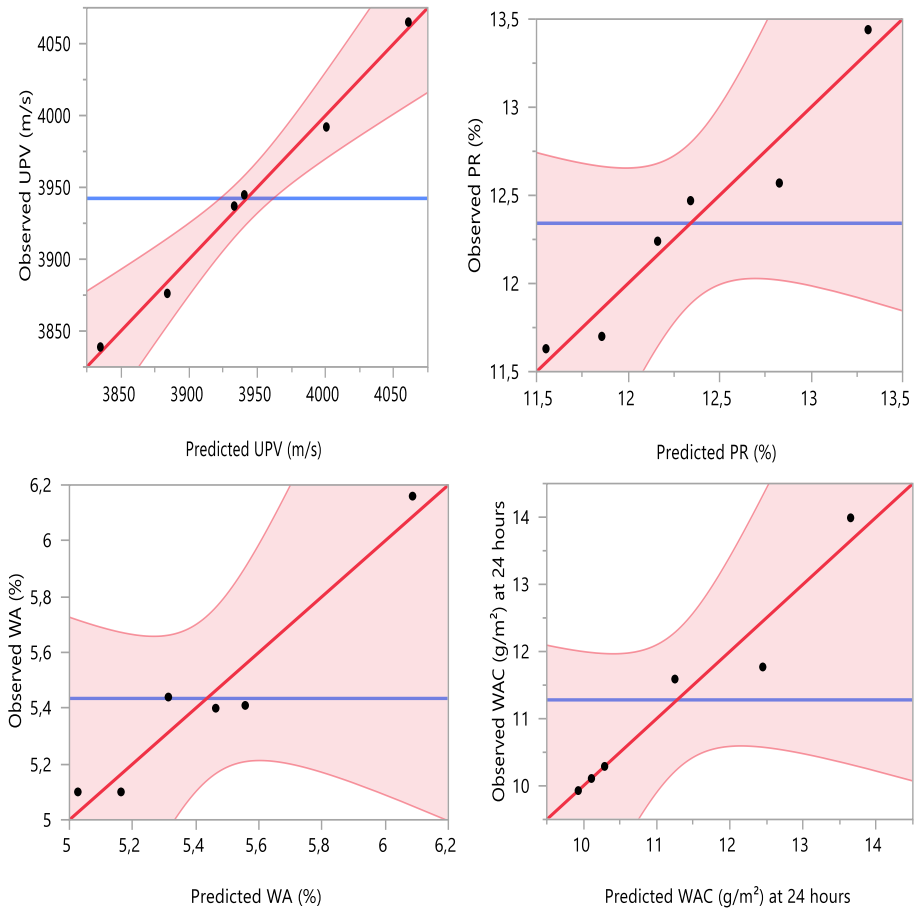

Figure 7: Evolution of correlation between observed and expected values

3.3.2 Ultrasonic pulse velocity (UPV)

Figure 8, displays the various plot types produced by examining the ultrasonic pulse velocity results while taking the rubber and plastic content into account. From Figure 8, it has been observed that the ultrasonic pulse velocity decreases from 4000 (m/s) to 3875 (m/s) due to the change in the level of rubber from 2% to 4% and the level of plastic from 2% to 6%. Specifically, the lowest ultrasonic pulse velocity was observed when the rubber content was less than 3.6% and the plastic content was less than 5.5%. This decrease in velocity can be attributed to the increased air content in the concrete mixture. Higher air content in the mixture leads to a reduction in ultrasonic velocity, as the presence of air pockets can interfere with the propagation of the ultrasonic waves, causing a decrease in velocity. These results are in agreement with those obtained by some authors [24, 37, 38]. Eq. 2 represents the ultrasonic pulse velocity mathematical model.

$$\text{UPV (m/s)} = 3942.32 - 58.29\,(\text{Rubber-3}) - 54.59\left(\frac{\text{Plastic}-4}{2}\right) + (\text{Rubber-3})\left(\frac{\text{Plastic}-4}{2}\right)(-5.53) \qquad (2)$$

Rubber's and plastic's coefficients are (-58.29) and (-54.59), respectively, making it abundantly evident that these factors have a negative impact on this response.

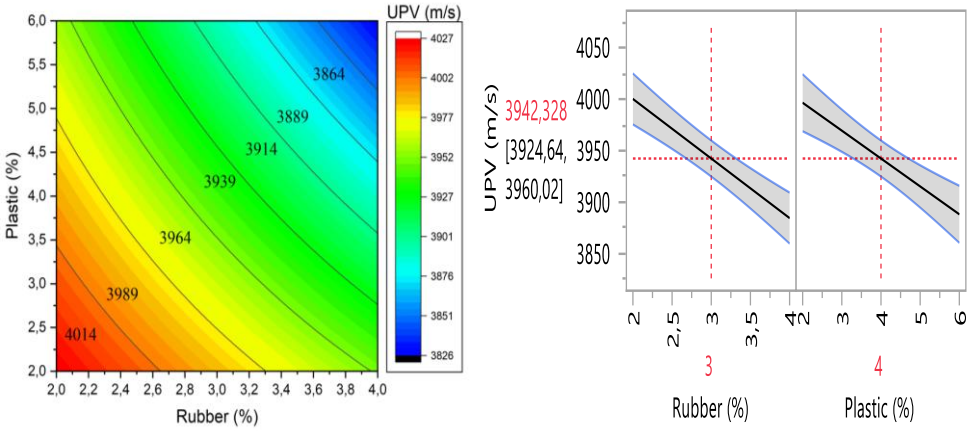

(a) (b)

Figure 8: **(**a) Isoresponse curves and (b) Main effect plots of ultrasonic pulse velocity

3.3.3 Porosity (PR)

Figure 9, shows the iso-response curve and main plots of the porosity. The porosity increases from 11.75% to 13.5% when increasing the level of rubber from 2% to 4% and plastic from 2% to 6%. It also recorded high porosity levels when the rubber content ranged from 3.2% to 4% and the plastic content ranged from 4% to 6%. This indicates that specific ranges of rubber and plastic content in the mixture can result in even greater porosity levels. The introduction of rubber and plastic into the concrete mixture contributed to the increase in porosity by creating small voids or bubbles within the concrete. These voids or bubbles act as spaces within the concrete that increase its overall porosity, allowing for higher levels of air to pass through the concrete. These results are in agreement with those obtained by some authors [17, 39]. Eq. 3 represents the porosity mathematical model.

$$PR\ (\%) = 12.34 + 0.48\ (Rubber-3) + 0.39\ \left(\frac{Plastic-4}{2}\right) + (Rubber-3)\ \left(\frac{Plastic-4}{2}\right)(0.09) \quad (3)$$

The coefficients of rubber and plastic are (0.48) and (0.39), respectively, which shows that the effect of rubber and plastic is positive on the response.

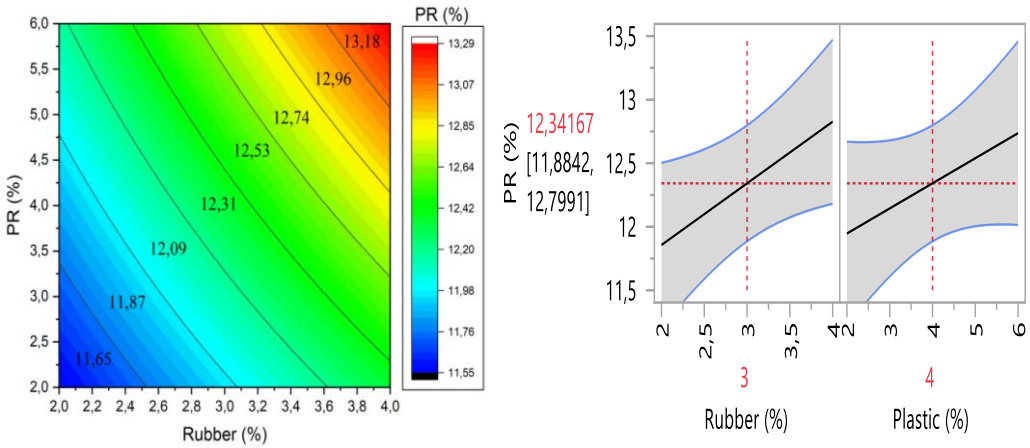

(a) (b)

Figure 9: (a) Isoresponse curves and (b) Main effect plots of porosity

3.3.4 Water absorption by total immersion (WA)

Figure 10, shows the iso-response curve and main effect of water absorption by total immersion. Water absorption increases with increasing levels of rubber and plastic. The water absorption increases, reaching a maximum of 13.44% in concrete containing 4% rubber and 6% plastic. Rubber and plastic in the concrete mix can create interfaces with the cement matrix, potentially leading to the formation of holes or voids within the concrete. These voids can act as channels for water to seep into the concrete, ultimately increasing the water absorption in the concrete. These results are in agreement with those obtained by some authors [17, 30, 31, 40]. Eq. 4 represents the porosity mathematical model.

$$WA\ (\%) = 5.43+0.12\ (Rubber-3) +0.19\ \left(\frac{Plastic-4}{2}\right) + (Rubber-3)\ \left(\frac{Plastic-4}{2}\right)\ (0.34) \quad (4)$$

The coefficients of rubber and plastic are (0.12) and (0.19), respectively, which shows that the effect of rubber and plastic is positive on the response.

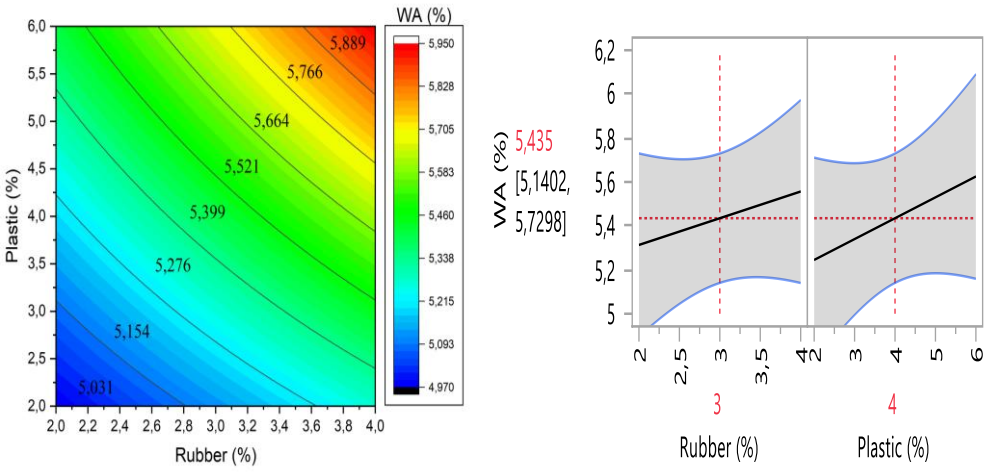

(a) (b)

Figure 10: (a) Isoresponse curves and (b) Main effect plots of the total immersion water absorption

3.3.5 Water absorption by capillary (WAC)

Figure 11 (a) and (b), show the iso-response and main effect plots of water absorption by capillary. It was seen that as the level of rubber and plastic increased, the water absorption by capillary increased. The mixture of 4% rubber and 6% plastic registered a high water absorption by capillary of 49% as compared to ordinary concrete. It was observed that the rubber and plastic had a positive effect on water absorption by capillaries. This increase can be attributed to the fact that plastic and rubber do not bond with concrete components, so plastic and rubber create voids in the concrete mix. These additional voids allow water to penetrate the concrete more easily, so water absorption by capillary action increases. These results are in agreement

with those obtained by some authors [22–33].The mathematical model of water absorption by capillaries is written in Eq.5.

$$\text{WAC } (g/m^2) = 11.28 + 1.17\ (\text{Rubber-3}) + 0.69\ \left(\frac{\text{Plastic}-4}{2}\right) + (\text{Rubber-3})\ \left(\frac{\text{Plastic}-4}{2}\right)(0.51) \quad (5)$$

The coefficients of the rubber and the plastic, are (1.17), and (0.69), respectively. As well the effect of rubber is tow times greater than effect of plastic on the water absorption by capillary.

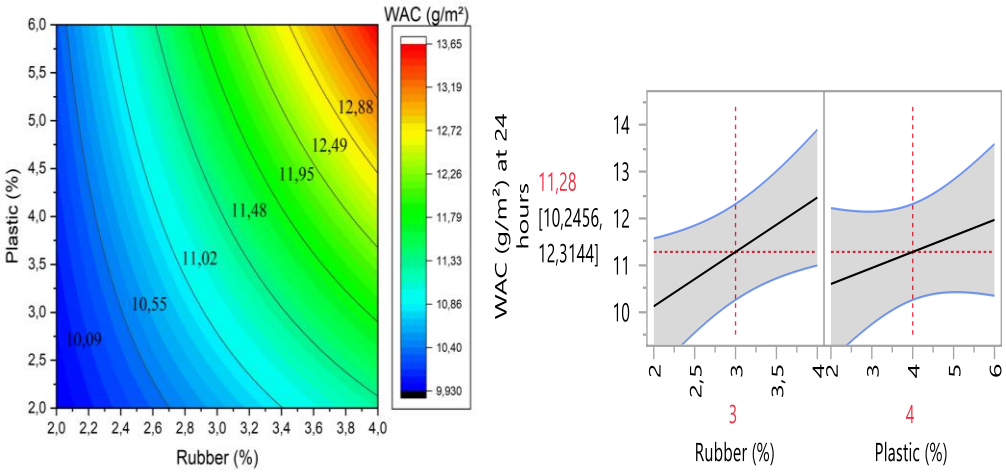

(a) (b)

Figure 11: (a) Isoresponse curves and (b) Main effect plots of the total immersion water absorption by capillary

3.3.6 Coefficient Estimates

From Tables 8, 9, 10, and 11 estimating the response coefficients, it is quite clear that the rubber effect is the most influential on the ultrasonic pulse velocity, porosity, and capillary water absorption; they have the lowest value of (prob.>|t|). Except for water absorption by complete immersion, the interaction between rubber and plastic is the factor that most affects it.

Table 8: Coefficient Estimates of UPV

Term	Estimate	Standard Error	t ratio	Prob. > |t|
Rubber (%) (2,4)	-58.29167	4.110983	-14.18	0.0049*
Plastic (%)(2,6)	-54.59	5.034905	-10.84	0.0084*
Rubber (%) *Plastic (%)	5.535	5.034905	1.10	0.3863

Table 9: Coefficient Estimates of PR

Term	Estimate	Standard Error	t ratio	Prob. > |t|
Rubber (%) (2,4)	0.485	0.106315	4.56	0.0448*
Plastic (%)(2,6)	0.395	0.130208	3.03	0.0936
Rubber(%)*Plastic (%)	0.09	0.130208	0.69	0.5609

Table 10: Coefficient Estimates of WA

Term	Estimate	Standard Error	t ratio	Prob. > |t|
Rubber (%) *Plastic (%)	0.34	0.083915	4.05	0.0559
Plastic (%)(2,6)	0.19	0.083915	2.26	0.1518
Rubber (%) (2,4)	0.1216667	0.068516	1.78	0.2178

Table 11: Coefficient Estimates of WAC

Term	Estimate	Standard Error	t ratio	Prob. > |t|
Rubber (%) (2,4)	1.17	0.240416	4.87	0.0397*
Plastic (%)(2,6)	0.69	0.294449	2.34	0.1438
Rubber (%) *Plastic (%)	0.51	0.294449	1.73	0.2254

3.4 Microstructural analysis

According to the SEM images in Figures 12 and 13, ordinary concrete contains fewer air bubbles, while the rubber and plastic particles in the concrete lead to the formation of larger air bubbles inside the concrete structure. These results are in agreement with those obtained by some authors [41]. When rubber and plastic are mixed with concrete, they do not bond properly with the cement paste, leading to the formation of voids and cracks as the concrete cures, as shown in Figure 14. These voids and cracks can increase the porosity of the concrete, which increases the rate of water absorption, as shown in Figures 9, and 10.

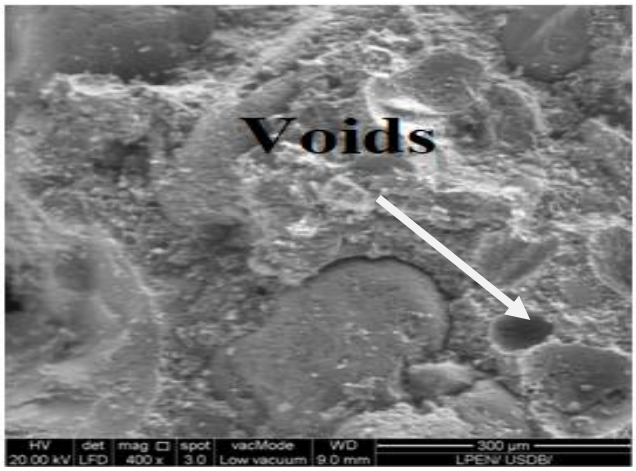

Figure 12: SEM image of ordinary concrete (x400)

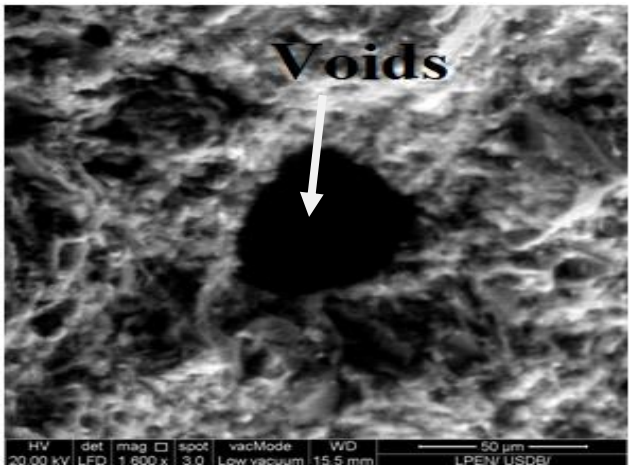

Figure 13: SEM image of concrete containing 4% rubber and 6%plastic (x1600)

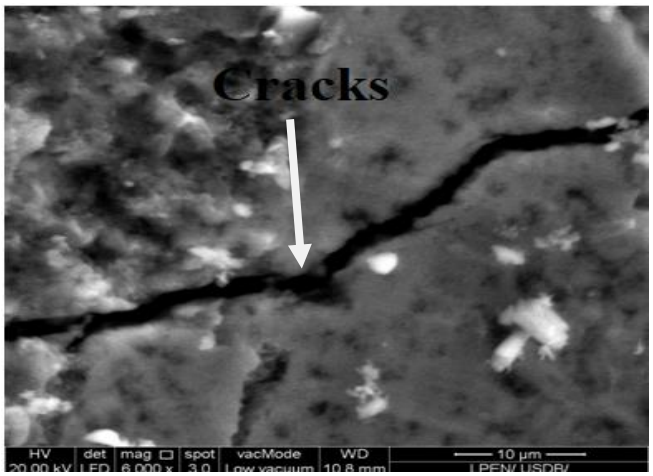

Figure 14: SEM of concrete containing 4% rubber and 6% plastic (x6000)

3.5. Image J analysis

In this study, SEM images of conventional concrete and concrete blended with residual rubber and plastic materials are examined using Image J software.
The area occupied by the pores for concrete samples can be found by analysis using image J [42], a public domain Java image processing program.
The results for the concrete samples are shown in Figures 15, and 16 and the results for the pores area of the various specimens are obtained in Table 12.
These findings showed that the percentage of pores in ordinary concrete was lower than that of concrete with plastic and rubber in it. In ordinary concrete (BO), the percentage of pores is 2.862%, and in concrete with 4% rubber and 6% plastic (B6), the percentage of pores is 6.502%. Because plastic and rubber are non-adherent, they can create cavities in concrete. These substances might not properly bind with the surrounding cementitious material when added to fresh concrete, which would increase the percentage of porosity in the concrete.

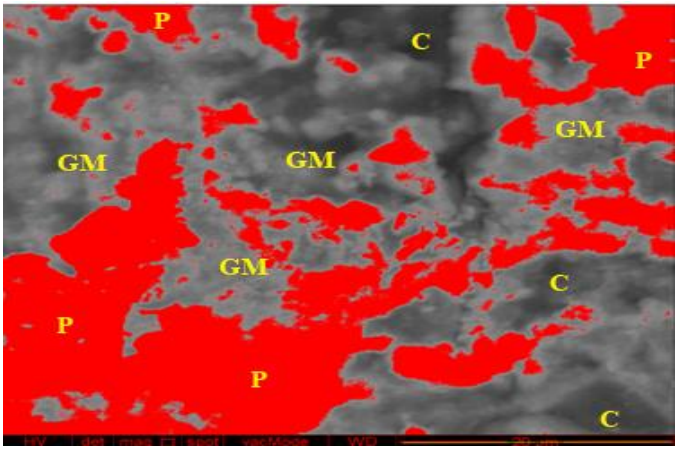

Figure 15: SEM images showing the BO after Image J analysis (GM: granular material, sand/gravel; P: pore; C: cement)

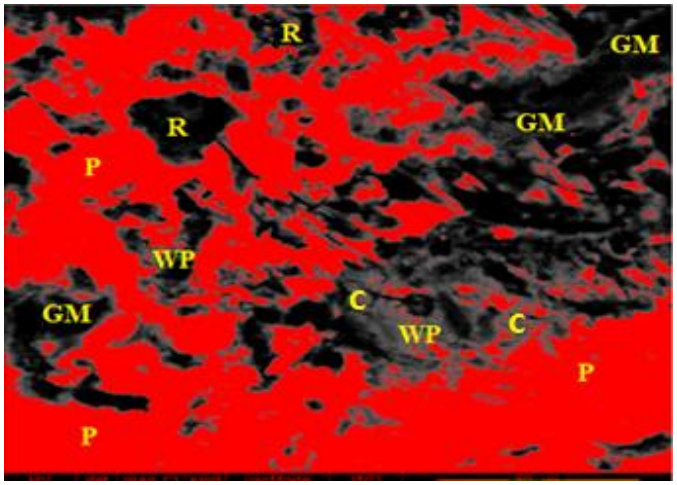

Figure 16: SEM images showing the B6 after Image J analysis (GM: granular material, sand/gravel; P: pore; C: cement; R: rubber; WP: plastic)
Table 12: % Pores area of BO and B6 from image J analysis

Specimen	% pores area
BO	2.862
B6	6.502

4 Conclusion

The experimental results and numerical modeling of the use of waste rubber and plastic in concrete allowed us to draw the full conclusions:

- The ultrasonic pulse velocity and porosity had a strong association relationship with a coefficient of R^2= 0.90.
- Porosity and water absorption have a correlation coefficient of R^2 = 0.67, and porosity increases lead to higher water absorption.
- The increase in the level of rubber and plastic causes a decrease in the ultrasonic pulse velocity of the concrete. The mixture of 4% rubber and 6% plastic registers a low ultrasonic pulse velocity of 6.33% as compared to ordinary concrete.
- Concrete with waste plastic and rubber shows increases in porosity, water absorption by total immersion, and water absorption by capillary; a mixture of 4% rubber and 6% plastic recorded high values for these parameters, registering 26.43%, 38.73%, and 49.30%, respectively, compared to ordinary concrete.
- Statistical parameters show good correlation coefficients (R^2= 0.99; 0.93; 0.92; and 0.94) for ultrasonic pulse velocity, porosity, water absorption by total immersion, and water absorption by capillary, respectively.
- From estimating the coefficients of the response, it was observed that the influence of rubber has the most effect on these responses.
- Adding rubber and plastic aggregates to concrete leads to the formation of larger air bubbles within the structure compared to regular concrete, as revealed by SEM and Image J analysis. This difference is because plastic and rubber aggregates do not adhere to the concrete components, resulting in increased air bubble size.

This study provides valuable information about the reuse of this waste in the field of civil engineering. By incorporating these waste materials into concrete production, we can not only reduce waste but also create lightweight, soundproof concrete solutions. This has the potential to have a positive impact on the environment and improve sustainability in building practices.

Acknowledgments

The auteurs express their great gratitude to the University of SKIKDA in Algeria.

References

[1] Aziz, P L., & Abdulkadir, M. R. (2022). Mechanical Properties and Flexural Strength of Reinforced Concrete Beams Containing Waste Material as Partial Replacement for Coarse Aggregates. *International Journal of Concrete Structures and Materials, 16*(1).

[2] Daghistani, F., Baghbani, A., Naga, H. A., & Faradonbeh, R. S. (2023). Internal Friction Angle of Cohesionless Binary Mixture Sand–Granular Rubber Using Experimental Study and Machine Learning. *Geosciences*, *13*, 7–197. https://doi.org/10.3390/geosciences13070197

[3] Meles, D., Bayat, A., & Chan, D. (2013). One-dimensional compression model for tire-derived aggregate using large-scale testing apparatus. *International Journal of Geotechnical Engineering*, *8*(2), 197–204. https://doi.org/10.1179/1939787913y.0000000019

[4] Rouhanifar, S., & Ibraim, E. (2015). *Laboratory investigation on the mechanics of soft-rigid soil mixtures*. 1073–1080. https://doi.org/10.3233/978-1-61499-601-9-1073

[5] Lamba, P., Kaur, D. P., Raj, S., & Sorout, J. (2021). Recycling/reuse of plastic waste as construction material for sustainable development: a review. *Environmental Science and Pollution Research International*, *29*(57), 86156–86179. https://doi.org/10.1007/s11356-021-16980-y

[6] Mansouri, I., Safa, M., Ibrahim, Z., Kisi, O., Tahir, M., Baharom, S., & Azimi, M. (2016). Strength prediction of rotary brace damper using MLR and MARS. *STRUCTURAL ENGINEERING AND MECHANICS*, *60*(3), 471–488. https://doi.org/10.12989/sem.2016.60.3.471

[7] Kou, S., Lee, G., Poon, C., & Lai, W. (2009). Properties of lightweight aggregate concrete prepared with PVC granules derived from scraped PVC pipes. *Waste Management, 29(2),* 621–628. https://doi.org/10.1016/j.wasman.2008.06.014

[8] Senhadji, Y., Escadeillas, G., Benosman, A., Mouli, M., Khelafi, H., & Ould Kaci, S. (2015). Effect of incorporating PVC waste as aggregate on the physical, mechanical, and chloride ion penetration behavior of concrete. *Journal of Adhesion Science and Technology, 29(7),* 625–640. https://doi.org/10.1080/01694243.2014.1000773

[9] Haghighatnejad, N., Mousavi, S. Y., Khaleghi, S. J., Tabarsa, A., & Yousefi, S. (2016). Properties of recycled PVC aggregate concrete under different curing conditions. *Construction and Building Materials, 126,* 943–950. https://doi.org/10.1016/j.conbuildmat.2016.09.047

[10] Gesoglu, M., Güneyisi, E., Hansu, O., Etli, S., & Alhassan, M. (2017). Mechanical and fracture characteristics of self-compacting concretes containing different percentage of plastic waste powder. *Construction and Building Materials, 140,* 562–569. 140, 562–569. https://doi.org/10.1016/j.conbuildmat.2017.02.139

[11] Najjar, A.M. K., Basha, E. A., & Bashaand, Milad, M.B.K. (2013). Rigid polyvinyl chloride waste for partial replacement of natural coarse aggregate in concrete mixture. *Int. J. Chem. Environ. Eng, 4 (6)* 399–403.

[12] Aly, A. M., El-Feky, M., Kohail, M., & Nasr, E. S. A. (2019). Performance of geopolymer concrete containing recycled rubber. *Construction and Building Materials, 207,* 136–144. https://doi.org/10.1016/j.conbuildmat.2019.02.121

[13] Guo, S., Dai, Q., Si, R., Sun, X., & Lu, C. (2017). Evaluation of properties and performance of rubber-modified concrete for recycling of waste scrap tire. *Journal of Cleaner Production, 148,* 681–689. https://doi.org/10.1016/j.jclepro.2017.02.046

[14] Senhadji, Y., Escadeillas, G., Benosman, A., Mouli, M., Khelafi, H., & Ould Kaci, S. (2015). Effect of incorporating PVC waste as aggregate on the physical, mechanical, and chloride ion penetration behavior of concrete. *Journal of Adhesion Science and Technology, 29(7),* 625–640. https://doi.org/10.1080/01694243.2014.1000773

[15] Akçaözoğlu, S., Atiş, C. D., & Akçaözoğlu, K. (2010). An investigation on the use of shredded waste PET bottles as aggregate in lightweight concrete. *Waste Management, 30(2),* 285–290. https://doi.org/10.1016/j.wasman.2009.09.033

[16] Saikia, N., & de Brito, J. (2012). Use of plastic waste as aggregate in cement mortar and concrete preparation: A review. *Construction and Building Materials, 34,* 385–401. https://doi.org/10.1016/j.conbuildmat.2012.02.066

[17] Colangelo, F., Cioffi, R., Liguori, B., & Iucolano, F. (2016). Recycled polyolefins waste as aggregates for lightweight concrete. *Composites. Part B, Engineering, 106,* 234–241. https://doi.org/10.1016/j.compositesb.2016.09.041

[18] Coppola, B., Courard, L., Michel, F., Incarnato, L., Scarfato, P., & Di Maio, L. (2018). Hygro-thermal and durability properties of a lightweight mortar made with foamed plastic waste aggregates. *Construction and Building Materials, 170,* 200–206. https://doi.org/10.1016/j.conbuildmat.2018.03.083

[19] Albano, C., Camacho, N., Hernandez, M., Matheus, A., & Gutiérrez, A. (2009). Influence of content and particle size of waste pet bottles on concrete behavior at different w/c ratios. *Waste Management, 29(10),* 2707–2716. https://doi.org/10.1016/.wasmaan.2009.05.007

[20] Kou, S., Lee, G., Poon, C., & Lai, W. (2009). Properties of lightweight aggregate concrete prepared with PVC granules derived from scraped PVC pipes. *Waste Management, 29(2),* 621–628. https://doi.org/10.1016/j.wasman.2008.06.014

[21] Senthil Kumar, K., Gandhimathi, R., & Baskar, K. (2016). Assessment of Heavy Metals in Leachate of Concrete Made With E-Waste Plastic. *Advances in Civil Engineering Materials, 5(1),* 256–262. https://doi.org/10.1520/acem20160003

[22] Chidiac, S., & Mihaljevic, S. (2011). Performance of dry cast concrete blocks containing waste glass powder or polyethylene aggregates. *Cement and Concrete Composites, 33(8),* 855–863. https://doi.org/10.1016/j.cemconcomp.2011.05.004

[23] Kumar, R., & Dev, N. (2021). Mechanical and Microstructural Properties of Rubberized Concrete After Surface Modification of Waste Tire Rubber Crumb. *Arabian Journal for Science and Engineering, 47(4),* 4571–4587. https://doi.org/10.1007/s13369-021-06154-w

[24] Djebien, R., Bouabaz, A., & Abbas, Y. (2022). Effect of Recycled Tire Rubber and Marble Waste on Fresh and Hardened Properties of Concrete. *Civil and Environmental Engineering Reports*, *32*(1), 218–239. https://doi.org/10.2478/ceer-2022-0013

[25] Si, R., Wang, J., Guo, S., Dai, Q., & Han, S. (2018). Evaluation of laboratory performance of self-consolidating concrete with recycled tire rubber. *Journal of Cleaner Production, 180,* 823–831. https://doi.org/10.1016/j.jclepro.2018.01.180

[26] Ramdani, S., Guettala, A., Benmalek, M., & Aguiar, J. B. (2019). Physical and mechanical performance of concrete made with waste rubber aggregate, glass powder and silica sand powder. *Journal of Building Engineering, 21,* 302–311. https://doi.org/10.1016/j.jobe.2018.11.003

[27] Khan Raja, Bilal Nasar., & Khitab, Anwar. (2020). Enhancing Physical, Mechanical and Thermal Properties of Rubberized Concrete. *In: Engineering and Technology Quarterly Reviews, Vol.3, No.1,* 33-45. https://www.asianinstituteofresearch.org/

[28] Uratsinze, A., & Garros, M. (2008). On the modulus of elasticity and strain capacity of Self-Compacting Concrete incorporating rubber aggregates. *Resources, Conservation and Recycling, 52(10),* 1209–1215. https://doi.org/10.1016/j.resconrec.2008.06.012

[29] Gupta, T., Chaudhary, S., & Sharma, R. K. (2014). Assessment of mechanical and durability properties of concrete containing waste rubber tire as fine aggregate. *Construction and Building Materials, 73,* 562–574. https://doi.org/10.1016/j.conbuildmat.2014.09.102

[30] Yilmaz, A., & Degirmenci, N. (2009). Possibility of using waste tire rubber and fly ash with Portland cement as construction materials. *Waste Management, 29(5),* 1541–1546. https://doi.org/10.1016/j.wasman.2008.11.002

[31] Ganjian, E., Khorami, M., & Maghsoudi, A. A. (2009). Scrap-tyre-rubber replacement for aggregate and filler in concrete. *Construction and Building Materials, 23(5),* 1828–1836. https://doi.org/10.1016/j.conbuildmat.2008.09.020

[32] Thomas, B. S., & Gupta, R. C. (2016). A comprehensive review on the applications of waste tire rubber in cement concrete. *Renewable & Sustainable Energy Reviews, 54,* 1323–1333. https://doi.org/10.1016/j.rser.2015.10.092

[33] Thomas, B. S., Gupta, R. C., Kalla, P., & Cseteneyi, L. (2014). Strength, abrasion and permeation characteristics of cement concrete containing discarded rubber fine aggregates. *Construction and Building Materials, 59,* 204–212. https://doi.org/10.1016/j.conbuildmat.2014.01.074

[34] Azimi-Pour, M., & Eskandari-Naddaf, H. (2020). Synergistic effect of colloidal nano and micro-silica on the microstructure and mechanical properties of mortar using full factorial design. *Construction and Building Materials, 261,* 120497. https://doi.org/10.1016/j.conbuildmat.2020.120497

[35] Mutuk, T., & Mesci, B. (2014). Analysis of mechanical properties of cement containing boron waste and rice husk ash using full factorial design. *Journal of Cleaner Production, 69,* 128–132. https://doi.org/10.1016/j.jclepro.2014.01.051

[36] Belmouhoub, A., Abdelouahed, A., & Noui, A. (2023). Experimental and factorial design of the mechanical and physical properties of concrete containing waste rubber powder. *Research on Engineering Structures and Materials*. https://doi.org/10.17515/resm2023.54me0810rs

[37] Najim, K. B., & Hall, M. R. (2012). Mechanical and dynamic properties of self-compacting crumb rubber modified concrete. *Construction and Building Materials, 27(1),* 521–530. https://doi.org/10.1016/j.conbuildmat.2011.07.013

[38] Belmokaddem, M., Mahi, A., Senhadji, Y., & Pekmezci, B. Y. (2020). Mechanical and physical properties and morphology of concrete containing plastic waste as aggregate. *Construction and Building Materials, 257,* 119559. https://doi.org/10.1016/j.conbuildmat.2020.119559

[39] Hannawi, K., Kamali-Bernard, S., & Prince, W. (2010). Physical and mechanical properties of mortars containing PET and PC waste aggregates. *Waste Management, 30(11),* 2312–2320. https://doi.org/10.1016/j.wasman.2010.03.028

[40] Silva, R., de Brito, J., & Saikia, N. (2013). Influence of curing conditions on the durability-related performance of concrete made with selected plastic waste aggregates. *Cement and Concrete Composites, 35(1),* 23–31. https://doi.org/10.1016/j.cemconcomp.2012.08.017

[41] Gupta, T., Siddique, S., Sharma, R. K., & Chaudhary, S. (2021). Investigating mechanical properties and durability of concrete containing recycled rubber ash and fibers. *Journal of Material Cycles and Waste Management, 23(3),* 1048–1057. https://doi.org/10.1007/s10163-021-01192-w

[42] Nanes, B. A. (2015). Slide Set: Reproducible image analysis and batch processing with ImageJ. *BioTechniques, 59(5),* 269–278. https://doi.org/10.2144/0001

DOI: 10.2478/sspjce-2024-0009

A Proposal for a Simplified Mesoscale Simulation Model of a Reinforced Concrete Frame with and without Masonry Infill

Karim Benyahi[1*], Amar Messas[1]

[1] Laboratoire de Modélisation des Matériaux et Structures en Génie Civil (L2MSGC), Faculté du Génie de la Construction, Université Mouloud Mammeri de Tizi Ouzou, 15000 Tizi-ouzou, Algeria
*e-mail: karim.benyahi@ummto.dz

Abstract

This article proposes a simplified micro-modeling of masonry infill walls, as well as a method for modeling reinforced concrete frames without infill. This model uses the Drucker-Prager criterion to simulate the non-linear compression behavior of bricks. And for the frame elements, the concrete damaged plasticity (CDP) model was used. This numerical modeling strategy is characterized by the absence of discrete elements either at the portal frame level, or at the masonry unit level, the latter often used to simulate the onset of damage in areas susceptible to plasticization. This model was checked against experimental results and analytical solutions. Subsequently, the use of the concrete damaged plasticity (CDP) model to simulate the non-linear behavior of bricks demonstrated the model's ability to simulate and reproduce experimental damage.

Keywords: numerical modelling, meso-scale model, masonry infilled frames, collapse resistance

1 Introduction

For a long time, the masonry wall was considered as a non-structural element, neglected during the design of the reinforced concrete (RC) frame structures, these have been considered solely for their thermal and sound insulation properties. It was only after the occurrence of the various earthquakes that the post-seismic reports showed their importance and influence. As a result, the study of the behavior of these structures, as well as their simulation, has become a key subject in earthquake engineering.

Frame structures with infill exhibit complex behavior; on one side we have a frame which exhibits a flexible but ductile behavior, and on the other a masonry wall which exhibits a rigid but fragile behavior. The introduction of the masonry walls to the frame increases considerably the rigidity of the structure, greater than the sum of the member stiffness taken individually, this increase is due to the interaction between the frame and the filling wall. This increase in stiffness has a direct impact on the structure, this has the effect of reducing the period of the structure (El-Ouali et al., 1991 [1]). Among other things, an increase in seismic forces can be

observed [2] (Wakabayashi, 1986). Many experimental and analytical studies have been carried out on frame structures.

Murty and Jain (2000) [3] conducted an experimental study on the influence of masonry on frame structures, the results show that infill walls increase the strength, stiffness, and overall energy dissipation of the structure. Dawe and Seah (1989) [4] conducted experimental studies on steel frames with concrete infill, the study looked at the influence of many parameters on the behavior and resistance of infilled frame structures subjected to horizontal loading. Crisafulli (1997) [5] carried out experimental tests, with the aim of setting up a capacity dimensioning method for frames with infill. The author recommends the introduction of diagonal frames at each of the frame nodes, with "U" bars linked to the longitudinal reinforcement, allowing a better transfer of the lateral forces from the frame to the infill panel. Yuen and Kuang (2012) [6] conducted an analytical study on the seismic behavior of framed structures with infill under dynamic loading in-plane and out-of-plane. Chrysostomou (1991) [7] during a dynamic analytical study, observes a clear reduction in the bending moments as well as the shear force in the elements of the infilled frame structures in comparison with the elements of the frame without infill. He also observes a considerable increase in the normal forces in the members of the infilled frame structures in comparison with the members of the frame without infill.

Through years of research, many authors have focused on the study of these structures and their modeling has become widespread, especially with the arrival of the finite element method. Many authors have looked into the modeling of infill walls, proposing many strategies over time. The authors D'Altri et al. (2019) [8], Ali and Page (1988) [9] report that in the history of masonry modeling, Page (1978) [10] was the first to consider the masonry units as well as the mortar separately, in this first attempt the bricks are elastic elements acting in conjunction with connecting elements simulating mortar joints. Ali and Page (1988) [9] subsequently proposed a modeling of masonry walls by finite elements subjected to a loading in plan, the bricks and mortar joints are modeled separately. In this method, failure can occur by crushing or cracking of the constituents, or by failure of the bond at the brick-mortar interface. Lotfi and Shing (1994) [11] propose a constitutive model capable of simulating fracture initiation and propagation under combined normal and shear stresses. The model is of the meso-modeling type where the mortar units are modeled with continuous elements, the mortar joints are modeled by interface elements. Lourenço and Rots (1994) [12]; Lourenço and Rots (1997) [13] propose an interface model that takes into account all types of masonry failure, the bricks are modeled by continuous elements, and the mortar joints by interface elements. The damage is then concentrated in the mortar joints and potential cracking elements are introduced into the center of the masonry units. Lourenço and Rots (1997) [13] based on the approach of Lourenço and Rots (1994) [12], the author proposes a simplified micro modeling approach where the damage is concentrated in the mortar joints, through interface elements that replace the different mortar joints, potential cracks are introduced into masonry units through interface elements. Aref and Dolatshahi (2013) [14] offer a simplified micro-modelling, the model allows the simulation of filling walls subjected to a three-dimensional loading, monotonic or cyclic. The mortar joints are replaced by zero-thickness interface elements; a constitutive material model was subsequently introduced through a subroutine in Abaqus software. The brick elements are modeled by solid elements (C3D8R) and the interface elements by plane elements (C0H3D8). The authors introduced the cyclic behavior of masonry, using the model proposed by Lourenço and Rots

(1997) [13]. Nasiri and Liu (2017) [15] propose a simplified modeling of the infill in order to take into account the out-of-plane loading. The model was established by replacing the mortar joints with zero-thickness interface elements, the masonry units are connected and interact with each other through these interface elements. Kuang and Yuen (2013) [16] propose an approach based on the surface-based interaction modeling technique to simulate the interfacial ten-sile-separation behavior between the contact surfaces of masonry units. Bolhassani et al. (2015) [17] offer experimental tests for determining the mechanical characteristics of masonry elements, as well as their numerical simulation using micro-simplified modelling. Abdulla et al. (2017) [18] propose a simplified micro-modeling method by introducing the extended finite element method (XFEM). The method allows simulation of in-plane and out-of-plane infill walls for monotonic or cyclic loading. Zhai et al. (2017) [19] propose the use of discrete elements in order to circumvent one of the limitations of the diffuse crack model which is the dependence of the solution on the size of the mesh, relying on the element method finite extended (XFEM), the author introduces discrete elements in the frame and the masonry units in order to simulate the possible cracks of the latter. D'Altri et al. (2018) [20] proposed a detailed micro-modeling model for masonry structures, the model allows the prediction of the mechanical behavior of these structures until their failure.

The aim of this paper is to propose a method for modeling reinforced concrete frames without infill, with the commercial software Abaqus, using the appropriate behavior laws for concrete and steel. Then, in a second step, the introduction of the infill wall according to the appropriate plastic model, enables the global behavior of a reinforced concrete frame with infill to be modeled through the use of a trial-and-error method to calibrate the analytical model on the experimental model. As this method can be classified as a simplified micro-modeling of reinforced concrete frames with infill, while bypassing the use of discrete elements, it presents by its simplicity an easy and accessible alternative to the complex models present in the literature.

2 Materials and methods

The nonlinear behavior of the concrete can be simulated according to various models in the literature, it can be simulated by using the theory of plasticity or damage models, the theory of plasticity makes it possible to describe the irreversible deformations, the damage model is al-lowing to describe the gradual degradation of the initial rigidity. For a better simulation of the non-linear behavior of concrete, the coupling between the models of plasticity and damage is essential (Nguyen and Korsunsky, 2008 [21]).

In this paper, the non-linear behavior of concrete will be simulated with the CDP (Concrete Damaged Plasticity) model integrated in Abaqus, this model is based on the formulation of Lubliner et al. (1989) [22] and Lee and Fenves (1998) [23], makes it possible to represent in a complete way the plastic behavior of the concrete, by taking into account its damage. The model assumes a non-associated plastic flow potential, the flow function used for this model is the Drucker-Prager hyperbolic function.

2.1 Concrete

According to the methodology proposed by Alfarah et al. (2017) [24], the behavior of concrete in compression goes through three stages (see Figure 1(a)), two ascending segments and another descending one, the ascending segments in compression follow the recommendations of CEB-FIP (2010) [25] and the descending segment follow the recommendation of Krätzig and Pölling (2004) [26].

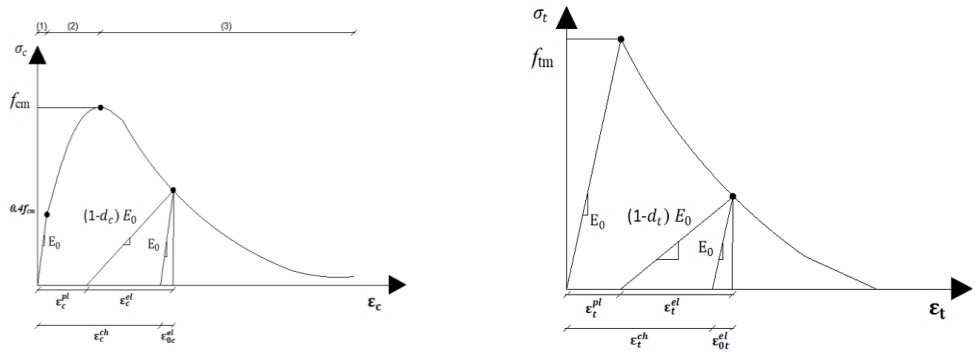

(a) (b)

Figure 1: Compressive and tensile behavior of concrete: (a) Compression, (b) Tension

The first is linear elastic, it is expressed by the following relation:

$$\sigma_c = E_0 \varepsilon_c \tag{1}$$

The second follows a quadratic law, which is expressed by:

$$\sigma_c = \frac{E_{ci}\dfrac{\varepsilon_{ci}}{f_{cm}} - \left(\dfrac{\varepsilon_c}{\varepsilon_{cm}}\right)^2}{1 + \left(E_{ci}\dfrac{\varepsilon_c}{f_{cm}} - 2\right)\dfrac{\varepsilon_c}{\varepsilon_{cm}}} f_{cm} \tag{2}$$

$$E_{ci} = 10000\left(f_{cm}\right)^{1/3} \tag{3}$$

$$E_0 = \left(0.8 + 0.2\left(\frac{f_{cm}}{88}\right)\right)E_{ci} \tag{4}$$

$$f_{cm} = f_{ck} + 8 \tag{5}$$

The third is a downward curve, which is expressed by:

$$\sigma_c = \left(\frac{2 + \gamma_c f_{cm}\varepsilon_{cm}}{2f_{cm}} - \gamma_c\varepsilon_c + \frac{\varepsilon_c^2\gamma_c}{2\varepsilon_{cm}}\right)^{-1} \tag{6}$$

$$\gamma_c = \frac{\pi^2 f_{cm} \varepsilon_{cm}}{2\left[\frac{G_{ch}}{l_{eq}} - 0.5 f_{cm}\left(\varepsilon_{cm}(1-b) + b\frac{f_{cm}}{E_0}\right)\right]^2} \quad (7)$$

$$b = \frac{\varepsilon_c^{pl}}{\varepsilon_c^{ch}} \quad (8)$$

The tension curve follows two segments:

A first linear elastic, it is expressed by the following relation:

$$\sigma_t = E_0 \varepsilon_t \quad (9)$$

A second segment that follows the law:

$$\sigma_t = \left[\left[1 + \left(c_1 \frac{w}{w_c}\right)^3\right] e^{-c_2 \frac{w}{w_c}} - \frac{w}{w_c}\left(1 + c_1^3\right) e^{-c_2}\right] f_{tm} \quad (10)$$

$$f_{tm} = 0.3016 \left(f_{ck}\right)^{2/3} \quad (11)$$

With:
C_1= 3 and C_2=6.93 according to the values recommended by Alfarah et al. (2017) [24].

$$w_c = 5.14\left(\frac{G_f}{f_{tm}}\right) \quad (12)$$

$$G_f = 0.073\left(f_{cm}\right)^{0.18} \quad (13)$$

$$G_{ch} = \left(\frac{f_{cm}}{f_{tm}}\right)^2 G_f \quad (14)$$

Equation (10) can be written in terms of tensile strain using the following equation:

$$\varepsilon_t = \varepsilon_{tm} + \left(\frac{w}{l_{eq}}\right) \quad (15)$$

The damage model proposed by Alfarah et al. (2017) [24] was also used to calculate the concrete damage variable, a program under Fortran following the methodology recommended by the authors was written for this purpose.

The strain relationship of the concrete damaged plasticity (CDP) model (Figure 1) is expressed as follows:

$$\varepsilon = \varepsilon^{el} + \varepsilon^{pl} \quad (16)$$

The stress-strain relationship, taking into account the isotropic damage parameter, can be expressed as follows:

$$\sigma = (1-d)D_0^{el}:(\varepsilon - \varepsilon^{pl}) = D^{el}:(\varepsilon - \varepsilon^{pl}) \quad (17)$$

The expression for the load function is given by:

$$F(\bar{\sigma}, \tilde{\varepsilon}^{pl}) \leq 0 \quad (18)$$

The flow law is expressed as follows:

$$\dot{\varepsilon}^{pl} = \dot{\lambda}\frac{\partial G(\bar{\sigma})}{\partial(\bar{\sigma})} \quad (19)$$

When the concrete sample is unloaded, resulting in a drop in material stiffness (Figure 1), the latter is characterized by two damage variables d_c and d_t, expressed as follows:

$$d_t = d_t(\tilde{\varepsilon}^{pl}) \ \ and \ \ 0 \leq d_t \leq 1 \quad (20)$$

$$d_c = d_c(\tilde{\varepsilon}^{pl}) \ \ and \ \ 0 \leq d_c \leq 1 \quad (21)$$

The stress-strain relationship under tensile and compressive loading, taking into account the damage variables d_c and d_t, can be expressed as follows:

$$\sigma_t = (1-d_t)E_0(\varepsilon_t - \tilde{\varepsilon}_t^{pl}) \quad (22)$$

$$\sigma_c = (1-d_c)\,E_0(\varepsilon_c - \tilde{\varepsilon}_c^{pl}) \quad (23)$$

The effective tensile and uniaxial compressive stresses resulting from crack propagation are then given as follows:

$$\tilde{\sigma}_t = \frac{\sigma_t}{(1-d_t)} = E_0(\varepsilon_t - \tilde{\varepsilon}_t^{pl}) \quad (24)$$

$$\tilde{\sigma}_c = \frac{\sigma_c}{(1-d_c)} = E_0(\varepsilon_c - \tilde{\varepsilon}_c^{pl}) \quad (25)$$

The inelastic stress-strain curves to be used in the modelling are given as follows:

$$\tilde{\varepsilon}_c^{in} = \varepsilon - \frac{\sigma_c}{E_0} \quad (26)$$

$$\tilde{\varepsilon}_c^{pl} = \tilde{\varepsilon}_c^{in} - \frac{d_c}{(1-d_c)}\frac{\sigma_c}{E_0} \quad (27)$$

$$\tilde{\varepsilon}_t^{pl} = \tilde{\varepsilon}_t^{ck} - \frac{d_t}{(1-d_t)}\frac{\sigma_t}{E_0} \quad (28)$$

2.2 Rebar steel

The rebar steel is modeled with an elastoplastic behavior with isotropic hardening (Figure 2). The stress is described by the following BAEL99 (1999) [27]:

$$\sigma = \begin{cases} E_a \cdot \varepsilon & \text{for} \quad 0 \leq \varepsilon_r < \varepsilon_e \\ \sigma_e & \text{for} \quad \varepsilon_e \leq \varepsilon \leq \varepsilon_u \\ 0 & \text{for} \quad \varepsilon > \varepsilon_u \end{cases} \tag{29}$$

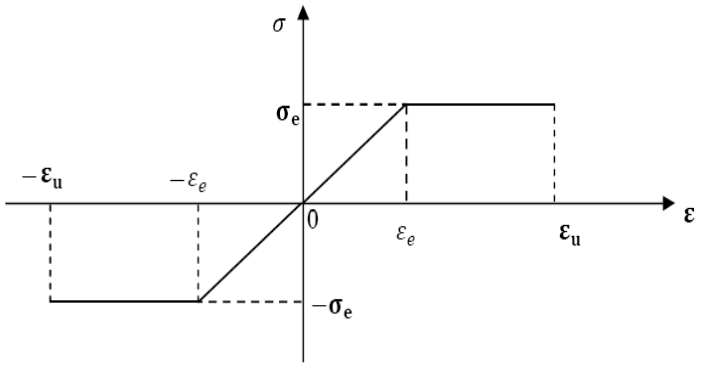

Figure 2: Perfect elastoplastic law of a reinforced concrete steel according to BAEL99 [27]

3 Nonlinear Behavior Modeling of Concrete Masonry Units

In this method, the simulation of the nonlinear behavior of the concrete masonry units can be represented by two models, the CDP model or by using the Drucker-Prager plastic model. In this paper, the Drucker-Prager model will be mainly used for experimental validation and the CDP model for masonry unit will be discussed later.

3.1 Drucker Prager Model

For materials with internal friction, such as sands, soils, rocks and concrete, it is not possible to neglect the effect of the first invariant I1 in the yield condition (Jirasek and Bazant, 2001 [28]). The first effective criterion written in terms of I1 and J2 was proposed by Burzyński (1929) [29] according to Jirasek and Bazant (2001) [28]. Later, Drucker and Prager (1952) [30] will propose his model, and his criterion is usually stated as follows:

$$f\left(I_1, J_2\right) \equiv \alpha I_1 + \sqrt{J_2} - \tau_0 \tag{30}$$

α and τ_0 are the material parameters, I_1 and J_2 are respectively the first invariant and the second deviatoric invariant. This model has been widely used, particularly in the modeling of confined concrete Oh (2003) [31]; Karabinis and Kiousis (1994) [32]. Later, many authors will propose modifications to this model (Yu et al., 2010 [33]; Zhang et al., 2015 [34]; Mohammadi et al., 2019 [35]), in this article the extended Drucker-Prager model will be used to simulate the non-linear behavior of bricks in compression.

Three yield criteria with different shapes of yield surfaces in the meridian plane (p-t plane) can be used in this model: a linear form, a hyperbolic form and a general exponent form. In our case the linear form was chosen, according to the recommendation of Yu et al. (2010) [33], which recommends the use of a criterion taking into account the third deviatoric invariant, as well as a function of yield non-circular.

The yield criteria in a linear form is expressed as Abaqus (2011) [36]:

$$F = t - \tan\beta - d = 0 \tag{31}$$

$$t = \frac{1}{2}q\left[1+\frac{1}{K}-\left(1-\frac{1}{K}\right)\left(\frac{r}{q}\right)^{3}\right] \tag{32}$$

With:

$$q = \sqrt{3J_2} \tag{33}$$

$$J_2 = \frac{1}{2}s:s = \frac{1}{2}s_{i.j}s_{i.j} = \frac{1}{6}\left[\left(\sigma_1-\sigma_2\right)^2+\left(\sigma_2-\sigma_3\right)^2+\left(\sigma_3-\sigma_1\right)^2\right] \tag{34}$$

In this paper, hardening is defined by the elastic compressive stress, we will have:

$$d = \left(1-\frac{1}{3}tan\beta\right)\sigma_c \tag{35}$$

3.2 Modeling of the Connection Between the Concrete Masonry Units

Usually the connection between the different concrete masonry units is represented by a cohesive relationship of the traction-separation type.
After failure of the cohesive bond, Coulomb's law is applied to express the friction between the different concrete masonry units.

In the case of a frame with infill, this same connection is applied between the frame and the masonry. In our case, the connection between the different concrete masonry units will be modeled in this way. The contact between the different surfaces of the concrete masonry units is expressed through two types of behavior included in Abaqus software. The first is "hard contact behavior" which supposes a transmission of stresses for the surfaces in contact. It minimizes the penetration of the slave surface in the master surface at stress locations and does not allow tensile stress transfer across the interface (Abaqus, 2011 [36]). The second is tangential where a coefficient of friction will be determined by groping to simulate the behavior of the concrete masonry units in contact with each other. As for the connection between the reinforced concrete (RC) frame and the concrete masonry units, it will be done using the "Tie" module included in Abaqus explicit.

This type of contact has been used to model confined masonry in the past by Borah et al. (2021) [37]; Chandel and Sreevalli (2019) [38]; Okail et al. (2016) [39]. In this paper, its use will be

generalized for classical masonry. Furthermore, the model proposed here, offers a slight improvement by taking into account the masonry units separately, this makes it possible to take into account the mode of failure by horizontal slip of the bed joints of the masonry.

One of the limits of the proposed model is the dependence of the solution on the size of the mesh, as mentioned by Borah et al. (2021) [37], the mesh size must be calibrated in order to have the numerical solution close to the experimental solution.

4 Results and discussion

The experimental test of Mehrabi and Shing (1994) [41] shown in Figure 3, this test consists of a progressive thrust until the failure of a reinforced concrete (RC) frame with masonry infills. The reinforced concrete (RC) frame being the same as that which was validated during the first part.

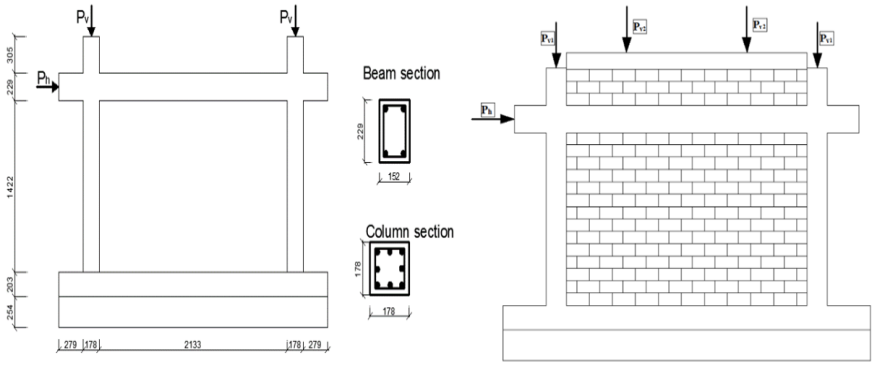

Figure 3: Experimental model of the reinforced concrete (RC) frame with masonry infill

The mechanical characteristics of concrete and steel reinforcement are given in Table 1 and 2.

Table 1: Mechanical characteristics of concrete

E_c (MPa)	f_{c28} (MPa)	f_{t28} (MPa)
21930	30.9	3.29

Table 2: Mechanical characteristics of steel reinforcement

Type of reinforcement	E_S (MPa)	f_y (MPa)	f_u (MPa)
Longitudinal	195000	420.7	662.1
Transverse	195000	367.6	449.6

Even though the masonry units are perforated units, in our model they are represented as complete units with the following dimensions: 204 x 102 x 102 mm. This simplification was used by Bolhassani et al. (2015) [17] and showed satisfactory results.

Even though the masonry units are perforated units (Fig. 15), in our model they are represented as complete units with the following dimensions: 204 x 102 x 102 mm. This simplification was used by Bolhassani et al. (2015) [17] and showed satisfactory results. Fig. 15 shows the dimensions of the masonry units used during the experimental test by Mehrabi and Shing (1994) [41].

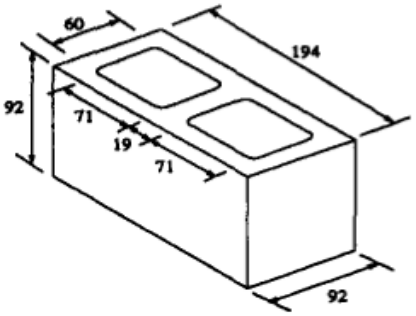

Fig. 15 Concrete masonry units of the experimental test (Mehrabi and Shing, 1994 [41])

The following Tables summarize the different parameters assigned when modeling concrete masonry units in Abaqus.

Table 3: Values assigned for the mechanical behavior of concrete masonry units

Parameters	ν	E (MPa)	fc (MPa)
Values	0.15	15400	16.48

The different parameters assigned when modeling concrete masonry units in Abaqus follow Drucker Prager model with: R of 1, ψ of 27 and β of 2.

The experimental test conducted by Mehrabi and Shing (1994) [41] consists of imposing two loads were imposed on the frame along the analysis, first a fixed vertical load with a value of 293 kN; distributed between the columns (195.4 kN) and the beam (97.6 kN), and another laterally incremented monotonic load, applied according to the controlled displacement mode. The vertical load was applied first and was kept constant until the frame collapsed.

4.1 Results of the Reinforced Concrete (RC) Frame without Masonry Infill

Figure 4 shows a comparison between the analytical results with those of the experimental test conducted by Mehrabi and Shing (1994) [41], from the curves we can see that our numerical model describes in a suitable way the behavior of the frame, we can even see that the elastic behavior is obtained in a more specific way than the numerical model of Mehrabi and Shing (1997) [40], this demonstrates the robustness of the proposed model. The agreement of the ultimate load between experience and our calculation is satisfactory; a slight overestimation of the ultimate load can be seen towards the end.

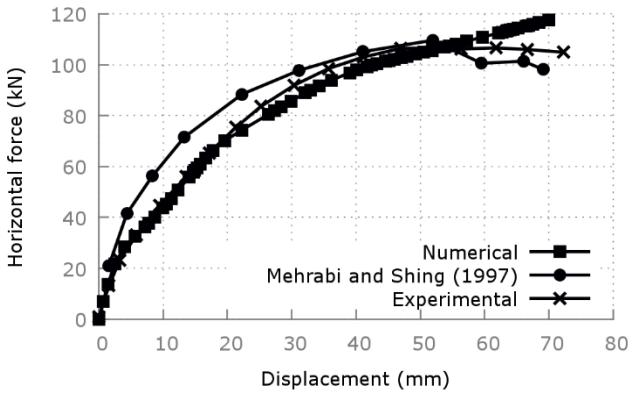

Figure 4: Load-displacement curves for the RC frame without masonry infill

In the elastic part, the experimental test conducted by Mehrabi and Shing (1994) [41] has an initial stiffness of 474.77 N/mm; in comparison, the numerical model presented by this study presents an initial stiffness of 463.22 N/mm, for the numerical model of Mehrabi and Shing (1997) [40] the latter is 675.63 N/mm. The numerical model presents a difference in terms of initial stiffness of 2.43%, for the numerical model of Mehrabi and Shing (1997) [40], this difference is 20.9 %.

Table 3: Comparison between initial stiffness's

Frame without masonry infill	Ultimate load P_u (kN)	Error (%)	Initial stiffness (N/mm)	Error (%)
Experimental	106.62	-	4747.7	-
Numerical	117.47	10.17	4632.2	2.43
Mehrabi and Shing (1997)	108.65	1.90	6756.2	20.9

The results in Table 3 indicate an ultimate experimental load of 106.62 kN and that obtained by our calculation of 117.47 kN, i.e. a difference of about 10.17 %.
Our numerical model presents an average error estimated at 4.83% of the experimental load, that of Mehrabi and Shing (1997) [40] presents an average error estimated at 9.1% of the experimental load. This demonstrates that our numerical model manages to simulate the plastic behavior of the experimental curve more adequately than that of Mehrabi and Shing (1997) [40].

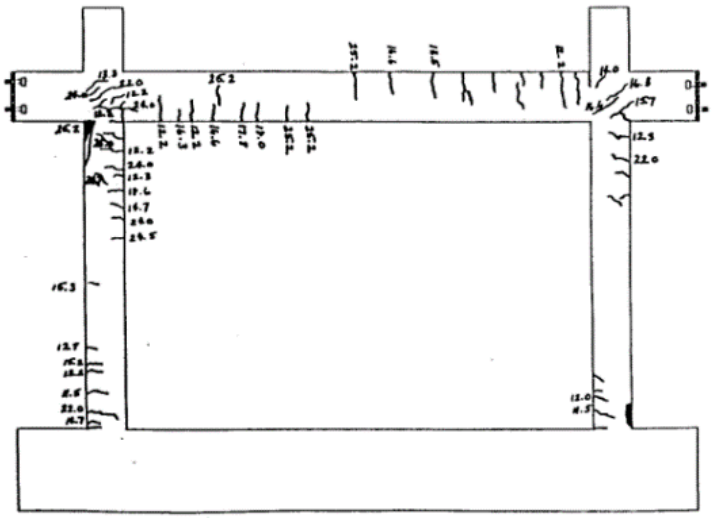

(a)

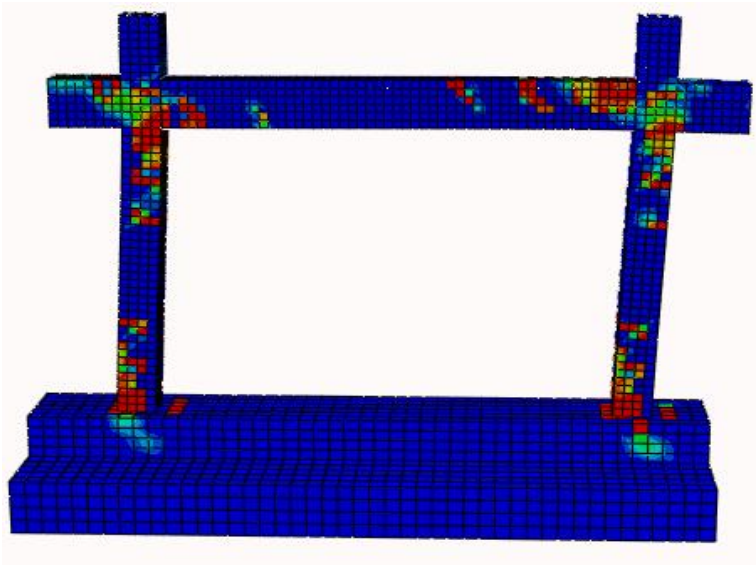

(b)

Figure 5: Damage evolution of the reinforced concrete (RC) bare frame: (a) Experimental test (Mehrabi and Shing, 1994 [41]), (b) Numerical study

By comparing the damage in Figure 5(a) which shows the level of damage suffered by the reinforced concrete (RC) frame during the experimental test, the damage given by the numerical model (Figure (5b)) succeeds in reproducing the damaged zones well, especially in the nodal and tense zones, we can therefore conclude that the damage model proposed by Alfarah et al. (2017) [24] is perfectly suited for modeling the damage of reinforced concrete.

4.2 Results of the Reinforced Concrete (RC) Frame with Masonry Infill

Figure 6 shows a comparison between the experimental and numerical model, where we can see an acceptable similarity of the proposed model.

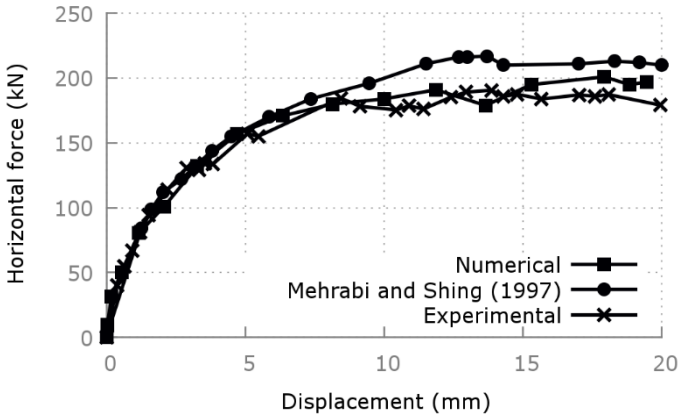

Figure 6: Load-displacement curves for the RC frame with masonry infill

The ultimate experimental load of 190 kN and the ultimate load obtained by our calculation of 201 kN. The agreement between the ultimate load found by our calculation and that measured is satisfactory. Our model overestimates the ultimate load by about 5.78%.

It can be seen that our simulation and that of Mehrabi and Shing (1997) [40] give an appearance close to the experimental curve. However, the two curves obtained differ at the level of the ultimate load, where our calculation seems to approach the experimental better than the simulation carried out by Mehrabi and Shing (1997) [40].

From Figure (6), it can be also seen that the Drucker-Prager model more accurately describes the behavior of the frame with masonry infill than the Concrete Damage Plasticity (CDP) model. The ultimate experimental load of 190 kN, and the ultimate load obtained by the Drucker-Prager model of 201 kN, and that obtained by the Concrete Damage plasticity (CDP) model is 208 kN. The agreement between the ultimate load found by the Concrete Damage Plasticity (CDP) model and that measured is satisfactory. The Concrete Damage Plasticity (CDP) model overestimates the ultimate load by about 9.47% compared to the experimental.

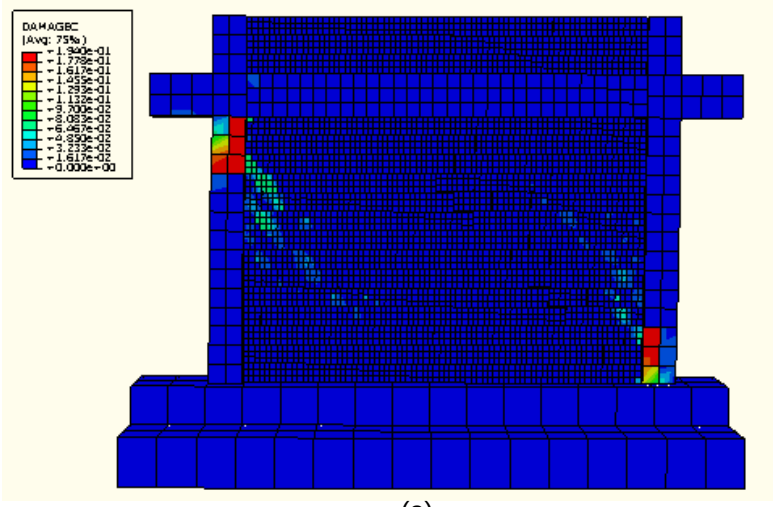

(a)

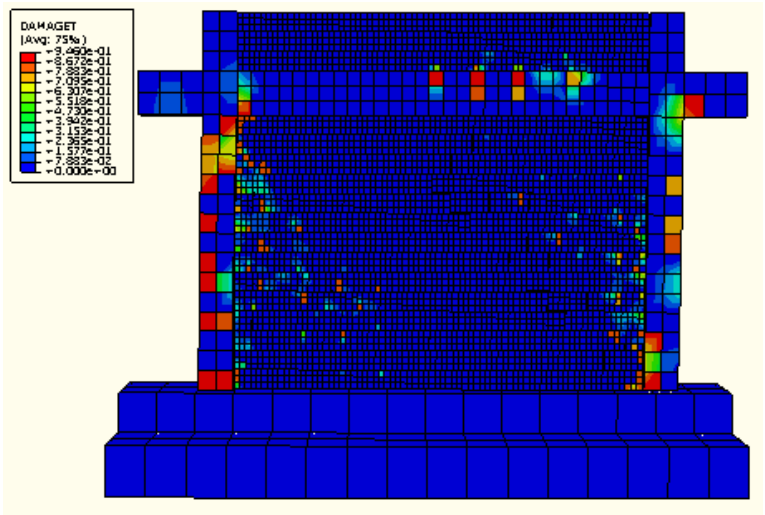

(b)

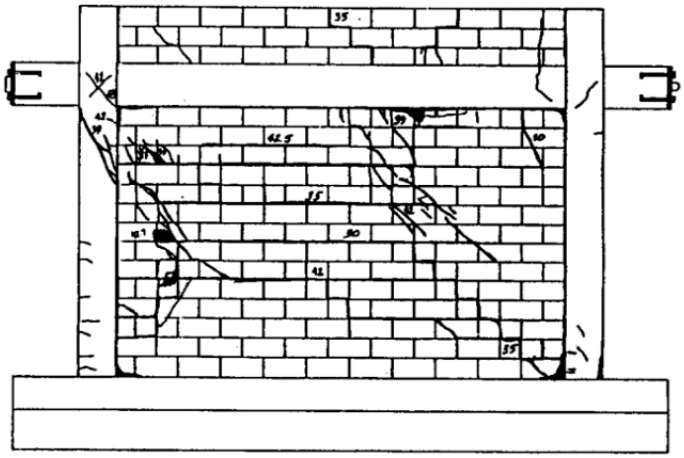

(c)

Figure 7: Numerical and experimental damage evolution of the RC frame with masonry infill: (a) Compression damage, (b) Tension damage, (c) Experimental damage

The use of the Concrete Damage Plasticity (CDP) model makes it possible to obtain a numerical damage, the results obtained are in Figure (7a) for the damage in compression and Figure (8b) for the damage in tension.

By comparing the results obtained numerically in Figure (7a) and Figure (7b) with those obtained experimentally in Figure (7c), we can see that our model manages to reproduce the experimental damage in an acceptable way. Here the mode of failure of the infilled frame by crushing of the corners as well as the diagonal cracking could be reproduced.

5 Conclusion

In this article a modeling method for reinforced concrete (RC) frames with the Abaqus computer code, with and without masonry infill, has been introduced. At first, the use of a damage model present in the literature, added to the various modules integrated in Abaqus allows us to model the damage in a reinforced concrete (RC) frame structure.

The introduction of discrete elements is the most widespread method to simulate the behavior between the concrete masonry units in contact, as well as the damage likely to appear in the frame or in the masonry units, this method often requires the use of relatively complex subroutines. This paper proposes an alternative to this by proposing a simplified micro-modeling which makes it possible to simulate the behavior of a reinforced concrete (RC) structure with masonry infill.

The results obtained from our numerical modeling relating to the frame with and without masonry infill are very close to the analytical and experimental results. Which allows us to say that the adopted simplified micro-modeling allows us to simulate in a correct way the nonlinear behavior of the reinforced concrete (RC) frames with and without masonry infill until the rupture.

List of notations

E_0	Elastic modulus corresponding to 0.4 of the characteristic resistance of concrete
ε_c	Strain of concrete in compression
f_{cm}	Compressive strength of concrete
f_{ck}	Characteristic value of concrete strength
ε_{cm}	Strain corresponding to the maximum strength of the concrete
G_{ch}	Concrete crushing energy
l_{eq}	Characteristic length which corresponds to mesh of the element
ε_c^{pl}	Plastic strain due to element damage
ε_c^{ch}	Concrete crushing strain
ε	Total strain

ε^{el} Elastic strain
σ Elastic stress
d The damage variable
D_0^{el} The elastic stiffness matrix
D^{el} The deteriorated stiffness matrix
$\bar{\sigma}$ Effective stress
$\tilde{\varepsilon}^{pl}$ Equivalent plastic strain
$\dot{\lambda}$ Not-negative multiplier
$\tilde{\varepsilon}_t^{pl}$ Equivalent plastic strains in tension
$\tilde{\varepsilon}_c^{pl}$ Equivalent plastic strains in compression

References

[1] El-Ouali, T., Houde, J., Tinawi, R. (1991). Comportement d'un cadre rempli soumis à un chargement cyclique : modélisation pour une analyse dynamique non linéaire. *Canadian Journal of Civil Engineering*. 18(6), pp. 1013-1023. https://doi.org/10.1139/l91-124

[2] Wakabayashi, M. (1986). Design of earthquake-resistant buildings. McGraw-Hill Companies

[3] Murty, C.V.R., Jain, S.K. (2000). Beneficial influence of masonry infill walls on seismic performance of RC frame buildings. In 12th world conference on earthquake engineering

[4] Dawe, J., Seah, C.K. (1989). Behaviour of masonry infilled steel frames. *Canadian Journal of Civil Engineering*. 16(6), pp. 865-876. https://doi.org/10.1139/l89-129

[5] Crisafulli, F.J. (1997). Seismic behaviour of reinforced concrete structures with masonry infills. Doctoral dissertation, University of Canterbury

[6] Yuen, Y.P., Kuang, J.S. (2012). Nonlinear response and failure mechanism of infilled RC frame structures under biaxial seismic excitation. In Proceedings of the 15th World Conference on Earthquake Engineering, Lisboa, Portugal

[7] Chrysostomou, C.Z. (1991). Effects of degrading infill walls on the nonlinear seismic response of two-dimensional steel frames. Doctoral dissertation, Cornell University

[8] D'Altri, A.M., Sarhosis, V., Milani, G., Rots, J., Cattari, S., Lagomarsino, S., Sacco, E., Tralli, A., Castellazzi, G., de Miranda, S. (2019). Modeling strategies for the computational analysis of unreinforced masonry structures: review and classification. *Archives of computational methods in engineering*, pp. 1-33. https://doi.org/10.1007/s11831-019-09351-x

[9] Ali, S.S., Page, A.W. (1988). Finite element model for masonry subjected to concentrated loads. *Journal of structural engineering*. 114(8), pp. 1761-1784. https://doi.org/10.1061/(ASCE)0733-9445(1988)114:8(1761)

[10] Page, A.W. (1978). Finite element model for masonry. *Journal of the Structural Division*. 104(8), pp 1267-1285. https://doi.org/10.1061/JSDEAG.0004969

[11] Lotfi, H.R., Shing, P.B. (1994). Interface model applied to fracture of masonry structures. *Journal of structural engineering*. 120(1), pp. 63-80. https://doi.org/10.1061/(ASCE)0733-9445(1994)120:1(63)

[12] Lourenço, P.B., Rots, J. (1994). Analysis of masonry structures with interface elements. Rep. No. 03-21-22-0, 1

[13] Lourenço, P.B., Rots, J.G. (1997). Multisurface interface model for analysis of masonry structures. *Journal of engineering mechanics.* 123(7), pp. 660-668. https://doi.org/10.1061/(ASCE)0733-9399(1997)123:7(660)

[14] Aref, A.J., Dolatshahi, K.M. (2013). A three-dimensional cyclic meso-scale numerical procedure for simulation of unreinforced masonry structures. Computers & Structures. 120, pp. 9-23. https://doi.org/10.1016/j.compstruc.2013.01.012

[15] Nasiri, E., Liu, Y. (2017). Development of a detailed 3D FE model for analysis of the in-plane behaviour of masonry infilled concrete frames. *Engineering Structures*. 143, pp. 603-616. https://doi.org/10.1016/j.engstruct.2017.04.049

[16] Kuang, J.S., Yuen, Y.P. (2013). Simulations of masonry-infilled reinforced concrete frame failure. *Proceedings of the Institution of Civil Engineers-Engineering and Computational Mechanics.* 166(4), pp. 179-193. https://doi.org/10.1680/eacm.13.00002

[17] Bolhassani, M., Hamid, A.A., Lau, A.C., Moon, F. (2015). Simplified micro modeling of partially grouted masonry assemblages. *Construction and Building Materials.* 83, pp. 159-173. https://doi.org/10.1016/j.conbuildmat.2015.03.021

[18] Abdulla, K.F., Cunningham, L.S., Gillie, M. (2017). Simulating masonry wall behaviour using a simplified micro-model approach. *Engineering Structures*. 151, pp. 349-365. https://doi.org/10.1016/j.engstruct.2017.08.021

[19] Zhai, C., Wang, X., Kong, J., Li, S., Xie, L. (2017). Numerical simulation of masonry-infilled RC frames using XFEM. *Journal of Structural Engineering.* 143(10), pp. 04017144. https://doi.org/10.1061/(asce)st.1943-541x.0001886

[20] D'Altri, A.M., de Miranda, S., Castellazzi, G., Sarhosis, V. (2018). A 3D detailed micro-model for the in-plane and out-of-plane numerical analysis of masonry panels. *Computers & Structures.* 206, pp. 18-30. https://doi.org/10.1016/j.compstruc.2018.06.007

[21] Nguyen, G.D., Korsunsky, A.M. (2008). Development of an approach to constitutive modelling of concrete: isotropic damage coupled with plasticity. *International Journal of Solids and Structures*. 45(20), pp. 5483-5501. https://doi.org/10.1016/j.ijsolstr.2008.05.029

[22] Lubliner, J., Oliver, J., Oller, S., Oñate, E. (1989). A plastic-damage model for concrete. *International Journal of solids and structures.* 25(3), pp. 299-326. https://doi.org/10.1016/0020-7683(89)90050-4

[23] Lee, J., Fenves, G.L. (1998). Plastic-damage model for cyclic loading of concrete structures. *Journal of engineering mechanics.* 124(8), pp. 892-900. https://doi.org/10.1061/(ASCE)0733-9399(1998)124:8(892)

[24] Alfarah, B., López-Almansa, F., Oller, S. (2017). New methodology for calculating damage variables evolution in Plastic Damage Model for RC structures. *Engineering Structures.* 132, pp. 70-86. https://doi.org/10.1016/j.engstruct.2016.11.022

[25] CEB-FIP (CEBFIP) (2010). Model code 2010. Comité euro-international du béton 594. https://doi.org/10.1007/978-3-642-41840-2_1

[26] Krätzig, W.B., Pölling, R. (2004). An elasto-plastic damage model for reinforced concrete with minimum number of material parameters. *Computers & structures.* 82(15-16), pp. 1201-1215. https://doi.org/10.1016/j.compstruc.2004.03.002

[27] Rules BAEL91 revised 99 (1999). Technical design rules and calculation of works and structures reinforced concrete according to the limit states method. Publisher: Association Francaise de Normalisation.

[28] Jirasek, M., Bazant, Z.P. (2001). Inelastic analysis of structures. John Wiley & Sons.

[29] Burzyński, W.V. (1929). Über die Anstrengungshypothesen. Schweizerische Bauzeitung. 94(21), pp. 259-262.

[30] Drucker, D.C., Prager, W. (1952). Soil mechanics and plastic analysis or limit design. *Quarterly of applied mathematics.* 10(2), pp. 157-165. https://www.jstor.org/stable/43633942

[31] Oh, B. (2003). A plasticity model for confined concrete under uniaxial loading. Doctoral dissertation, Lehigh University.

[32] Karabinis, A.I., Kiousis, P.D. (1994). Effects of confinement on concrete columns: plasticity approach. *Journal of structural engineering.* 120(9), pp. 2747-2767. https://doi.org/10.1061/(ASCE)0733-9445(1994)120:9(2747)

[33] Yu, T.T.J.G., Teng, J.G., Wong,Y.L., Dong, S.L. (2010). Finite element modeling of confined concrete-I: Drucker–Prager type plasticity model. *Engineering structures.* 32(3), pp. 665-679. https://doi.org/10.1016/j.engstruct.2009.11.014

[34] Zhang, Y., Bernhardt, M., Biscontin, G., Luo, R., Lytton, R. (2015). A generalized Drucker–Prager viscoplastic yield surface model for asphalt concrete. *Materials and Structures*. 48(11), pp. 3585-3601. https://doi.org/10.1617/s11527-014-0425-1

[35] Mohammadi, M., Dai, J.G., Wu, Y.F., Bai, Y.L. (2019). Development of extended Drucker–Prager model for non-uniform FRP-confined concrete based on triaxial tests. *Construction and Building Materials.* 224, pp. 1-18. https://doi.org/10.1016/j.conbuildmat.2019.07.061

[36] Abaqus (2011). Analysis user's manual 6.14. Dassault Systemes Simulia Corp., Providence, RI.

[37] Borah, B., Singhal, V., Kaushik, H.B. (2021). Assessment of seismic design provisions for confined masonry using experimental and numerical approaches. *Engineering Structures.* 245, pp. 112864. https://doi.org/10.1016/j.engstruct.2021.112864

[38] Chandel, V.S., Yamini Sreevalli, I. (2019). Numerical study on influence of masonry infill in an RC frame. *Asian Journal of Civil Engineering.* 20, pp. 1-8. https://doi.org/10.1007/s42107-018-0083-7

[39] Okail, H., Abdelrahman, A., Abdelkhalik, A., Metwaly, M. (2016). Experimental and analytical investigation of the lateral load response of confined masonry walls. *HBRC journal.* 12(1), pp. 33-46. https://doi.org/10.1016/j.hbrcj.2014.09.004

[40] Mehrabi, A.B., Shing, P.B. (1997). Finite element modeling of masonry-infilled RC frames. *Journal of structural engineering.* 123(5), pp. 604-613. https://doi.org/10.1061/(ASCE)0733-9445(1997)123:5(604)

[41] Mehrabi, A.B., Shing, P.B. (1994). Performance of masonry-infilled R/C frames under in-plane lateral loads: analytical modeling. In Proc., NCEER Workshop on Seismic Response of Masonry, San Francisco.

DOI:10.2478/sspjce-2024-0010

Impact of the Courtyard Geometry on Cooling Energy Demand in Arid Zones. Univariate Regression-based Approach.

Boukarta Soufiane

Blida 1 university, Algeria
Institute of architecture and urban planning, ETAP laboratory.
e-mail: boukarta.soufiane@univ-blida.dz

Abstract

Vernacular architecture, often described as architecture without an architect, never ceases to show us the extent to which the building system was linked to its environment and clearly expressed the *genius loci*. This paper looks at the role that courtyard geometry can play as a thermal and energy regulator in traditional houses. To do this, the study is based on a historical reading of the evolution of the courtyard, with the aim of characterising its geometry in terms of its size in relation to the house, its depth, its position (centred or off-centre), its shape and finally its orientation. To assess the performance of each type of courtyard, the study is based on a campaign of dynamic thermal simulations (DTS) carried out under DesignBuilder for the arid climate of the city of Laghouat in Algeria. The results of the study are based on a comparative approach and modelling using univariate linear regression. The best configuration obtained for the courtyard is that of a rectangular courtyard, with a 10% opening ratio, elongated on the axis east-west direction, a central position and a depth of three levels, as this best combines solar gain and shading protection.

Keywords: vernacular architecture, courtyard geometry, energy performance, dynamic thermal simulation, univariate linear regression.

1 Introduction

Vernacular architecture, often defined as architecture without an architect, never ceases to impress us with its potential to adapt to its environment [1]. The accelerated urbanisation that is taking place in Algerian towns and cities is taking place in partial or total denial of the virtues of local architecture in terms of spatial organisation and the materials chosen for construction. This urbanisation is directly involved in the proliferation of energy-guzzling buildings, which play a full part in exacerbating the phenomenon of climate change. Algeria, a signatory to the Kyoto Protocol and the 2015 Paris Agreement, has put in place a national energy management strategy structured by Law 09-99, the implementation of which is based on national energy management plans [2, 3] and whose objective is the gradual introduction of renewable energies (RE) to reach 20% by 2030 [4] and the reduction of energy demand by introducing energy efficiency in the residential, transport, industrial and agricultural sectors. The residential sector alone is responsible for 46% of final energy consumption [5]. Algeria is also committed to

reducing its greenhouse gas emissions by 7% by 2030 without financial assistance, and by 20% if Algeria receives financial assistance to do so [4].

The thermal regulations also corroborate the government's goal to reduce energy demand by improving architectural studies via the DTR C3-2, the use of which is only made by architects on a voluntary basis. In line with this purpose to reduce energy demand and the associated greenhouse gas emissions, architectural practice seems to be neglecting the virtues of vernacular architecture, despite the fact that it offers promising ideas for reducing energy demand. Some Algerian researchers have set themselves the goal of demonstrating the virtues of local architecture by promoting the use of local materials in housing design [6] or the microclimatic aspect [7, 8] or by evoking the organisation of interior space as a thermal regulator [9] or by testing the thermal behaviour of architectural elements such as balconies [10]. In another study carried out by Boukarta (2023) [11], the author found that by increasing insulation and even using local materials, energy demand in arid zones remains high for air conditioning. The author concludes that vernacular architecture with its spatial organisation around courtyards and chebaks, covered passageways and other elements of architectural composition common in arid zones can in turn improve the thermal behaviour of the house and reduce the energy demand for air conditioning in arid zones, which account for more than 80 per cent of Algerian territory. In this paper we aim to identify the impact of courtyard geometry on the energy demand of an individual house by considering the case of the arid climate of the city of Laghouat.

2 Literature Review

A review of the scientific literature shows that the courtyard is an architectural element present in ancient civilisations, namely the Egyptian civilisation in the Kahn area in 5000 BC and the Chaldean city of Ur before 2000 BC [12]. Courtyard houses did not appear in the West until later, in cities such as Greece and Rome [13]. Courtyard houses have evolved in line with the lifestyle of the inhabitants and as a climatic response in hot and dry climates [14]. In Italy, for example, the courtyard was transformed into an atrium from 700 AD onwards, the purpose of which was to create a private space [15], while in China the primary houses conceived of the courtyard as a private and meditative space [16]. In Algeria, on the other hand, courtyard houses are available for climatic and social reasons and can be found in almost all Algerian cities with *ksour* or *kasbahs* as their old centre, see Figure 1 below.

A review of the scientific literature has enabled us to characterise courtyards geometry by: (i) Its shape, which is most often rectangular, square or even circular [17]. Tablada et al (2005) [18] have shown that the rectangular shape provides better protection from solar radiation and limits the impact of sand winds; (ii) the scale or size of the courtyard is another distinctive element. The size calculated in relation to the house's area varies from one house to another; (iii) the position of the courtyard may be central or off-centre, or the courtyard may be semi-enclosed, bordered by the house on one side and by enclosing walls on the other [19]; (iv) The depth of the courtyard, which may vary from one region to another. (V) The orientation of the courtyard plays an important role in defining wind movement, solar protection and solar gains [20].

(a) (b)

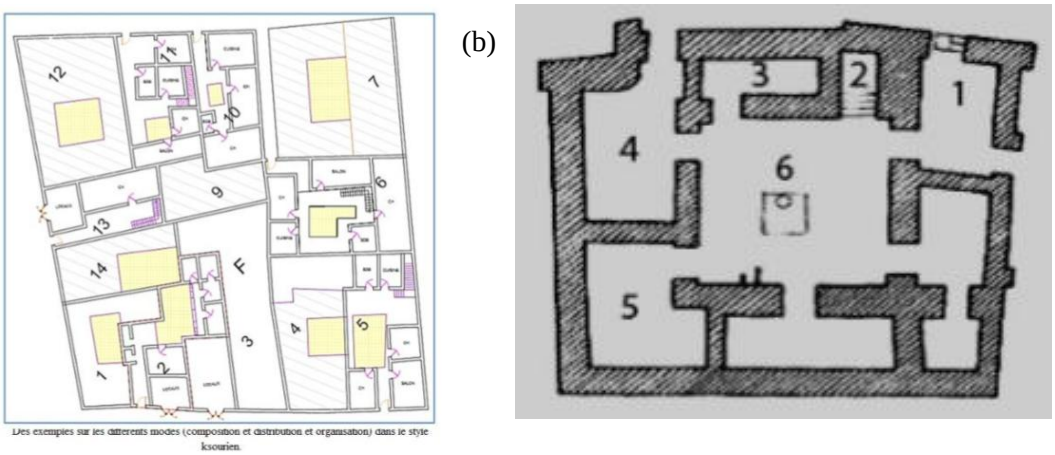

Figure 1: (a) Examples of the different modes of composition and organisation in the ksourien style. Source: PPSMVSS of ksar Laghouat, Algeria. (b) Courtyard house in Mesopotamia. Source: Abass et al: 2016[14].

Research into the role of courtyards has been the subject of several studies around the world since the early 2000s, with the rise of sustainable development principles. The most frequently asked questions concern several aspects of environmental performance, namely energy demand, daylighting [21], natural ventilation [22] and microclimate generated [23]. The energy aspect is the most widely studied and focuses mainly on the summer period, with fewer studies looking at both aspects at the same time. The summer period is the most studied because the courtyard still exists in arid zones and is still an element of architectural composition. Studies of the adaptability of courtyards to the two periods, summer and winter, are few Akbari et al (2021) [24] demonstrated a higher adaptability for the summer period with 73% and 20% for winter, which explains the tendency of researchers to deal only with the summer period. Also, some studies state that courtyards are better adapted to hot climates than cold climates [25, 26]. It is also worth noting that in some climatic regions the trend is reversed, Yaşa et Ok (2014) [27] found that the maximisation of solar radiation is greater for the winter period than the summer period giving a better adaptability of patios to winter than summer.

De la Flor et al (2021) [28] carried out a comparative study using a simulation-based approach between a house with a courtyard and a reference case without a courtyard. They found that the courtyard could improve energy savings by more than 10% and that the geometry of the courtyard is a key parameter for controlling cooling energy demand. Diz-Mellado et al (2023) [29] explored the impact of courtyard geometry on energy demand in the climate of the city of Seville. They found that the temperature gap between the courtyard and outdoor temperature can vary according to the geometry of the patio from 10 to 14°C. And that the geometry of the yard can vary the cooling energy demand from 8 to 18% and by 15 to 22% once the floor level is combined with the orientation. Tabadkani et al (2022) [30] simulated in Grashooper with the environmental plugins ladybug and honeybee several possible combinations of courtyards in Tehran and found that the rectangular shape with an opening of 12% and the best configuration to satisfy summer and winter comfort is obtained for a rectangular patio of 10*5 and 4.5m deep in Tehran. Seddik et al (2024) [31] also studied the impact of the shape of the courtyard with the length-width ratio, the placement of the courtyard in relation to the centre of the houses and in relation to the facades, as well as the axis of orientation in the city of Kharga in Egypt. The

study was carried out using DesignBuilder. The results show an energy saving of 18.73% with a rectangular shape at a ratio of 2.5:1 and a positioning of the patio on the south-west façade. Soflaei et al (2020) [32] carried out a parametric study using Grashooper, generating 8,600 cases and combining parameters relating to the geometry of the courtyard, the window to wall ratio and the material chosen for the walls. This study shows that the thermal behavior of courtyard depends initially on the construction materials, and that the depth of the courtyard is more important than its orientation.

The review of the scientific literature suggests that the combined effect of variables controlling courtyard geometry and the comparison between them are missing from the studies. this is why, In the present study, we aim to quantify the impact of courtyards geometry on cooling energy demand by specifying the effects of the parameters considered alone and in combination with each other under arid climatic conditions.

3 Methods

The methodology used in this paper to determine the impact of the courtyard geometry on energy demand is based on a parametric approach aimed at varying the elements characterising the courtyard obtained from scientific literature. Each variation is considered as a case study and the energy requirement for cooling is identified by dynamic thermal simulation carried out using DesignBuilder V.7.The variables considered in this paper are: the size of the courtyard considered by the ratio of courtyard area to ground floor house area (Ac/Ah); the depth of the courtyard considered according to the number of floors in the house; the shape of the courtyard, square or rectangular and finally the orientation which is considered according to the axis running along the courtyard, either North-South or East-West. The parametric variation considered is presented in Table 1 below.

Table 1 : parametric variation applied to selected parameters.

Courtyard parameters	**Variation**
Ac/Ah	10, 20 et 30%
Courtyard depth	Ground floor (3.5m), 1st floor (7m), 2nd floor (10.5m)
Courtyard shape	Square, rectangular
Orientation of the courtyard axis	North-South, East-West

The simulation protocol is designed so that the parametric variations combine to assess the impact of each parameter in relation to the other parameters. In all, a campaign of 27 simulations was run in DesignBuilder. Table 3 shows the parametric variation applied for each simulation and the results of the simulations containing the cooling requirement and solar gain.

The case study is a generic model house with a square shape and 15 m sides (see Appendix A1, Table A1-1). The glazing ratio applied is 10% of the external wall surface and the ceiling height is 3.5m. To simplify interpretation and speed up simulation time, the house is considered as a single thermal zone. The thermal characteristics of the building materials are presented in Table 2 below.

Table 2 : The thermal characteristics of building materials

Construction elements	Heat loss coefficient W/m².k
Exterior stone walls	1.698
High floor, traditional (earthen)	1.778
Low floor on earth	1.778
6mm single glazing	5.778

4 Results and discussion

The climate data used for the simulations covers the period from 2007 to 2021 for the city of Laghouat-Medaghri and was obtained from the climate.onebuilding.org website. The bioclimatic analysis was carried out using the Climate Consultant V6 psychometric diagram developed by the University of California. See figure 2 below. By applying the ASHRAE Standard 55, adaptive thermal comfort model for naturally ventilated buildings, the comfort thresholds are limited to between 18.4°C for heating and 30.6°C for cooling (90% acceptability).

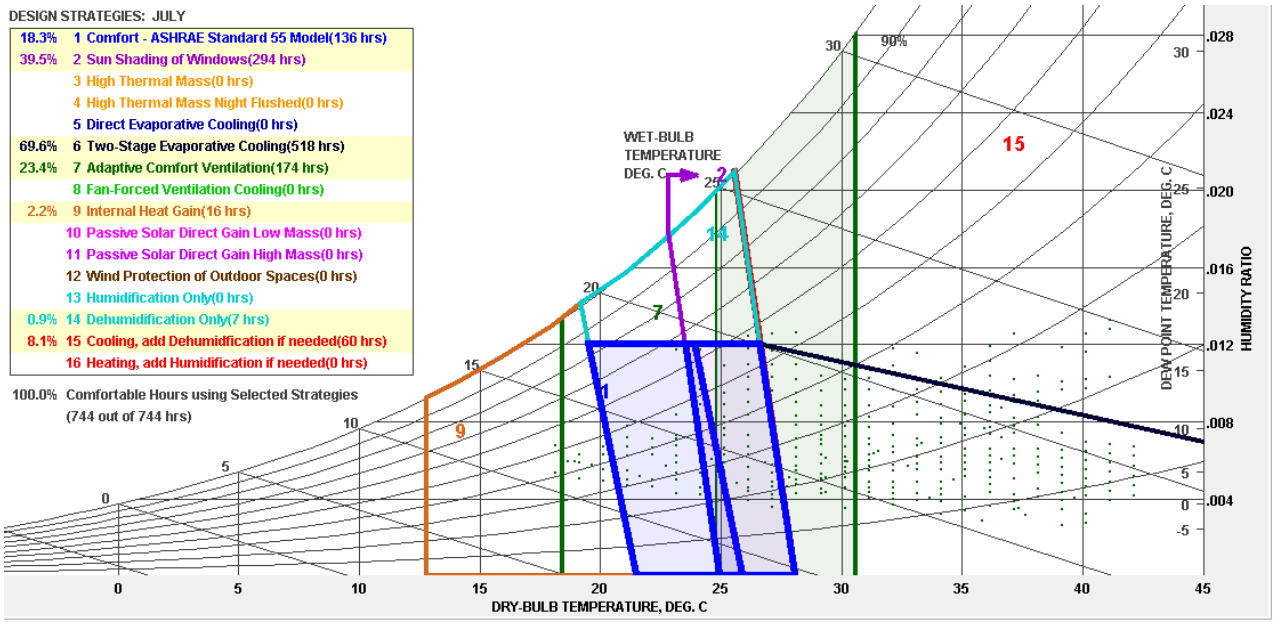

Figure 2: psychometric diagram of the city of Laghouat for the month of July.

The psychometric diagram shows that during the month of July, the climate is only comfortable for 18.3% because of the high temperatures experienced in the city of Laghouat, which can exceed 42°C. With ventilation management, comfort can be improved by 23.4%, while the need for air conditioning remains high at 62.5%. The passive strategies proposed by the model focus mainly on solar protection (nearly 40%) and evaporative cooling (nearly 70%). The role of the courtyard revolves around ventilation and solar protection. In this paper, the courtyard is studied to assess its role in solar protection and its potential for reducing energy demand.

4.1 Presentation of simulation results:

The results of the 27 simulations carried out are presented in the table below, which contains, in addition to the parametric variation applied, the cooling requirement and solar gain calculated by intensity per m².

Table3 : Parametric variation and simulation results

Case	Ac/ Ah	Depth	Shape	Orient	Cooling Kwh	EPI (w/m²)	Solar gain(W)	SG/m²	Dif %
1	10%	GF	Square	Neutral	47,56	234,86	22,51	111,15	8,94
2	10%	GF+1	Square	Neutral	84,77	235,48	42,86	119,06	9,23
3	10%	GF+2	Square	Neutral	119,82	221,89	62,63	115,99	2,92
4	20%	GF	Square	Neutral	48,34	238,73	24,65	121,74	10,73
5	20%	GF+1	Square	Neutral	86,79	241,08	46,48	129,1	11,82
6	20%	GF+2	Square	Neutral	123,49	228,69	67,34	124,7	6,08
7	30%	GF	Square	Neutral	48,02	237,14	26,39	130,31	10
8	30%	GF+1	Square	Neutral	87,39	242,75	49,73	138,14	12,6
9	30%	GF+2	Square	Neutral	123,56	228,82	71,72	132,82	6,14
10	10%	GF	Rectangle	North-South	49,6	244,95	22,88	112,98	13,62
11	10%	GF+1	Rectangle	North-South	85,03	236,19	43,05	119,57	9,56
12	10%	GF+2	Rectangle	North-South	117,93	218,39	62,81	116,31	1,3
13	20%	GF	Rectangle	North-South	50,62	249,96	25,5	125,94	15,94
14	20%	GF+1	Rectangle	North-South	89,45	248,46	47,24	131,21	15,25
15	20%	GF+2	Rectangle	North-South	124,34	230,26	67,95	125,83	6,8
16	30%	GF	Rectangle	North-South	50,72	250,45	27,36	135,11	16,17
17	30%	GF+1	Rectangle	North-South	90,07	250,19	50,45	140,13	16,05
18	30%	GF+2	Rectangle	North-South	126,84	234,89	72,07	133,46	8,95
19	10%	GF	Rectangle	East-West	46,56	229,94	22,07	108,97	6,66
20	10%	GF+1	Rectangle	East-West	81,69	226,91	42,7	118,62	5,25
21	10%	GF+2	Rectangle	East-West	116,41	215,58	62,78	116,25	0
22	20%	GF	Rectangle	East-West	46,79	231,08	24,18	119,42	7,19
23	20%	GF+1	Rectangle	East-West	83,13	230,92	46,24	128,46	7,11
24	20%	GF+2	Rectangle	East-West	120,15	222,5	67,53	125,05	3,21
25	30%	GF	Rectangle	East-West	45,59	225,12	25,78	127,3	4,42
26	30%	GF+1	Rectangle	East-West	83,21	231,13	48,99	136,08	7,21
27	30%	GF+2	Rectangle	East-West	119,54	221,37	71,22	131,88	2,68

SG: solar gain. Dif: the difference in cooling requirement compared with the best case (21 in green).

Based on the results described in Table 3 above, we can identify the role of each parameter on the energy demand for air conditioning. (i) The size of the courtyard, expressed as the Ac/Ah ratio, clearly shows a linear trend: the larger the courtyard, the greater the energy demand. 10% is the ideal scale for the courtyard to reduce its energy demand for air conditioning. This result is explained by the reduction in solar gain. (ii) The depth of the courtyard also makes it possible to reduce the energy demand for air conditioning by reducing solar gain, and GF+2 is the best

case. (iii) The shape of the courtyard also helps to regulate solar radiation, and, in fact, the rectangular shape provides better protection than the square shape. (iv) The orientation of the courtyard axis, combined with the shape, scale and depth of the courtyard, provides the best case and reduces energy demand by more than 16%.

4.2 Sensitivity analysis

There are several methods of sensitivity analysis, but for this study we chose the univariate linear regression method because it allows assessing the importance of each parameter in relation to the other variables based on the F statistics. (ii) This method also allows assessing the importance of all the variations by parameter on the energy demand for air conditioning.

The collinearity test is verified if all the variables have a VIF of less than 3 and a tolerance well above 0.2, see Table 4 below. The heteroscedasticity test is satisfied by applying White's test, see Table 5 below. Linearity and normality are also validated; see Figure A1-1 in Appendix A1.

Table 4 : Collinearity statistics

	Tolérance	**VIF**
Ac/Ah	1,000	1,000
Depth	1,000	1,000
Orientation	1,000	1,000

Table 5 : White's test for heteroskedasticity

Khi-carré	**ddl**	**Signification**
27,000	26	**0,409**

The results of the modelling of energy demand for air conditioning gave us an explanatory model with 99.6% accuracy. The details of the model are presented in Table 4 below and the comparison in terms of effect on energy demand is developed from F statistics and the estimated marginal mean of each parameter, see Figure 6 below.

Table6 : Summary of the univariate linear model.

Source	**Somme des carrés de type**	**ddl**	**Carré moyen**	**F**	**Signification**
Corrected model	544,526[a]	18	30,251	101,166	0,000
Constant	1888,609	1	1888,609	6315,804	0,000
Ac/A_h	52,822	2	26,411	88,322	0,000
Depth	230,550	2	115,275	385,498	0,000
Orientation	201,161	2	100,581	336,358	0,000
Ac/A_h * Depth	14,623	4	3,656	12,225	0,002
Ac/A_h * Orientation	17,671	4	4,418	14,774	0,001
Depth * Orientation	27,699	4	6,925	23,157	0,000
Error	2,392	8	0,299		
Total	2435,528	27			
Corrected total	546,918	26			
R^2 = ,996 (R^2 adjusted = ,986)					

Based on the values of F, it seems clear to us that depth is the most important followed by orientation combined with the shape of the courtyard and finally the scale of the courtyard Ac/Ah. See figure 3 below.

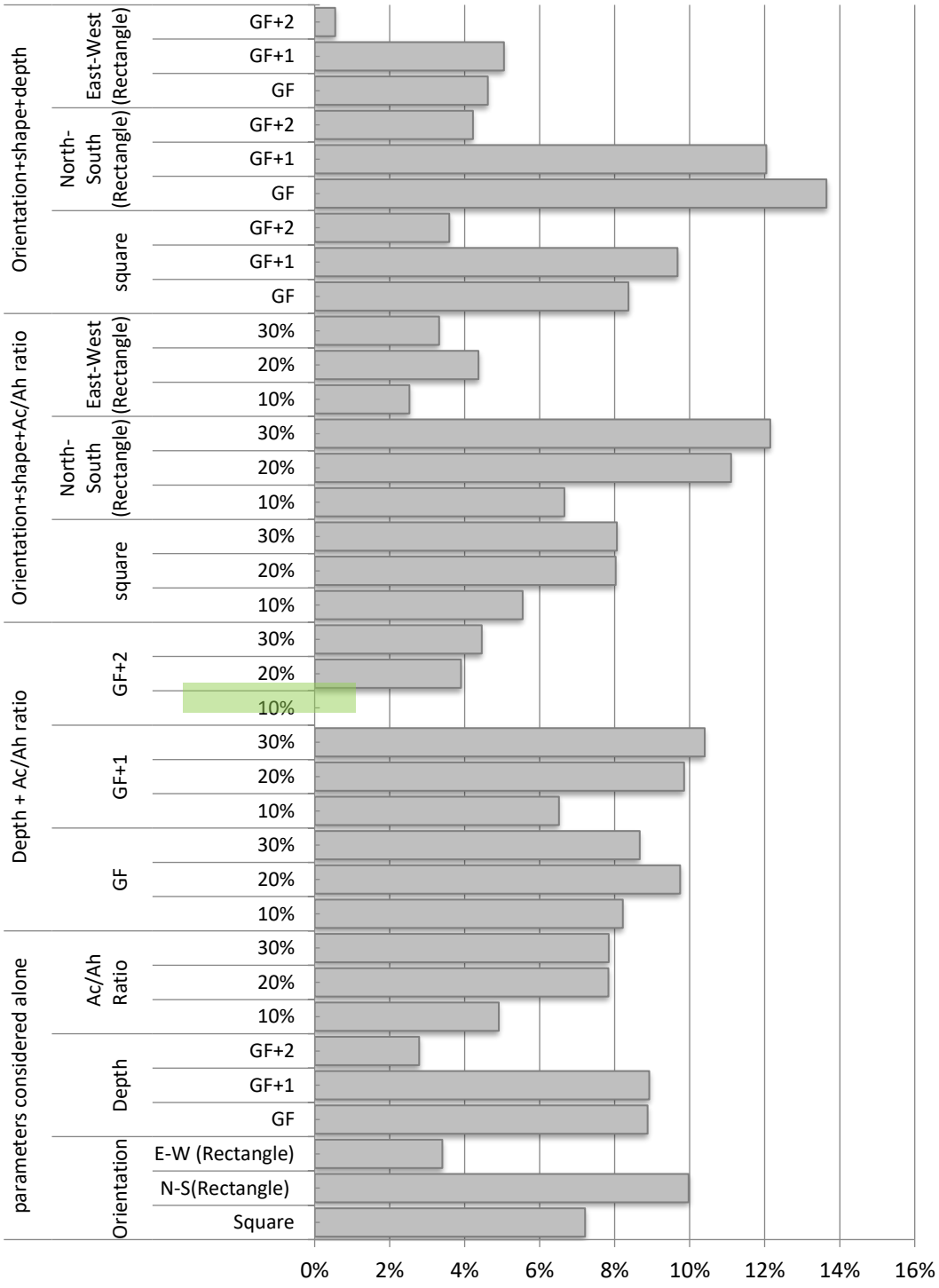

Figure 3: Impact of varying the influencing parameters on the energy demand for air conditioning. In green: the best case considered as a reference.

The impact of the parameters considered alone:
The parameter with the greatest impact on energy demand is the depth of the courtyard, an element which concords with the results of Akbar et al (2021) [24] and Solfei et al (2020) [32] because the best sunshade is achieved inside deeper courtyard. It achieves a performance 2.79% better than the reference case (combining depth with Ac/Ah), but with shallower depths (ground floor and first floor), energy demand rises to almost 9% compared with the reference case. In second place comes the orientation and shape of the courtyard. An east-west orientation of the courtyard axis combined with a rectangular shape, elongated on the same axis; is the best configuration and limits energy demand to 3.40% compared with the reference case. On the other hand, a north-south orientation, even with a rectangular shape, increases energy demand by almost 10%, as it also increases solar gain. The square shape of the courtyard also increases energy demand by almost 7% compared with the reference case. The size of the courtyard, expressed as an Ac/Ah ratio, comes in 4th place, and the most favourable case is a 10% opening with an increase in energy demand of almost 5% compared with the reference case. An opening of 20 and 30% of the courtyard surface will increase solar gains and the resulting energy demand to almost 8% compared with the reference case.

The impact of the courtyard's "depth and size" combination
This combination results in the most favorable case for reducing cooling energy demand, with a depth of GF+2 or 10.5m and a courtyard opening of 10%. The most unfavorable cases are obtained with courtyard opening of 20 to 30% and depths of ground floor to first floor. Energy demand rises to 10.40%. The depth and openness of the courtyard considerably reduces solar gain.

The impact of the "Orientation - shape and the size of the courtyard" combination
The rectangular shape combined with an east-west orientation of the courtyard axis and a 10% opening reduces energy demand by 2.53% compared with the reference case. And even with courtyard openings of up to 20 and 30%, energy demand remains virtually stable, increasing by only 4.3% and 3.7%, because the rectangular shape reduces solar radiation from the south-facing orientation. On the other hand, when the courtyard is elongated along the north-south axis, the opening of the courtyard is more detrimental to solar protection and increases energy demand by more than 12%.

The impact of the combination of orientation, shape and depth of the courtyard
With this combination, it is also possible to achieve the best configuration by combining a 10% courtyard opening with a depth of GF+2 and a rectangular shape elongated along the East-West axis. On the other hand, a North-South orientation of the courtyard axis considerably reduces solar protection and increases the energy demand for air conditioning by almost 15%. The square shape is sensitive to the depth of the courtyard and increases energy demand by up to 9.6% compared to the reference best case.

The results obtained in the present study support the results obtained by other researchers and by the application of other sensitivity analysis methods in the arid regions, as demonstrated by De la Flor et al (2021) [28] and Diz-Mellado et al (2023) [29], Solfei et al (2020) [32] and Akbari et al (2021) [24]. The findings suggest that deep, narrow courtyards are better adapted to warmer climates and the orientation of the courtyard performs well with rectangular east-

west elongated courtyards. The explanation for these results lies in two factors, the first is the solar radiation, which is more direct in shallow courtyards and the second is the thermal layering that happens inside the courtyard.

5 Conclusion

The courtyard, as an element of architectural design, has emerged as a regulator of comfort in vernacular houses. This paper examines the importance of the courtyard's influencing geometry parameters on the energy demand for air conditioning. The method of analysis is based on univariate linear regression modelling applied to the results of 27 dynamic thermal simulations. The results show that the geometrical parameters with the greatest impact are the depth of the courtyard, followed by the orientation and shape of the courtyard, and finally the size of the courtyard. The rectangular shape of the east-west-facing courtyard reduces solar gain, and even with a larger courtyard opening, energy demand varies only slightly. The North-South orientation, on the other hand, is very sensitive to the size of the courtyard and its depth, and constitutes the most unfavourable case, since it increases energy demand by more than 15% compared with the reference case.

In the present paper, the role of the courtyard geometry has only been considered for its role as a thermal regulator in the summer period, the winter period could provide ample information on the dimensioning of the influencing parameters. In addition, other parameters can influence the thermal regulation role of the courtyard, such as window to wall ration, envelope materials, the terrain relief, the oasis effect and the compactness of the urban form, as is generally the case in the *Ksours*, ancient cities in southern Algeria. Considering other parameters allow to generate some simple-to-use rules for architects to conceive better eco-friendly housings and limit the energy consumption and the greenhouse gas emissions.

References

[1] Gaillard, Clément. "L'approche énergétique de l'architecture vernaculaire: genèse et développement." *Socio-anthropologie* 42 (2020): 67-80

[2] Sénit, C. A. (2008). L'efficacité énergétique dans le secteur résidentiel: une analyse des politiques des pays du Sud et de l'Est de la Méditerranée. *IIddri, Idées pour le débat*, *14*.

[3] Boukarta, S., & Berezowska-Azzag, E. (2018). Assessing Households' Gas and Electricity Consumption: A Case Study of Djelfa, Algeria. *Quaestiones Geographicae*, *37*(4), 111-129.

[4] Chaker, M., (2023), Modélisation d'une symbiose urbaine bas carbone « Sur-BC » dans une perspective d'atténuation des émissions de GES à l'échelle locale à Alger. Thèse de doctorat, EPAU.

[5] APRUE. (2019), L'Agence Nationale pour la Promotion et la Rationalisation de l'Utilisation de l'Energie, La situation énergétique nationale, chiffre 2017, édition 2019.

[6] Hadji, F., Ihaddadene, N., Ihaddadene, R., Betga, A., Charick, A., & Logerais, P. O. (2020). Thermal conductivity of two kinds of earthen building materials formerly used in Algeria. Journal of Building Engineering, 32, 101823.

[7] KHELIFI L., Boukarta S,. BENSALEM R,. KEHILA Y., (2017). Le passage couvert comme régulateur socio-climatique dans le tissu traditionnel, Cas d'étude : le ksar de Timimoun (climat chaud aride). In Conférence Internationale sur les Matériaux, le Patrimoine et l'Environnement en Zones Arides. Université Ahmed DRAIA,

[8] Kitous, S., Bensalem, R., & Adolphe, L. (2012). Airflow patterns within a complex urban topography under hot and dry climate in the Algerian Sahara. *Building and Environment*, *56*, 162-175.

[9] Messaoudi, T. (2017, January). L'architecture vernaculaire une solution durable : Cas de la maison traditionnelle kabyle (nord algérien). In *Les 4ème RIDAAD*.

[10] Boukarta, S. (2021). Exploring the impact of balconies on cooling energy demand in an arid climate zone. *Selected Scientific Papers-Journal of Civil Engineering*, *16*(2), 25-35.

[11] Boukarta, S. (2023). Impact of Passive Design Strategies on Environment, Cooling and Lighting Energy Demand. A Weighted Least Squares-Based Approach. *Selected Scientific Papers-Journal of Civil Engineering*, *18*(1).

[12] Oliver P., (2003). Dwelling: The House across the world. Oxford: Phaidon Press Ltd.

[13] Abdulac, S. (1982). Traditional housing design in the Arab countries. Paper presented at the urban housing. Proceedings of the second seminar... Harvard, august 17-21, 1981

[14] Abass, F., Ismail, L. H., & Solla, M. (2016). A review of courtyard house: history evolution forms, and functions. *ARPN Journal of Engineering and Applied Sciences*, *11*(4), 2557-2563.

[15] Al-Azzawi, S. (1994). Indigenous courtyard houses: A comprehensive checklist for identifying, analysing and appraising their passive solar design characteristics Regions of the hot-dry climates. Renewable energy, 5(5), 1099-1123.

[16] Schoenauer N., & Seeman S., (1962). The court-garden house: McGill University Press Montreal.

[17] Edwards, B. (2006). Courtyard housing: past, present and future: Taylor & Francis.

[18] Tablada, A., Blocken, B., Carmeliet, J., De Troyer, F., & Verschure, H. (2005). Geometry of building's courtyard to favour natural ventilation: Comparison between wind tunnel experiment and numerical simulation.

[19] Meir, I. A., Pearlmutter, D., & Etzion, Y. (1995). On the microclimatic behavior of two semi-enclosed attached courtyards in a hot dry region. *Building and Environment, 30*(4), 563-572.

[20] Bagneid, A. (2006). The creation of a courtyard microclimate thermal model for the analysis of courtyard houses (Doctoral dissertation, Texas A&M University).

[21] Omrani, M., Lian, Z., & Xuan, H. (2019, August). Effects of the courtyard's geometry in dig pit underground dwellings on the room's daylighting performance. In *Building Simulation* (Vol. 12, pp. 653-663). Tsinghua University Press.

[22] Ferrari, S. (2022). Ventilation in a group of courtyard buildings. In *EPJ Web of Conferences* (Vol. 264, p. 01014). EDP Sciences.

[23] Zhu, J., Feng, J., Lu, J., Chen, Y., Li, W., Lian, P., & Zhao, X. (2023). A review of the influence of courtyard geometry and orientation on microclimate. *Building and Environment*, *236*, 110269.

[24] Akbari, H., Cherati, S. M., Monazam, N. H., & Noguchi, M. (2021). Effect of courtyards' geometrical parameters on climate adaptability and shading performance in hot-arid climate of Yazd (Iran). *Sustainable Energy Technologies and Assessments*, *48*, 101594.

[25] Aldawoud, A. (2008). Thermal performance of courtyard buildings. *Energy and Buildings*, *40*(5), 906-910.

[26] Martinelli, L., & Matzarakis, A. (2017). Influence of height/width proportions on the thermal comfort of courtyard typology for Italian climate zones. *Sustainable Cities and Society*, *29*, 97-106.

[27] Yaşa, E., & Ok, V. (2014). Evaluation of the effects of courtyard building shapes on solar heat gains and energy efficiency according to different climatic regions. *Energy and Buildings*, *73*, 192-199.

[28] e la Flor, F. J. S., Ruiz-Pardo, Á., Diz-Mellado, E., Rivera-Gómez, C., & Galán-Marín, C. (2021). Assessing the impact of courtyards in cooling energy demand in buildings. *Journal of Cleaner Production*, *320*, 128742.

[29] Diz-Mellado, E., Ruiz-Pardo, Á., Rivera-Gómez, C., de la Flor, F. J. S., & Galán-Marín, C. (2023). Unravelling the impact of courtyard geometry on cooling energy consumption in buildings. *Building and Environment*, *237*, 110349.

[30] Tabadkani, A., Aghasizadeh, S., Banihashemi, S., & Hajirasouli, A. (2022). Courtyard design impact on indoor thermal comfort and utility costs for residential households: Comparative analysis and deep-learning predictive model. *Frontiers of Architectural Research*, *11*(5), 963-980.

[31] Seddik Hassan, A. M., Abd El Aal, R. F. A., Fahmi, A. A. E., Ali, S. M. A., & Abdelhady, M. I. (2024). Courtyard geometry's effect on energy consumption of AlKharga city residential buildings, Egypt. *Scientific Reports*, *14*(1), 11149.

[32] Soflaei, F., Shokouhian, M., Tabadkani, A., Moslehi, H., & Berardi, U. (2020). A simulation-based model for courtyard housing design based on adaptive thermal comfort. *Journal of Building Engineering*, *31*, 101335.

Appendix A1

Table A1-1 : Some examples of courtyard configurations.

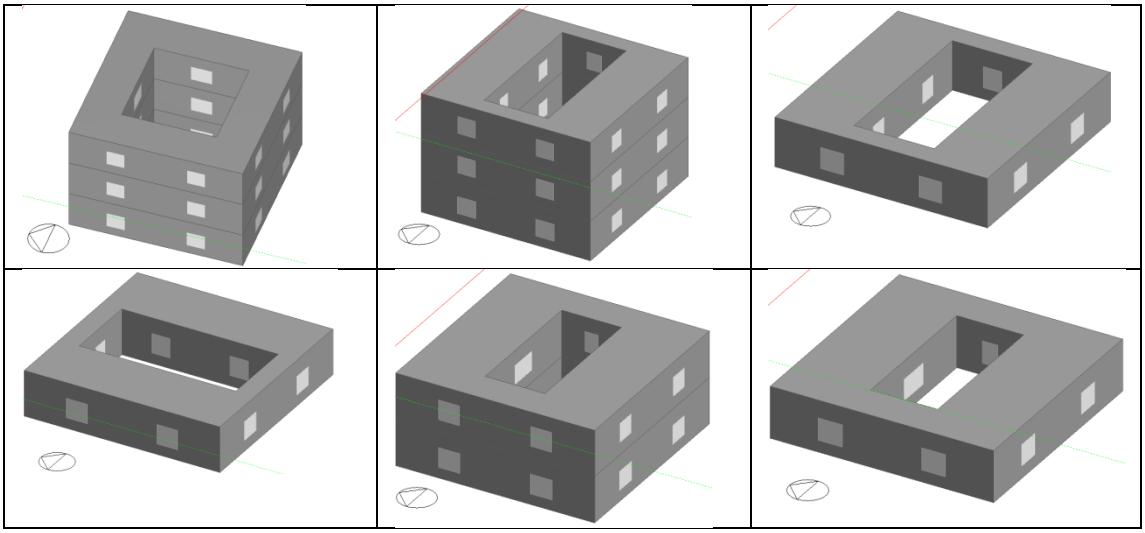

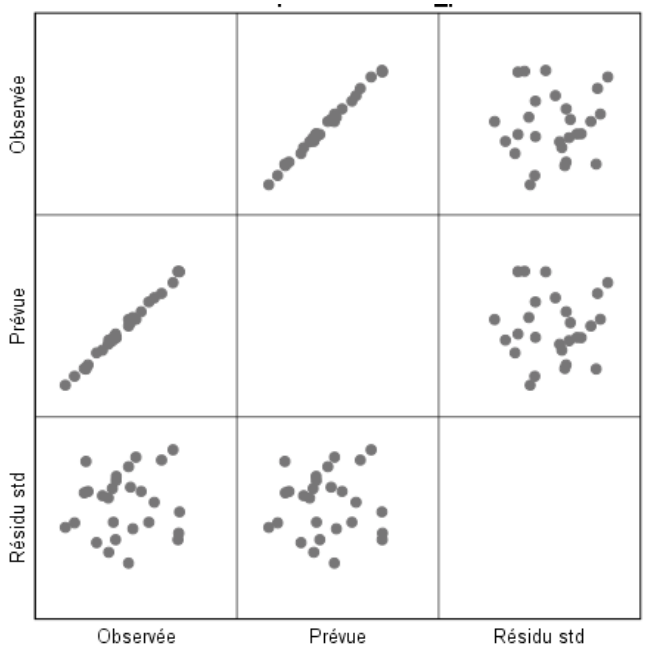

Figure A1-1 : QQ plot and comparison between simulated results and those obtained by the model

DOI: 10.2478/sspjce-2024-0011

Optimal Treatment Methods for Anti-Tartar Management in Circulating Water Systems

Kherouf Mazouz

University of 8 May 1945, Guelma, Algeria, BP 401 Guelma 24000 – Algeria
Faculty of Science and Engineering, Civil Engineering and Hydraulic Department, Guelma, Algeria
e-mail: kherouf.mazouz@univ-guelma.dz

Abstract

Utilizing seawater in industrial water systems leads to scale formation on heat exchange surfaces, reducing efficiency significantly. Even a 1 mm deposit causes a 30% decrease in effectiveness, raising cooling or condensation temperatures by 6°C and increasing electrical power consumption by 18%. Preventive measures include chemical treatments, which require careful balancing to avoid corrosion risks, and physical treatments like magnetic or electronic conditioners, which vary in efficacy. Water softening replaces metals with sodium ions but may increase mineral content, exacerbating scale buildup. Corrosion control is essential to counter metal degradation. Balancing prevention strategies is crucial. Research explores using Mediterranean seawater in cyclic systems to conserve freshwater and enhance coastal water availability. The aim is to find economically viable methods to stabilize cooling systems for both soft and saline water.

Keywords: corrosion control, heat exchangers, seawater, tartar formation, water industry.

1 Introduction

Water scarcity is a global concern exacerbated by increasing demand, particularly in industrial sectors. The demand for water is projected to double in the next two decades, underscoring the urgency of addressing water availability challenges [1, 2]. In Algeria, where water access remains a critical issue, water resources play a pivotal role in supporting economic and social development [3]. The industrial water supply is essential for maintaining the functionality and product quality of industrial facilities [4, 5]. However, utilizing seawater in industrial processes poses significant challenges due to its chemical composition, which leads to scale formation and corrosion on equipment surfaces [6, 7]. To address these challenges, various methods have been developed to improve seawater's technological characteristics and mitigate scale formation and corrosion [6, 7].
Water scarcity also impacts industrial water consumption globally, necessitating the adoption of water recycling practices [8, 9]. However, water recycling often exacerbates scale formation on equipment surfaces, reducing thermal efficiency and operational performance [10, 11]. To mitigate scale formation, water treatment agents particularly synthetic phosphorus-free scale

inhibitors have gained popularity for their effectiveness and stability [12, 13]. Traditional water treatment agents, such as inorganic salts and synthetic phosphine organic compounds, are limited by environmental concerns [14, 15]. While natural polymers are affordable, they require large quantities and lack stability at high temperatures [16]. Consequently, synthetic phosphorus-free scale inhibitors represent a promising alternative for effective scale inhibition in industrial water recycling systems [13, 16].
This article investigates various methods for stabilizing cooling water, whether soft or saline (Table 1), to identify a simple and efficient approach. Experimental studies were conducted to evaluate these methods and assess the feasibility of using seawater in industrial water distribution systems.

Table 1: Salinity and chemical composition in % comparison [17]

Designation	Salinity (g/l)	Chloride (Cl^-)	Sodium (Na^+)	Magnesium (Mg++)	Sulfate (SO_4^{2-})	Calcium (Ca^{++})	Potassium (K^+)	Bicarbonate (HCO_3^{--})
Sea Mediterranean	37.0	55.1	0.2	7.9	0.2	30.6	1.1	1.2
Soft water	1.5	25.1	-	25.1	-	5.01	-	10

2 Methods

2.1 Methods to combat tartar formation

Typically, two methods are employed for stabilizing water circulated within industrial systems:
- Chemical methods,
- Physical methods.

Chemical methods include acidification, decarbonation, phosphatation, the use of surfactant agents, and combined methods (such as phosphatation with acidification, etc.). However, there is a current trend towards methods that don't involve chemical agents, such as physical methods like ultrasonic treatment, and the application of magnetic and electric fields.
Among these chemical methods, acidification is commonly employed, with the principle as follows:

2.1.1 Acidification

To prevent the formation of tartar on heat exchange surfaces, sulfuric acid (H2SO4) or hydrochloric acid (Hcl) is utilized. During the acidification of circulating water, a portion of the bicarbonate salts converts into an equal quantity of non-bicarbonate salts that are easily soluble. This process involves the following reactions:
- The reduction of bicarbonate concentration in water leads to a decrease in the required level of carbon dioxide.
- The release of carbon dioxide during chemical reactions aids in stabilizing remaining bicarbonates in the water after acidification.

The acidification method is applicable to all types of natural waters.
According to Koutcherenko, acidification allows for the reduction of soft water quantity (balance water). During cyclic water treatment, determining the optimal dosage of acid is

crucial, and it depends on the alkalinity of the water. Specifically, the concentration of acid will be adjusted based on the reduction in water alkalinity and stabilization conditions.
Currently, acidification is a common method, but it comes with certain drawbacks such as difficulty in dosing under natural conditions and the potential for acid-induced metal corrosion. The dosage of acid (mg/l) can be calculated using the Koutcherenko [18] formula (1):

$$D_a = e\left(A_{ap} - \frac{A_{cir}}{K_{cs}}\right)\frac{100}{C_a} \quad (1)$$

Where:
Da: the concentration of acid in the technical acids of it %;
e: represents the equivalent mass of the acid (in mg/meq), for sulfuric acid e = 49;
Aap: denotes the alkalinity of the balance water (in meq/l);
Acir: signifies the alkalinity of the circulation water (in meq/l);
Kcs: stands for the coefficient of salt concentration

2.2 Objectives and applied study focus

The applied studies aim to assess the rate of tartar formation on heat exchange surfaces and the balance water dosage. The specific goals of these studies include:
- Investigating the influence of temperature within the cyclic system on tartar formation speed,
- Analyzing the impact of hydraulic regime variations on tartar formation speed,
- Evaluating the effect of pH levels in acidified seawater solutions on tartar formation speed when using the acidification method.

2.3 Factors influencing scaling processes in cooling systems

The process of scaling is influenced by various complex physicochemical phenomena occurring within the cyclic system. Factors affecting both qualitative and quantitative aspects of scaling include:
- Chemical composition of Mediterranean seawater,
- Turbidity of the water,
- Temperature variations,
- Carbon dioxide (anhydride) content in the water and its loss during the cooling process,
- Hydraulic and thermal regime of the cooling water system operation,
- Quantity of balance water used.

For a comprehensive understanding of scaling processes, it is essential to consider all these factors. However, practical limitations in laboratory settings often necessitate simplification of the methodology in applied studies.

2.4 Description of the Experimental Setup

The schematic diagram of the laboratory setup, as illustrated in Figure. 1, is designed as follows: An electric thermostat (1) is utilized to maintain the temperature within the range of 40 to 45°C, simulating typical industrial cooling temperatures. Water is drawn from the feeding reservoir (2) using a pump and circulated back into the same reservoir to maintain a closed-loop cyclic system. Within this reservoir, another vessel (3), constructed of organic glass, contains test

samples made of steel (5) to mimic materials used in industrial settings. Temperature regulation is monitored by a contact thermometer (4).
For acidification treatment, a valve-equipped vessel facilitates two modes of operation: continuous and discontinuous addition of balance water. The quantity of balance water, representing a percentage of seawater, varies between 1.24 % and 1.96 % of the total balance of seawater used.

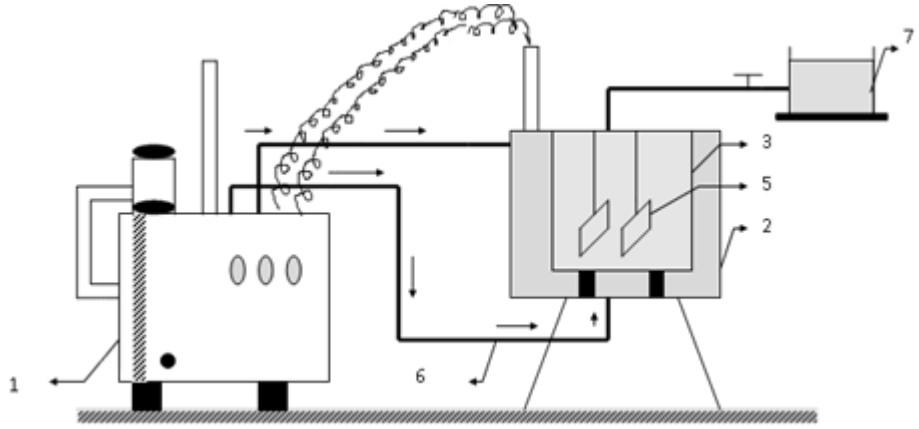

Figure 1: Experimental setup diagram

Legend:
1. Electric thermostat; 2. Reservoir for maintaining the temperature of seawater desalination; 3. Seawater accumulation reservoir; 4. Contact thermometer; 5. Testing samples; 6. Circulation system for the heat exchange agent; 7. Balanced water accumulation reservoir.

3 Results and discussion

3.1 Influence of temperature on tartar formation intensity

Experiments were conducted at temperatures of 40°C and 45°C under continuous and discontinuous regimes of balance water addition. The rate of tartar formation was determined using gravimetric methods, with test plates dried in an electric oven at 105°C until reaching a constant weight. The following table illustrates the tartar formation speed for the discontinuous regime at various temperatures (Tables 2 and 3):

Table 2: Influence of temperature on tartar formation intensity

Temperature (°C)	Time of operation (hours)	Intensity of Tartar Formation (mg/cm².year)	Alkalinity (meq/l)	HCO_3 Concentration (mg/l)
35	27	337.6	3.5	212.2
40	27	460.5	3.0	183.0
45	27	567.9	2.5	152.5

The results indicate that increasing the temperature in the cyclic system leads to a corresponding increase in tartar formation intensity (Figure 2). Additionally, as shown in the table, the concentration of bicarbonate ions (HCO_3) decreases with rising temperatures, explaining the observed increase in tartar formation speed due to decreased alkalinity of the seawater.

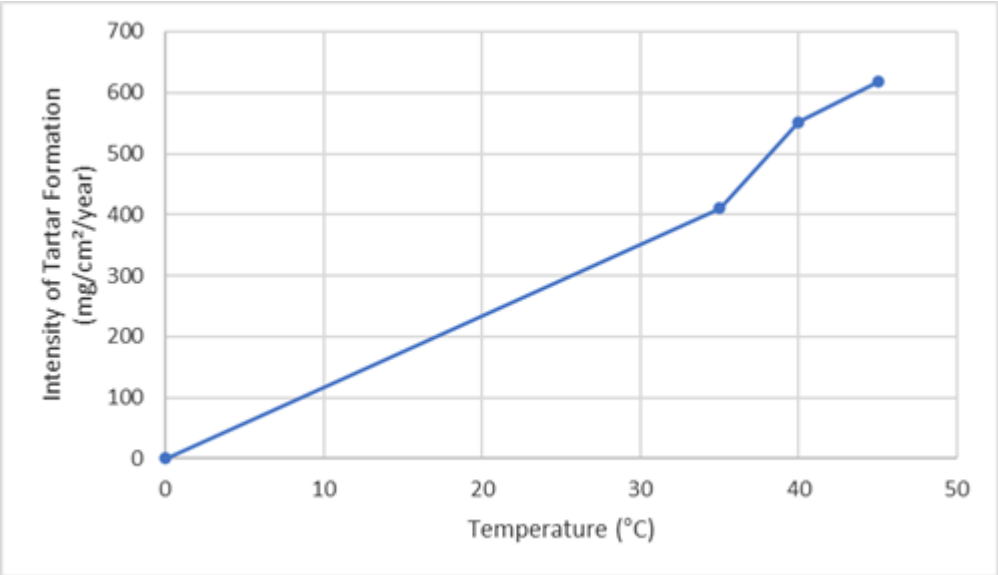

Figure 2: Influence of temperature on the intensity of tartar formation

3.2 Influence of hydraulic regime on tartar formation

Experiments were conducted under continuous and discontinuous regimes of balance water addition. The continuous regime involves a steady addition of balance water, while the discontinuous regime entails periodic addition every 6 hours. The following table (Table. 3) illustrates the variation in tartar formation speed at temperatures of 40°C and 45°C under the continuous regime:

Table 3: Influence of hydraulic regime on tartar formation

Temperature (°C)	Time of operation (hours)	Intensity of tartar formation (mg/cm²/year)	Alkalinity (meq/l	HCO3 Concentration (mg/l)	Final pH
35	27	490.7	3.2	172.6	5.2
40	27	551.8	3.0	183.0	4.8
45	27	617.6	2.7	195.2	4.5

The results (Figure 3) indicate that increasing the temperature of the circulating water enhances the intensity of tartar formation under both balance water addition regimes. However, the rate of tartar formation is more gradual under the continuous regime compared to the discontinuous regime. This can be explained by the continuous increase in salt concentration under the continuous regime, leading to reduced alkalinity as temperature rises.

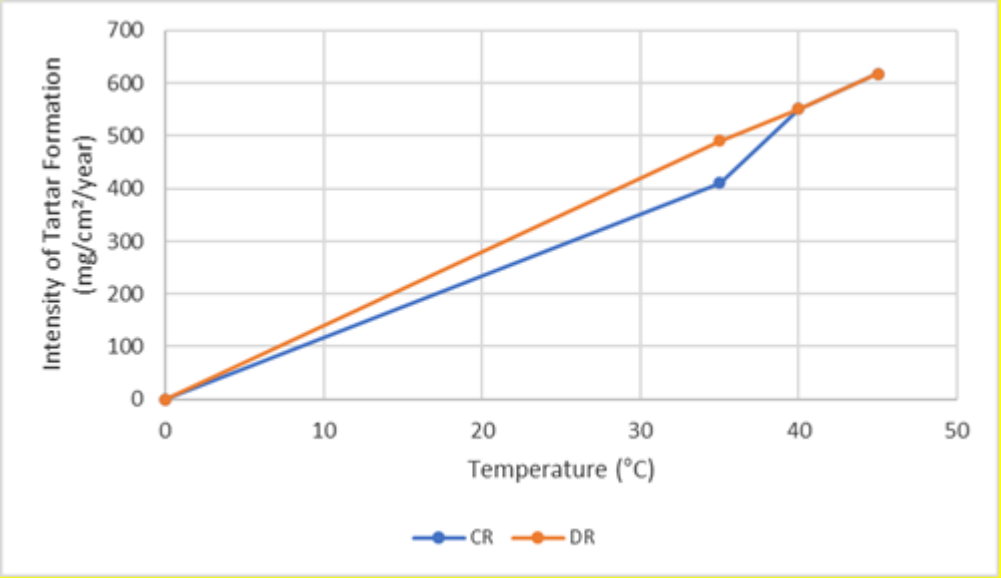

Figure 3: Influence of hydraulic regime on tartar formation

3.3 Influence of pH of circulating water

Experiments were conducted under continuous regime conditions using varying doses of sulfuric acid. Table 4 below illustrates the results:

Table 4: Influence of pH on Circulating Water in Scaling Processes

T (°C)	pH of Balance Water	Time (h)	Intensity of Tartar Formation (mg/cm²/year)	Intensity of Corrosion (mg/cm²/year)	pH of Circulating Water	Alkalinity (meq/l)	HCO_3 Concentration (mg/l
40	4.0 5.2 6.0 7.9	19 19 19 27	91.5 122.6 242.0 551.8	578.0 402.9 198.7 -	8.3 9.2 9.3 4.8	1.5 2.8 2.6 2.7	91.6 170.8 156.6 195.2
45	3.0 6.0 7.9	19 19 27	166.4 268.6 617.6	631.2 335.8 297.8	6.8 9.2 4.5	2.0 3.0 2.7	122.0 183.0 195.0

The analysis (Figure 4) reveals that increasing the acid dose in the balance water reduces the intensity of tartar formation but concurrently accelerates corrosion speed. To counteract corrosion, corrosion inhibitors are introduced. At a balance water pH of 4 and a circulating water temperature of 40°C, the tartar formation intensity is minimal, measuring 0.1 mg/cm²/year.

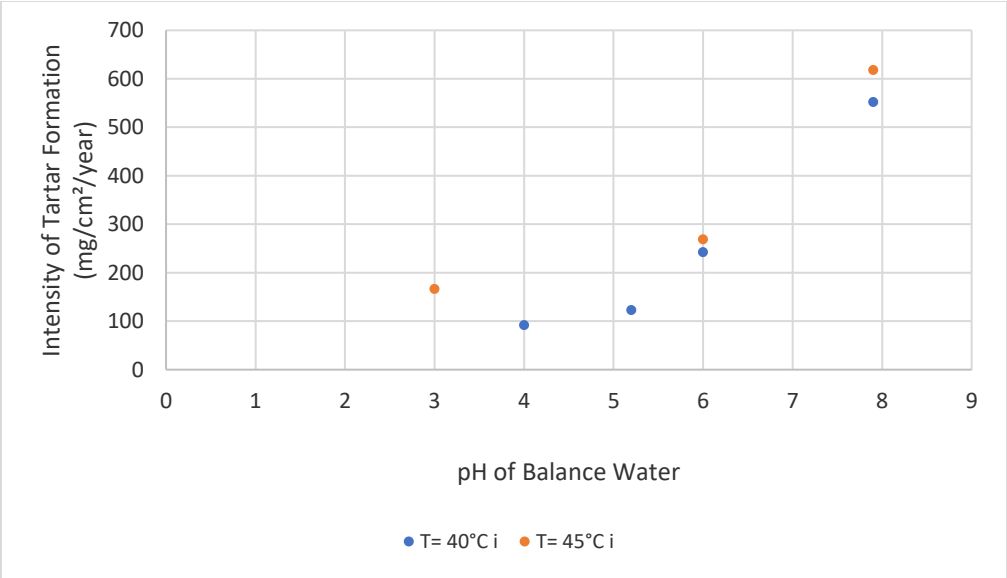

Figure 4: Influence of pH on circulating water and tartar formation

Increasing the acid dose indeed accelerates corrosion speed. However, a dose corresponding to a pH of 5.5 effectively controls corrosion for both temperatures. To practically address this issue, corrosion inhibitors are added (Figure 5).

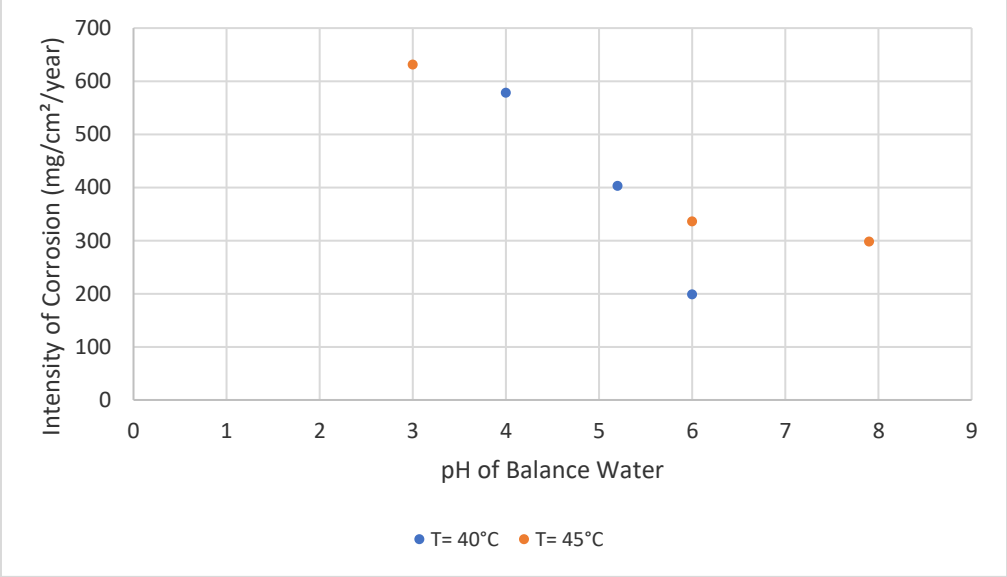

Figure 5: Influence of pH on circulating water and corrosion intensity

4 Conclusion

In conclusion, the findings of this study suggest that seawater could serve as a viable alternative to soft water in industrial and network circuits. However, its effective utilization requires

comprehensive anti-scaling and anti-corrosion treatments. Various techniques can achieve these desired results, but they must be evaluated not only based on their efficacy but also on cost-effectiveness and environmental impact.

Experimental results demonstrate that employing an acid dose corresponding to a pH of 4 for balanced water significantly reduces scaling by a factor of six compared to untreated water. The acidification method proves effective due to its use of inexpensive reagents, minimal equipment requirements, straightforward implementation, ease of treatment control, and minimal additional pollution.

However, this method does have drawbacks. Treated water tends to become corrosive due to its lowered pH, the liberation of CO_2, and increased salt content at elevated temperatures. Consequently, anti-corrosion treatment, coupled with decarbonation, becomes imperative, albeit at an increased cost. Careful dosing of strong acids is essential to mitigate potential adverse effects.

Comparatively, physical methods such as ultrasonic treatment show promise in reducing scaling. However, the mechanisms underlying their effectiveness remain poorly understood. Additionally, they pose potential health risks to personnel due to the operation of ultrasonic generators.

Overall, this investigation demonstrates that seawater can be integrated into industrial water distribution systems, particularly when adequate technical expertise is available for water treatment. The choice of treatment method ultimately depends on the specific characteristics of the water and the proficiency of the personnel managing the system. Therefore, the selection of a suitable process should be based on a thorough evaluation of all relevant factors.

Acknowledgments

The authors very much appreciate the support by the university 8 May 1945 Guelma, Algeria and Ministry of Higher Education and Scientific Research.

References

[1] Jones, A. (2019) Global Water Supply Trends: Challenges and Solutions. *Journal of Water Resource Management, 15(2), 101-115.*

[2] Smith, B. et al. (2022) Trends in Industrial Water Usage and Solutions for Sustainability. *Environmental Engineering Journal, 28(4), 301-315.*

[3] Algerian Ministry of Water Resources. (2023) Current State and Future Prospects of Water Resources in Algeria. *Algerian Water Journal, 10(3), 45-56.*

[4] Johnson, C. et al. (2020) Challenges and Solutions in Seawater Usage for Industrial Applications: A Review. *Marine Engineering Review, 25(1), 78-92.*

[5] Nguyen, T. et al. (2017) Methods for Improving Seawater Quality for Industrial Use: A Comparative Study. *Journal of Industrial Water Treatment, 12(3), 201-215.*

[6] European Commission. (2021) Best Practices for Seawater Desalination and Industrial Water Treatment Brussels: European Commission Publications

[7] World Health Organization (2016) Guidelines for Drinking-water Quality: Incorporating First Addendum. Geneva: World Health Organization Press.

[8] Aryal, A. Thapa, B.R. Poudel, et al. (2022) Effective biosorption of arsenic from water using La (III) loaded carboxyl functionalized watermelon rind. *Arab J Chem., 15 (2022), p. 10364*. DOI: 10.1016/j.arabjc.2021.103674.

[9] Zabihi, S. Jamshidian, R. Soltani, et al 2021 In Situ Polymerized FDU-12/Poly (methyl methacrylate. *Chem. Eng. Technol., 44 (3) (2021), pp. 431-440*. DOI:10.1002/ceat.202000298.

[10] I.K. Basha, E.M. El-Monaem, R.E. Khalifa, et al. (2022) Sulfonated graphene oxide impregnated cellulose acetate floated beads for adsorption of methylene blue dye: optimization using response surface methodology. DOI: 10.1038/s41598-022-13105-4.

[11] F. Zareia, A. Marjani, R. Soltania. (2019) Novel and green nanocomposite-based adsorbents from functionalised mesoporous KCC-1 and chitosan-oleic acid for adsorption of Pb (II). *Euo Polym J., 119, pp. 400-40*. DOI: 10.1016/j.eurpolymj.2019.07.043.

[12] D. Zeng, T. Chen, S. Zhou. (2015) Synthesis of Polyaspartic Acid/Chitosan Graft Copolymer and Evaluation of Its Scale Inhibition and Corrosion Inhibition Performance.*Int. J. Electrochem. Sci., 10 (11), pp. 9513-9527.* DOI: 10.1016/S1452-3981(23)11197-7.

[13] Soltani, M. Pishnamazi, R. Pelalak, et al (2020) Preparation of COOH-KCC-1/polyamide 6 composite by in situ ring-opening polymerization: synthesis, characterization, and Cd (II) adsorption study. *J. Environ. Chem. Eng., 9, Article 104683*. DOI: 10.1016/j.jece.2020.104683.

[14] Al-Roomi, K.F. Hussain. (2015) Application and evaluation of novel acrylic based CaSO4 inhibitors for pipes. *Desalination, 355, pp. 33-44. H*. DOI: 10.1016/j.desal.2014.10.010

[15] Liu, Y.M. Zhou, J.Y. Huang, Q.Z. Yao, L. Ling, P.X. Zhang, C.E. Fu, W.D. Wu, W. Sun, Z.J. Hu. (2015) Acrylic acid-allylpolyethoxy carboxylate copolymer as an effective inhibitor for calcium phosphate and iron (III) scales in cooling water systems. *Clean-Soil. Air. Water., 43), pp. 989-994.*

[16] S. Dowlatshah, M. Saraji, M. Dinari. (2021) A novel nanocomposite based on covalent organic polymer and nanocellulose for thin film microextraction of imipramine from biological samples. *J. Sep. Sci., (44) (pp. 2972-2981*. DOI: 10.1002/jssc.202001245.

[17] Futura Sciences, Chemical Composition of Seawater. Futura Sciences. Available at: https://www.futura-sciences.com/planete/questions-reponses/terre-composition-chimique-eau-mer-18637/ (accessed: March 2020).

[18] Xinyu Guo, Jaspe Sumalangcay Christsam Joy, Yamin Cheng, Xiaowei Zhao, Zongyang Liu & Ying Xu. (2021) Scale Inhibitors for Industrial Circulating Water Systems: A Review. *Journal of Water*. DOI: 10.3103/S1063455X21060102.

DOI: 10.2478/sspjce-2024-0012

Rapid Measurements of Damaged Areas and Cavities Formed on Highways Caused by Heavy Rain Falls, Earthquakes or Similar Catastrophes

Syama P. Bhattacharya[1], Asis Ghosh[2*]

[1] Professor and Scientist., College of Science,
Howard University Washington D.C. and MEDT program, The University of Maryland, Baltimore city, U.S.A.
[2] Computer Science Engineer and Scientist. Department of Computer Science Engineering, West Bengal University of Technology, Kolkata, West Bengal, India.
[*]e-mail- asis.ghosh0@gmail.com

Abstract

An abnormal damaged area and the volume of a deep cavity formed underneath this area on a highway cannot be measured correctly by any of the existing methods. However, in this study Bhattacharya's theorem was applied for the measurement of an abnormal area with success. An abnormal volume of the cavity formed underneath of this damaged area was also measured by a newly proposed rule of volume measurement. The authors hope that the theorem and the rule described in this paper can be applied in the measurements of various abnormal damaged areas and cavities of highways for quick restoration of the spots. In fact the method of area measurements as well as the measurements of volumes of the cavities formed underneath the area can be done in the small or large scale if needed. Measurements of volumes by filling method of the cavities by foam beads however can be removed from the cavities quickly by an electric vacuum suction machine and the beads are reusable many times.

Keywords: flow materials, uniform density, foam beads, damaged area, abnormal volume

1 Introduction

Serious damages on the surface of highways are often noticed after heavy rain falls, earthquakes, or similar causes of disasters. As a consequence, people suffer from the acute problems in the traffic. In this situation immediate restoration of the damages is needful. Additionally, prompt estimation of the loss is also important. Normally the measurements of simple bended damaged areas are done according to any of the existing methods, such as: - graphical method, the mid ordinate rule, the average ordinate rule or Simpson's rule [1,2,3,5]. But correct measurements of complicated areas with many bends and deflections are difficult to perform, because no method is known to us at present. In the past famous scientists namely, Archimedes (287 B.C-212 B.C), Newton (1643), Pythagoras (6th century B.C.), Ptolemy (2nd century A.D.), Euclid (3rd century B.C.), Heron of Alexandria (dates unknown) etc gifted their

contributions in geometry of simple surface measurements but an accurate method for the measurements of complicated areas had never been reported. However a method was reported by Thomas Simpsons (1710-1761) which is presently a well-known method for the measurements of bended flat areas but Simpson's rule is sometimes difficult to apply when the areas appear to have many bends and deflections. Additionally, prolonged time is required to complete a measurement. As a matter of fact, a mathematical theorem has been reported recently based on Ghosh and Bhattacharya's principle which claims that correct measurements of all complicated areas are possible [2, 3, 6, 7]. The abnormal volumes of cavities formed on highways under the damaged areas can also be measured according to the newly proposed rule of volume measurements. The details of these measurements will be described in this paper

2 Methods and materials

Some special instruments were required for the study of alternative method of area and volume measurements such as: a photographic camera, a slide projector, a micro electric balance, a roll of polyethylene sheet (PES), a needle affixed with a pen which was connected with an electric heating device and a set of custom-made volume measuring containers. A damaged area on a highway was selected which was formed due to severe rainfalls followed by earthquake. Two photographs in the form of transparent slides were taken by a professional photographer from the appropriate high of a damaged area. One photographic slide was then projected vertically onto a large piece (40cm*60cm) of PES. This piece of PES was previously examined to confirm its special property of uniform density (2). This piece of PES was placed properly on a table and the bended curve line of the image of the damaged area was clearly focused on the PES. This image was then cut carefully and separated by an electrically heated needle. The cut piece was marked and weighed in an electric balance. This procedure was performed separately by an author and four surveyors. The average data were recorded in Table 1.

2.1 Measurements of the volume of a hollow space (cavity) formed underneath the damaged area of the road

After the area measurement was completed our next attempt was to measure the volume of the cavity. It was noticed that various forms of solid materials were present on the floor and some were attached on the walls of the cavity. So, this irregular shaped cavity was measured according to Bhattacharya's rule of volume measurement. This new rule claims that the volume of an irregular cavity (C) is directly proportional to the volume of filling material (fm) when its volume per unit mass is constant. This rule is briefly written as: $V_c \propto V_{fm}$ when the volume of (fm) per unit mass is constant. In this experiment three different types of materials were used separately as the fillers of the hollow space such as: water, dry sand and tiny beads of foam.

Water filling method:
In ancient time this method was originally invented by Archimedes (287 BC- 212 BC.). However this method is applicable only to measure the abnormal volumes by water displacement method as long as the sizes of the volumes are limited. We suspected that presence of invisible leakages inside the cavity. In spite of that we did this experiment rapidly and noticed

some loss of water was occurred during the fill up of the cavity. This procedure was considered to be simple as long as no leakage will be found in the cavity.
The water was evacuated by a pump machine. This was a lengthy and expensive procedure.

Dry sand filling method:
The damaged area was covered with a large piece of nylon cloth. Then strong packages made of nylon cloth were filled with known volumes of sand. These were dropped onto the cloth until the space was completely filled. Some known volumes of loose sand were used to cover the small spaces of the cavity. The total volumes of sand required to fill out the cavity were recorded which were considered as the volume of the cavity. Practically this procedure was easy and correct but long time was required to remove the sand from the cavity.

Foam beads filling method:
The large cavity was filled with known volumes of foam beads. This was an easy and prompt procedure for the measurements of abnormal volumes. These tiny beads were removed quickly from the cavity by suction device and were used repeatedly. These beads however do not absorb moisture and so its volume remained unchanged. This procedure cannot be used in windy weather. The tiny beads were extremely light which might scatter in all directions if it were handled carelessly, followed by pollution problem on the road. In spite of this simple problem, the authors considered this new procedure as a suitable method when many measurements were required to complete.

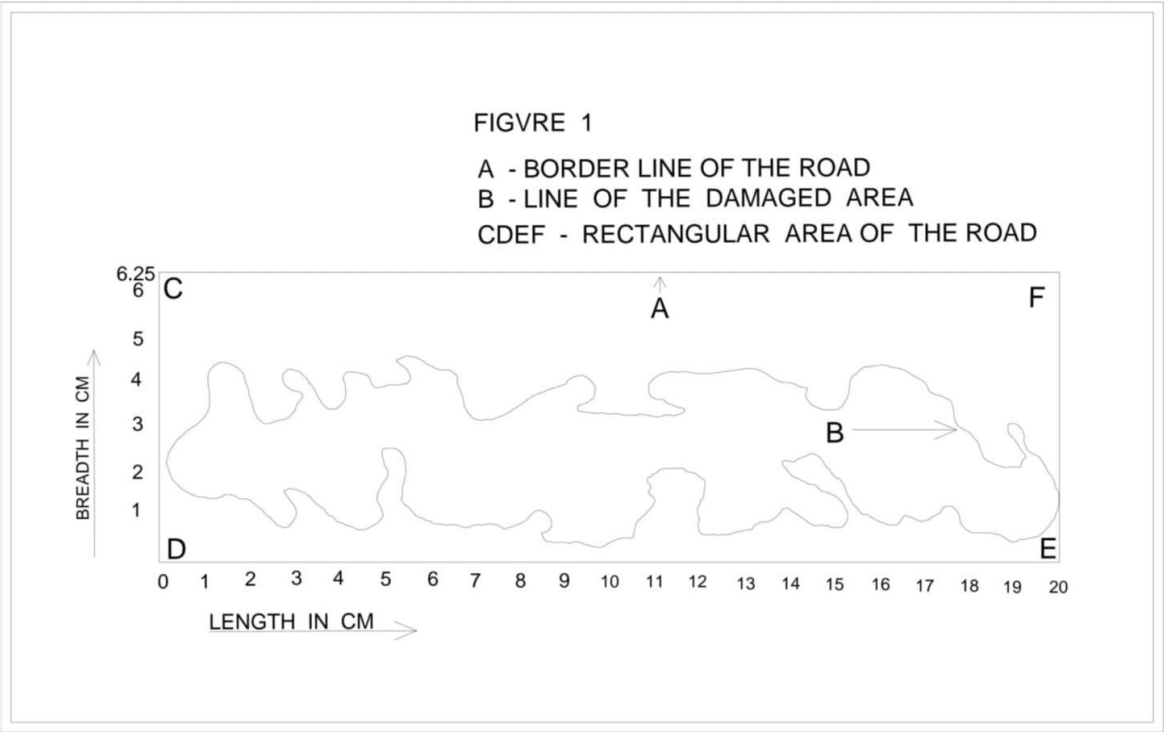

Figure 1: Diagram of the photographic image of the road including the damaged area. (Figure 1

indicates the irregular shape of the damaged area on the road. A = Border line of the road, B = Line of the damaged area, CDEF = A portion of the road (rectangular area)).

3 Results and discussion

Calculation of areas:

The measurements of the photographic images: The Gravitational weight (GW) of the piece of PES which was obtained from the photographic image of the rectangular area of the road including the damaged area= 0.92 gram (measured in a balance).

The GW of the piece of PES which was equivalent to the damaged area of the road only is 0.413 gram (measured in a balance).

The weight of 1 gram of PES= 1362 cm.

Hence, 0.92-gram PES will be equivalent to 136*0.92=1252 cm of PES. That is the area of the rectangular road including the damaged area.

The GW of the PES covering the damaged area only= 0.413 gram (determined by balance) which will be equivalent to 136*0.413=56.1682 cm.

Bhattacharya's Theorem is, I = W102 when I is the index and W is w1/w2, w1 = 0.413 gm weight of the photographic image of the bended area marked on PES and w2 = 0.92 gm weight of the image of the rectangular road marked on PES.

Therefore, W= 0.413/0.92 when expressed in percentage 0.413/0.92 * 100 = 44.9 % that is index I = 44. 9 % of the total area. (1)

Alternatively, we know 1 gm of PES = 1362 cm of PES

w1 = 0.413 gm of PES = 56.1682 cm of PES. w2 = 0.92 gm of PES = 1252 cm of PES. w1/w2 = 56.168/125 * 100 = 44.9 % = I (index). (2)

3.1 Calculation of the area of the road including of the damaged area at the original spot

This area was measured by a measuring tape and the following measurements were recorded:

The length of the area was measured = 320 cm and the breadth was 100 cm.The area should be 320*100 = 320002 cm

In the photographic image the area of a rectangle including damaged area was measured 1252 cm. Now if we divide 32000/125, we obtain 256. So the original spot area would be 256 times bigger than the area of the photographic image. The damaged area on the spot will be 56.25*256 = 144002 cm.

In Summary: Total original area of the road including the damaged area is 320002 cm and only the damaged area is 144002 cm.

Calculation of the volume of the cavity:

We know the area of the abnormal damaged portion is 144002 cm. In order to measure the volume accurately a custom made large plastic measuring container was used which was capable to measure 30 cm3 of flow material. The number of times of 30 cm3 of flow material which were required to fill out the cavity was recorded in table 2.

4 The statistical procedure

The standard deviation of the means and t-test for the significance at the level $P < 0.5$ were determined adopting the procedure described in SPSS Computer program. (4)

Table 1: Measurements of a damaged area on a highway. Data are expressed in square centimeter ± SD of the mean

Measurements of the photo images		**Direct measurements of the original spots**	
A rectangular portion of the road including damaged area. 125^2 cm ±1.8	The damaged portion of the road 56. 25^2 cm ±0.7	A rectangular portion including damaged area 32000^2 cm ±00	The damaged portion of the road * 14400^2 cm ±2.5

* Calculated from the data of photo image.

Table 2: Direct measurements of the hollow space formed underneath the damage area on a highway. Data are expressed in cubic centimeters ± SD of the mean.

Materials used to fill the hollow space.	Time required to completing the task in minutes.	Volumes of material required to fill the hollow space in cubic cm.	Remarks

Water	14.5 $\pm$1.8	58*30 $\pm$4.7 cm^3	This method is not applicable if there is any leakage present in the cavity. If water is found mixed with dirt cannot be reused. The data indicate the presence of an invisible leakage in the cavity.
Dry sand	16.2 $\pm$2.5	49.8*30 $\pm$1.9 cm^3	This is also an accurate method, but it is a lengthy procedure and costly. Complete evacuation from the cavity is possible and the sand can be reused.
Foam beads (pea shaped)	11.8 $\pm$2.7	47.5*30 $\pm$2.1 cm^3	This is an accurate, prompt and inexpensive method, but difficult to work in windy weather. Complete evacuation is easy by an electric vacuum suction method and the beads are reusable number of times.

5 Discussion

In our previous study we discussed in details about a correct method for the measurements of all kinds of abnormal areas. We used Bhattacharya's theorem for rapid determination of these areas (1,6). In this study we applied the same alternative procedure and were able to determine a damaged area on a highway which was noticed after a violent catastrophe. In this study we have included a new method of volume determination of an abnormal cavity which was found to exist underneath the same damaged area.

In reference to the volume measurement of abnormal cavities on highways some investigators believe that Ground Penetrating Rader (GPR) can be used for this purpose. We strictly object to this idea because GPR can only locate the hidden cavities if formed underneath a highway but unable to measure the exact volume. Therefore, we tried three different techniques to determine the abnormal volume of the cavity. We recorded nearly correct results of this volume measurement which was based on the concept of fill out the cavity with known volumes of filling material. When the area and the volume of a damaged portion of a road were known we were able to calculate the cost for restoration of the road. It is expected that not only the

highways but also many spots of similar problem can be found in many other locations, such as: front and back yards of buildings, run ways of airports, playgrounds, rail road's, sea ports, coal mines and many other important locations. We hope that authorities of municipalities, corporations and even astronauts may be interested to use these techniques for rapid measurements of damaged locations. In summary, the innovations mentioned in this paper are: Rapid measurements of abnormal areas from the photo images and measurements of volumes by filling method of the cavity by selected filling material such as foam beads. These beads however can be removed from the cavity quickly by an electric vacuum suction machine and the beads are reusable many times.

6 Conclusion

All types of damaged areas on highways can be determine by the application of our newly developed theorem I=W102. The method is prompt, easy, economic and accurate in comparison to other existing methods. The novel idea of this study is that the determination of gravitational weight of the portion of a paper occupied by the photographic image of the damaged area can be converted to an area in square centimeters of the same portion of the paper and by applying simple method of calculation.

In addition to the determination of damaged area the volume of the cavity which was formed underneath the damaged area was measured on the concept of fill out the cavity with the known volume of filling material, such as foam beads. The authors hope that the theorem and the rule can be applied in various types of damaged areas as well as abnormal cavities for quick restoration of the spots.

Acknowledgments

The authors are indebted to the photographer and technical experts who assisted them in various aspects of this study.

References

[1] Basak, N. N. (2017). *Surveying and leveling* (2nd ed.). Tata McGraw Hill Education Private Limited.

[2] Bhattacharya, S. P., & Ghosh, A. (2018). An observation on the interrelationship between the gravitational weight and the area of a flat sheet: A new concept of rapid measurement of areas bended by irregular outlines. *International Journal of Mathematics and Its Applications*, 6(4), 13–20. https://doi.org/10.1234/56789

[3] Ghosh, A., & Bhattacharya, S. P. (2019). Does the gravitational weight vary with the area of a flat sheet? A comparative study of area measurements: With special references to Simpson's rule and Bhattacharya's theorem. *Russian Journal of Mathematical Research. Series A*, 5(1), 10-15. https://doi.org/10.1234/56789

[4] Nie, N. H., Hull, C. H., Jenkins, J. G., Steinbrenner, K., & Bent, D. H. (1975). *Statistical packages for social sciences* (2nd ed.). McGraw-Hill.

[5] Saxelby, F. M., & Saxelby, C. H. (1917). *The Mathematical Gazette*.

[6] Ghosh, A., & Bhattacharya, S. P. (2023). Ghosh and Bhattacharya's theorem for measurement of skin areas: Burns, infections, and surgical scars. *British Journal of Surgery*, 110(3), 372. https://doi.org/10.1234/56789

[7] Ghosh, A., & Bhattacharya, S. P. (2024). The theorem I=W102 highlights an accurate method of rapid measurements of abnormal areas on the moon's surface. *American Journal of Planetary and Space Science*, 3(2). https://doi.org/10.1234/56789

DOI: 10.2478/sspjce-2024-0013

Analysis of Crack Propagation in Composite Materials Using Mixed Finite Elements

Ahmed Bougueroua*, Hamoudi Bouzerd

University 20 August 1955, Skikda, Algeria
Department of Civil Engineering, Faculty of Technology.
*e-mail: ah_ba21@yahoo.fr

Abstract

This study investigates the application of fracture mechanics to analyze cracked structures, particularly focusing on cracks along interfaces in multilayer materials. Assuming perfectly plastic elastic behavior, small displacements, and plane structures, the research employs a new mixed finite element, RMQ-7, derived from Reissner's variational principle. The RMQ-7 element, designed to model both the free edge effect along the crack and continuity in the rest of the material, is used in conjunction with the virtual crack extension method to evaluate the energy release rate and the size of the plastic zone around the crack tip.
Numerical modelling is conducted on various configurations, including plates with central and inclined cracks under different loading conditions. The study concludes that the RMQ-7 mixed finite element is an effective and precise tool for analyzing interface cracks in multilayer materials, providing valuable insights into the mechanical behavior of such structures under stress.

Keywords: fracture mechanics, mixed finite element; rmq-7 element, interface cracks, plastic zone energy release rate.

1 Introduction

The study of cracking has been a significant research focus for several decades. Two primary approaches have emerged: fracture mechanics, which involves a local study of cracks and their progression to fracture, and damage theory, which considers cracking on a global level by analyzing a larger volume of material to study the evolution of microcracks or even cracked material.

Between 1960 and 1980, fracture mechanics gained substantial scientific attention, especially with the advent of nonlinear fracture mechanics, which better accounted for the plastic behavior of materials. Notable works from this period include J.R. Rice in 1968 [1] and D. Bui in 1973 [2], who introduced the concept of contour-independent integrals like the J-integral. These integrals helped characterize the toughness of a material when plasticity extends beyond the crack tip. Additionally, this era saw the first studies on fracture mechanics in multilayer

materials [3-4-5]. In this work, we adopt the fracture mechanics approach to study structures with interface cracks under the following assumptions:

- Perfectly plastic elastic behavior of materials
- Small displacements
- Plane structures.

Studying structures with cracked interfaces necessitates the use of specialized mixed finite elements. A new class of mixed finite elements, known as interface elements, emerged by refining Reissner elements using various techniques. For instance, the RMQ-7 element [6], combined with the virtual crack extension method, facilitates the calculation of energy release rate in a single analysis. This element was initially used for identical and different isotropic bimaterials [6] and later for laminate multilayers [7]. An isoparametric formulation of the RMQ-7 element was subsequently developed to model inclined or curved interfaces [8]. Under this formulation, in combination with the virtual crack extension method, the element was used for inclined and curved interfaces [9]. Our work will focus on applying this element to perfectly plastic elastic materials to determine the size of the plastic zone around the crack tip.

Numerous experimental and analytical techniques are available in the literature for determining the size of the plastic zone [10-11-12-13-14-15].

2 Plastic zone around crack tip in two-dimensional medium

2.1 Shape of the plastic zone

The stresses in the vicinity of the crack in mode I (see Figure1) [16]:

$$\begin{aligned} \boldsymbol{\sigma_{11}} &= \frac{\mathbf{K_I}}{\sqrt{\mathbf{2\pi r}}}\mathbf{cos}\frac{\boldsymbol{\theta}}{\mathbf{2}}\left[\mathbf{1}-\mathbf{sin}\frac{\boldsymbol{\theta}}{\mathbf{2}}\mathbf{sin}\frac{\mathbf{3\boldsymbol{\theta}}}{\mathbf{2}}\right] \\ \boldsymbol{\sigma_{22}} &= \frac{\mathbf{K_I}}{\sqrt{\mathbf{2\pi r}}}\mathbf{cos}\frac{\boldsymbol{\theta}}{\mathbf{2}}\left[\mathbf{1}+\mathbf{sin}\frac{\boldsymbol{\theta}}{\mathbf{2}}\mathbf{sin}\frac{\mathbf{3\boldsymbol{\theta}}}{\mathbf{2}}\right] \\ \boldsymbol{\sigma_{12}} &= \frac{\mathbf{K_I}}{\sqrt{\mathbf{2\pi r}}}\mathbf{sin}\frac{\boldsymbol{\theta}}{\mathbf{2}}\mathbf{cos}\frac{\boldsymbol{\theta}}{\mathbf{2}}\mathbf{cos}\frac{\mathbf{3\boldsymbol{\theta}}}{\mathbf{2}} \end{aligned} \tag{1}$$

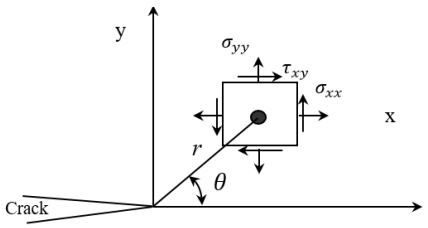

Figure 1: Crack mode I in an infinite plate, definition coordinate system at crack tip

- **Plane stresses**

In plane stresses, the Von-Mises criterion is written [16]:

$$\sigma_y^2 = \frac{1}{2}[(\sigma_{11}-\sigma_{22})^2+\sigma_{22}^2+\sigma_{11}^2]+3\sigma_{12}^2 \tag{2}$$

By replacing equation (01) in this equation, we obtain:

$$r = \frac{K_I^2}{2\pi\sigma_y^2} cos^2\frac{\theta}{2}\left(1 + 3\,sin^2\frac{\theta}{2}\right) \quad (3)$$

When one considers an elastic linear initial state, one writes $\sigma_y = \sigma_e$ elastic limit. Figure 2.a shows the shape of the plasticized area.

- **plane strains**

In plane strains, the criterion of Von-Mises is written in this case [16]:

$$\boldsymbol{\sigma_y^2 = 3\left[(\sigma_{11} - \sigma_{22})^2 + (\sigma_{22} - \sigma_{33})^2 + (\sigma_{33} - \sigma_{11})^2\right] + 18\sigma_{12}^2} \quad (4)$$

With: $\sigma_{33} = \nu(\sigma_{11} + \sigma_{22})$

In the same way, we deduce by replacing equation (01) in equation (02), we obtain:

$$r = \frac{K_I^2}{2\pi\sigma_y^2} cos^2\frac{\theta}{2}\left((1-2\nu)^2 + 3\,sin^2\frac{\theta}{2}\right) \quad (5)$$

When one considers an elastic linear initial state, one writes $\sigma_y = \sigma_e$.

Figure 2.b shows the shape of the plasticized area.

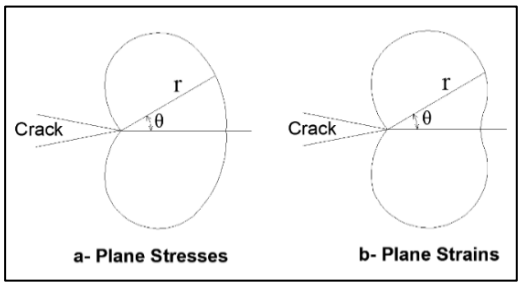

Figure 2: Shape of the plastic zone

2.2 Irwin's approach

This approach fixes an objective[17]: the determination of the stress intensity factor in mode I taking into account the presence of a supposedly small plastic zone in comparison with the length of the crack. (However, strictly speaking of a stress intensity factor in elastoplasticity, does not seem rational); the value thus obtained of this factor K_I will be used to establish an "intrinsic" value ! K_{IC} critical corresponding to elastoplastic fracture.

Irwin therefore supposes an increase in the crack of $r_y \ll a$, and considers that the stress σ_{22} obtained in this zone does not exceed the elastic limit σ_e (perfect elastoplastic constitutive law therefore without hardening). It is therefore a question of estimating the value r_y for a given value of the stress applied to the distance $\sigma_{22\infty}$. From the stress field determined in linear elasticity (equation 02), one writes in mode I and for $\theta = 0$ [16].

$$\sigma_{22}|_{\theta=0} = \sqrt{\frac{K_I}{2\pi r}} \qquad \text{avec} \qquad K_I = \sigma_{22\infty}\sqrt{\pi a} \quad (6)$$

Let us calculate the sum S_1 of the stresses $\sigma_{22}|_{\theta=0}$ between $r = 0$ and $r = r_y$, we obtain:

$$S_1 = \int_0^{r_y} \frac{K_I}{\sqrt{2\pi r}} dr = \sqrt{\frac{2}{\pi}} K_I \sqrt{r_y} \quad (7)$$

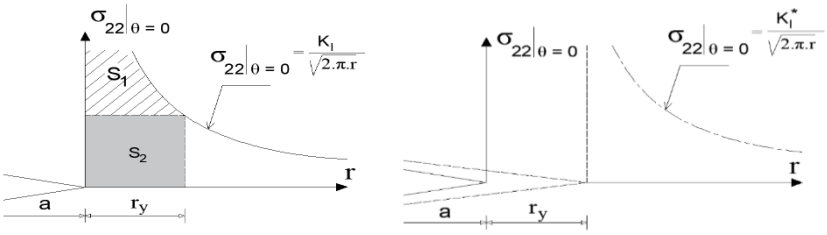

Figure 3: Depth of plastic area

Assuming $\sigma_{22}|_{\substack{\theta=0 \\ r=r_y}} = \sigma_e$, we obtain from equation (06)

$$\sigma_e = \frac{K_I}{\sqrt{2\pi r_y}} r_y = \frac{K_I^2}{2\pi\sigma_e} \quad (8)$$

By replacing equation (08) in equation (07), we write: $S_1 = 2\sigma_e r_y$

If we consider Irwin's hypothesis of perfect plasticity inside the plastic zone, the sum of the stresses corresponds to $S_2 = \sigma_e r_y$

The comparison between (S_1) and (S_2)shows that we must double the depth of the plastic zone to have the same sum of stresses, hence we write:

$$R_y = 2r_y = \frac{K_I^2}{2\pi\sigma_e^2} \quad (9)$$

From the value r_y , Irwin defines a plastic stress intensity factor K_I^* which is written:

$$K_I^* = \sigma_{22\infty}\sqrt{\pi(a + r_y)} \quad (10)$$

3 Numerical modeling

3.1 Presentation of the RMQ-7 element

3.1.1 Use of Reissner's principle

Along a crack one distinguishes two parts, one coherent where it is necessary to ensure the mechanical and geometrical continuity and the other cracked, geometrically discontinuous and incompetent to transmit the mechanical forces due to the loads. To attempt to numerically model this problem by the finite element technique, it is necessary to develop a special element that meets the two requirements above, namely the free edge effect along the cracked part and perfect consistency on the rest. Moreover, it is necessary to take account of the singularity of the stresses at the crack tip.

Classical finite element based on the method of displacement or the method of forces are unable to meet these requirements. This insufficiency led to the use of s two-field methods, because

the latter make it possible to act simultaneously on the displacement and stress fields, and can thus solve the problems of continuity and of free edge. In this work, we used the mixed formulation [18] of where all the kinematic quantities (u_i) and all the static quantities (σ_{ij}) appear as explicit variables independently.

3.1.2 Element proposal

Based on Reissner's variational principle, the proposed RMQ-7 element (Figure 4) is rectangular with seven nodes. Three of its sides are compatible with classical linear elements, featuring a displacement node at each end. The fourth side, besides its two kinematic nodes of end, offers three additional nodes: a median displacement node (which will represent the crack tip later) and two intermediate nodes in the middle of each half- side, introducing the components of stress vector along the interface. The continuities of displacement vectors s and stress can be taken into account at this particular side, which must be placed along the interface. In the case of cracked structures, the median node is associated with the crack tip and the static nodes on both sides allowing to satisfy the two essential requirements of such a situation, which are the condition of the free edge on the lips of the crack and the conditions of continuity along the coherent part.

For the configuration final element [6], has developed a new rectangular mixed finite element based on the functional Reissner. It has five nodes and 22 degrees of freedom (Figure 4). Four of these nodes are placed at the ends and each have static and kinematic variables, the fifth node is located in the middle of a horizontal side and has only two cinematic unknown. This element called RMQ-5 will be useful later as a starting point for the construction of the final element. In a first phase, the technique of relocation of degrees of freedom is used to drive of the RMQ-11 member (Figure 4), then in a second phase by static condensation interior degrees of freedom are eliminated to obtain the RMQ-7 element, which will be used to model coherent or cracked interfaces.

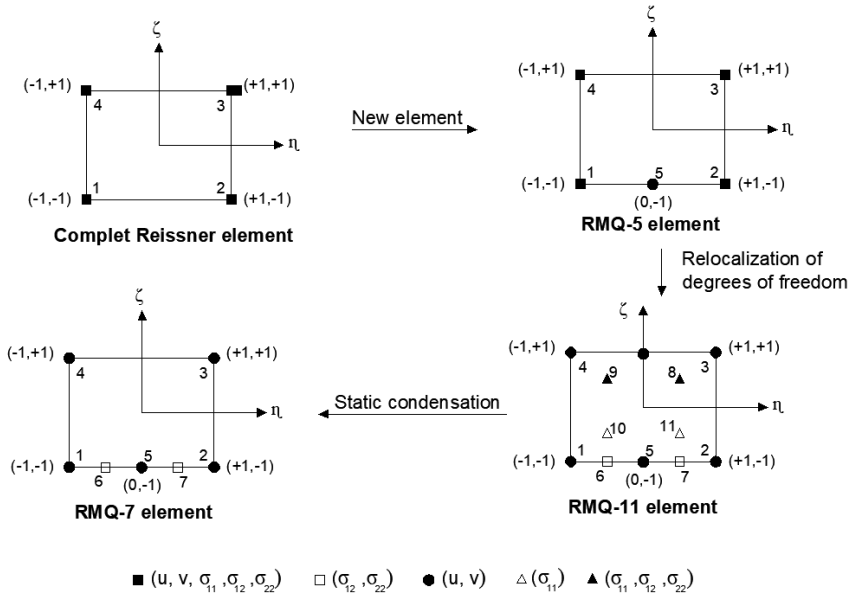

Figure 4: Phases of construction of RMQ-7 element

3.2 Evaluation of the energy release rate G

In this section, we discuss the adaptation of the technique of virtual crack extension to the case of composites laminates with slant crack. The mixed finite element RMQ-7 associated with this technique has shown a good performance in the case of cracked isotropic materials [6] and orthotropic bimaterial [7].
To test its effectiveness in the case of composites laminates with slant crack, we reformulated the implementation of this method to take into account the specificity of this type of structures. In this new formulation, we do not need "the equivalent element" placed in the mesh to represent the initial configuration of the crack. The following steps show how to operate to calculate the energy release rate.

Whereas a change δa of the crack length, leading to a release of an amount of energy $\Delta\Pi$ (where Π represents the deformation energy), the energy release rate G is defined as follows:

$$G = \frac{\delta\Pi(a+\delta a)-\delta\Pi(a)}{\delta a} = \frac{\delta\Pi}{\delta a} \qquad (11)$$

The virtual crack extension method [19]is used in this work to evaluate G. Two elements RMQ-7, named crack tip elements (upper and lower), are placed along the cracked interface with the displacement median common node associated with the crack tip (Figure 5a).

The crack length "a" can be increased by an amount Δa acting within strict both elements surrounding the crack tip by a translation of the common node associated with the crack tip without disturbing the surrounding mesh of structure (Figure 5b).

If we consider a small perturbation Δa compared to the dimensions of one of the two elements of crack with the hypotheses (linear elastic behaviour in small displacements) we can write with a good approximation:

$$\mathrm{v}(a) \cong \mathrm{v}(a + \Delta a)$$

Where $\mathrm{v}(a)$ and $\mathrm{v}(a + \Delta a)$are solution vectors of the finite element analysis in the configurations "a" and " $a + \Delta a$ " of the studied structure.

Therefore, the energy release rate G is evaluated from the variations of the stiffness-flexibility matrices in the elements of crack from one finite element discretization using the following equation:

$$G = \sum_{f=1}^{2} \{v\}_f^t \frac{[\Delta K]_f}{\Delta a} \{v\}_f = \frac{\Delta\Pi}{\Delta a} \qquad (12)$$

$$With \quad [\Delta \mathrm{K}]_{\mathrm{f}} = [\mathrm{K}(\mathrm{a} + \Delta \mathrm{a})]_{\mathrm{f}} - [\mathrm{K}(\mathrm{a})]_{\mathrm{f}} \qquad (\mathrm{f} = 1{,}2)$$

Where $[\Delta \mathrm{K}]_{\mathrm{f}}$ $(\mathrm{f} = 1{,}2)$ is the variation of the elementary matrix of the element of crack during the variation Δa of the length of the crack, and the subscript f indicates that quantities used are those of crack tip elements only. The other elements are unchanged $([\Delta \mathrm{K}] = [0])$.

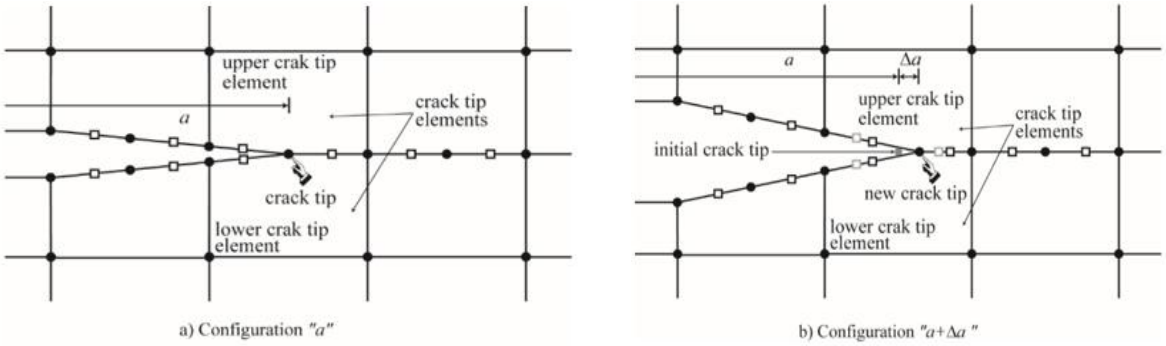

Figure 5: Position of crack tip and length of the crack before and after virtual extension

In practice, the discretization of the cracked structure is performed in the configuration " $a + \Delta a$ " (Figure 4b) of the crack and during the operation of assembly the elementary matrices of the upper and lower crack elements are calculated in the configuration " a" and " $a + \Delta a$ ". The matrices of the configuration " $a + \Delta a$ " are used in the assembly to build the finite element solution $\mathrm{v}(a + \Delta a)$, while the matrices of the configuration " a" do not participate in the assembly and they are stored separately. After the resolution, they will be restored to calculate the energy release rate G by the formula (8).

4 Validation of the proposed model

4.1 Angle cracked plate under tension

The specimen is a plate with inclined center crack, load in tension by $\sigma = 1\ unit$ with the following geometrical: $W = 10\ units$, $a/W = 0.05$. The Young's modulus $E = 100\ units$, the poisson's ratio $\nu = 0.33$ [20]

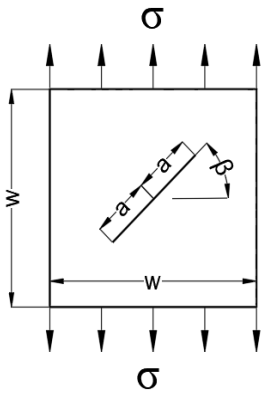

Figure 6: Geometry and loads of an angle-cracked plate under tension.

Table 1 presents the K_I results obtained by RMQ-7 element for different crack inclination angles and compares them with numerical and analytical results.

Table 1: Results for K_I of inclined center crack in a homogeneous, isotropic elastic plate under tension

Crack inclination angle β	RMQ-7	LIU [20]	Error (%)	Exact solution [20]	Error (%)
	K_I	K_I		K_I	
0	1,2746	1.271	-0.28	1.253	-1.72
5	1,2640	1.263	-0.08	1.244	-1.60
10	1,2210	1.238	1.37	1.216	-0.41
15	1,1739	1.194	1.68	1.169	-0.42
20	1,0982	1.126	2.46	1.107	0.79
25	1,0055	1.047	3.96	1.029	2.28
30	0,8995	0.960	6.30	0.940	4.31
35	0,7845	0.853	8.38	0.841	6.72
40	0,6997	0.745	6.08	0.735	4.80
45	0,5787	0.625	7.41	0.627	7.71
50	0,4768	0.520	8.31	0.518	7.95
55	0,4052	0.392	-3.36	0.412	1.66
60	0,3087	0.288	-7.18	0.313	1.37
65	0,2234	0.197	-13.40	0.224	0.28
70	0,1338	0.144	7.08	0.147	8.97
75	0,0803	0.084	4.40	0.084	4.45
80	0,0359	0.036	0.28	0.038	5.65
85	0,0089	0.009	1.11	0.010	11.24

It can be seen that the K_I values calculated using the mixed finite element method are very close to the numerical results (Liu) ant the exact solution, with a difference not exceeding 12% in any case.

4.2 Evaluation of the plastic zone in mode I

The specimen is a plate with central crack, plate of width $B = 100\ mm$, length $L = 200\ mm$ and thickness $2.5\ mm$.the specimen is an aluminium alloy sheet (2024-T351) with the Young's modulus $E = 73$ GPa , the Poisson's ratio $\nu = 0.3$ and the yield stress $\sigma_Y = 370\ MPa$ [21].

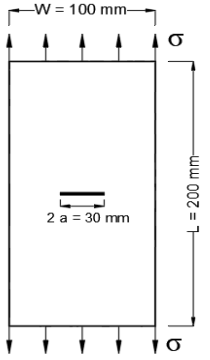

Figure 7: Geometry and loads of plate under tension.

Table 2 gives all the results obtained by different model with the measured plastic zone computed for angle $\theta = 0°$.

Table 2: Size of plastic zone ahead of crack tip ($\theta = 0°$)

Models	RMQ-7	Irwin	Dugdale	Kujawski power law	T.E. Tay [21]	Benrahou [13]
Plastic zone r_y [mm]	0.98	0.88	1.06	0.80	0.84	0.54
Error (%)	0.00	-11.36	7.54	22.5	-16.66	9.25

The calculation of the plastic zone size around the crack tip using the RMQ-7 element (a mixed finite element) according to the Von Mises plasticity criterion shows good concordance with values calculated by Irwin's model, with an error not exceeding 12%. The error ranges from 7% to 16% for the models of Dugdale, Benrahou, and Tay. However, the error is around 22% when compared to the Kujawski model.

4.3 Evaluation of the plastic zone bi-axial case of loading

In the numerical calculation , a plate width of 2W and 2L length having a central crack 2a [22] is used to investigate the size of the plastic zone in the vicinity of the crack tip under a load voltage bi- axial σ, as shown in figure 8 . The plane stress condition is assumed. The plate being symmetrical, only a quarter of the plate is modeled.

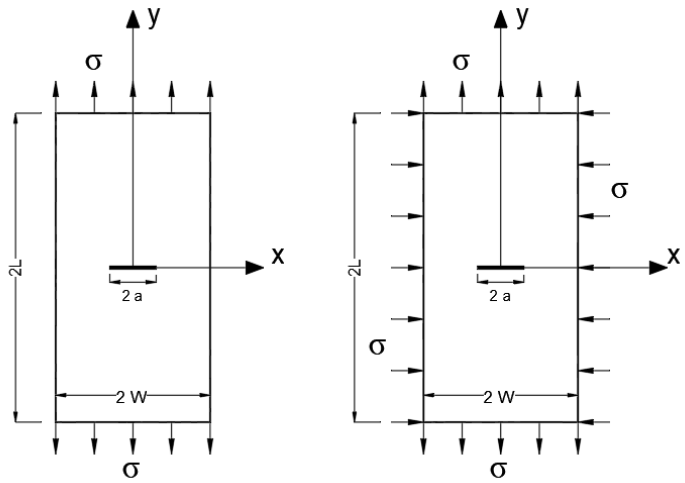

Figure 8: A center cracked plate in tension a) the case to uniaxial stress (transverse stress is zero); b) the case to uniaxial stress (transverse is compressive stress, which is equal to tensile stress).

The material is supposed to have a perfectly plastic elastic stress-strain relationship, the Von-Mises criteria are used in the calculations. The Young's modulus E is 210 GPa and the Poisson's ratio v is 0.3 [22].

4.3.1 Case of the uniaxial stress (the transverse stress is zero)

Table 3: The results of R_y calculated by the three methods in the case of $\lambda = \sigma_{xx}/\sigma_{yy} = 0$.

σ [Mpa]	σ_s $[Mpa]$	a/W	a $[mm]$	R_y by RMQ7 $[mm]$	R_y by MCOD $[mm]$[22]	Error (%)	R_y by Irwin $[mm]$ [22]	Error (%)
60	235	0.067	10	0.2945	0.3082	4.44	0.2995	1.66
60	255	0.067	10	0.2430	0.2599	6.50	0.2531	3.99
60	275	0.067	10	0.2230	0.2225	-0.22	0.2167	-2.90
60	300	0.067	10	0.1730	0.1863	7.13	0.1814	4.63
60	235	0.125	17	0.5125	0.5277	2.88	0.5092	-0.64
40	325	0.1	10	0.0650	0.0694	6.34	0.0678	4.12
40	350	0.1	10	0.0550	0.0594	7.40	0.0584	5.82
80	375	0.1	10	0.1950	0.2129	8.40	0.2070	5.79
80	400	0.1	10	0.1850	0.1866	0.85	0.1814	-1.98
80	350	0.143	17	0.3850	0.4215	8.65	0.4054	5.03

The results obtained from the size of the plastic zone Ry by the element RMQ-7 are compared with the results by the MCOD method and by the Irwin formula, it can be seen that the results of Ry calculated by the mixed finite element RMQ -7 are very close to those of Irwin and the method of MCOD where the difference does not exceed in any case 6%.

4.3.2 Case of uniaxial stress (transverse is the compressive stress, which is equal to the tensile stress)

Table 4 show the results of R_y calculated by the three methods in the case of $\lambda = \sigma_{xx}/\sigma_{yy} = -1$

Table 4: The results of R_y calculated by the three methods in the case of $\lambda = \sigma_{xx}/\sigma_{yy} = -1$

σ [Mpa]	σ_s $[Mpa]$	a/W	a $[mm]$	R_y by RMQ7 $[mm]$	R_y by MCOD $[mm]$[22]	Error (%)	R_y by Irwin $[mm]$[22]	Error (%)
30	305	0.100	12	0.0900	0.1011	10.97	0.0988	8.90
40	355	0.100	12	0.1300	0.1305	0.38	0.1274	-2.04
50	355	0.100	15	0.2300	0.2458	6.42	0.2412	4.64
60	275	0.100	16	0.5500	0.5904	6.84	0.5819	5.48
60	275	0.083	14	0.4900	0.5158	5.00	0.5092	3.77
80	325	0.083	15	0.7100	0.6987	-1.61	0.6864	-3.43
90	400	0.083	20	0.7900	0.7817	-1.06	0.7710	-2.46
100	400	0.083	20	0.8800	0.9607	8.40	0.9429	6.67
80	325	0.125	17	0.7500	0.7973	5.93	0.7779	3.58
60	300	0.111	18	0.5500	0.5643	2.53	0.5559	1.06
70	270	0.091	11	0.5800	0.5686	-2.00	0.5564	-4.24

The results obtained for the size of the plastic zone Ry by the model with the element RMQ-7 are compared with the results by the MCOD method and by the Irwin formula. It can be seen that the results of Ry calculated by the mixed finite element RMQ -7 are close to those of Irwin and the method of MCOD where the difference does not exceed in any case 9 %.

5 Conclusion

This work highlights the efficacy of the RMQ-7 mixed finite element in the analysis of interface cracks in multilayer materials. By utilizing Reissner's principle, the RMQ-7 element successfully models the mechanical and geometrical continuity required for accurate fracture analysis. Validation against experimental and analytical results demonstrates the element's reliability in predicting stress intensity factors and plastic zone sizes. The study confirms that the RMQ-7 element is a robust tool for fracture mechanics applications, offering precise insights into the behavior of cracked structures under various loading conditions.

References

[1] Rice, J. R. (1968). A Path Independent Integral and the Approximate Analysis of Strain Concentration by Notches and Cracks. *Journal of Applied Mechanics*, 379-386.

[2] Bui, H. (1974). Dual path Independent Integral in the boundary value problems of crack. *Engineering Fracture Mechanics*, *6*, 287-296. https://doi.org/10.1016/0013-7944(74)90027-7

[3] Sih, G., & Rice, J. (1964). The Bending of plates of Dissimilar Materials With Cracks. *Journal of Applied Mechanics*, *31*, 477-482. https://doi.org/10.1115/1.3629665

[4] Erdogan, F. (1965). Stress Distribution in Bonded Dissimilar Materials Containing Circular or Ring-Shaped Cavities. *Journal of Applied Mechanics*, *32*(4), 829-836. https://doi.org/10.1115/1.3627323

[5] Comninou, M. (1977). The Interface Crack. *Journal of Applied Mechanics*, *44*(4), 631-636. https://doi.org/10.1115/1.3424148

[6] Bouzerd, H. (1992). *Mixed finite element for cohesive or cracked interface*. Doctoral Thesis. Claude Bernard University, Lyon I, France.

[7] Bougueroua, A. (2006). *Delamination propagation in laminates*. Master's Thesis. University 20 August 1955, Skikda, Algeria.

[8] Bouziane, S. (2009). *Mixed finite element for cracked interfaces in anisotropic bimaterials*. Doctoral Thesis. University 8 May 1945 , Guelma , Algeria.

[9] Bouziane, S., Bouzerd, H., Boulares, N., & Guenfoud, M. (2014). Energy release rate for kinking crack using mixed finite element. *Structural Engineering and Mechanics*, *50*, 665-677. https://doi.org/10.12989/sem.2014.50.5.665

[10] Huang, X., Liu, Y., & Huang, X. (2019). Analytical characterizations of crack tip plastic zone size for central-cracked unsti ff ened and sti ff ened plates under biaxial loading. *Engineering Fracture Mechanics*, *206*, 1-20. https://doi.org/10.1016/j.engfracmech.2018.11.047

[11] Fernando, L., Marques, N., Antonio, M., Tupiassú, J., Castro, P. De, & Fernando, L. (2020). Elastoplastic 3D analyses of plastic zone size dependencies on load-to-yield strength and on crack size-to-width ratios under mixed mode I / II. *Theoretical and Applied Fracture Mechanics*, *107*, 102490. https://doi.org/10.1016/j.tafmec.2020.102490

[12] Kumar, K. G., Silpa, V. J. K., Vamsi, B. V. S. R., & Bhadauria, S. S. (2018). Studies on the Critical Size of the Plastic Zone in Pure Mode-I and Mixed Mode (I / II) Fracture. *Materials Today: Proceedings*, *5*(2), 7765-7774. https://doi.org/10.1016/j.matpr.2017.11.454

[13] Benrahou, K. H., Benguediab, M., & Belhouari, M. (2007). Estimation of the plastic zone by finite element method under mixed mode (I and II) loading. *Computational Materials Science*, *38*, 595-601. https://doi.org/10.1016/j.commatsci.2006.04.001

[14] Heung-Bae, P., Kyung-Mo, K., & Byong-Whi, L. (1996). Plastic zone size in fatigue cracking. *International Journal of Pressure Vessels and Piping*, *68*(3), 279-285. https://doi.org/10.1016/0308-0161(95)00066-6

[15] Tieying, W., Danièle, W., & Daniel, K. (2016). Analysis of the plastic zone of a circle crack under very high cycle fatigue. *International Journal of Fatigue*, *93*, 415-421. https://doi.org/10.1016/j.ijfatigue.2016.08.021

[16] Naman, R. (1995). *Rupture par Fissuration des Structures* (Hermès). Paris, France

[17] G.R Irwin. (1963). Structural aspects of brittle fracture. *AGARD 17th S and M Panel Meeting, Applied Materials Research*, 65-81.

[18] Reissner, E. (1950). On variational theorem of elasticity. *Journal of Mathematics and Physics*, 90-95. https://doi.org/10.1002/sapm195029190

[19] D.M. Parks. (1974). A stiffness derivative finite element technique for determination of crack tip stress intensity factors. *International Journal of Fracture*, *10*, 478-502. https://doi.org/10.1007/BF00155252

[20] Liu, X. Y., Xiao, Q. Z., & Karihaloo, B. L. (2004). XFEM for direct evaluation of mixed mode SIFs in homogeneous and bi-materials. *international journal for numerical methods in engineering*, *1118*, 1103-1118. https://doi.org/10.1002/nme.906

[21] TAY, T. E., YAP, C. M., & TAY, C. J. (1995). Crack tip and notch tip plastic zone size measurement by the laser speckle technique. *Engineering Fracture Mechanics*, *52*(5), 879-893. https://doi.org/10.1016/0013-7944(95)00060-9.

[22] Yi, H., Jingjie, C., & Gang, L. (2010). A new method of plastic zone size determined based on maximum crack opening displacement. *Engineering Fracture Mechanics*, *77*(14), 2912-2918. https://doi.org/10.1016/j.engfracmech.2010.06.026.

DOI: 10.2478/sspjce-2024-0014

Qualitative Seismic Evaluation of the Existing UR Masonry Shear Walls – Reinforced Concrete Frames System

Petru Mihai[1], Ion Sococol[1*]

[1]"Gheorghe Asachi" Technical University of Iasi, Romania
Faculty of Civil Engineering and Building Services, Department of Concrete Structures, Building Materials, Technology and Management
[*]e-mail: ion.sococol@academic.tuiasi.ro

Abstract

The dual system buildings consisting of Unreinforced Masonry (URM) Shear Walls and Reinforced Concrete (RC) Frames are part of the existing buildings patrimony in Romania. Being a seismic zone, the qualitative evaluation of this type of structural system represents both a specific and a holistic approach. Thus, the in-depth knowledge of the initial situation of the building, including the level of degradation as well as the causes that produced these damages represents the present study. Also, notions such as: the level of degradation importance, the level of damage (destruction), the correction coefficient of the bending stiffness, the level of knowledge, the evaluation methodology are interpreted, in order to establish a score of the degree of seismic configuration of the lateral system and degree of structural damage. This information leads to the establishment of the seismic risk class of the analyzed building and to the establishment of the intervention works necessity.

Keywords: unreinforced masonry (URM), RC frames, dual system, level of damage, seismic assessment

1 Introduction

The dual structures formed by Unreinforced Masonry (URM) Shear Walls and Reinforced Concrete (RC) Frames represent an important part of buildings located in seismic zones [1,2], including in Romania. Their seismic evaluation becomes a national obligation in the conditions of buildings "aging", as the level of damage increases annually [3-5]. These buildings are inhabited, which implies a major assurance of the evaluation quality.
In current practice, there are two types of seismic evaluations:

- qualitative seismic assessment;
- quantitative seismic assessment.

Qualitative seismic assessment of the building is based on:

- in-situ investigations (including identification of the types of damage through the visual inspection [4]);
- a holistic approach to the existing problems in the building;
- identifying the Level of Degradation Importance (LDI);

- identification of Level of Damage (Destruction) in Percentage (LDP) [6,7];
- establishing the impact of the damage level to lateral stiffness of the structural elements [8];
- establishing the level of knowledge;
- establishing the evaluation methodology;
- establishing the degree of seismic configuration of the lateral system (by agreeing a score);
- establishing the degree of structural damage (by agreeing a score);
- the preliminary classification of the building in a seismic risk class;
- establishing at a general level the need for intervention works.

The current study only approach this type of assessment. The quantitative seismic assessment of the building is based on the qualitative seismic assessment (and in-situ information) to be able to perform numerical analyzes of the superstructure and the infrastructure [9-11]. The current study does not approach this type of evaluation.

2 Preliminary data regarding the analyzed building

The analyzed building is located in Romania, Suceava County, and falls into importance category C and earthquake importance and exposure class III in accordance with HG. 766/1997 [12] and P100-1/2013 [13] norms.
The structural system consists of Unreinforced Masonry (URM) Shear Walls and Reinforced Concrete (RC) Frames, with the height regime GF+1F (Ground Floor + 1 Floor). The wall thickness varies between 30 and 50 cm. The foundation system is composed of a RC grid beams. The height of the foundation beams is 2.00 m and their width is 0.60 m.
Centralized information regarding the analyzed building is specified in Table 1. The main facades of the building are represented in Figure 1.

Table 1: Centralized information regarding the analyzed building

The purpose of qualitative seismic evaluation	Establishing the conditions for additional floor construction and thermal retrofitting [14]		
County and Country	Suceava County, Romania		
Importance category [12]			C
Earthquake importance and exposure class [13]			III
Year of completion of the building construction works:	1952		
Building function	Commercial space/ offices		
Total height of the structure (m):	+10.14	Number of floors:	Ground Floor+1 Floor (GF+1F)
Built area (sqm):	404.00	Unfolded area (sqm):	804.00
Structural system:	The structural (lateral) system of the building is made up of UR (Unreinforced) Masonry Shear Walls (MSW) and Reinforced Concrete Moment Frames (RCMF). The outward MSW are 47 cm thick on the GF and 47 cm/ 42 cm		

	thick on the 1F. The internal MSW are 40 cm thick on the GF and 30 cm/ 40 cm thick on the 1F. The Reinforced Concrete Columns (RCC) have a cross section of 35x56 cm and the Reinforced Concrete Beams (RCB) have a section of 30x60 cm. The Reinforced Concrete Slabs (RCS) above the GF and 1F are 10 cm thick. The roof of the building is composed of the timber frame system with metal sheet covering.				
Foundation system	The foundation system is composed of a Reinforced Concrete grid beams. The height of the foundation beams is 2.00 m and their width is 0.60 m.				
Non-structural components:	-				
Seismic action (probability of exceedance in 50 years):	*SLS:	80% (*ARI 30)	*ULS:	40% (*ARI 100)	
Seismic evaluation methodology used (in accordance with P 100-3 norm) [15]	1 ☐		2 ☒	3 ☐	
*where: SLS – Service Limit State; ULS – Ultimate Limit State; ARI – Average Recurrence Index.					

(a) (b)

(c) (d)

Figure 1: Representation of the: (a) main facade of the analyzed building; (b) right side facade; (c) left side facade; (d) rear facade

The building was built in 1952 and has experienced earthquakes over 6 degrees M_w until this moment (see details in Table 2).
The main phenomena affecting the site of the analyzed building are (see details in Table 3):

- Earthquake action;
- Snow action;
- Wind action;
- Freezing effect;
- Presence of underground water etc.

Table 2: The list of the most important earthquakes in Romania that the analyzed building went through

Date	Magnitude	Intensity	Epicenter
March 4, 1977	7.20 M_w	XI. Extreme	Nereju, Vrancea
August 30, 1986	7.10 M_w	VIII. Destructive	Gura Teghii
30 May, 1990	6.9-7.00 M_w	VIII. Destructive	Vrancea

Table 3: The main phenomena affecting the site of the analyzed building

Analysed phenomenon	Results
Seismic area [13]	*ARI = 225 years, *a_g = 0.20g and the period *T_C =0.7 sec from the design spectrum
Snow load (action) [16]	*s_k=2.5 kN/mp
Wind load (action) [17]	*q_b=0.60 kPa
Maximum freezing depth [18]	100 -110 cm deep of the natural soil
*Soil stratification	0.00 - 1.00 m – Fills from topsoil and construction material scraps; 1.00 - 7.00 m – Brown loamy sandy dust, with calcareous intercalations, with medium plasticity, plastic stout, with high compressibility
The presence of underground water	Groundwater was intercepted at -2.00 m and stabilized at -1.10 m from *L.S.L.
Plastic pressure (P_{pl}) and Critical pressure (P_{cr}) of the soil	P_{pl} =169.00 (kPa) P_{cr} =183.00 (kPa)
*where: ARI – Average Recurrence Index; a_g – horizontal ground acceleration; T_C – the period from the design spectrum; s_k – characteristic snow loading on the ground; q_b - characteristic wind pressure; Soil stratification – according to the geotechnical study; L.S.L. – Landscaped Soil Level.	

3 Identification of damages

3.1 Identification of the types of damage through the visual inspection

Following the visual investigation of the dual structural system, a series of local structural and non-structural degradations of low, medium and high importance were observed (Figure 2, Figure 3 and Table 4).
The observable Non-Structural Degradations (NSD) are represented in Figure 2 and are explained as follows:

- NSD.1 - non-structural physical degradation of mortar and masonry through the capillary rise of water, freeze-thaw effects, and mortar degradation on exterior masonry shear walls (see Figure 2 (a), (b); Table 4, Table 5);
- NSD.2 - sidewalks deterioration, defective presence of concrete sidewalks or their absence favored the appearance and development of vegetation, which facilitates the stagnation of rainwater in the foundation area (see Figure 2 (c), (d); Table 4, Table 5);
- NSD.3 - the deficient presence of gutters and downspouts or their non-existence favored the flow of rainwater on the structural masonry walls and respectively on the socle as well as on the partially destroyed sidewalk (see Figure 2 (e), (f), (g); Table 4, Table 5);
- NSD.4 - cracks and dislocations of the finishes (Table 4, Table 5);
- NSD.5 - local degradation of the ceiling and interior walls (Table 4, Table 5).

(a) (b) (c)

(d) (e)

(f) (g)

Figure 2: Representation of the non-structural degradations: (a), (b) physical degradation of mortar and masonry through the capillary rise of water, freeze-thaw effects, and mortar degradation on exterior masonry shear walls; (c), (d) The defective presence of concrete sidewalks or their absence; (e), (f), (g) the deficient presence of gutters and downspouts or their non-existence

The observable Structural Degradations (SD) are represented in Figure 3 and are explained as follows:

- SD.1 - structural degradation and micro/ macro-cracks of the external masonry shear walls (see Figure 3 (a); Table 4, Table 5);
- SD.2 - horizontal cracks in the masonry shear walls (between the gaps) caused by tensile stresses from bending moments resulting from seismic or non-seismic actions (see Figure 3 (b), (c); Table 4, Table 5);
- SD.3 - inclined cracks (at 45°) above the masonry coupling beams caused by ”vault” action of the masonry in that area (see Figure 3 (d), (e); Table 4, Table 5);
- SD.4 - cracks under the support of the beams (the crushing effect of the local area) caused by compression stress (see Figure 3 (f); Table 4, Table 5);
- SD.5 - local separation cracks between RC floor and masonry shear wall (see Figure 3 (g); Table 4, Table 5);
- SD.6 - inclined macro-cracks (at 45°) in the field (plain) of masonry shear walls caused by axial tensile stresses from seismic or non-seismic actions (see Figure 3 (h), (j), (k); Table 4, Table 5);
- SD.7 - multiple cracks in the RC slab above the ground floor from excessive deformations, vibrations and differential vertical displacements of the structure (see Figure 3 (i); Table 4, Table 5).

(a)

(b)

(c)

(d)

(e)

(f)

(g)

(h) (i)

(j) (k)

Figure 3: Representation of the structural degradations: (a) degradation and micro/ macro-cracks of the external masonry shear walls; (b), (c) horizontal cracks in the masonry jamb between the gaps; (d), (e) inclined (45°) cracks above the masonry coupling beams; (f) cracks under the support of the beams (the crushing effect of the local area); (g) local separation cracks between RC floor and masonry shear wall; (h), (j), (k) inclined (45°) macro-cracks in the field (plain) of masonry shear walls; (i) multiple cracks in the RC slab above the ground floor

Table 4 shows the Level of Degradation Importance (LDI) for structural and non-structural elements which can be Low (L), Medium (M) or High (H). In Table 5 it is represented the Level of Damage (Destruction) in Percentage (LDP) of the structural and non-structural elements in accordance with type of observable structural or non-structural degradation. The range of LDP is wide for every Type of Degradation (TD) because the lateral system dispose a multiple number of structural and non-structural elements which are affected differently. Thus, an average percentage in extensive line of the damage (destruction) was chosen.

Table 4: Level of Degradation Importance (LDI) in accordance with type of degradation

		Level of Degradation Importance (LDI)		
		Low (L)	Medium (M)	High (H)
Type of Degradation (TD)	Non-structural (NSD)	NSD.4; NSD.5	NSD.1; NSD.2; NSD.3	It is not the case
	Structural (SD)	It is not the case	SD.1; SD.2; SD.7	SD.3; SD.4; SD.5; SD.6

Table 5: The Level of Damage (Destruction) in Percentage (LDP) representation

Type of observable structural or non-structural degradation	Percentage level of damage (destruction) (%)									
	10	20	30	40	50	60	70	80	90	100
*NSD.1										
*NSD.2										
*NSD.3										
*NSD.4										
*NSD.5										
*SD.1										
*SD.2										
*SD.3										
*SD.4										
*SD.5										
*SD.6										
*SD.7										
*where: NSD – Non-Structural Degradation; SD – Structural Degradation										

3.2 Establishment the impact of the damage level to lateral stiffness of the structural elements

To check the lateral displacements at the Service Limit State (SLS) and at the Ultimate Limit State (ULS), the corrected stiffness of the component materials (concrete and masonry) $K_{SLS}{}^{c}$ and $K_{ULS}{}^{c}$ with the correction coefficient μ according to Equation 3, Equation 4 and Table 6 – which takes into account the degradation degree of structural elements before the occurrence of the seismic event. It is mentioned that the corrected lateral stiffness at both limit states is based on the stiffness calculated according to the norm P100-3/2019 [15], with Equation 1 and Equation 2, being affected by the coefficients k_{SLS} and k_{ULS} predetermined by the norm - which take/do not take into account the cracking of the material (masonry; concrete) during the seismic event.

Table 6: The establishment of the correction coefficient μ of the lateral (bending) stiffness K_{SLS} and K_{ULS} at SLS and ULS and the corrected lateral stiffness $K_{SLS}{}^{c}$ and $K_{ULS}{}^{c}$

Type of observable structural degradation	Type of structural element with damages	*k_{SLS}	*k_{ULS}	*μ	*K_{SLS}	*K_{ULS}	*$K_{SLS}{}^{c}$	*$K_{ULS}{}^{c}$
*SD.1	*EMSW	1	0.5	0.6	EI	0.5EI	0.6EI	0.3EI
*SD.2	*MSW			0.4			0.4EI	0.2EI
*SD.3	*MCB or *MS			0.2			0.2EI	0.1EI
*SD.4	*RCB and *MSW			0.4			0.4EI	0.2EI
*SD.5	*RCS and *MSW			0.3			0.3EI	0.15EI
*SD.6	*MSW			0.2			0.2EI	0.1EI
*SD.7	*RCS			0.5			0.5EI	0.25EI

*where: k_{SLS} – bending stiffness (EI) correction coefficient at SLS that takes into account material (masonry; concrete) cracking during the seismic event (established by the P100-3/2019 norm [15]); k_{ULS} - bending stiffness (EI) correction coefficient at ULS that takes into account material (masonry; concrete) cracking during the seismic event (established by the P100-3/2019 norm [15]); μ - correction coefficient of the bending stiffness K_{SLS} and K_{ULS} at SLS and ULS that takes into account the degradation state of structural elements prior to the seismic event; K_{SLS} – lateral stiffness calculated with k_{SLS} coefficient at SLS in accordance with P100-3/2019 norm [15]; K_{ULS} - lateral stiffness calculated with k_{ULS} coefficient at ULS in accordance with P100-3/2019 norm [15]; $K_{SLS}{}^{c}$ – corrected lateral stiffness calculated with μ coefficient and K_{SLS} value at SLS; $K_{ULS}{}^{c}$ – corrected lateral stiffness calculated with μ coefficient and K_{ULS} value at ULS; EI – bending stiffness; SD – Structural Degradation; EMSW – External Masonry Shear Walls; MSW – Masonry Shear Walls; MCB - Masonry Coupling Beams or MS - Masonry Spandrels; RCB – Reinforced Concrete Beams; RCS – Reinforced Concrete Slabs.

The correction coefficient μ was established based on the information in Table 5 and Table 4 as well as on the experience of the qualified personnel who performed the in-situ inspection. Thus, it can be calculated with Equation 5 the transverse modulus of elasticity G_c for masonry and concrete related to each type of degraded structural element.
It is mentioned that the use of the coefficient μ in the checks of the lateral stiffness of the structure at SLS and ULS, implies in the numerical calculation stage, the concrete assignment of each structural element the imposed value, so that the same type of structural element positioned differently in the structure has different stiffness, so that the type of degradation is different.

$$K_{SLS} = k_{SLS} \cdot EI \tag{1}$$

where: K_{SLS} - lateral rigidity at SLS calculated in accordance with the P100-3/2019 norm [15]; k_{SLS} – bending stiffness (EI) correction coefficient at SLS that takes into account material (masonry; concrete) cracking during the seismic event; EI – bending stiffness.

$$K_{ULS} = k_{ULS} \cdot EI \tag{2}$$

where: K_{ULS} - lateral rigidity at ULS calculated in accordance with the P100-3/2019 norm [15]; k_{ULS} – bending stiffness (EI) correction coefficient at ULS that takes into account material (masonry; concrete) cracking during the seismic event; EI – bending stiffness.

$$K_{SLS}^{c} = \mu \cdot K_{SLS} \tag{3}$$

where: K_{SLS}^{c} - corrected lateral stiffness at SLS; μ – correction coefficient of the bending stiffness K_{SLS} and K_{ULS} at SLS and ULS that takes into account the degradation state of structural elements prior to the seismic event; K_{SLS} - lateral rigidity at SLS calculated in accordance with the P100-3/2019 norm [15].

$$K_{ULS}^{c} = \mu \cdot K_{ULS} \tag{4}$$

where: K_{ULS}^{c} - corrected lateral stiffness at ULS; μ – correction coefficient of the bending stiffness K_{SLS} and K_{ULS} at SLS and ULS that takes into account the degradation state of structural elements prior to the seismic event; K_{ULS} - lateral rigidity at ULS calculated in accordance with the P100-3/2019 norm [15].

$$G_c = 0.4 \cdot E_c \tag{5}$$

where: G_c - corrected transverse modulus of elasticity for masonry/ concrete; E_c - corrected longitudinal modulus of elasticity for masonry/ concrete (see Equation 6).

$$E_c = \mu \cdot E \tag{6}$$

where: E_c - corrected transverse modulus of elasticity for masonry/ concrete material; E - longitudinal modulus of elasticity for masonry/ concrete material.

3.3 Establishment the level of knowledge

The design values of the material characteristics of the existing structure are established according to the values of the confidence factors, CF. The confidence factor is unique to a building, characterizing the level of overall knowledge. The values of the confidence factors are chosen according to the level of knowledge achieved, as follows:

- Limited knowledge level, KL1: CF=1.35;
- Normal knowledge level, KL2: CF=1.20;
- Complete knowledge level, KL3: CF=1.00.

In the case of the analyzed structure, the limited level of knowledge KL1 and a confidence factor CF = 1.35 were chosen, since:

- the geometry of the building was established from a complete survey;
- the detailed project was established on the basis of the simulated design in accordance with the practice at the time of the building construction and on the basis of a limited inspection in the field;
- the mechanical properties of the materials were established on the basis of the values from the valid standards and on the basis of the construction practices from the period of the construction of the building as well as from limited tests in the field.

3.4 Establishment the evaluation methodology

In the case of the analyzed structural system, the Level 2 evaluation methodology was chosen because this methodology can be applied to buildings with any type of structural system, belonging to any earthquake exposure-importance class.
Thus, Level 2 evaluation methodology involves:

- the qualitative assessment of the building based on the criteria of structural configuration, composition and detailing of the constructions and the level of degradation, according to the annexes related to the type of structural system from P100-3/2019 [15];
- quantitative assessment based on a linear static structural analysis and behavior factors.

It is mentioned that the current research study addresses only the qualitative assessment of the structural system.

4 Degree of seismic configuration of the lateral system

In accordance with the Level 2 methodology, compliance with the configuration requirements specified in Table 7 for the UR Masonry structural system is verified, as per the P100-3/2019 code:

Table 7: Configuration requirements for the UR Masonry lateral system in accordance with P100-3/2019 code

No.	Criterion	*Score	Calculation
1	The quality of the structural system	5	Table 8

2	The quality of the masonry	6	-
3	The type of slabs	8	-
4	Horizontal configuration	5	Table 9
5	Vertical configuration	8	-
6	Distances between walls	3	-
7	Elements that provide lateral thrusts	10	-
8	The type of foundation soil and foundation system	7	-
9	Possible interactions with adjacent buildings	9	-
10	Non-structural elements	10	-
	*Sum ∑ =	71	**R_1= 71**
*where: Score – Points are attributed based on the achievement, partial achievement, or non - achievement of the criteria. For full compliance with the criterion, the maximum value of 10 is attributed; for partial compliance with the criterion, a score between 1 and 9 is attributed; for non-fulfillment of the criterion, a score of 0 is given; Sum – the sum of points for all criteria; R_1 – indicator correlated to the degree of seismic configuration of the lateral system.			

Table 8: Checking the density of UR Masonry walls

Level	Global direction of the structure	*$A_{m,net}$ (mm^2)	*A_{sl} (mm^2)	*p (%)	*p_{min} (%)	*Verification
Ground floor (±0.00m)	X direction	20285200	398963200	5.084479	5.5	Not OK
Ground floor (±0.00m)	Y direction	22629000	398963200	5.671951	5.5	OK
First floor (+3.30m)	X direction	26542200	398963200	6.652794	4.5	OK
First floor (+3.30m)	Y direction	21819000	398963200	5.468925	4.5	OK
*where: $A_{m,net}$ - the total net area of structural UR Masonry walls in the global X or Y direction of the structure (see Equation 7); A_{sl} - the total slab area (see Equation 8); p - density of the structural walls (see Equation 9); p_{min} - minimum density of structural walls for UR Masonry buildings with GF+1F height regime and a_g=0.20g at the Ground Floor level (±0.00m) – (see Equation 10) or First Floor level (+3.30m) – (see Equation 11) in accordance with P100-1/2013 norm [13]; Verification – see Equation 12 and Equation 13.						

$$A_{m,net} = \sum A_i \ (mm^2) \tag{7}$$

where: $A_{m,net}$ - the total net area of structural UR Masonry walls in the global X or Y direction of the structure; A_i – the cross-sectional area of each UR Masonry pier.

$$A_{sl} = L \cdot l \ (mm^2) \tag{8}$$

where: A_{sl} – the total slab area; L – floor length; l – floor width.

$$p = A_{m,net}/A_{sl} \cdot 100\ (\%) \tag{9}$$

where: p – the density of the structural walls; $A_{m,net}$ - the total net area of structural UR Masonry walls in the global X or Y direction of the structure (see Equation 7); A_{sl} – the total slab area (see Equation 8).

$$p_{min} = 5.5\ (\%) \tag{10}$$

where: p_{min} – minimum density of structural walls for UR Masonry buildings with GF+1F height regime and a_g=0.20g at the Ground Floor level (±0.00m) in accordance with P100-1/2013 norm [13].

$$p_{min} = 4.5\ (\%) \tag{11}$$

where: p_{min} – minimum density of structural walls for UR Masonry buildings with GF+1F height regime and a_g=0.20g at the First Floor level (+3.30m) in accordance with P100-1/2013 norm [13].

Density verification of the UR Masonry walls:

$$if: p > p_{min} \rightarrow \text{OK} \tag{12}$$

$$if: p < p_{min} \rightarrow \text{NOT OK} \tag{13}$$

where: p – the density of the structural walls (see Equation 9); p_{min} – minimum density of structural walls for UR Masonry buildings (see Equation 10 and Equation 11).

Table 9: Horizontal geometric compactness check

*L (m)	*B (m)	*L/B	*$(L/B)_{max}$	*Verification
35.12	11.36	3.091549	2.0	Not OK
*where: L - the dimension of the building's long side; B - the dimension of the building's short side; L/B - the ratio between long side and short side of the analyzed building; L/B_{max} - the maximum ratio between long side and short side of the analyzed building; Verification – see Equation 14 and Equation 15.				

Horizontal geometric compactness verification of the structure:

$$if: L/B > (L/B)_{max} \rightarrow \text{NOT OK} \tag{14}$$

$$if: L/B < (L/B)_{max} \rightarrow \text{OK} \tag{15}$$

where: L/B – the ratio between long side and short side of the analyzed building; $(L/B)_{max}$ – the maximum ratio between long side and short side of the analyzed building.

5 Degree of structural damage

The degree of structural damage is calculated in accordance with P100-3/2019 norm [13] with Equation 16 depending on the type of material existing in the structural system. In the case of the analyzed building, masonry and concrete were considered as the fundamental types of structural material.

$$R_2 = A_h + A_v \tag{16}$$

where: R_2 – the indicator corresponding to the degree of structural damage; A_h - the score appointed to the damage state of the horizontal structural elements (see Table 10); A_v - the score appointed to the damage state of the vertical structural elements (see Table 10).

Table 10: Calculation of the degree of structural damage for horizontal and vertical elements [13]

Damage category	Vertical elements (A_v)			Horizontal elements (A_h)		
	The affected area			The affected area		
	≤ 1/3	1/3÷2/3	>2/3	≤ 1/3	1/3÷2/3	>2/3
Minor	70	70	70	30	30	30
Moderate	65	60	50	25	**20**	15
Critical	50	**45**	35	20	15	10
Highly critical	30	25	15	15	10	5

Using the information collected in situ, the following values are obtained (see Table 10): A_h = 20; A_v = 45 and $\boldsymbol{R_2}$ = 20+45 = **65**.

6 Discussion

The seismic risk determination for a certain building is done by placing it in one of the following 4 risk classes (in accordance with P100-3/2019 norm [13]):

- RsI - Seismic risk class which includes buildings with total or partial collapse susceptibility to the earthquake action corresponding to the Ultimate Limit State (ULS);
- RsII - Seismic risk class which includes buildings susceptible to major damage to the earthquake action corresponding to the Ultimate Limit State (ULS), which expose to danger the safety of users, but where total or partial collapse is improbable;
- RsIII - Seismic risk class which includes buildings susceptible to moderate damage to the earthquake action corresponding to the Ultimate Limit State (ULS), which may expose to danger the safety of users;
- RsIV - Seismic risk class which includes buildings whose expected seismic response under the effect of the earthquake, corresponding to the Ultimate Limit State (ULS), is similar to that expected seismic response for modern buildings designed with the current technical norms.

Thus, the seismic risk class is established for the R_1 and R_2 indicators based on the score obtained and based on the requirements imposed by the P100-3/2019 norm [13] (see Table 11 and Table 12). The seismic risk class in which the building has been classified, R_s, is established according to Equation 17.

Table 11: R_1 values associated with seismic risk classes [13]

Seismic risk class			
I	II	III	IV
Values			
$R_1<30$	$30\leq R_1<60$	$60\leq R_1<90$	$90\leq R_1\leq100$

Table 12: R_2 values associated with seismic risk classes [13]

Seismic risk class			
I	II	III	IV
Values			
$R_2<50$	$50\leq R_2<70$	$70\leq R_2<90$	$90\leq R_2\leq100$

$$R_s = min(R_1; R_2) \tag{17}$$

where: R_s – seismic risk class in which the building has been classified; R_1 - indicator correlated to the degree of seismic configuration of the lateral system; R_2 – indicator corresponding to the degree of structural damage.

The centralized information of the qualitative seismic evaluation results of the investigated dual structural system can be found in Table 13.

Table 13: The results of the qualitative seismic evaluation of the investigated dual structural system

Degree of seismic configuration of the lateral system, R_1 :	71			
The seismic risk class associated to the R_1 indicator:	III			
Degree of structural damage (affectation), R_2:	65			
The seismic risk class associated to the R_2 indicator:	II			
The seismic risk class in which the building has been classified, R_s (see Equation 17):	I ☐	II ☒	III ☐	IV☐
Ultimate Limite State check:	The existing dual system building follow the Rs II seismic risk class, after ULS examination.			
Description of the seismic risk class [13]:	Rs II - Seismic risk class which includes buildings susceptible to major damage to the earthquake action corresponding to the Ultimate Limit State (ULS), which expose to danger the safety of users, but where total or partial collapse is improbable.			
Check at Service Limit State (SLS):	It is checked the lateral displacements requirements at SLS.			

Conclusions:	According to the obtained results, intervention works on the structural system of the building are needed to increase the degree of seismic structural resistance. In these conditions, it is possible to carry out work for additional floor construction and thermal retrofitting.			
The necessity of the intervention works:	☒ Yes		☐ Not	
Seismic risk class after intervention works, R_s:	I ☐	II ☐	III ☐	IV ☒

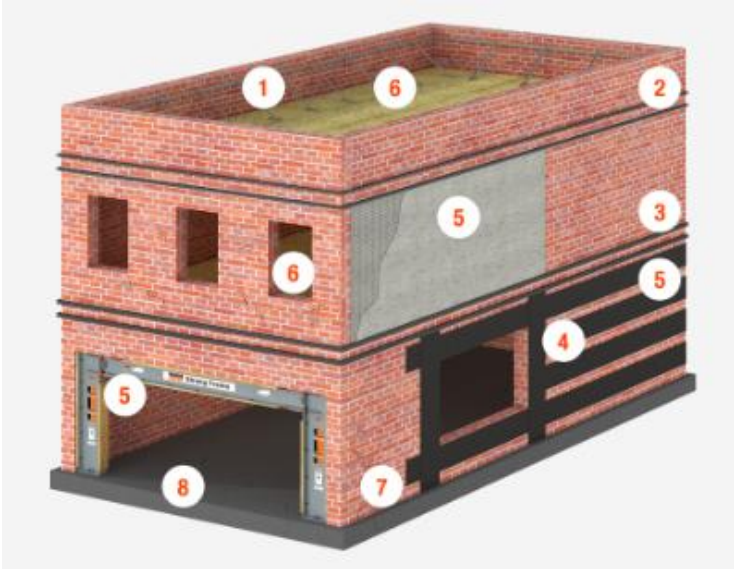

Figure 4: Representation of the retrofit applications for URM buildings [20]: (a) (1) parapet bracing; (2) wall-to-roof anchorage; (3) wall-to-floor anchorage; (4) out-of-plane wall bracing; (5) lateral shear resistance; (6) diaphragm strengthening; (7) veneer anchoring and stitching; (8) concrete foundation

7 Conclusion

The analyzed building with the dual structural system consisting of UR Masonry shear walls and Reinforced Concrete Frames requires intervention work on the lateral structure. Following retrofitting works, additional floor construction and thermal rehabilitation can also be carried out.

The basic approach to improving the seismic performance of URM building is to [19-21] (see Figure 4):

- secure all unrestrained parts that represent falling hazards to the public (e.g. chimneys, parapets and ornaments);
- improve the wall-diaphragm connections or provide alternative load paths; improve the diaphragm; and improve the performance of the face-loaded walls (gables, facades and other walls) by improving the configuration of the building and in-plane walls;
- strengthen specific structural elements, and consider adding new structural components to provide extra support for the building.

The intervention works concern the following rehabilitation techniques for analyzed UR Masonry building [19], [21] (see Figure 4):

- in-plane lateral resistance strengthening with: (a) FRP; (b) FRCM; (c) Reinforced Concrete Shear Walls; (d) Concrete or CMU Infill; (e) Steel special moment frame;
- out-of-plane wall bracing; out-of-plane wall strengthening with: (a) FRP; (b) FRCM;
- diaphragm strengthening;
- concrete foundation for new concrete shear walls.

The necessary intervention works will be executed in compliance with the architectural and structural proposals according to the technical execution project, respectively the measures from the energy audit and the installation proposals.
After the execution of the intervention works, the analyzed building falls under seismic risk class IV. It is also mentioned that the qualitative seismic assessment is a complex and laborious analysis that requires qualified personnel in the field, and an advanced knowledge of the seismic response of the building as well as the rehabilitation methods specific to the analyzed building.

References

[1] Khattak, N., Derakhshan, H., Thambiratnam, D.P., Perera, N.J. (2022). Typological characterisation of vintage unreinforced masonry buildings of Queensland, Australia. *Structures*. 41, pp. 99-116. DOI: https://doi.org/10.1016/j.istruc.2022.04.095.

[2] Khattak, N., Derakhshan, H., Ferreira, T.M., Perera, N.J., Thambiratnam, D.P. (2024). Seismic vulnerability assessment of pre-1945 unreinforced masonry buildings located in Queensland, Australia, using an index-based approach. *Structures.* 67, 106900. DOI: https://doi.org/10.1016/j.istruc.2024.106900.

[3] Buonocunto, V., Acconcia, E., Parisi, F. (2023). Seismic fragility modelling of unreinforced masonry buildings in Campania region. *Procedia Structural Integrity*. 44, pp. 67-74. DOI: https://doi.org/10.1016/j.prostr.2023.01.010.

[4] Yon, B. (2021). Identification of failure mechanisms in existing unreinforced masonry buildings in rural areas after April 4, 2019 earthquake in Turkey. *Journal of Building Engineering*. 43, 102586. DOI: https://doi.org/10.1016/j.jobe.2021.102586.

[5] Cima, V., Tomei, V., Grande, E., Imbimbo, M. (2023). Fragility curves for residential unreinforced masonry buildings prone to out-of-plane mechanisms: the case of the historical center of Sora. *Procedia Structural Integrity*. 44, pp. 211-218. DOI: https://doi.org/10.1016/j.prostr.2023.01.028.

[6] Kaya, A., Adanur, S., Bello, R. A., Genc, A. F., Okur, F. Y., Sunca, F., Gunaydin, M., Altunisik, A. C., Sevim, B. (2023). Post-earthquake damage assessments of unreinforced masonry (URM) buildings by shake table test and numerical visualization. *Engineering Failure Analysis*. 143, 106858. DOI: https://doi.org/10.1016/j.engfailanal.2022.106858.

[7] Shabani, A., Zucconi, M., Kazemian, D., Kioumarsi, M. (2023). Seismic fragility analysis of low-rise unreinforced masonry buildings subjected to near- and far-field ground motions. *Results in Engineering.* 18, 101221. DOI: https://doi.org/10.1016/j.rineng.2023.101221.

[8] Zarzour, N., Avila, M. P. S., Mercerat, E. D., Lenti, L., Oggero, M. (2023). Behavior factor estimation for seismic design of unreinforced masonry buildings. *Case Studies in Construction Materials.* 19, e02483. DOI: https://doi.org/10.1016/j.cscm.2023.e02483.

[9] Mezzina, M., Sollazzo, A., Uva, G. (2023). Torsional response of unreinforced masonry buildings. *Procedia Structural Integrity*. 44, pp. 566-573. DOI: https://doi.org/10.1016/j.prostr.2023.01.074.

[10] Bracchi, S., Rota, M., Penna, A. (2023). Comparison of refined and code-compliant modelling strategies for the seismic analysis of unreinforced masonry buildings. *Procedia Structural Integrity*. 44, pp. 442-449. DOI: https://doi.org/10.1016/j.prostr.2023.01.058.

[11] Kayirga, O. M., Altun, F. (2021). Investigation of earthquake behavior of unreinforced masonry buildings having different opening sizes: Experimental studies and numerical simulation. *Journal of Building Engineering*. 40, 102666. DOI: https://doi.org/10.1016/j.jobe.2021.102666.

[12] Guvernul României. (1997). *Hotărârea nr. 766/1997 pentru aprobarea unor regulamente privind calitatea în construcții*. Monitorul Oficial al României.

[13] Ministerul Dezvoltării Regionale și Administrației Publice (MDRAP). (2013). *Cod de proiectare seismică – Partea I – Prevederi de proiectare pentru clădiri.* Indicativ P100-1/2013. Romania.

[14] Besen, P., Boarin, P. (2023). Integrating energy retrofit with seismic upgrades to future-proof built heritage: Case studies of unreinforced masonry buildings in Aotearoa New Zealand. *Building and Environment*. 241, 110512. DOI: https://doi.org/10.1016/j.buildenv.2023.110512.

[15] Ministerul Dezvoltării Regionale și Administrației Publice (MDRAP). (2013). *Cod de proiectare seismică – Partea a III-a – Prevederi pentru evaluarea seismică a clădirilor existente.* Indicativ P100-3/2019. Romania.

[16] Ministerul Dezvoltării Regionale și Turismului (MDRT). (2012). *Cod de proiectare. Evaluarea acțiunii zăpezii asupra construcțiilor.* Indicativ CR 1-1-3/2012. Romania.

[17] Ministerul Dezvoltării Regionale și Turismului (MDRT). (2012). *Cod de proiectare. Evaluarea acțiunii vântului asupra construcțiilor.* Indicativ CR 1-1-4/2012. Romania.

[18] Institutul Român de Standardizare (IRS). (1977). *Adâncimi maxime de îngheț.* Indicativ STAS 6054-77. Romania.

[19] Federal Emergency Management Agency (FEMA). (2006). *Techniques for the Seismic Rehabilitation of Existing Buildings: FEMA 547*. U.S., Washington D.C.: U.S. Department of Homeland Security.

[20] SIMPSON Strong-Tie Company. (2024). *https://www.strongtie.com/solutions/unreinforced-masonry-seismic-retrofit/out-of-plane-wall-bracing*. Date of access: 24.09.2024

[21] Ministry of Business, Innovation and Employment and the Earthquake Commission. (2017). *Unreinforced Masonry Buildings. Part C – Detailed Seismic Assessment*. C8 – Part C. New Zealand.

DOI: 10.2478/sspjce-2024-0015

Cognitive and Environmental Benefits of Blue-Green Infrastructure and Green Skills Training

Zuzana Vranayova[1*], Daniela Kaposztasova[2], Anna Lis[3]

[1]Institute of Architectural Engineering, Faculty of Civil Engineering, Technical University of Kosice, Vysokoškolská 4, 042 00 Kosice, Slovakia
[2]Center of Research and Innovation in Construction, Park Komenského 10/A, Faculty of Civil Engineering, Technical University of Kosice, 042 00 Kosice, Slovakia,
[3]Czestochowa University of Technology; Faculty of Civil Engineering, Poland, anna.lis@pcz.pl
*e-mail: zuzana.vranayova@tuke.sk

Abstract

As cities face escalating challenges related to urbanization, public health, and climate change, innovative solutions are needed to create resilient, sustainable urban environments. Blue-green infrastructure, which integrates green spaces and water management elements, offers significant cognitive, environmental, and social benefits. This paper explores how blue-green infrastructure, coupled with initiatives like the SECOVE project, can enhance urban resilience, promote community well-being, and reduce environmental impact. By fostering vocational training in green building skills, cities can support sustainable development, job creation, and improve quality of life for urban residents. The findings emphasize the importance of integrating ecological design with skilled labor to build urban environments that are healthier, more resilient, and aligned with sustainability goals.

Keywords: cognitive health, sponge city model, dementia prevention, sustainable energy, vocational excellence

1 Introduction

As cities expand and urbanization accelerates, the challenges they face grow increasingly complex and interconnected. Urban heat islands, for instance, can elevate city temperatures by up to 7°C compared to surrounding rural areas, exacerbating health risks and energy demands during heatwaves. Simultaneously, the global population affected by dementia—currently estimated at 55 million—is projected to more than double by 2050, raising urgent questions about public health in urban contexts. These trends underline the need for innovative urban solutions that address environmental, social, and health-related challenges comprehensively. This paper explores how blue-green infrastructure—integrating natural and water management elements—can mitigate these urban challenges while promoting cognitive health, environmental resilience, and social well-being. Specifically, it examines the interplay between green urban spaces, vocational training in green skills, and sustainable urban design. By reviewing global case studies, conducting environmental impact assessments, and analyzing the

outcomes of vocational training initiatives like the SECOVE project, this study highlights practical strategies for creating healthier, more sustainable cities.

The concept of blue-green infrastructure combines ecological, water management, and urban planning strategies, integrating green elements like parks, green roofs, and water bodies within urban settings. These features provide “ecosystem services” that improve air quality, regulate temperature, and mitigate flood risks, while offering recreational spaces that benefit mental health [2]. The sponge city model, for example, originated in China as a sustainable response to flooding and urban runoff. It utilizes permeable surfaces, rain gardens, and other water management features that naturally capture and filter stormwater. This model not only addresses flooding but also creates spaces that enhance urban aesthetics and promote physical activity, both of which are linked to better cognitive health outcomes [3].

In addition to infrastructure changes, addressing the growing demand for green building skills is crucial for the sustainability of urban spaces. Initiatives like the Sustainable Energy Centers of Vocational Excellence (SECOVE) are designed to cultivate vocational skills that align with sustainability goals, offering training in green building techniques and renewable energy systems. These vocational programs prepare a workforce equipped to design, implement, and maintain sustainable urban features, making them essential to expanding blue-green infrastructure and supporting the mental and physical health benefits it provides [4].

This paper argues that by integrating blue-green infrastructure with skilled green building professionals, cities can foster environments that support cognitive health and resilience. The interconnected benefits of blue-green infrastructure and sustainable vocational training extend beyond individual health impacts, reinforcing broader environmental goals such as biodiversity conservation and climate adaptation. It aims to contribute to the growing body of knowledge on sustainable urban planning by demonstrating how ecologically friendly design and skilled labor can create cities that are both healthier for residents and more resilient to climate challenges.

2 Methods

Green infrastructure encompasses a network of green and blue elements designed to support biodiversity, improve air quality, and regulate urban microclimates. Examples include urban parks, green roofs, permeable pavements, and water retention systems. Blue-green infrastructure specifically integrates water and green spaces, functioning as urban "sponges" that absorb rainwater, reduce flood risks, and contribute to the ecological balance within urban spaces [3]. Sponge city elements, inspired by traditional Chinese water management, use rain gardens, bioswales, and other permeable surfaces to naturally manage stormwater while providing aesthetic and recreational benefits to residents [5].

Green buildings are an essential part of this framework, constructed with materials and technologies that minimize environmental impact and optimize energy efficiency. In the European Union, green building certification systems like BREEAM and LEED are setting industry standards by promoting renewable energy, sustainable materials, and efficient waste

management. The SECOVE project aligns with these goals, emphasizing the importance of upskilling in green construction and energy technologies to meet evolving market demands.

We used the methods that collectively provide a well-rounded approach, combining quantitative, qualitative, and spatial data to support a comprehensive analysis of the cognitive and environmental impacts of blue-green infrastructure and the importance of vocational training in green building skills.

A comprehensive literature review was conducted to gather existing research on the links between blue-green infrastructure, cognitive health, and sustainable urban design. This review included peer-reviewed studies on ecosystem services, green infrastructure's impact on health, and the role of vocational training in sustainable skill development. The literature review provided a theoretical foundation for understanding how blue-green infrastructure and sustainable skills can contribute to cognitive health and environmental resilience.

To examine real-world examples, a case study analysis was conducted on specific cities that have implemented blue-green infrastructure, such as the sponge city model in China and green building initiatives in Europe. These case studies were analyzed for their impact on urban resilience, flood mitigation, and community well-being. Each case was evaluated on key indicators such as air quality improvement, temperature regulation, and mental health outcomes.

A survey was designed to assess the cognitive and mental health benefits experienced by individuals who regularly access blue-green infrastructure in urban areas. Survey questions focused on variables such as perceived stress levels, mood, and mental clarity. Statistical analysis was then used to evaluate the relationship between access to natural urban spaces and reported cognitive health benefits.

An Environmental Impact Assessment (EIA) was used to evaluate the effects of blue-green infrastructure on urban ecosystems, focusing on water quality, biodiversity, and air quality improvements. This method involved collecting data on pollutants, biodiversity levels, and heat island mitigation in areas with green infrastructure and comparing it to control areas without such features.

A comparative analysis was conducted on vocational training programs related to green skills, such as those provided by the SECOVE project. Training outcomes, employment rates, and skill proficiency levels of graduates were compared across programs to assess the efficacy of green skills training. This analysis helped identify best practices for training a skilled workforce that can effectively support and maintain sustainable urban infrastructures.

Focus groups were conducted with vocational trainees, urban planners, and residents to gain qualitative insights into perceptions of blue-green infrastructure. The focus groups explored participants' experiences with green spaces, attitudes toward sustainable urban design, and suggestions for improvements. The qualitative data collected provided additional context to the quantitative survey results.

2.1 Case Studies: Practical Applications of Blue-Green Infrastructure

Real-world implementations of blue-green infrastructure provide compelling evidence of its effectiveness in addressing urban challenges. For instance, Guangzhou, China, has significantly reduced flooding through its sponge city model, utilizing rain gardens and permeable pavements that doubled as community green spaces. Similarly, Copenhagen's Cloudburst Management Plan transformed urban landscapes with pocket parks and retention lakes, cutting flood risks while promoting biodiversity. Singapore's Bishan-Ang Mo Kio Park exemplifies the dual benefits of flood management and public recreation by converting concrete canals into naturalized rivers. In Europe, Milan's Bosco Verticale integrates vertical forests into residential architecture, improving air quality and reducing energy use. These examples highlight how innovative urban design not only mitigates environmental risks but also enhances community well-being, biodiversity, and economic resilience.

3 Results and discussion

Ecosystem services in urban environments - especially those provided by green and blue infrastructure - play an essential role in supporting cognitive health and overall mental well-being. According to Kaplan and Kaplan's Attention Restoration Theory [6], natural environments provide "soft fascinations," like the sound of water or the movement of leaves, which gently engage the mind and offer cognitive restoration by alleviating mental fatigue. This theory is supported by findings indicating that individuals who spend time in natural settings experience improved concentration, reduced stress, and enhanced cognitive performance [7]. Urban green spaces, such as parks and water features integrated within the sponge city framework, offer city dwellers opportunities for physical activities, relaxation, and social interaction, all of which contribute to mental resilience. The link between blue-green infrastructure and cognitive health benefits, with elements like parks, water features, and sponge city rain gardens that support mental well-being, reduce stress, and improve air quality. This clean and visually engaging design highlights the urban-nature integration and health advantages effectively (Fig. 1).

In urban areas where stress and mental fatigue are prevalent due to pollution, noise, and crowding, access to nature has shown measurable health benefits. For instance, research by Hartig et al. [8] demonstrates that people living near green spaces report fewer stress-related conditions and better overall health. Blue spaces - water bodies like rivers, lakes, and constructed water retention systems - also play a significant role in reducing stress, promoting physical activity, and enhancing social connectivity, all of which are beneficial for mental health and potentially protective against dementia and other cognitive impairments [9-11].

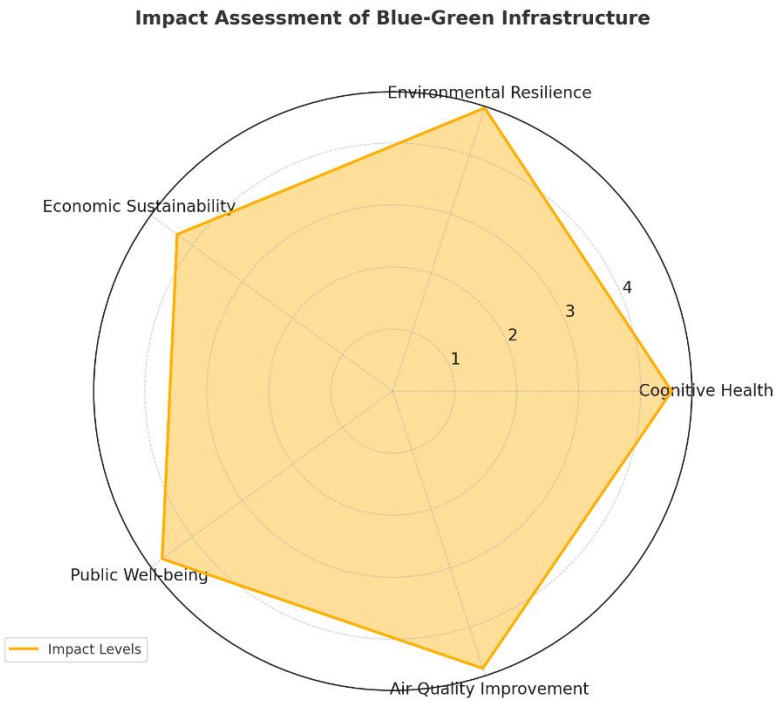

Figure 1: The radar chart that visually represents the impact of blue-green infrastructure across various benefit categories, such as cognitive health, environmental resilience, and economic sustainability

Green infrastructure and vocational training in sustainable skills contribute to cognitive health by creating a meaningful connection to the environment, enhancing community engagement, and providing career pathways in environmentally friendly fields. The SECOVE project exemplifies how vocational training in sustainable energy and green building practices prepares a workforce skilled in creating and maintaining these cognitively beneficial spaces [4]. Training programs not only address ecological needs but also enhance personal well-being, as individuals trained in sustainability roles report a higher sense of purpose and satisfaction in contributing to environmental and community health [4].

The connection between ecosystem services and cognitive health also extends to economic and educational dimensions. Research indicates that environmental literacy and hands-on training in sustainable skills can improve mental well-being by instilling a sense of environmental stewardship and personal efficacy. This vocational approach allows individuals to participate in the design and maintenance of green spaces, reinforcing the impact of these spaces on collective mental health. Additionally, creating job opportunities in green sectors supports cognitive health at a community level, as it fosters a sense of ownership and empowerment among residents and professionals involved in sustainable urban development [12].

By equipping individuals with vocational skills to support and expand these infrastructures, projects like SECOVE contribute to a cycle of positive reinforcement: well-designed urban green spaces support cognitive health, and those working to create and sustain these spaces benefit from their effects as well. This comprehensive approach not only addresses public health

but also aligns with broader sustainability goals, thereby reinforcing the resilience of both individuals and communities in an increasingly urbanized world.

The successful integration of blue-green infrastructure and green building practices in urban areas relies on collaborative efforts across sectors. Health researchers, urban planners, and industry leaders must work together to embed these green elements into city planning policies. The SECOVE project exemplifies how partnerships between vocational institutions and industry stakeholders provide students with hands-on experience in green skills, reinforcing the workforce needed to sustain these infrastructures. Policy initiatives aimed at incentivizing green building certifications, sustainable energy adoption, and urban green spaces can help catalyze the widespread adoption of these practices [13].

Economic advantages are significant, with potential healthcare savings resulting from reduced pollution-related illnesses and lower dementia prevalence. A recent study by Marselle et al. [12] found that green spaces contribute to lower healthcare costs by reducing symptoms of anxiety, depression, and cognitive decline in urban populations. Additionally, green building practices offer substantial energy savings, reduce operational costs, and contribute to higher property values, making them economically appealing to developers and municipalities alike.

4 Conclusion

The convergence of blue-green infrastructure and green building practices presents an opportunity to address multiple urban challenges, from cognitive health and environmental sustainability to economic resilience (See Table 1).

Table 1: The Outcome Benefits of blue-green infrastructure

Benefit Category	**Specific Benefits**
Cognitive Health	Reduced stress, improved mental clarity
Environmental Resilience	Mitigation of urban heat effects, flood control
Economic Sustainability	Lower energy costs, increased property values
Public Well-being	Enhanced opportunities for physical activity, relaxation
Air Quality Improvement	Reduced pollution, improved overall air quality

Our review study underscores the potential of blue-green infrastructure to promote cognitive health, environmental resilience, and economic sustainability in urban settings. By integrating features like green spaces, water bodies, and sustainable building practices, cities can foster environments that enhance public well-being, mitigate urban heat effects, and improve air quality. The cognitive benefits of blue-green infrastructure, such as reduced stress and improved mental clarity, are particularly significant in urban areas where individuals face high levels of environmental stressors. Furthermore, the role of vocational training, exemplified by initiatives like SECOVE, is crucial in equipping a skilled workforce to support and sustain these green urban elements effectively.

The economic benefits extend beyond immediate cost savings on energy and maintenance. Investments in green infrastructure can also lead to lower healthcare expenses due to reduced pollution-related illnesses and mental health improvements. This dual impact of environmental and health gains suggests that blue-green infrastructure is not just an aesthetic addition to urban landscapes but a foundational aspect of sustainable urban planning. Additionally, the integration of vocational training programs in sustainable practices enhances community resilience by fostering local expertise, creating job opportunities, and promoting environmental stewardship among future generations.

However, successful implementation requires a multi-disciplinary approach. Collaboration between urban planners, policymakers, healthcare providers, and educational institutions is essential to realizing the full potential of these infrastructures. Policymakers can play a transformative role by providing incentives for green buildings, enforcing sustainable urban designs, and integrating vocational training into the educational framework [7, 8, 13, 14].

Future research could further explore long-term cognitive benefits of access to blue-green infrastructure in diverse urban settings, examining factors like accessibility, design quality, and social engagement [9, 11]. Additionally, studies on the economic impact of green infrastructure at various stages of urban development could provide valuable insights for regions considering its adoption. By continuing to investigate the comprehensive benefits of blue-green infrastructure, cities can better design, implement, and maintain resilient environments that promote well-being, sustainability, and equity.

Acknowledgments

The authors are grateful for the support of the Erasmus+ Programme of the EU **“**SECOVE Sustainable Energy Centres for Vocational Excellence” (Project No. 101056201).

References

[1] World Health Organization. (2021). *Dementia fact sheet.* https://www.who.int/news-room/fact-sheets/detail/dementia

[2] Milcu, A. I., Hanspach, J., Abson, D., & Fischer, J. (2013). Cultural ecosystem services: A literature review and prospects for future research. *Ecology and Society*, *18*(3), Article 44.

[3] Li, Z., He, B. J., & Liu, W. (2021). Blue-green infrastructure for sustainable urban stormwater management. *Water Resources Management, 35*, 1121–1139. https://doi.org/10.1007/s11269-021-02748-0

[4] SECOVE. (2023). *Sustainable Energy Centres of Vocational Excellence: Advancing skills in green building and renewable energy*. European Commission, Erasmus+ Programme. Retrieved from [https://secove-project.eu/]

[5] Ma, X., & Jiang, Y. (2022). Sponge city implementation in China: A review of outcomes and challenges. *Water*, *14*(1), 24. https://doi.org/10.3390/w14010024

[6] Kaplan, R., & Kaplan, S. (1989). *The experience of nature: A psychological perspective.* Cambridge University Press.

[7] Berto, R. (2014). The role of nature in coping with psycho-physiological stress: A literature review on restorativeness. *International Journal of Environmental Research and Public Health, 11*(9), 10025–10052. https://doi.org/10.3390/ijerph110910025

[8] Hartig, T., Mitchell, R., de Vries, S., & Frumkin, H. (2014). Nature and health. *Annual Review of Public Health, 35*, 207-228. https://doi.org/10.1146/annurev-publhealth-032013-182443

[9] White, M. P., Alcock, I., Wheeler, B. W., & Depledge, M. H. (2010). Would you be happier living in a greener urban area? A fixed-effects analysis of panel data. *Psychological Science, 24*(6), 920-928. https://doi.org/10.1177/0956797612464659

[10] Heckert, M., & Mennis, J. (2021). Green infrastructure for public health improvement: A systematic review. *International Journal of Environmental Research and Public Health, 18*(3), 976. https://doi.org/10.3390/ijerph18030976

[11] Markevych, I., Tiesler, C. M. T., Fuertes, E., Romanos, M., Dadvand, P., Nieuwenhuijsen, M. J., & Heinrich, J. (2017). A systematic review of the influence of green space on health. *Environmental Research, 158*, 268–280. https://doi.org/10.1016/j.envres.2017.06.028

[12] Roe, J. J., Thompson, C. W., Aspinall, P. A., Brewer, M. J., Duff, E. I., Miller, D., & Clow, A. (2013). Green space and stress: Evidence from cortisol measures in deprived urban communities. *International Journal of Environmental Research and Public Health, 10*(9), 4086-4103. https://doi.org/10.3390/ijerph10094086

[13] European Commission. (2013). *Building a green infrastructure for Europe.* Publications Office of the European Union.

[14] Marselle, M. R., Warber, S. L., & Irvine, K. N. (2019). Growing resilience through green infrastructure: The role of biodiversity in enhancing restorative environments. *Urban Forestry & Urban Greening, 39*, 128–139. https://doi.org/10.1016/j.ufug.2018.03.016

DOI: 10.2478/sspjce-2024-0016

Influence of the Angular Position of a New Tunnel on Movement in the Surrounding Existing Tunnel

Bousbia Nawel

Faculty of Technology, Department of Civil Engineering, LMGHU Laboratory, University of 20 August 1955, Skikda, Algeria
e-mail: bousbia1101@yahoo.com /n.bousbia@univ-skikda.dz

Abstract

The development of transportation in large cities requires the construction of new structures subterranean in close proximity to existed structures subterranean. Finding the best appropriate position of the new structure subterranean will help to minimize the magnitude of movement there will be in soil surrounding the existing one. The purpose of this study is to involve assessing the immediate influences that will result from the new tunnel excavation in close proximity to existed tunnel at different angular positions ß (0° to 180°) relative to existing one, especially destabilization of the soil surrounding, including movements, displacements of soil mass and surface settlement, in addition to internal efforts generated in lining of old tunnel, and to provide a solution by selecting an ideal angular position for the tunnel that will be excavated relative to the existing one. This is a crucial factor when searching for a full solution to the problem of interactions between subterranean structures. This study uses numerical analysis to examine the movements and displacements of soil mass surrounding, the settlement and the internal efforts induced in the old tunnel's lining impacted by the new tunnel excavation. Several factors, such as the excavation technique, tunnel spacing, liner thickness, etc., had a favorable impact on diminishing the extreme values acquired at the critical angle position (ß =135°). A parametric study was conducted to minimize the maximum values obtained. As a result, these elements could affect planning and security objectives.

Key words: tunnel, displacement, settlement, angular position, Plaxis

1 Introduction

Subterranean space is a solution that works well over an extended period of time and can even help handle specific problems that are difficult to resolve on the surface, as the overpopulation of infrastructure and facilities gets more. In certain towns, new tunnels must be constructed adjacent to the existing ones due to subsurface and geotechnical characteristics. The impact of the construction of new subterranean structure on old one and its surroundings, particularly structurally, where it seems to be of significance to evaluate the

interaction between underground constructions. Among the most significant subterranean structures are the tunnels, whose construction requires careful planning, particularly with regard to dimensionality and interaction with other subterranean structures in crowded cities [1]. Many new tunnels must be planned and constructed either parallel to or next to an existing tunnel. Due to the significant connection between these tunnels brought about by the increase in their use in urban areas, study on the interactions between tunnels and soil is essential. Thus, the designer has to take into account a minimum of two crucial factors: The way the new tunnel interacts with the old tunnel: To maintain the integrity of the current tunnel, the additional predicted movements and displacements caused in the surrounding soil. Many studies have been carried out in order to understand the mechanics of the interaction between the tunnel and soil [2]. A summary of the impact of tunnel construction on the nearby existing tunnel was also provided by a number of researchers [3-4-5-6-7-8]. The goal of this research is to simulate numerically the effect of constructing a new tunnel in the shallow cover zone at different angular positions ß (0°à 180°) relative to an existing tunnel on soil mass surrounding. The tunnel T4 at twin tubes is still being studied in our research case. The 2500 m long highway tunnel is made up of two tubes that are essentially parallel to one another. (Figures 1 and 2). The present case involves assessing the vertical and horizontal displacements of soil mass as well as the displacements and movements. The tunnel T4 at twin tubes is still being studied in our research case. The present case involves assessing the vertical and horizontal displacements of soil mass as well as the displacements and movements.

Figure 1: General view of the tunnel T4

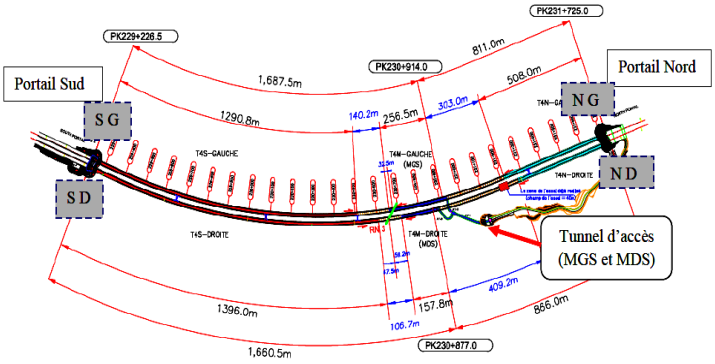

Figure 2: Trace in plane of the Tunnel T4

2 Presentation of tunnel t4

The relief between the kilometer point (KP 229+220 and 231+750) will be crossed by double tubes, and the Tunnel T4 functions as an underground way. The transverse section of each tube is 17.9 m wide and 13 m high. The 320-meter access tunnel's goal is to speed up construction toward the South Portal while establishing two more fronts of attack in the center of the tunnel. It links to the main tube at 811 meters to the North Portal. The tunnel's tracing is elevated at 1/50.000th on the S'mendou geological card [9].

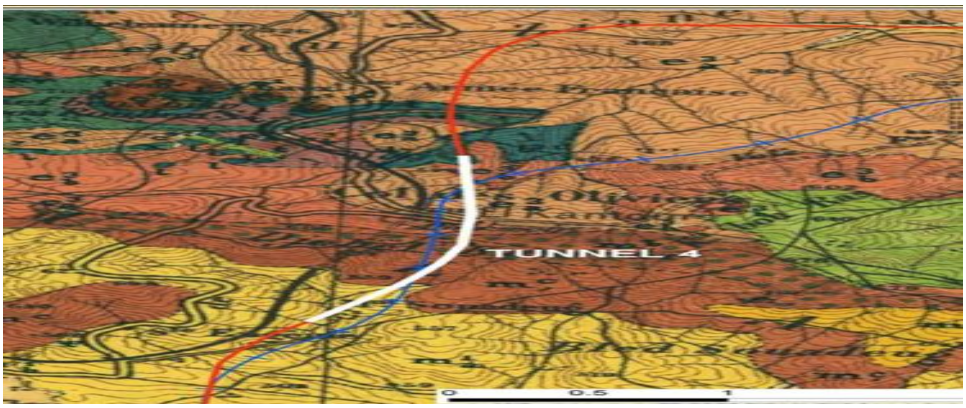

Figure 3: Site of the tunnel T4 on S'mendou the geological card (Constantine-Algeria)

3 Numerical model of tunnel section

One useful method for studying difficult problems of tunneling in the deep cover zone is numerical analysis [10]. The commercial program Plaxis2D was developed specifically to analyze the behavior of soil and infrastructure under stress. The program allows a repetitive geometric cross section to be used as the basis for the creation of a two-dimensional finite element mesh. This section had a 200 m wide by 100 m deep. In this study, we examined at the effects of changing the new tunnel's angular position that will be excavated relative to an old tunnel on the movements and displacements of surrounding soil. It was assumed that the first tunnel would be excavated before moving on to the second.

3.1 Numerical model definition

The cross-section of the tunnels is circular, with an outside diameter of 15 m and a concrete lining thickness of 0.40 m. The tunnel's crown C was 32 m below the soil's surface, meaning that C/D=2,13. 200 m x 100 m was the chosen grid space for the problem analysis. The Mohr-Coulomb failure criteria was utilized to obtain the requisite Elasto-plastic response of the soil.

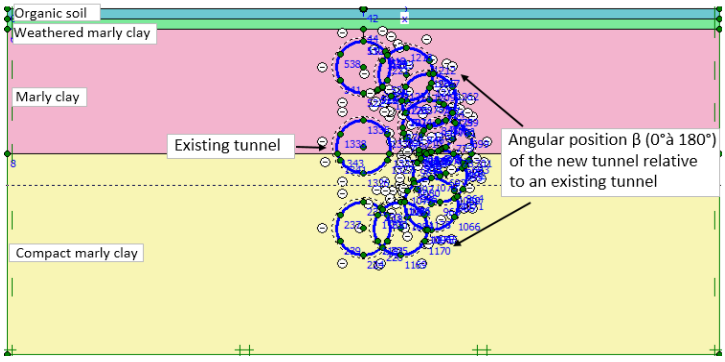

Figure 4: Angular position β (0°à 180°) relative to an existing tunnel via Plaxis 2D model

3.2 Model simulation

The behavior of the soil was described by the Mohr-Coulomb model. The two tunnels, each with a circular piece of 15 meters in diameter, were supposed to open in a circle. After completely excavating the pre-existing bored tunnel, the tunnel is immediately secured to its lining. The tunnel is assumed to have been built in homogeneous soil. Furthermore, the research was conducted using the linear elastic model of the tunnel lining. There are four distinct layers of soil around the two tunnels. The following is a precis of the geotechnical section that was chosen for the analysis:
0.0-3.0m Unit 1 / Organic soil /
0-5.5m Unit 2 / Weathered marly clay
5.5m -41.0m Unit 5 / Marly clay
H >41.0m Unit 4 / Compact marly clay

An elastic-plastic constitutive model provided by the properties listed in table 1.
Tunnel lining properties used in the present study are shown in table 2.

Table 1: Parameters of the soil layers applied in the numerical modelling

Soils	Thick (m)	γ (kN/m^3)	E (MPa)	ν	C (KPa)	ø (°)
Unit 1	3	16,50	5	0.30	5	27
Unit 2	2.5	27,50	25	0.30	5	27
Unit 3	35.5	20	140	0.30	25	20
Unit 4	24.5	22	240	0.30	30	22

Table 2: Properties of lining tunnel's thickness (40cm)

	E (MPa)	A (m^2)	I (m^4)	d	EA$_{eq}$ (kN/m)	EI$_{eq}$ (kN.m^2/m)	ν	d$_{equival}$ (m)
Shotcrete	2.8x10^4	0,4	5.33*10 $^{-3}$	1	5,18x10^6	6,9x10^4	0,20	0,4
Steel H200*200	2.1x10^5	78.1x10 $^{-4}$	0.569x10^{-4}	1				

4 Presentation of tunnel T4

The "NATM" will be followed in the construction of the tunnels, what characterizes it notably is the precocious application of the support in order to control the first deformation and to prevent all laxity to the tunnel front. We selected a simplified model in the form of a circular section for this study. In this section, we aim to compute the kilometer point [231 + 253] to the left of the north portal (weak cover zone = 32 m). Measurements taken up to this point indicate that, following a 10-meter excavation, settlement Z1 reached a height of 15 cm. Up to 20 cm, settlement stabilizes. (Figure 5)

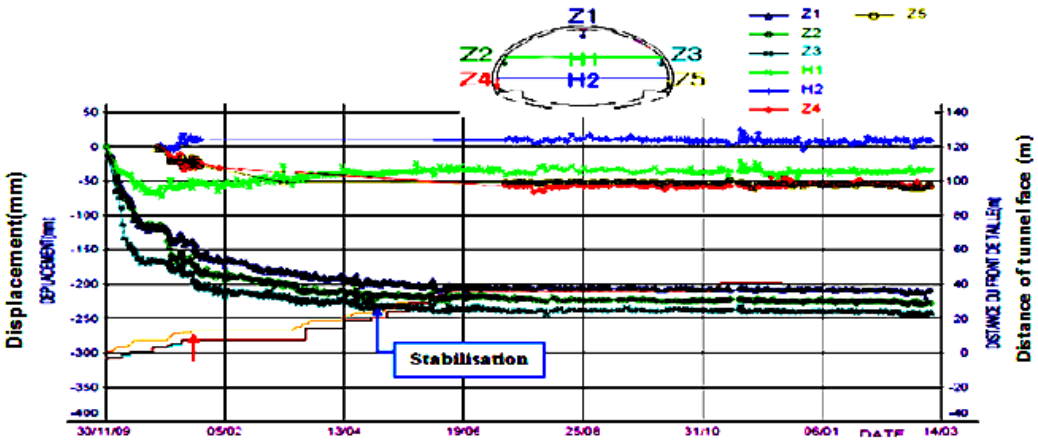

Figure 5: Settlement & convergence of point (231+253) (Reference case)

5 Influence of the new tunnel angular position relative to an existing on movements and displacements surrounding soil

5.1 Modelling of excavation according to bored tunnel type

The convergence confinement method has been applied in this study for analyzing the tunnel-soil interaction, according to [11-12]. Each tunnel's construction process has been modeled; we use a step-by-step approach. Generally, the process has been modeled in two steps, with each stage's excavation process consisting of: (I) fully deactivating any soil elements contained in the segment that needs to be excavated; (II) fully activating the tunnel lining and relieving all stresses in that segment. The second tunnel's excavation followed the same methodology used for the first tunnel's completion. As part of this process, the movements, displacements, and settlement at surface soil at each position ß of the new tunnel in relation to an existing tunnel are to be determined numerically: The approval for the finite element modeling of the two tunnel buildings is as follows: (I-1) Excavation of the first tunnel with λ_1 = 0.3 stress release factor. This factor relates to the proportion of the stress release prior to the liner installation. (I-2) Installing the first tunnel's lining (II-1) utilizing the same technique and stress release factor for the construction of the second tunnel. In terms of boundary conditions, displacements are restricted in both directions at the bottom and must be zero horizontal at lateral limits.

5.2 Result of analyses

5.2.1 Description of the problem

The fundamental issue for analysis is depicted in figure 6. It includes building a circular tunnel with a diameter of 15 meters and a concrete liner that is 0.40 meters thick. The tunnel is 32 meters below the level of the soil. The distance between the two tunnels was kept at three times the tunnel radius (3R) measured from center to center. There could be intolerable

soil movement as a result of building the new tunnel. The position, space, and stiffness of the lining between tunnels determine the type of interaction that occurs between them.

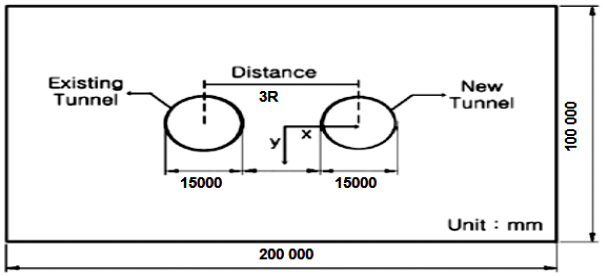

Figure 6: Description of the problem

5.2.2 Settlement and displacements due to tunneling

Möller, S.C. et al. [13], state that the tunneling causes the in situ stress to decrease. The section and position of the tunnel to be constructed, and the excavation technique to be used, also the soils type all influence the magnitude of movement there will be. The ground movements in surrounding tunnel are the cause of the surface soil subsidence. This study has to examine at the immediate effects of a new tunnel's angular position in respect to the surrounding soil displacements. We proceed to determine the impact of the newly excavated tunnel next to the existing tunnel based on different angular locations β. Initially, we will limit the movements occurring from the excavation of one tunnel, followed by the excavation of both tunnels.

❖ **First Case: Single tunnel**

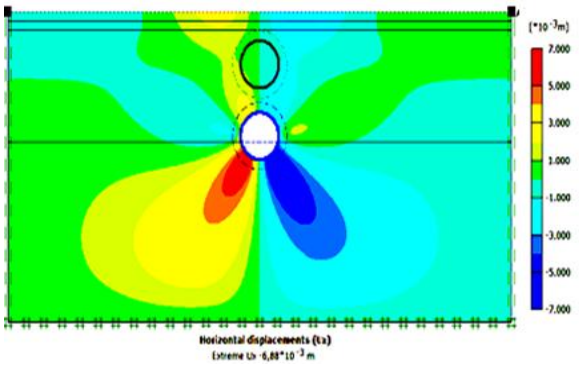

Figure 7: Contours of horizontal displacements (U_x= -6.88mm) around the single tunnel

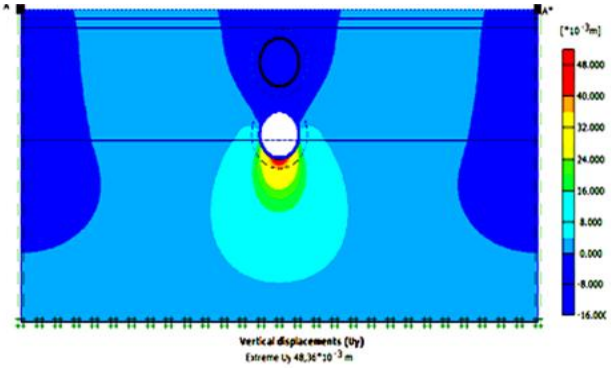

Figure 8: Contours of vertical displacements (U_y= -48.36mm) around the single tunnel

❖ **Second Case: Both tunnels (New – old)**

Secondly, we go to test the influence the angular position of the new tunnel to be excavated relative to an existing on the movements soil surrounding. Nine positions ß (0°; 22.5°; 45°; 67.5°; 90°; 112.5°; 135°; 157.5°; 180°) were modelled. The results are showing in the table 3.

Table3: Summary of settlement and displacements values generated by new tunnel excavation

Positions	Angle (ß)	Settlement (mm)	Horiz displ (mm)	Vert displ (mm)
1	0°	11.71	-10.62	58.65

2	22.5°	13.32	8.29	59.62
3	45°	10.10	8.41	60.39
4	67.5°	-5.70	9.76	58.73
5	90°	-5.14	7.99	52.96
6	112.5°	-15.76	12.48	62.28
7	135°	-19.55	-10.94	66.11
8	157.5°	-15.31	-16.57	65.02
9	180°	-11.96	-18.24	63.85

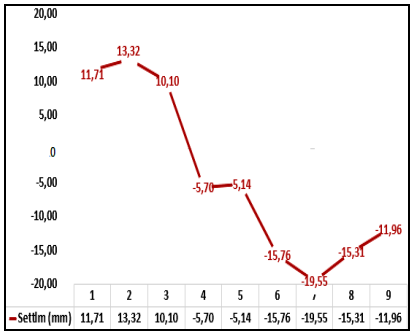

Figure 9: Variation of settlement

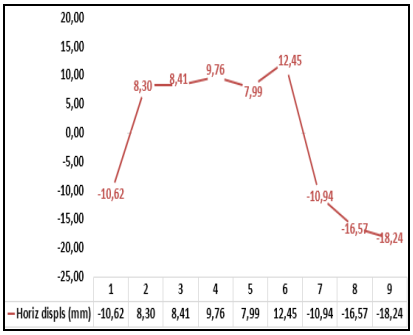

Figure. 10 Horiz-displacement

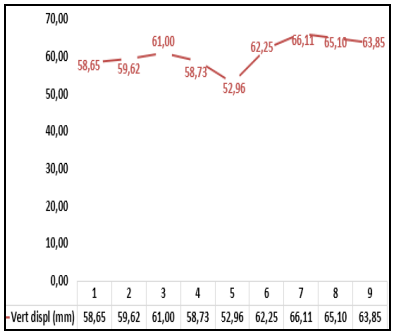

Figure.11: Vert-displacement

Figures 9, 10, and 11 show the maximum settlement, horizontal displacement, and vertical displacement values that correspond to the various angular positions ß of the new tunnel (0° to 180°). it is clear that the minimal values of displacement and settlement occur at 90°. The two tunnels are designed to be horizontally aligned on the same elevation (ß = 90°),

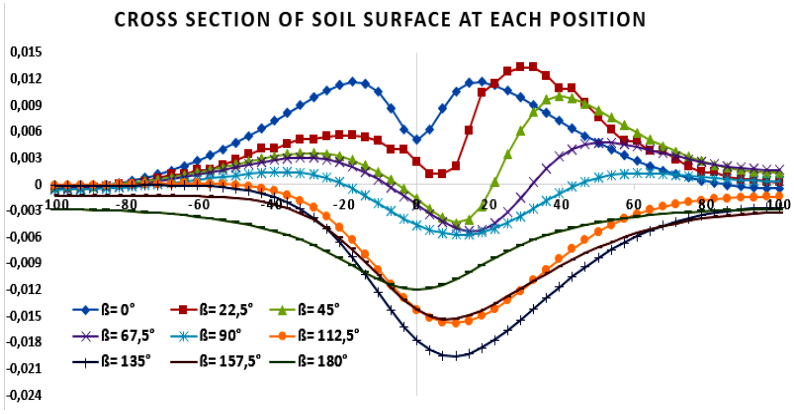

Figure 12: Shape of ground surface profiles

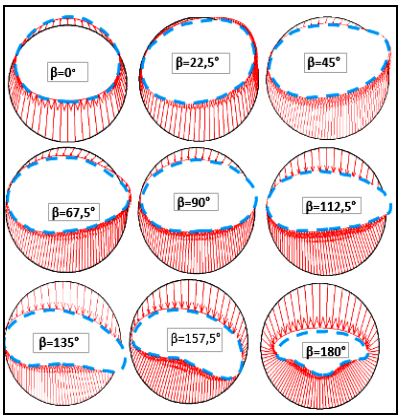

Figure 13: Contour of convergence around the tunnel

The shape of ground surface settlement profiles along the longitudinal axis X at each angular position β, and the contour of the convergence around the old tunnel caused by new excavating, are shown in the figures 12 and 13 respectively. The position of the new tunnel in

relative to the old one has a substantial effect on the movements and convergence around the old tunnel. The angular positions of the new tunnel, which range from 0° to 45°, make an ascendance of soil level (Fig.12). However, at 90°, the settlement at surface soil is easily visible. An angle of 135° indicates the maximum settlement value. This can be explained by the fact that excavating a new tunnel beneath an existing one reduces the ground's vertical stiffness, which results in more vertical deformation. The extreme convergence around the existing tunnel lining is 61.56 mm for a position of 45o (Fig. 13), when the new tunnel interacts with the old tunnel. This position was arranged in a way to cover the zone of influence that is designated by lines extending 45° from the tunnel spring-line.

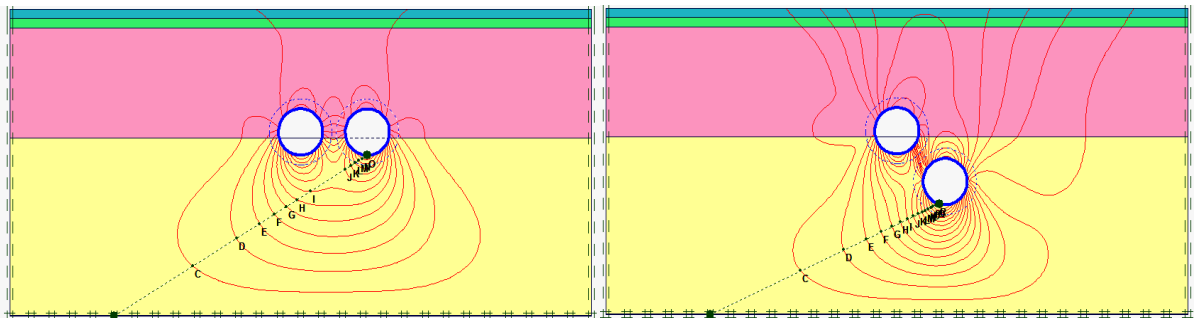

Figure 14a: Contour lines of total displacements at 90° (Extreme Utot=52.96 mm)

Figure 14b: Contour lines of total displacements a t 135° (Extreme Ut =66.11 mm)

The contour lines showing the total displacements in the surrounding soil mass caused by the second tunnel excavation (Fig.14a) and (14b) at two angles positions (90° and 135°), in relation to the existing tunnel. The analysis' findings demonstrate that the angular position of the new tunnel has a significant impact on the surrounding soil movement (displacements). As expected, a large gradient of displacements in the surrounding at an angle of 135° is visible. This results from the excavation of the new tunnel beneath the old tunnel, which weakens the earth's vertical stiffness and produces more vertical deformation. This instability of the soil is the reason of this.

6 Influence of the new tunnel angular position on the lining behavior of the existing tunnel.

Ngoc Anh Do et al. [1] examined the impact of distance between tunnels on the bending moment generated in the jointed and continuous lining of the existing tunnel. The new tunnel in the present analysis has a circular cross section, a 15-meter outer diameter, and 0.40-meter-thick concrete lining. The internal efforts (axial force, bending moment, and shear force) generated in the old tunnel's lining as a result of the newly excavated are shown in table 4.

Table 4: Summary of internal efforts values generated in the lining of the existing tunnel

Positions	Angles	Axial force (kN/m)	Bending moment (kN.m/m)	Shear force (kN/m)
1	0°	$-3.50*10^3$	24.38	16.46
2	22.5°	$-3.77*10^3$	100.61	66.80
3	45°	$-3.93*10^3$	154.40	107.65

4	67.5°	$-4.20*10^3$	122.69	77.25
5	90°	$-3.30*10^3$	52.25	24.72
6	112.5°	$-4.80*10^3$	130.72	-63.33
7	135°	$-4.85*10^3$	218	-127.73
8	157.5°	$-3.96*10^3$	119.35	-52.56
9	180°	$-3.38*10^3$	52.45	34.3

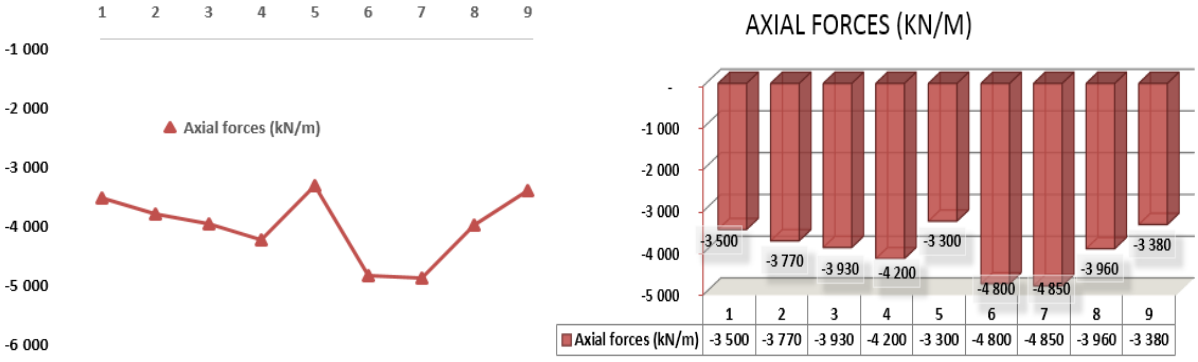

(a) Axial force profile

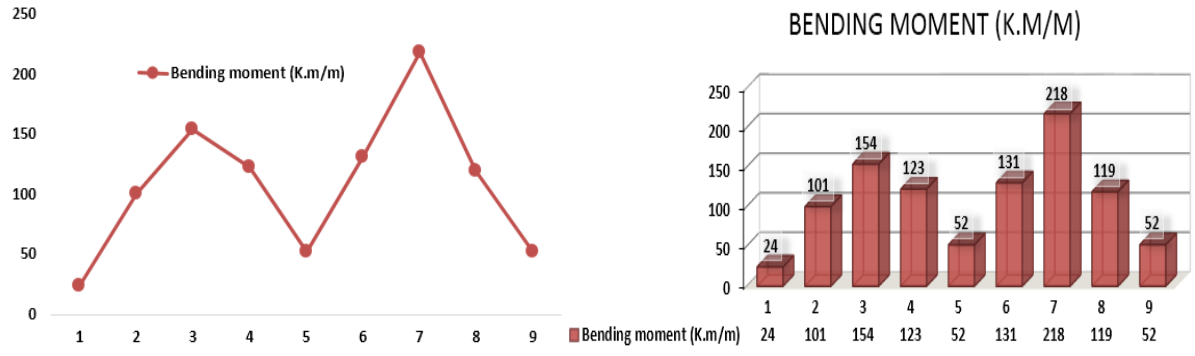

(b) Bending moments profile

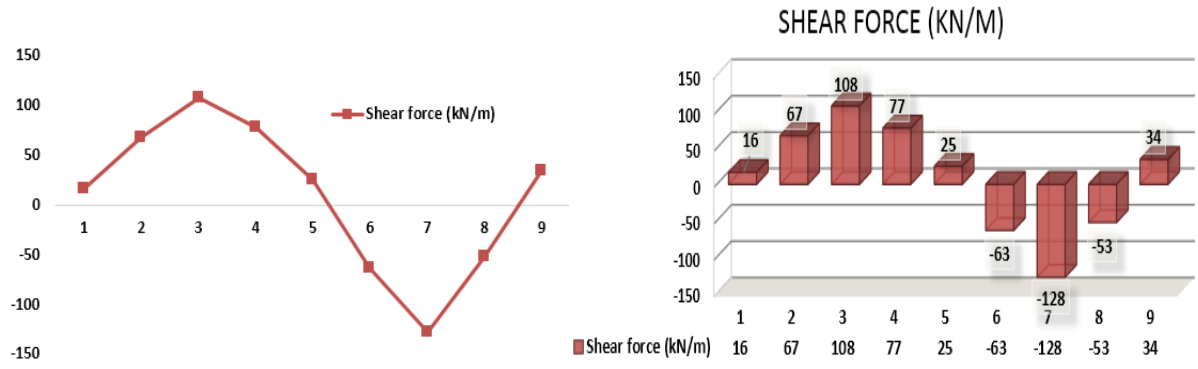

(c) Shear force profile

Figure 15: Variation of internal efforts (existing tunnel) in relation to the location of a new one

Figure 15 illustrates how the new tunnel position in relation to the old tunnel has a major impact on the internal efforts generated in the old tunnel's lining. Excavation of the new tunnel induces internal effort in the existing tunnel due to interaction with it. At an angular position of 135°, the values of internal efforts generated in the old tunnel's lining increased by approximately 75% compared to values before excavation, which are maximum values compared to other positions. On the other hand, we obtained the minimum values of the internal efforts generated in the lining of the old tunnel, when excavating the new tunnel at an angle of 90°. Thus, because of what we observed, we may say that:

- ❖ There is a decrease in settlement at surface soil, displacements in soil mass surrounding, and internal efforts generated in the existing tunnel lining, when the new tunnel is excavated parallel and aligned horizontally to the existing one, on the same elevation (ß = 90°)
- ❖ There is an increase in the settlement, displacements and internal efforts generated in the existing tunnel lining, when the new tunnel is excavated at an angular position of 135°

7 Parametric study at a critical angular position of 135°

7.1 Investigation the excavation method of the new tunnel on an old tunnel

According to previous results, excavation of the new tunnel at an angle of 135° in relation to old one. This led to significant instability in the soil surrounding the old tunnel as well as the extreme values of settlement, displacements and internal efforts generated in the lining of the old tunnel. A parametric study will be investigated of some factors related to the two tunnels and their surroundings in an attempt to reduce the maximum values obtained in the critical angular position of 135°. An investigation has been undertaken into the impact of the excavation method of the new tunnel at an angle position of 135° on the old tunnel and its soil surrounding. The tunnel's cross-section was divided into different headings as needed (heading, bench, invert), the partial excavation method was used. The effect impact is demonstrated by simulating a sequential process in which each portion is dug at full face. We examined and compared five different partial-face excavation scenarios with full-face excavation.

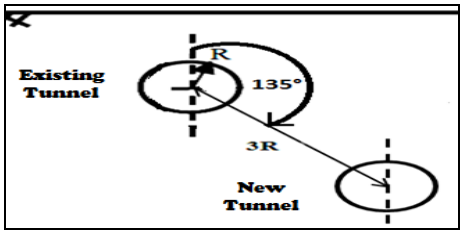

Figure 16: The new tunnel relative to an existing tunnel

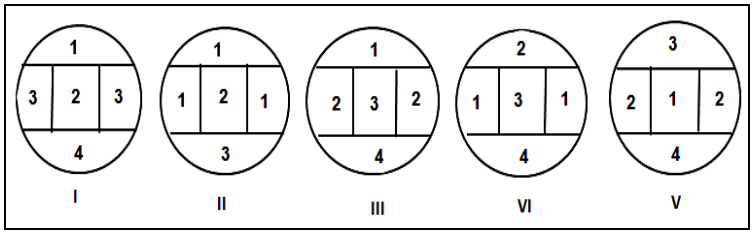

Figure 17: Cases partial-face schematic

In five distinct scenarios, the effects of several method of partial-face excavation with partial support installation were examined. In all investigation, face advance was applied only after the whole segment had been excavated. Table 5 displays the analysis of the displacements of soil mass surrounding and the settlement surface soil based on an angle of 135°.

Table 5: A Summary of displacements and settlement according to different excavation method

Position (ß)	Settlement (mm)	Horiz displ (mm)	Vert displ (mm)
Full face Excavation 0	-19.55	-10.94	66.11
Partial-face Excavation I	-13.72	-11.43	58.13
Partial -face Excavation II	-16.38	-10.12	60.60
Partial -face Excavation III	-7.42	-9.23	35.56
Partial -face Excavation IV	-14.16	-10.11	48.78
Partial -face Excavation V	-16.53	-10.12	51.63

Based on the present investigation, we can conclude that the tunneling technique significantly affects the settlement and displacements. A difference in results was observed when comparing the five partial-face excavation technique with the reference case at a fixed angular position of 135°. The partial-face excavation method gives lower results in terms of displacements (Ux= -9.23 and Uy=35.56) and settlement (δ= -7.42) compared to the full section method (Ux= -10.94 and Uy=66.11) and settlement (δ= -19.55). This difference in results is mainly due to more galleries being opened in the tunnel front. Digging with a large number of galleries causes ground movement which may last a short time due to the implementation as quickly as possible of support, on the other hand the excavation of the tunnel using the section method, the displacements will be important because the excavating section is large. So, excavating with a partial-face offers a front stable than the method of full section method. Moreover, we note that the third scenario provides less displacements than the other scenarios. We must admit that to dig a tunnel, we must return to the third scenario because it is the best solution to reduce displacements.

7.2 Investigating of the impact of tunnels spacing on interaction

Three various tunnel spacing (1, 1.5, and 2) L; where L=3R have been used to study the effect of the inclination spacing between the two tunnel centers (L) on soil stability. An angle of 135° was chosen for the new tunnel's position.

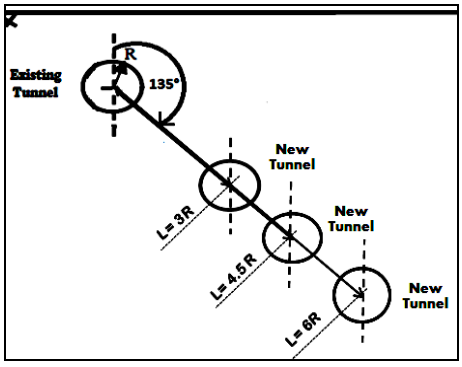

Figure 18; The new tunnel relative to an existing tunnel at 135° according to different spacing

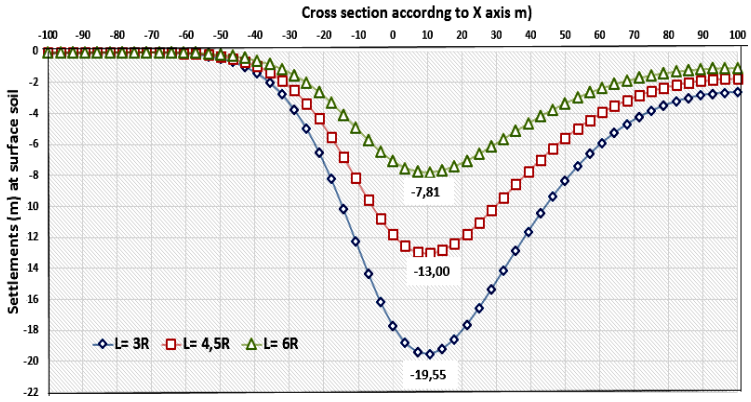

Figure 19: Settlement troughs for inclined spacing L, 1.5 L, 2 L

Figure 19 shows the settlements at surface soil caused by the new tunnel excavation for the different inclined spacing between the two tunnels (3R, 4.5R, and 6R). It is evident that the distance between tunnels has a significant effect on the settlements. At the distance equal 2L = 6R, we observe as the minimum value (-7.81mm). However, we see a maximum value (-19.55mm) at L = 3R. As expected, the settlements diminish as the distance between the tunnels increases. This demonstrates that there are more vertical constraints and less horizontal constraints designated as the distance between tunnels decreases, which explains why settlement is increasing.

7.3 Impact of lining thickness on interaction

In this study, four lining thickness values were used: 100 mm and 150 mm (indicating very elastic lining), 400 mm (indicating equitably rigid lining), and 700 mm (indicating very rigid lining). The lining thickness of the new tunnel has been changed from 100 mm to 700 mm for a fixed value of the lining thickness of the existing tunnel (40 cm). The effects of the thickness of the new tunnel's lining are assessed in terms of displacement, settlement, and internal efforts that accumulate during the construction. The results of this analysis for different new tunnel lining thicknesses at an angle of 135° are shown in table 6.

Table 6: Results of the settlements, displacements, moment, and stress for different thicknesses

Thickness	Settlement(mm)	Displacements (mm)	Moments (Kn.m/m)	Stresses (Kn/m^2)
100mm	-43.00	63.66	-7.29	1115
150mm	-41.05	60.15	51	1132
400 mm	-19.55	48.06	218	1220
700 mm	-15.03	37.25	553.9	1270

7.3.1 Settlement analysis

Figure 20 shows the settlement after the completion of the new tunnel's excavation for different lining thicknesses. These data suggest that reducing the lining's thickness had a substantial impact on the settlement. This indicates that more flexible the lining will occur the more settlements. Therefore, it is evident that lining thicknesses of 150 mm or less cause the most settlement at surface soil, suggesting that lining thicknesses of less than 150 mm should not be selected. These analysis' findings, which demonstrate that excessive surface settlement is caused by lining thicknesses of even less than 150 mm, support this claim [15]

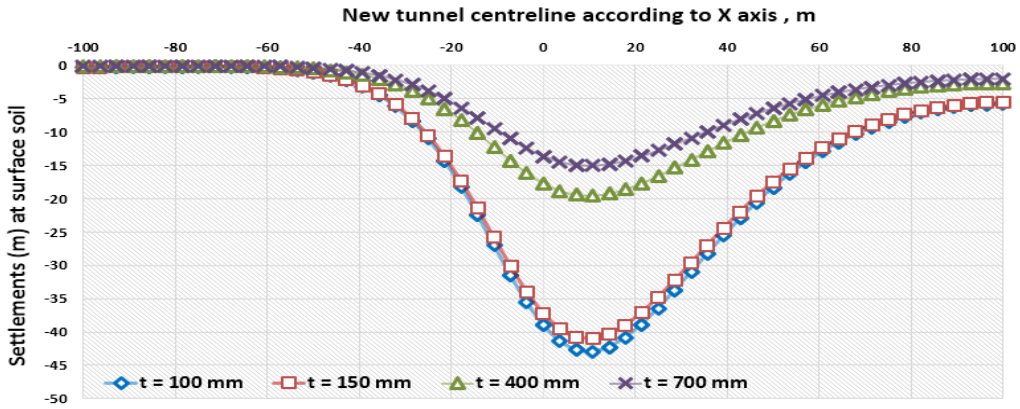

Figure 20: Surface settlement curves for different lining thickness

7.3.2 Analysis of displacements total, moments and stresses in existing tunnel lining

Figure 21 shows the extreme total displacement in the existing tunnel lining hoop for various lining thicknesses after the new tunnel is completed. The results show that increasing more thickness to the new tunnel's liner actually affects the total displacements. This indicates that a greater degree of lining flexibility allows for the prediction of larger displacements. Thus, it is clear from the lining thickness equal to 150 mm or less causes an increase in the displacement in the existing tunnel, suggesting that a lining thickness of less than 150 mm should not be selected. Changing the lining thickness has a major impact on the lining hoop moment. The moment distribution was very large at the 700 mm liner thickness. Increasing the lining thickness led to the lining behaving in a stiffer mode, i.e., with a decrease in the flexibility of the lining, Large moment profiles were therefore predicted. Changing the lining thickness had no marked impact on the stress expected in the lining. The maximum stress distribution was produced by the 700 mm liner thickness. The ground stresses surrounding the tunnel can be used to explain variations in the lining's hoop stress concentration.

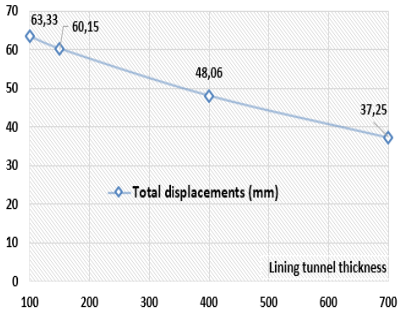

Figure 21: Total displacements

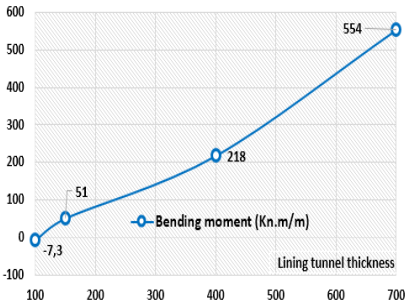

Figure 22: Hoop moments

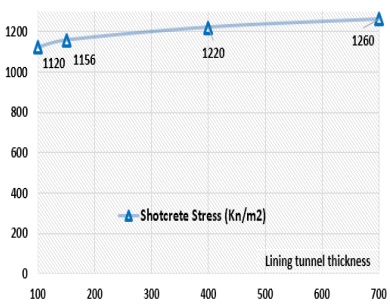

Figure 23: Maximum stress

Figure 24 shows how changing the lining thickness can change the hoop stress in lining while at few points (E, F, G, and H).

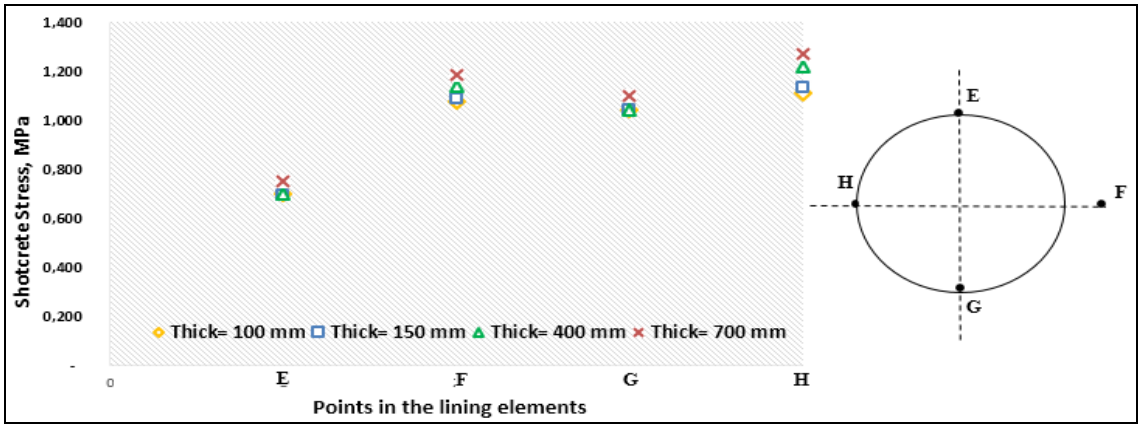

Figure 24: Hoop stress in lining with positions of some points for different lining thicknesses

Figure 24 illustrates that varying the lining thickness affects the lining hoop stress along with the projected positions of few points (E, F, G, and H) in the lining elements. A significant stress distribution was produced by the 700 mm lining thickness, especially at point H (the tunnel's crown). We also see that, for varying lining thicknesses, the stress values are approximately identical at every point (at point E, it is very similar; the stress value = 700 kN/m^2 for the four lining thicknesses); it is also the minimum value).

8 Conclusion

Effect of new tunnel construction in close proximity to an existing tunnel at different angular positions ß (0° to 180°) relative to an existed one are investigated in this paper. A numerical study was evaluated this impacts on the surrounding soil in terms of movements, displacements, settlement, and internal efforts generated in the lining of the existed tunnel using the finite element method. The results of the study allow for the following conclusions.

- Constructing process of a new tunnel has a significant influence on the soil's internal stability, and its position relative to the existed one, significantly impacts on the disturbance of the surrounding soil, which causes movements, displacements, settlement and internal efforts in the existed tunnel.
- A decrease in the settlement, displacements and internal efforts generated in the existing tunnel lining, when the new constructing at an angular position ß equal to 90°, where the two tunnels are regarded as aligned horizontally, on the same elevation (ß = 90°)
- A max increase in the settlement, displacements and internal efforts, when the new constructing at an angular position ß equal to 130°. This can be explained by the fact that the new tunnel's excavation beneath the existed one decreases the earth's vertical stiffness, which leads to additional vertical deformation because of the unstable soil.
- A parametric study will be carried out at angle position 135° (critical angular position) in order to reduce the influences of new constructing in this critical position

1. New constructing technique at the fixed angular position of 135° had a most influence on soil surrounding, including displacement, settlement and internal forces generated in the existed tunnel. The investigation found that the new constructing according to third technique (scenario) gave small values regarding settlement and displacements soil compared to the other remarkable scenarios and reference case. We conclude that new

constructing technique according to the third scenario has a great advantage in reducing the values of settlement and displacements.

2. Tunnel spacing between the new constructing and existed tunnels has an evident influence on the soil surrounding movement. When the distance is equal or more than 6R, the influence on settlement surface is not significant, while the effect increases rapidly with its decrease when it is equal or less than 3R. Therefore, it is explained that there are more vertical limitations and fewer horizontal constraints as the distance between tunnels gets smaller, this suggests that settlement increases.
3. Investigating how the thickness of the new tunnel's lining affects the old one. It is essential to determining the settlement, total displacements, moment and stresses in the existing tunnel lining. The interaction between the two tunnels is relatively important in a tunnel with a very flexible lining, while it is fairly inconsequential in a tunnel with a stiff or very rigid lining. The lining thickness must always be at least 150 mm; it was also mentioned.

The development of transportation in large cities requires a new tunnels construction in close proximity to existing tunnels. This work can provide a practical experience in the field and reference to real-world for the construction of new tunnel at different positions relative to existed one. The angular position of the new to be constructed have been demonstrated to have significant influence on the movement in the soil surrounding the existed tunnel in this study. This impact might be diminished by constructing the new tunnel at precise position relative to the other, which requires further investigations.

References

[1] Ngoc Anh Do, Daniel Dias. (2014). 2D numerical investigations of twin tunnel interaction. *Geomechanics and Engineering*. Vol. 6, No.3, pp. 263- 275

[2] Bousbia Nawel, Messast Salah. (2015). Numerical modeling of two parallel tunnels interaction using Three- dimensional Finite Elements Method. *Geomechanics and Engineering*. Vol. 9, No.6, pp 775-791.

[3] Bousbia Nawel, Messast Salah, Houssou Noura. (2021). A simplified 3D model for existing tunnel response to piles construction. *SSP Journal of civil engineering*. Vol.16, No. 2, pp. 87-103.

[4] Bousbia Nawel. (2021). Effects of different processes of tunneling on displacements soil using 3D Finite Element Method. *SSP Journal of civil engineering*. Vol.16 No. 2, pp. 203-217.

[5] Karakus, M, Ozsan, A. Basarır, H. (2007). Finite element analysis for the twin metro tunnel constructed in Ankar Clay, Turkey. *Bull. Eng. Geol*. Vol 66, No. 1, pp. 71-79

[6] Hage Chehade, F.- Shahrour, I. (2007). Numerical analysis of the interaction between twin-tunnels: Influence of the relative position and construction procedure. *Tunn. Undergr. Technol*. Vol. 23, No. 2, pp. 210- 214

[7] Wang Ran. (2017). *Effects of the existing tunnel shape on three dimensional crossing tunnels interaction in sand: Centrifuge and numerical modelling*. PhD. thess, University of Hong Kong.

[8] Yang, X.L.- Wang, H.Y. (2018). Catastrophe analysis of active-passive mechanisms for shallow tunnels with settlement. *Geomech. Eng*. Vol. 15, No. 1, pp. 621-63

[9] Dar Al-Handasah (Shair and Partners) (2009). Documents d'autoroute Est Oust Lot Unique Est", Consortium Japonais pour L'autoroute Algérienne COJAAL

[10] Nogueira, C. L, Azevedo, R. F, et al. (2011). Validation of coupled simulation of excavations in saturated clay: Camboinhas case history. *Int. J. Geomech*. Vol. 11, No. 3, pp. 202–210

[11] Panet, M, Guenot, A. (1982). *Analysis of convergence behind the face of a tunnel*. Proceedings of the 3rd International Symposium, Brighton, UK.
[12] Oreste, P.P. (2003). Analysis of structural interaction in tunnels using the convergence – confinement approach. *Tunn. Undergr. Sp. Tech*. Vol.18, No. 4, pp. 347-36
[13] Möller, S.C, Vermeer, P.A. (2008). On numerical simulation of tunnel installation. *Tunn. Undergr. Sp.Tech*. Vol. 23, pp. 461- 475
[14] Thompson, R. (1999). HEX collapse case told of "50mm tunnel lining". *New Civil Engineer* p. 6
[15] C.W.W. Ng, H. Lu. (2014). Effects of the construction sequence of twin tunnels at different depths on an existing pile. *Canadian Geotechnical Journal*. Vol.51, No. 2, pp. 173-183
[16] Ding, Z., Wei, X.J, Wei, G. (2017). Prediction methods on tunnel-excavation induced surface settlement around adjacent buildings. *Geomech Eng*. Vol 12, No. 2, pp. 185-195
[17] Hassan Obaid Abbas. (2020). Influence of Tunnel Excavation on Tower Foundation Settlement Constructed on Sandy Soil. *Transportation Infrastructure Geotechnology*. Vol.7, pp. 651–663
[18] Hefny, A.M., Chua, H.C.- Jhao, J. (2004). Parametric studies on the interaction between Existing and new bored tunnels. *Tunn. Undergr. Space Technol*. Vol. 19, pp.4-5
[19] Giovanni Barla. (2016). Full face excavation of large tunnels in difficult conditions. *Journal of rock mechanics and geotechnical engineering*. Vol.8, pp. 294-303
[20] Jiao-Long Zhang, Christoffer Vida, Yong Yuan, Christian Hellmich, Herbert A. Mang, Bernhard Pichler. (2017). A hybrid analysis method for displacement-monitored segmented circular tunnel rings. *Engineering Structures*. Vol 148, pp. 839– 856
[21] Khadija Nejjar, Daniel Dias, Fahd Guira, et al. (2022). Numerical modelling of a 32 m deep excavation in the suburbs of Paris. *Journal of Engineering structures*, Vol 268
[22] M. Wasif Naqvi, M. F. Akhtar, Mohammad Zaid. (2021). Effect of Superstructure on the Stability of Underground Tunnels. *Transportation Infrastructure Geotechnology*. Vol.8, pp. 142-161
[23] Nahla .M Salim. (2013). Interaction between the Existing and the New Constructed Tunnels. *Eng. & Tech. Journal*. Vol 31, No. 19
[24] Nan Hua, Negar Elhami Khorasani, AnthonyTessari. (2022). Numerical modeling of the fire behavior of reinforced concrete tunnel slabs during heating and cooling, *Journal of Engineering structures*. Vol. 258 114-135
[25] Quoc Thien Huynh, Van Qui Lai, Tirawat Boonyatee, Suraparb Keawsawasvong. (2021). Behavior of a Deep Excavation and Damages on Adjacent Buildings: A Case Study in Vietnam. *Transportation Infrastructure Geotechnology*. Vol. 8, pp. 361-389

DOI: 10.2478/sspjce-2024-0017

Greening the Heat Investigating the Impact of Vegetative Roofs on Thermal Regulation in Buildings

Ján Domanický

Technical university of Kosice, Slovakia
Faculty of Civil Engineering, Institute of Architectural Engineering
jan.domanicky@tuke.sk

Abstract

Climate and its protection, use of renewable energy sources, global warming, etc. As for the projection of buildings, this is nowadays the most watched aspect in the creation of the concept of each of them. Whether it is a new building or a reconstruction. Various subsidy aspects are set up for this issue. In general, we know subsidies for the renewal of buildings in the form of a subsidy for insulation. It is also possible to obtain a subsidy for resources, either in the form of a heat pump or photovoltaic panels. For apartment buildings, renovations are adapted in so-called packages or combinations. All this should serve to reduce the need for energy for heating as well as electricity. This work is rather passive in how this need can be reduced.

Keywords: renewable energy sources, passive heating, vegetative roof

1 Introduction

1.1 Optimizing Building Energy Performance

In the contemporary world, the energy efficiency of buildings holds paramount importance, wielding a profound influence on both energy consumption and environmental sustainability. The imperative to enhance energy efficiency is a linchpin in curbing our carbon footprint and addressing the urgent challenges of climate change.
Global warming remains a persistent and critical concern, garnering frequent attention from media outlets, while public awareness of its ramifications continues to grow. The far-reaching consequences of climate change manifest in altered weather patterns, exerting a substantial impact on the global populace. Urbanization emerges as a primary catalyst for these transformations [1], marked by the mass migration and concentration of people in urban centers. Extensive observations substantiate an unbroken trajectory of escalating urbanization rates, showing no signs of reversal. Although occasional fluctuations may occur, the overarching trend is undeniably upward.

The case of Slovakia serves as a compelling illustration of this phenomenon. Research data [2] yields valuable insights into the unfolding dynamics of urban lifestyles, as outlined in Figure 1.

Place	1990	2014	2050 (forecast)
World	43%	54%	66%
Europe	70%	73%	82%
East Europe	68%	69%	78%
Slovakia	56%	54%	63%

Figure 1: World urbanism [2]

The expanding influence of urbanization has extensive repercussions on various facets of the climate crisis, establishing an intricate web of climatic effects. The progression of urban areas contributes significantly to the escalation of temperatures within cities, exacerbating the prevalent challenge of Urban Heat Islands (UHI). Moreover, it intensifies the local demand for heating and cooling, consequently resulting in a surge in greenhouse gas emissions. At present, the primary goal is to counteract this trajectory by curbing energy consumption. This article forms part of my dissertation research, which primarily seeks to identify strategies for reducing the dependence on additional energy for heating and cooling in our climate. While the complete elimination of this energy consumption may not be attainable, it is imperative to explore avenues for substantial reduction. Among the potential approaches, such as optimal architectural design, effective shielding, and suitable building envelopes, the utilization of passive heating and cooling elements emerges as a viable option. In my study, I specifically concentrate on the integration of vegetation elements and their influence on interior heating and cooling.

1.2 Vegetation elements

In the contemporary context, the myriad advantages of vegetation elements, particularly vegetation roofs, are indisputable. These elements offer a diverse array of benefits, encompassing the reduction of rainwater runoff, augmentation of urban biodiversity, mitigation of the urban heat island effect (UHI), improvement of air quality, moderation of temperature fluctuations on the roof surface to prolong the lifespan of the roof membrane, attenuation of noise levels, and a decrease in energy consumption. This article centers on delving into the impact of vegetation elements on energy consumption [1].

As temperatures soar both outdoors and indoors during the summer season, the demand for cooling escalates. In Slovakia, the recommended indoor temperature in winter is 20°C, while in summer, it is 26°C. Paradoxically, preferences often lean toward desiring a temperature of 20°C in summer and 24°C or higher in winter. Consequently, the demand for both heating and cooling rises. Since cooling is frequently achieved through air conditioning units, it contributes to elevated outdoor temperatures at both local and urban levels, exacerbating the UHI problem. Evapotranspiration, a process known for converting a substantial amount of solar radiation into latent heat that does not contribute to temperature rise [3], serves as an additional rationale for implementing passive cooling elements.

Why the emphasis on roofs? In our climate zone, maintaining vegetated exterior facades poses challenges. Moreover, horizontal building structures, such as roofs, undergo significant thermal stress during summer and require measures to prevent heat loss in winter [4]. Backed by proven benefits, several jurisdictions have opted to integrate vegetation elements into their cities and provide official support. Toronto, for instance, officially embraced this approach in 2009 [5], and other cities, including Chicago, have similarly demonstrated support for this initiative.

2 The Impact of Vegetative Roofs on Thermal Regulation in Buildings

Multiple factors contribute to the effectiveness of a vegetation roof in meeting a building's energy requirements. These factors include the substrate's thickness and thermal conductivity, volumetric humidity, vegetation height, leaf efficiency, emissivity, leaf coverage, stomatal resistance (which combines leaf water potential and solar flux), as well as the type and thickness of the roof insulation and local climate conditions [1]. Regarding the impact of vegetated roofs on heat flow and the thermal and technical parameters used in energy balances, relevant information was sourced from texts [4,6]. This particular case study focuses on the analysis conducted during the heating period. In the study [6], three roof types with varying insulation thicknesses were examined, emphasizing the importance of well-insulated roofs for our climate zone and country. This is only study, which can prove my concept to use in our well insulated roofs. Figure 2 presents the heat transfer coefficient values for these structures, both with and without a vegetated roof, considering three insulation levels [6].

1. uninsulated roof
    a. 25 cm concrete
    b. 10 cm concrete
2. slightly insulated roof
    a. 15 cm of concrete + 5 cm of insulation + 15 cm of concrete,
    b. 5 cm concrete + 5 cm insulation + 5 cm concrete
3. well-insulated roof
    a. 15 cm of concrete + 15 cm of insulation + 15 cm of concrete
    b. 10 cm of concrete + 10 cm of insulation + 10 cm of concrete

Type of roof		Heat conductivity coefficient ($W/m^2.K$)		Saving	
		Without vegetation	With vegetation	$W/m^2.K$	%
1	A	7,76	1,73	6,03	77,7
	B	18,18	1,99	16,19	89,1
2	A	0,74	0,55	0,19	25,7
	B	0,8	0,59	0,21	26,3
3	A	0,26	0,24	0,02	7,7
	B	0,4	0,34	0,06	15,0

Figure 2: Heat conductivity coefficient according to research [6]

3 Research focus and its procedure

The article introduces Case Study A, centered around an unconventional subject—an expansive warehouse-type hall measuring 100 x 200 x 10m (width x length x height), denoted as Part A1. In this instance, the roof area constitutes 43.48% of the entire heat exchange envelope of the structure. For the primary evaluation, Roof 3a, closely resembling our environmental conditions, was selected.
In the exploration of alternative objects or structures, it becomes pivotal to account for the building's configuration and the proportion between individual areas of the building's envelope and the vegetated region. This article underscores a structure characterized by a substantial roof-to-wall ratio. For comparative analysis, an apartment building measuring 14.76 x 31.66 x 23.1m (width x length x height), denoted as Part A2, was incorporated. In this case, the roof area constitutes a mere 15.13% of the total building area. Dimensions of the two objects for comparison are depicted in Figures 3 and 4.

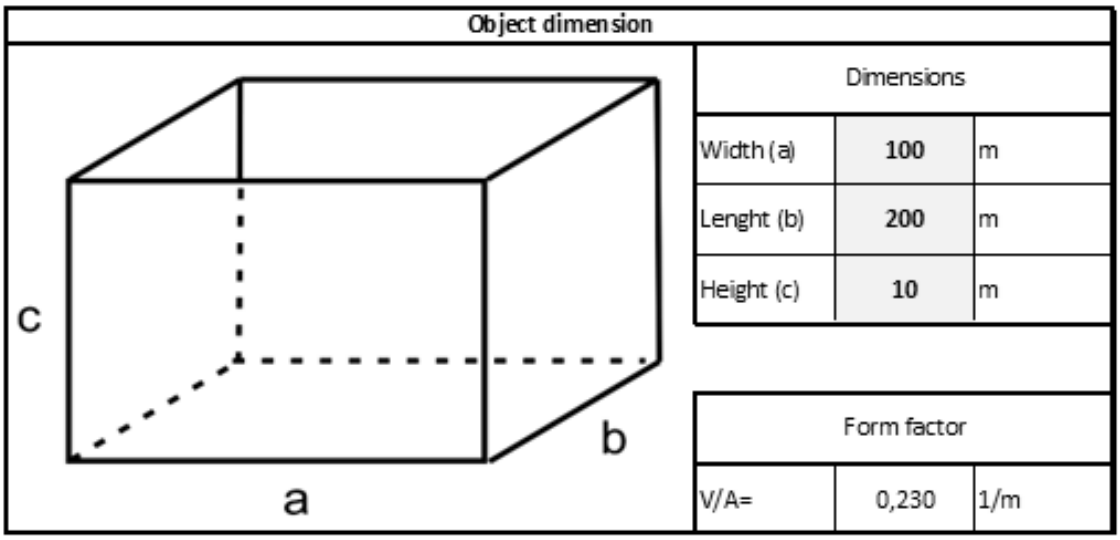

Figure 3: Dimensions of A1 object

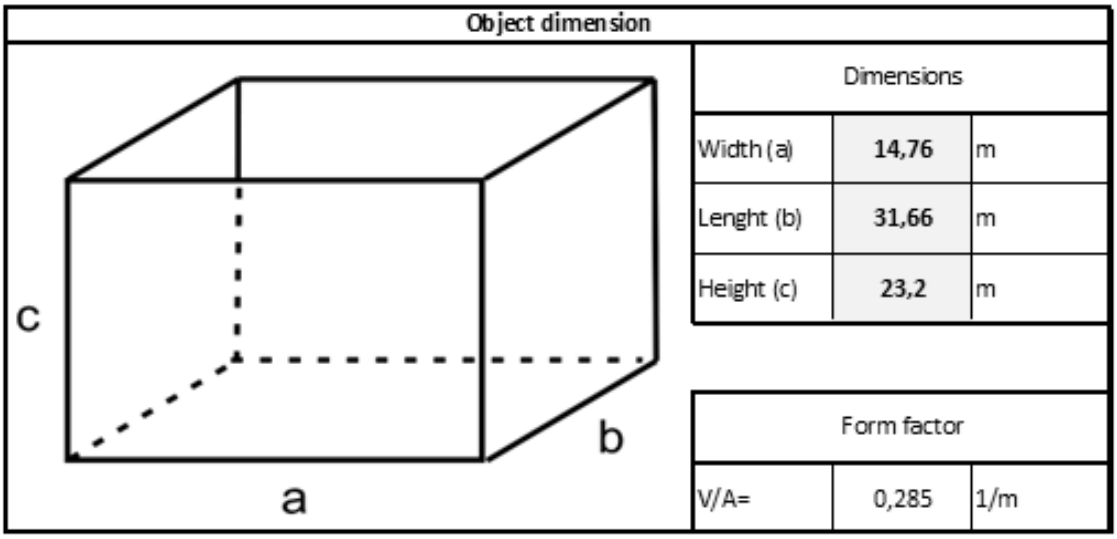

Figure 4: Dimensions of A2 object

Following the selection of objects, a thorough comparison was conducted, focusing on the surfaces of the perimeter structures, encompassing the floor, walls, and roof. This analysis is graphically depicted in Figure 5 and Figure 6, offering a visual representation that distinctly illustrates the proportions and areas involved in the comparison.

The ratio of the area of the walls to the roof		
Area	m2	%
Walls	6000	13,04%
Roof	20000	**43,48%**
Object	46000	100,00%

Figure 5: Areas of A1 building envelope parts

The ratio of the area of the walls to the roof		
Area	m2	%
Walls	2153,888	69,74%
Roof	467,3016	**15,13%**
Object	3088,4912	100,00%

Figure 6: Areas of A2 building envelope parts

The thermal and technical parameters of the structures remain consistent across both parts, facilitating an accurate comparison limited to the roof structures. Part A1 is delineated in Figure 7 and Figure 8, offering a detailed showcase of the specific characteristics of the roof in this context. Correspondingly, Part A2 is visually represented in Figure 10 and Figure 11, providing insight into the distinctive features of the roof structure in that particular case.

Heat loss of an object without a vegetation element							
	A	U	θi	θe	Δθ	Qj	α
	m2	W/m2.K	°C	°C	K	W	%
SO1	6000	0,144	20	-13	33	28465,80	12%
PDL	20000	0,191	20	3	17	65022,56	27%
S - without vegetation	20000	0,222	20	-13	33	146779,52	61%
						240267,88	

Figure 7: Heat losses without a vegetated roof – Part A1. (SO1 – walls, PDL – floor and S – roof)

Heat loss of an object with a vegetation element							
	A	U	θi	θe	Δθ	Qj	α
	m2	W/m2.K	°C	°C	K	W	%
SO1	6000	0,144	20	-13	33	28465,80	12%
PDL	20000	0,191	20	3	17	65022,56	28%
S - with vegetation	20000	0,2053	20	-13	33	135477,50	59%
						228965,86	

Figure 8: Heat losses with a vegetated roof – Part A1. (SO1 – walls, PDL – floor and S – roof)

Part	S - without veg.	S - with veg	Saving	
	W	W	W	%
Construction	3429,52	3165,44	264,07	7,70%
Object	15167,46	14903,39	264,07	1,74%

Figure 9: A1 Object heat balance

Part A1 demonstrates a significant decrease in heat loss through the roof structure, supported by the available data. This impact is visually emphasized in the comprehensive energy balance of the object, as depicted in Figure 9. The energy balance of Part A is further detailed in Figure 12, offering a comprehensive overview of the energy flows and exchanges within the system.

Heat loss of an object without a vegetation element							
	A	U	θi	θe	Δθ	Qj	α
	m2	W/m2.K	°C	°C	K	W	%
SO1	2153,888	0,144	20	-13	33	10218,69	67%
PDL	467,3016	0,191	20	3	17	1519,26	10%
S - without vegetation	467,3016	0,222	20	-13	33	3429,52	23%
						15167,46	

Figure 10: Heat losses without a vegetated roof – Part A2. (SO1 – walls, PDL – floor and S – roof)

Heat loss of an object with a vegetation element							
	A	U	θi	θe	Δθ	Qj	α
	m2	W/m2.K	°C	°C	K	W	%
SO1	2153,888	0,144	20	-13	33	10218,69	69%
PDL	467,3016	0,191	20	3	17	1519,26	10%
S - with vegetation	467,3016	0,2053	20	-13	33	3165,44	21%
						14903,39	

Figure 11: Heat losses with a vegetated roof – Part A2. (SO1 – walls, PDL – floor and S – roof)

Part	S - without veg.	S - with veg	Saving	
	W	W	W	%
Construction	3429,52	3165,44	264,07	7,70%
Object	15167,46	14903,39	264,07	1,74%

Figure 12: A2 Object heat balance

Through extrapolating these values to the annual energy balance for heating, we can compute the corresponding savings in kWh/year or GJ/year. When these savings are amalgamated with current energy prices, it enables the determination of the total annual economic savings. Specifically for Part A1, these outcomes are outlined in Figure 13 to Figure 15. Similarly, for Part A2, the corresponding results are exhibited in Figure 16 to Figure 18, offering a comprehensive assessment of the economic benefits linked to the energy savings.

Data of the object:

Town:		Košice	
External calculated temperature:	t_e	-13	°C
Length of heating period:	d	223	days
Average temperature in the heating season:	t_{es}	2,9	°C
Average indoor temperature:	t_{is}	20	°C
Heat loss of the object:	Q_{HL}	240,2679	kW

Calculation of the expected heat demand for heating

d	D	ε	η_r	Q_{HL}	$Q_{ÚK/rok}$	
days	K.days	-	-	kW	kWh/rok	GJ/rok
223	3813,3	0,63	0,98	240,267883	428359,57	1542,09

Figure 13: Heating energy demand without vegetated roof and ventilation – Part A1

Data of the object:

Town:		Košice	
External calculated temperature:	t_e	-13	°C
Length of heating period:	d	223	days
Average temperature in the heating season:	t_{es}	2,9	°C
Average indoor temperature:	t_{is}	20	°C
Heat loss of the object:	Q_{HL}	228,9659	kW

Calculation of the expected heat demand for heating

d	D	ε	η_r	Q_{HL}	$Q_{ÚK/rok}$	
days	K.days	-	-	kW	kWh/rok	GJ/rok
223	3813,3	0,63	0,98	228,96586	408209,85	1469,56

Figure 14: Heating energy demand with vegetated roof and without ventilation – Part A1

The results of comparison					
	Heat energy demand		Cost comparison		
			Electricity	Gas	Heatpump
	kWh/rok	GJ/rok	€/rok	€/rok	€/rok
S - withou veg.	428359,567	1542,094	68537,53	26772,47	17134,38
S - with veg.	408209,850	1469,555	65313,58	25513,12	16328,39
Saving	20149,72	72,54	3223,95	1259,36	805,99
	4,704%				

Figure 15: A1 Object comparison of heat energy demand

Data of the object:

Town:		Košice	
External calculated temperature:	t_e	-13	°C
Length of heating period:	d	223	days
Average temperature in the heating season:	t_{es}	2,9	°C
Average indoor temperature:	t_{is}	20	°C
Heat loss of the object:	Q_{HL}	15,1675	kW

Calculation of the expected heat demand for heating

d	D	ε	η_r	Q_{HL}	$Q_{ÚK/rok}$	
days	K.days	-	-	kW	kWh/rok	GJ/rok
223	3813,3	0,63	0,98	15,1674648	27041,19	97,35

Figure 16: Heating energy demand without vegetated roof and ventilation – Part A2

Data of the object:

Town:		Košice	
External calculated temperature:	t_e	-13	°C
Length of heating period:	d	223	days
Average temperature in the heating season:	t_{es}	2,9	°C
Average indoor temperature:	t_{is}	20	°C
Heat loss of the object:	Q_{HL}	14,9034	kW

Calculation of the expected heat demand for heating

d	D	ε	η_r	Q_{HL}	$Q_{ÚK/rok}$	
days	K.days	-	-	kW	kWh/rok	GJ/rok
223	3813,3	0,63	0,98	14,9033921	26570,39	95,65

Figure 14: Heating energy demand with vegetated roof and without ventilation – Part A2

The results of comparison					
	Heat energy demand		Cost comparison		
			Electricity	Gas	Heatpump
	kWh/rok	GJ/rok	€/rok	€/rok	€/rok
S - withou veg.	27041,187	97,348	4326,59	1690,07	1081,65
S - with veg.	26570,387	95,653	4251,26	1660,65	1062,82
Saving	470,80	1,69	75,33	29,42	18,83
	1,741%				

Figure 15: A2 Object comparison of heat energy demand

Table 1 furnishes a thorough comparison between Part A1 and Part A2, emphasizing the percentage savings realized with a vegetated roof, while considering the distinct ratios of roof area. It becomes apparent that the adoption of a vegetated roof offers stronger justification, especially concerning heating, for structures with larger horizontal construction areas in contrast to vertical ones. The table offers a lucid summary of the energy savings, highlighting the advantages associated with incorporating a vegetated roof in such scenarios.

Table 1: Final comparison of construction with and without vegetation

Roof	Area ratio roof/object	Heating energy demand		Savings	
		Without VR	With VR		
		MWh/a	MWh/a	MWh/a	%

A1	43,48%	428,36	408,21	20,15	4,71%
A2	15,13%	27,04	2,66	0,47	1,74%

4 Conclusion

The overall impact of the vegetation roof on the structure is contingent upon several factors, with the findings affirming its influence on heating. Simultaneously, a secondary comparison based on the ratio substantiated its suitability across various area ratios. It's important to note that the focus of this article does not adhere to economic principles, as the objective isn't a singular comparison of an indicator and its financial implications. Instead, the article aims to broaden the perspective on vegetated roofs and complement their advantages.

Acknowledgments

This work was supported by Development Agency under the contract (APVV APVV-18-0360 ACHIEve Active hybrid infrastructure for the sponge city).

References

[1] Susca, T. (2019). Green roofs to reduce building energy use? A review on key structural factors of green roofs and their effects on urban climate. Energy and Buildings.

[2] United Nations. (2014). World Urbanization Prospects: The 2014 Revision, Highlights. Retrieved from https://population.un.org/wup/Publications/Files/WUP2014-Highlights.pdf

[3] World Bank. (2021). Urban population (% of total population). Retrieved from https://data.worldbank.org/indicator/SP.URB.TOTL.IN.ZS?end=2021&name_desc=false&start=1960&view=chart

[4] Takakura, T., Kitade, S., & Goto, E. (2002). Cooling effect of greenery coverover a building. Energy and Buildings.

[5] Theodosiou, T. G. (2003). Summer period analysis of the performance of a planted roof as a passive cooling technique. Energy and Buildings.

[6] City of Toronto. (2009). Green Roof Bylaw. Retrieved from https://www.toronto.ca/legdocs/bylaws/2009/law0583.pdf

[7] Niachou, A., Papakonstantinou, K., Santamouris, M., Tsangrassoulis, A., & Mihalakakou, G. (2001). Analysis of the green roof thermal properties and investigation of its energy performance. Energy and Buildings.

DOI: 10.2478/sspjce-2024-0018

Energy Assessment of Thermal Water Utilization in Swimming Pools

Anna Predajnianska*, Ján Takács

Slovak University of Technology in Bratislava, Slovakia
Faculty of Civil Engineering, Department of Building Services
*e-mail: predajnianska.anna@gmail.com

Abstract

In Slovakia, thermal water is used to the greatest extent in recreational facilities, which includes thermal swimming pools, medical sanatoriums or balneological facilities. Generally recreational facilities are the largest producers of waste pool water, which is discharged through a cooling pond or cooling canal most often into rivers. Wastewater temperature discharged from the recreational facility can be a maximum of 26 °C according to requirements of laws and regulations. The rate of energy use is closely related to the temperature thermal and wastewater which enter the swimming pool. The article is aimed at analysis of the energy balance and management of thermal water in the proposed swimming pool. Conclusion will be focused on increasing the rate of use of thermal water, where the pros and cons will be summarized.

Keywords: geothermal energy, thermal water, thermal baths, energy evaluation

1 Introduction

In Slovakia, a survey is made every year before the summer season. This survey before the 2023 summer season showed that 80 natural water areas and 258 artificial swimming pools with a total number of 658 pools were registered in Slovakia – 197 of them is filled by heated cold water and 461 pools by thermal water. Currently in Slovakia, we have 47 thermal baths, which are the biggest consumers of thermal water [1, 3, 6].

In general, recreational facilities often struggle with the problem of discharging waste pool water with too high temperatures, even if the owners do not like to talk about this problem very much. Waste pool water is in most cases discharged into the rivers. Recreational facility owners are obliged to ensure the required quality conditions for safe discharge of waste pool water into the river [2, 6]. One of the most important conditions is the waste pool water temperature, which is set by laws to a maximum value of 26 °C. This temperature is set by the Law No. 364/2004 on water and amending the Law by Slovak National Council No. 372/1990 Coll. on offenses as amended (water law) and the Regulation of the Government of the Slovak Republic No.

269/2010 from May 2010, which establish requirements for achieving good water status [4, 5]. In many cases, this requirement is not met, resulting in penalties for environmental pollution.

The temperature of the waste pool water is also related to the energy utilization rate of the thermal water which is used in the recreational facility. Many thermal baths have pools in which they do not use thermal water directly, but thanks to its high temperature, they heat cold water, which is then drained into the pools (mainly pools for swimming). From cooperation with thermal baths in Slovakia, we know that there is often a phenomenon where only 40 % of thermal water energy potential is used in the operation. From experimental measurements that took place in a thermal bath in southern Slovakia, we know that the temperature of waste thermal water flowing from the engine room of the pool can reach a temperature of up to 55 °C. The article will further describe the methodology of calculating the energy balance of the thermal bath and the evaluation of thermal water energy utilization. The conclusion of the article will be devoted to possibilities for increasing the rate of use of thermal water energy.

2 Energy balance calculation methodology

Pavol Jurka (2009) and Igor Štefanička (2011) partially described the methodology for energy balance calculation for thermal baths in their dissertations. Later (2023), the dissertation of the author of this article was built on the previous theoretical foundations. In order to mathematically define the energy balance of a geothermal resource, it is necessary to know:

- thermal water flow m_0 (l/s),
- thermal water temperature θ_0 (°C),
- total pool water flow M_c (m^3).

The first step of energy balance calculation is the theoretically usable energy of geothermal source, which can be calculated by equation:

$$E_{theo} = \frac{M_c \cdot c_v \cdot (\theta_0 - \theta_r)}{3600} \quad (1)$$

where: E_{theo} – is theoretically usable energy of geothermal source (MWh),
c_v – specific heat capacity of water (kJ/(kg.K)),
θ_0 – thermal water temperature (°C),
θ_r – required waste pool water temperature (°C).

The calculation of theoretically usable energy is mainly based on temperature differences, while the temperature of the thermal water and the required temperature of the waste pool water, which is determined by laws, enter the calculation. The next step is to determine usefully used energy, which can be calculated by equation:

$$E_u = \frac{M_c \cdot c_v \cdot (\theta_0 - \theta_{pw})}{3600} \quad (2)$$

where: E_u – is usefully used energy (MWh),
c_v – specific heat capacity of water (kJ/(kg.K)),
θ_0 – thermal water temperature (°C),
θ_{pw} – waste pool water temperature (°C).

Compared to the first formula, the change in the temperature difference is key in the calculation. In order to calculate usefully used energy, it is necessary to use the temperature difference between the thermal water and the waste pool water, which is higher than the required temperature of the waste pool water (26 °C) set by laws.

If the theoretically usable and usefully used energy is known, the unused energy can be calculated by simple subtraction. The correctness of the result of unused or waste energy can by also verified using the equation:

$$E_w = \frac{M_c \cdot c_v \cdot (\theta_{pw} - \theta_r)}{3600} \tag{3}$$

where: E_w – is unused or waste energy (MWh),
c_v – specific heat capacity of water (kJ/(kg.K)),
θ_{pw} – waste pool water temperature (°C),
θ_r – required waste pool water temperature (°C).

The rate of use of the thermal water energy can be calculated by the equation:

$$\eta = \frac{E_u}{E_{theo}} \cdot 100 \tag{4}$$

where: η – is the rate of use of the thermal water energy (%),
E_{theo} – is theoretically usable energy (MWh),
E_u – is usefully used energy (MWh).

The total volume of pool water required for filling and operating pools is included in the previous calculation. The calculation can be applied to each pool separately, but also to the entire thermal bath. To calculate the total volume of water required for filling and operation, it is necessary to know the input values:

- volume of one pool or all pools in thermal bath (m^3),
- time need for pool filling or operating (hours, days),
- pool water temperature (°C),
- cold water temperature (°C),
- thermal water temperature (°C).

The calculation must be made separately for filling and operating of the pools. In the beginning, it is necessary to calculate the volume flow of pool water required for filling and operation. To calculate the filling, it is necessary to use the value T, which characterizes the time it takes for the empty pool to be filled. To calculate the operation, it is necessary to use the value T, which characterizes the number of days a year when the pool is in operation. The volume flow of pool water required can be calculated by the equation:

$$m_{pw} = \frac{V}{(\tau \cdot 3{,}6)} \tag{5}$$

where: m_{pw} – the total volume flow of pool water (l/s),
V – volume of pool/pools (m^3),
τ – the time needed for filling of the pool, or the number of days a year the pool is in operation (hours, days).

In many cases, thermal bath uses the principle of mixing thermal water with cold water in order to achieve the qualitative parameters (temperature) of pool water. In this case, it is necessary to calculate the volume flow of thermal and cold water needed during the filling and operation of the pool using equations:

$$m_{tw} = \frac{m_{pw} \cdot (\theta_{pw} - \theta_{cw}) \cdot P_r}{(\theta_0 - \theta_{cw})} \quad (6)$$

$$m_{cw} = m_{pw} - m_{tw} \quad (7)$$

where: m_{pw} – is the volume flow of pool water (l/s),
m_{tw} – the volume flow of thermal water (l/s),
m_{cw} – the volume flow of cold water (l/s),
θ_{pw} – required pool water temperature (°C),
θ_{cw} – cold water temperature (°C),
θ_0 – thermal water temperature (°C),
P_r – addition for heat losses in pipe system.

To achieve the required pool water temperature, it is necessary to mix thermal and cold water in a suitable ratio. The percentage of thermal and cold water can be calculated by equation:

$$\eta_1 = \frac{m_{tw}}{m_{pw}} \cdot 100 \quad (8)$$

$$\eta_2 = \frac{m_{sw}}{m_{pw}} \cdot 100 \quad (9)$$

where: m_{tw} – the volume flow of thermal water (l/s),
m_{cw} – the volume flow of cold water (l/s),
m_{pw} – the volume flow of pool water (l/s).

In addition to the flow rates, it is also necessary to calculate the volume of pool, cold and thermal water. The volume of pool water required to fill the pool depends on its volume and the number of days in operation. It can be summer season, winter season, or all-year operation. The number of fillings of the pool during its operating time and the required total volume of pool water will influence the volume of thermal and cold water which can be calculated by equations:

$$M_{tw} = \frac{\eta_1}{100} \cdot M_{pw} \quad (10)$$

$$M_{cw} = \frac{\eta_2}{100} \cdot M_{pw} \quad (11)$$

where: η_1 – is the percentage of thermal water (%),
η_2 – is the percentage of cold water (%),
M_{pw} – total volume of pool water needed during the filling or operation (m^3).

The total volume of pool water needed during the filling or operation of the pool can be calculated by equation:

$$M_{pw} = V \cdot n \quad (11)$$

where: V – is the volume of the pool/pools (m^3),
n – is the number of the pool filling, or the operation days during the year (days, x/operation).

In the Table 1 can be seen the summarization of all values which must be calculated according to mentioned equation. As mentioned, all equations must be calculated twice – first calculation for the filling of the pool and second calculation for the operation of the pool.

Table 1: Summarization of calculated values necessary for energy balance calculation [author]

Value	Filling	Operation
Volume flow of the pool water	$m_{pw,F}$	$m_{pw,Op}$
Volume flow of the thermal water	$m_{tw,F}$	$m_{tw,Op}$
Volume flow of the cold water	$m_{cw,F}$	$m_{cw,OP}$
The percentage of thermal water	$\eta_{1,F}$	$\eta_{1,OP}$
The percentage of cold water	$\eta_{1,F}$	$\eta_{1,OP}$
The volume of pool water	$M_{pw,F}$	$M_{pw,OP}$
The volume of thermal water	$M_{tw,F}$	$M_{tw,OP}$
The volume of cold water	$M_{cw,F}$	$M_{cw,OP}$

As was mentioned, it is necessary to make separated calculation for the filling and operation of the pool. All values can be marked with exponent "F – filling", or "Op – operation", which can be seen in the Table 1. If the separate values for filling and operation of the pool are known, it is possible to calculate the total volume of pool, thermal and cold water needed during the calculated period. This can be calculated by equations:

$$M_{tw,total} = M_{tw,F} + M_{tw,Op} \tag{12}$$

$$M_{cw,total} = M_{cw,F} + M_{cw,Op} \tag{13}$$

$$M_{pw,total} = M_{pw,F} + M_{pw,Op} \tag{14}$$

Where: $M_{tw,total}$ – the total volume of thermal water needed during the calculated time period,
$M_{cw,total}$ – the total volume of cold water needed during the calculated time period (m^3),
$M_{pw,total}$ – the total volume of pool water needed during the calculated time period (m^3).
This calculation method is applicable to the energy balance calculation for each pool separately, or for all pools in the thermal bath. In the next chapter will be the analysis of the energy balance for thermal bath described.

3 Energy balance of thermal bath analysis

From a geological point of view, the thermal bath is in the area called "Central depression of the Danube basin – Centrálna depresia podunajskej panvy", which has a largest geothermal energy potential in Slovakia. In this area are 48 geothermal wells located. Two of them, named GTV1 and GTV2, are used by thermal bath. The geothermal well GTV1 provides thermal water with flow 7,0 l/s with temperature of 78 °C. The second geothermal well GTV2 provides thermal water with flow 11,62 l/s with temperature of 56,5 °C.

Table 2: Summarization geothermal sources characteristics [author]

Geothermal well	Thermal water flow (l/s)	Thermal water temperature (°C)
GTV1	7,00	78,00
GTV2	11,56	56,50

By applying the input values to the equations described in the second chapter, it is possible to calculate the theoretically usable energy potential provided by the both geothermal wells. The theoretically usable energy potential can be seen in the Table 3.

Table 3: Theoretically usable energy potential of the geothermal wells GTV1 and GTV2 [author]

Geothermal well	Thermal water flow (l/s)	Thermal water temperature (°C)	Theoretically usable energy potential (kW)	Theoretically usable energy potential (GWh/year)
GTV1	7,00	78,00	1497,21	13,12
GTV2	11,56	56,50	1458,26	12,77

By applying the calorimetric equation, it is possible to calculate the theoretically usable energy potential. In the calculation the density of thermal water was considered to be 997 kg/m^3 due to the change in water density when its temperature increases. The specific heat capacity of water used in the calculation was 4,127 kJ/(kg.K).
In cooperation with the thermal bath, the data about the thermal water flow pumped from geothermal wells were provided and in the energy balance calculation used. Thermal, cold and waste water balance in the year 2019 can be seen in the Table 4 and Figure 1.

Table 4: Thermal, cold and waste water balance in the year 2019 [author]

2019	Thermal water				Cold water		Waste water	
	GTV1		GTV2		CW		WW	
	(m^3)	(l/s)	(m^3)	(l/s)	(m^3)	(l/s)	(m^3)	(l/s)
January	14 711	5,49	27 410	10,23	8 054	3,01	50 175	18,73
February	13 661	5,56	23 920	9,89	7 987	3,03	45 568	17,01
March	12 676	4,73	25 880	9,66	9 902	3,07	48 458	18,69
April	11 412	4,40	25 440	9,81	13 707	5,29	50 559	19,51
May	11 624	4,34	26 350	9,84	16 642	6,21	54 616	20,39
June	8 508	3,28	24 760	9,55	26 102	10,07	59 370	22,17
July	8 853	3,31	26 620	9,94	29 531	11,03	65 004	24,26
August	6 927	2,59	26 050	9,73	25 847	9,65	58 824	21,96
September	8 852	3,42	25 210	9,73	21 223	8,19	55 285	21,33
October	12 383	4,62	25 410	9,49	18 077	6,75	55 870	20,86
November	13 512	5,21	24 860	9,59	11 558	4,46	49 930	19,26
December	15 624	5,83	26 430	9,87	9 943	3,71	51 997	19,41

It is clear from the graph in the Figure 1 that the volume and water flow of waste pool water during each month is really large. By laws, the temperature of waste pool water should be a maximum of 26 °C. For the experimental measurements that were carried out in the thermal bath, is known that the real temperature of waste pool water reaches a value up to 50 °C. Wastewater with such a high temperature has relatively large energy potential without any utilization. By applying the formulas in the second chapter, it is possible to calculate the energy potential of the waste pool water if the maximum temperature of 26 °C was observed. The actual usable energy potential will also be calculated using the real temperature of the wastewater of 50 °C. An important value is also the real temperature of the thermal water, which is used in the operation of the thermal bath. This value was also measured during the experimental measurements, during which the temperature of the thermal water from both

geothermal wells (GTV1, GTV2) was measured. Considering that the thermal water is mixed during the operation, average thermal water temperature of 67,5 °C will be used in the calculation of energy balance.

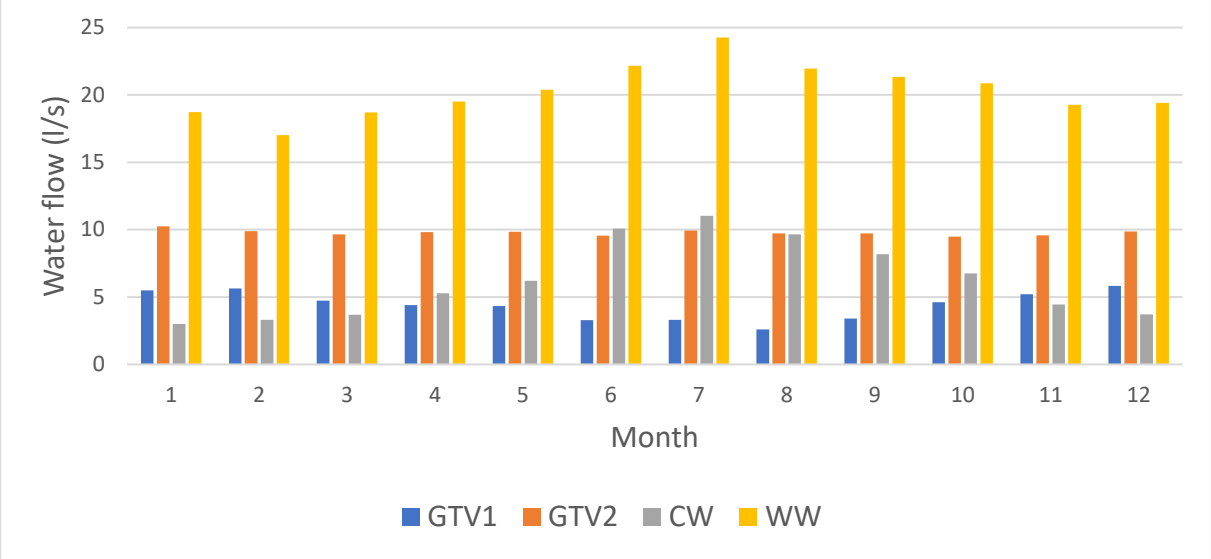

Figure 1: Thermal, cold and waste water balance in the year 2019 [author]

If we consider the actual flow of thermal water that is pumped from geothermal wells during the months, it is possible to calculate the theoretically usable energy potential of thermal water. The calculation will include the average temperature of thermal water found during the experimental measurements of 67,5 °C and the maximum waste pool water established by law 26 °C. The difference between the average thermal water temperature and the real waste pool water temperature of 50 °C will be included in the usefully used energy potential calculation. These results can be seen in Table 5 and Table 6.

Table 5: Theoretically usable energy potential of thermal water if the waste pool water temperature will be 26 °C [author]

2019	Thermal water			Average TW temperature	Maximum waste water temperature	Theoretically usable energy potential
	GTV1	GTV2	SUMM			
	(l/s)	(l/s)	(l/s)	(°C)	(°C)	(GWh/month)
January	5,49	10,23	15,72	67,5	26,0	2,010
February	5,56	9,89	15,45			1,794
March	4,73	9,66	14,39			1,840
April	4,40	9,81	14,21			1,759
May	4,34	9,84	14,18			1,813
June	3,28	9,55	12,83			1,588
July	3,31	9,94	13,25			1,693
August	2,59	9,73	12,32			1,574
September	3,42	9,73	13,15			1,626
October	4,62	9,49	14,11			1,804
November	5,21	9,59	14,80			1,832
December	5,83	9,87	15,70			2,007

Table 6: Usefully used energy potential of thermal water if the real waste pool water temperature will be 50 °C [author]

2019	Thermal water			Average TW temperature	Real waste water temperature	Usefully used energy potential
	GTV1	GTV2	SUMM			
	(l/s)	(l/s)	(l/s)	(°C)	(°C)	(GWh/month)
January	5,49	10,23	15,72	67,5	50,0	0,841
February	5,56	9,89	15,45			0,750
March	4,73	9,66	14,39			0,770
April	4,40	9,81	14,21			0,736
May	4,34	9,84	14,18			0,758
June	3,28	9,55	12,83			0,664
July	3,31	9,94	13,25			0,708
August	2,59	9,73	12,32			0,658
September	3,42	9,73	13,15			0,680
October	4,62	9,49	14,11			0,754
November	5,21	9,59	14,80			0,766
December	5,83	9,87	15,70			0,839

It can be seen in the Table 7 and Figure 2 that the real rate of thermal water energy usage reaches less than 42 %. The remaining thermal water energy potential is discharged as the wastewater into the cooling channel without any use. If the waste water were cooled to the maximum prescribed temperature of 26 °C the thermal water rate of usage would rise to almost 90 % which would be an ideal state.

Table 7: Rate of the thermal water energy potential usage [author]

2019	Theoretically usable energy potential	Usefully used energy potential	Rate of the thermal water energy potential usage
	(GWh/month)	(GWh/month)	(%)
January	2,010	0,841	**41,8**
February	1,794	0,750	
March	1,840	0,770	
April	1,759	0,736	
May	1,813	0,758	
June	1,588	0,664	
July	1,693	0,708	
August	1,574	0,658	
September	1,626	0,680	
October	1,804	0,754	
November	1,832	0,766	
December	2,007	0,839	

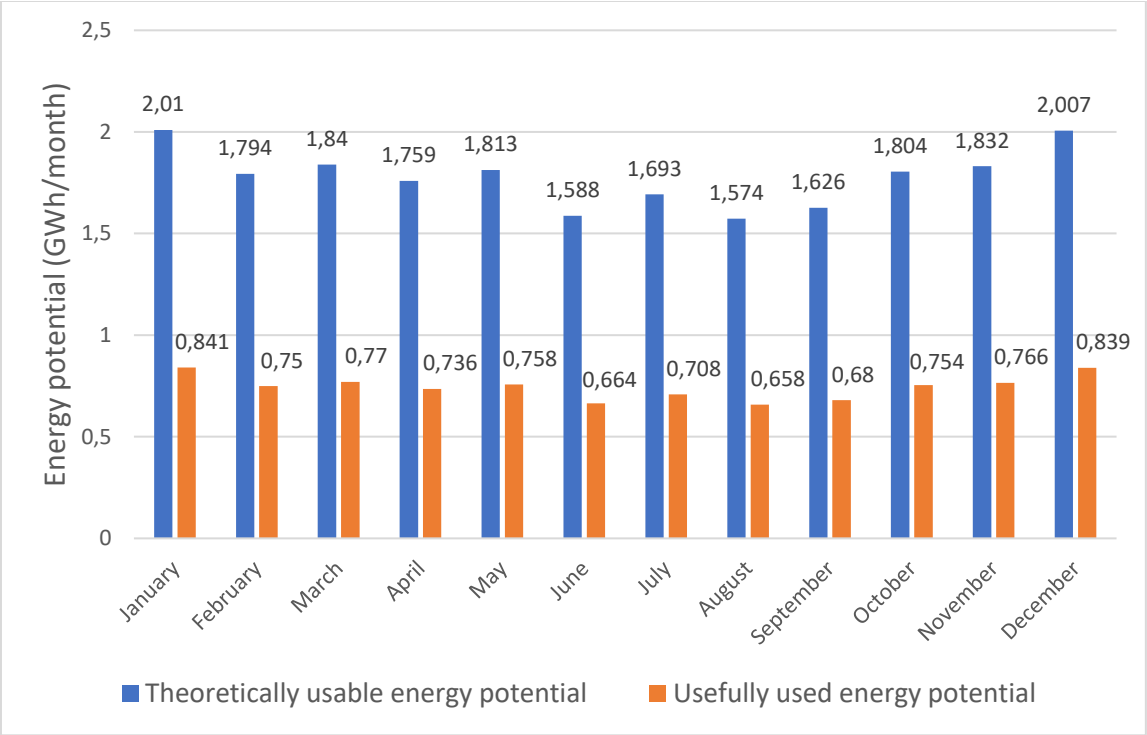

Figure 2: Comparison of the theoretically usable energy potential and usefully used energy potential of the thermal water [author]

4 Results and discussion

Through the mathematical model of the analysis of the use of thermal water energy in the swimming pool, it is possible to calculate the extent to which this energy is used. The analysis was performed with respect to the legally required maximum temperature of waste pool water, which is set by the laws at 26 °C, and with respect to the real temperature of waste pool water of 50 °C, which was found during experimental measurements. The results showed that the thermal water energy utilization rate in the solved case is only approximately 42 %. Other thermal swimming pools in Slovakia shows a similar rate of the thermal water energy use. If sufficient cooling of the waste pool water to the required temperature of 26 °C was ensured, the thermal water utilization rate would rise to approximately 88 %. With the increase in the rate of thermal water energy use, comes a decrease in the temperature of the waste pool water which is in accordance with the laws.

One of the most advanced countries in the field of geothermal energy utilization is Iceland, were, in addition to the high rate of geothermal energy use on the environment) [7]. According to studies by local experts such as Ragnarsson or Bjornsson, waste pool water from recreational facilities is used to melt snow on sidewalks and driveways. The energy utilization of thermal water drawn from many geothermal sources around Reykjavík is close to 90 %. These applications are used in the capital of Iceland, Reykjavík. This progressive country is an example that reusing the energy of waste pool water is possible, but it is technically and financially demanding [8, 9, 10].

5 Conclusion

The aim of the article was to acquaint the reader with the situation of thermal baths in Slovakia, to present the current and, above all, the real rate of thermal water energy use and to highlight applications that make it possible to comply with the requirements set by law for waste pool water. The mathematical model that was described in the article provides the possibility of calculating the energy balance of one pool or the entire swimming pool. It can be applied to any swimming pool. We know not only from calculations, but also from practice, that the rate of thermal water energy utilization in thermal swimming pools in Slovakia is very low. The excessively high temperature of the waste pool water is also connected with the rate of thermal water energy use. In order to achieve the legally required temperature of waste pool water, it is possible to apply many measures, either technologically and economically demanding, or simpler. By simply applying a heat exchanger to the waste pool water circuit, it is possible to ensure preheating for the domestic hot water preparation that is used in the showers of the thermal bath. Ensuring the melting of snow in the area of the thermal bath is a technologically and economically relatively demanding measure. In this case, Iceland is an exemplary country, where this measure is applied to a large extent not only in swimming pools, but in entire cities.

References

[1] Franko, O. et. al. (1995) Atlas of Geothermal Energy in Slovakia – text and map part. Dionýz Štúr Geological Department in Bratislava, Vašek Michal Print house, Prešov, ISBN 80-85314-38-X, 233 pp.

[2] Takács, J. (2017) Possibility of Geothermal Water´s Using in Geothermal Energy Systems. In Periodica Polytechnica Mechanical Engineering, 4 pp., ISSN 3246051

[3] Fričovský, B., Černák, R., Marcin, D., et. al. (2020) Geothermal Energy Use, Country Update for Slovakia, In European Geothermal Congress 2020, 11-14 June 2020, Reykjavik, Iceland, 19 pp.

[4] Regulation of the Government of the Slovak Republic No. 269/2010 of 25 May 2010 laying down requirements for achieving good water status

[5] Law No. 364/2004 on waters and on the amendment of the Law of the Slovak National Council No. 372/1990 Coll. on offenses (water law)

[6] Predajnianska, A. (2023) Heat recovery from pool systems waste water of thermal swimming pools, Dissertation thesis. Slovak University of Technology in Bratislava, Slovakia, Faculty of Civil Engineering, Department of Building Services.

[7] Kristmannsdóttir, H., Ármannsson, H. – Environmental aspects of geothermal energy utilization, In: Geothermics, Volume 32, Issues 4-6, August-December 2003, pp. 451-461, ISSN 0375-6505, 1879-3576 online

[8] Ragnarsson, Á. – Utilization of geothermal energy in Iceland, In: 14th Building Services, Mechanical and Building Industry days, International Conference, 30-31 October, Debrecen, Hungary, 2005

[9] Björnsson, S. – Geothermal Development and Research in Iceland, National Energy Authority and Ministries of Industry and Commerce, April 2006

[10] Ragnarsson, Á. – Geothermal Development in Iceland 2010-2014, In: Proceedings World Geothermal Congress 2015, Melbourne, Australia, 19-25 April 2015

DOI: 10.2478/sspjce-2024-0019

Investigating Water Balance Configuration in the Urban Areas of Mthatha, South Africa

S. Phelokazi[1], O.T. Amoo[1*], A. Ikudayisi[2] and MDV. Nakin[1]

[1]Centre for Global Change, Walter Sisulu University, Mthatha, South Africa.
[2]Civil Engineering Department, Walter Sisulu University, East London, Eastern Cape, South Africa
*e-mail: oamoo@wsu.ac.za

Abstract

Considering urbanization's effects, quantifying individual components of the hydrological cycle, especially at the catchment scale, has been challenging due to the influence of climate change and human activities. Accordingly, the study assesses the impacts of Land Use and Land Cover Changes (LULCC) on the water quantity degradation. It evaluates the effect of urbanization on water balance configuration between the period 2000-2020. The resultant result of LULC reflected a long-term increase in bare land by 11.72% and a marginal increase in built-up areas (0.52%). In contrast, the annual water balance results show an annual negative water deficit ranging from -19.40 mm to -624.955 mm. The result has demonstrated the use of QSWAT and SWMM in a Quick geographic information systems (QGIS) environment to drive the socio-hydrological framework to model spatially distributed and time-varying hydrologic and meteorologic datasets as an effective scientific visualization technique in water balance evaluation.

Keywords: environmental flows, LULC, water balance, sustainable development, urbanization

1 Introduction

Amongst the most important modifications that affect the urban water balance are the changes in land use and land cover that have increased the impervious cover [1,2]). Hence, most flow pathways in impervious areas contribute to urban water evaluation. These impervious land surfacing have impaired their filter capacity and runoff regulating functions [3]. Land, climatic conditions, and water availability are closely related in catchment water asset management [4]. Thus, the consequence of these impervious surfaces (land sealing) requires an analysis of the relationships between a catchment's socio and hydrological function because it relates to nature's effect with human activities triggering changes in the density and drainage network, soil-borne intensification and soil filtering capacity density in land changes. This development calls for a quantitative assessment of land use conversion under the influence of urbanization in safeguarding water resources.

Although urban growth impacts land use and cover, affecting catchment hydrology, processes like soil water retention and filtration capacity are in decline [5-8]. In addition, the increasing physiographic transition processes of societal and economic activities of built-up areas along the river, and continuous soil-floodplain creation have continuously been encroached by several springs of complex shopping malls, offices, and residential neighborhoods spread in the city's suburb periphery. All these have increased the occupied areas in urban cities, thereby causing more impervious layers with topography seal-off. Moreover, in adverse weather conditions, sewer systems and wastewater treatment plants are further flooded due to the increased capability of collecting large amounts of direct runoff resulting in an increased flood risk. Limited studies have investigated the impacts of inherent land use and land cover changes (LULCC) on urban water balance quantification [9,10]. Moreover, the choice of model and approach adopted has always been placed on the problem specific to the catchment.

Today, various techniques and models are evolving and used in different climatic zones to assess rainfall-runoff for urban water balance. [11] explored how current and future land consumption impacts urban growth and trajectory water balance using simple models based on publicly available data on evapotranspiration, precipitation, and water regulation in replacing the direct runoff and groundwater recharge value. [12] employed environmental tracers to determine the water balance and other hydrological functioning of lakes and reservoirs. Stable isotopes and environmental tracers have been used to quantify lake and wetland pond water loss due to evaporation and infiltration fluxes. [13]. Likewise, an accurate estimation of water budget components and the accompanying physical and chemical changes in a wetland pond, groundwater, and riparian zone has been achieved through the use of stale isotope [14]. Stable water isotopes have proved to be an efficient tool for determining the groundwater dependence of lakes, swamps, glaciers and ice sheets, inland seas, and the atmosphere [15,16]. [17] postulate the use of the hydrological model as a viable method that improves water budget calculation by dividing a watershed into smaller sub-hydrological systems (hydrological response unit), where the loss function is the basis for short-time models for reservoir operation in Nigeria. Other methods include the use of a drainage network and determining the amount of water to be collected from each sub-catchment using geo-informatics [18]. [19] postulates the use of an Ombro-thermic diagram gives a quick graphical component of water balance for a selected thermic place.

Also, the advent of computer modelling has eased time and labour consumption in consideration of other emerging approaches and modern urban models. Past literature work review on water balance shows modeling tools like WMS, STORM, KINEROS [20], SWMM [21,22], AGNPS [23], and HSPF [24] as a suitable option for urban water balance evaluation [25]. Some models are limited only to urban or peri-urban river catchments [26]. However, their choice has always been placed on the catchment characteristics and specific problems. HSPF has proved difficult to set up in gauge and ungauged watersheds [27]. KINEROS, AGNPS, BASINS, and ANSWERS model setup and developments required rigorous calibration with intensive data at different scales [28]. Furthermore, KINEROS, AGNPS, BASINS, and STORM reliability for short periods, especially if days or weeks are being simulated, is not particularly good. Their precision in average values prediction is questionable, unlike over longer periods which tends to be more dependable [29,30]. This is because the land and the rainfall within an area can vary

over space and time being simulated. Also, many of these predictive models have been developed based on the in-built parameters' parsimonious simplicity [31].

Hence, QSWAT and SWMM were selected for their robustness, flexibility, data availability, urban focus and accessibility. The components in their quantity analysis can be found in these two models for planning purposes. The QSWAT model has been one of the most sophisticated for simultaneous simulations of hydrology, sediment, and chemical movement prediction. It has enjoyed popular usage for simulating surface runoff into the stream network and defining filtration into the soil-segregated layers with the aquifer profile [32]. The semi-distributed, process-based, continuous-time models could effectively evaluate management strategies on water resources and pollution from sources in large basins. The model integrates specific hydrological soil properties, like porosity and infiltration rates as they affect plant growth and the movement of sediments, nutrients, pesticides, and pathogens. Extracts on how QSWAT simulates surface runoff, Evapotranspiration, percolation, and lateral flow in groundwater recharge estimation were well-detailed and documented in literature work [33-37].

To this end, the study intends to quantitatively assess urban water balance under the influence of urbanization using QSWAT and SWMM to drive an intuitive socio-hydrological approach with certain assumptions. The socio-hydrological approach views water crises from a different perspective not only about human use but also about balancing humans' water and natural water demands from an ecological perspective[38]. The socio-hydrological water balance concept modifies the storage continuity equation[39]. Besides defining the relationship between inflow and outflow variables, it considers water required for ecosystem sustainability. Details for the socio-hydrological water balance framework can be found in [40]. The socio-hydrological water balance framework partitions the evapotranspiration (ET) into societal (consisting of the drainage network and depletive sewer system) and ecological systems (environmental and outflow to the sea) as water that leaves the system. Hence, the groundwater level during the current time step h(t) is derived from equation 1.

$$\Delta H = P(t) + R_{in} - \mathrm{ET_s} - \mathrm{ET_e} - \mathrm{R_{out}} + {}^{\mathrm{dG}}/_{\mathrm{dt}} + \in_t \qquad (1)$$

Where:

$$\mathrm{ET_e} = \mathrm{ET_{ep}} + \mathrm{ET_{eR}} + \mathrm{ET_{eG}} \qquad (2)$$

$$\mathrm{ET_s} = \mathrm{ET_{sP}} + \mathrm{ET_{slR}} + \mathrm{ET_{sH}} + \mathrm{ET_{s,oth}} \qquad (3)$$

$$\text{And } D_R + D_G = ET_{sIR} + ET_{sH} + ET_{s,oth} \qquad (4)$$

Where ΔH is the total water change in the watershed, P = precipitation, ET = evapotranspiration; R = surface runoff, G = surface recharge/discharge and dG/dt = change in soil water storage (net groundwater flux) in the main drain of the manhole. groundwater (DG) represents irrigation water supply to croplands, grasslands, households, and industries. The leftover surface runoff is meant for ecological purposes, (ET_{eR}), and outflows to the sea (R_{out}).

Hence, the paper analyzes how urbanization and land cover changes impact water availability in Mthatha, South Africa, using hydrological models (QSWAT and SWMM) in QGIS environment to drive the socio-hydrological framework.

2. Materials and Methods

The solution for equation (1) is not straightforward because, at any given time, there are two unknowns: the urban storage level at the time (H_t) and the corresponding area change (A). So, the simplest approach to approximate the urban storage level is to use the previous month's ($R_{out}(t)$ and assume the initial storage change H is equal to the mean of the measured runoff. Also, for simplification, we assume that the rightmost term in the equation, $\in_t$, is negligible, and net groundwater flux has been considered as zero with no constructed urban land. The calculation of ET(s,e) depends on the corrected derivation of the soil field capacity derived from the soil texture as given in the QGIS maps. Subsequently, the study area description follows with data collection process, and the methods applied to quantitatively assess urban water balance under the influence of socio-hydrological urbanization are hereby presented.

2.1 Description of the Study Area

The Mthatha River Catchment (MRC) area houses Mthatha, which is the third biggest town in O.R. Tambo District Municipality. The town is a prime illustration of a rapidly urbanizing area in Eastern Cape, South Africa. It is within a 230-kilometer radius of the Transkei region. The city serves as an important economic and social hub for other towns in the area. Figure 1 depicts the study area with the South African Province.

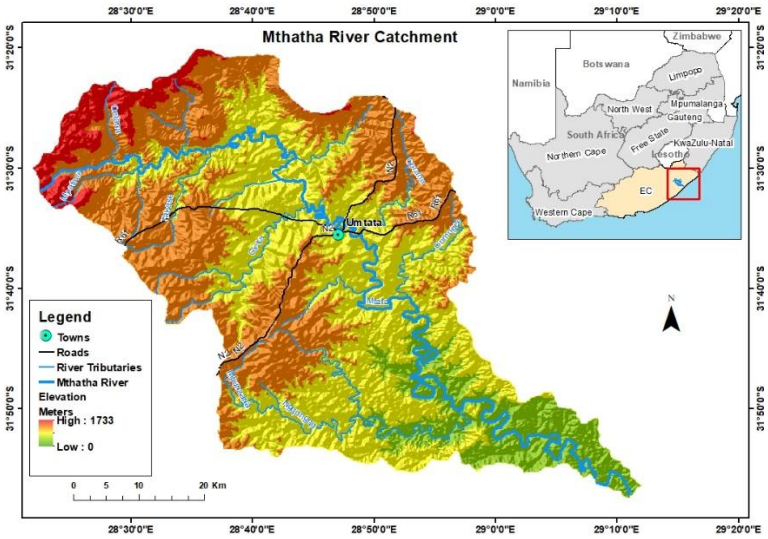

Figure 1: Location map of the Mthatha River catchment

The Mthatha River Catchment has a complex arrangement of commercial and residential settlements, including a range of dwelling types, which can be classified as rural; semi-urban, and urban spatial configurations. The Mthatha River originates in the plateau area of the Eastern Cape Province in South Africa, located about midway between the Drakensberg escarpment and before emptying into the Indian Ocean. The Mthatha River Catchment consists of the main river (Mthatha River) which is approximately 250 km long and 50 km wide and covers an area of about 5520 km^2 with two large tributaries winding their way to the sea north of Coffee Bay [41]. The catchment population densities and its distinct spatial characteristics are evident from

the city weather trend pattern from a moderate climate with over 40 inches of precipitation per year on average. Evapotranspiration, on the other hand, is relatively constant around the catchment while there is a wide variety of impacts that human activity (e.g., land development, movement of water and wastewater between watersheds, consumptive uses of water such as irrigation) which could pose challenges on the natural water budget [41].

2.1.1 Biophysical conditions

Figure 2 depicts the MRC soil raster classification and its impacts in determining water balance.

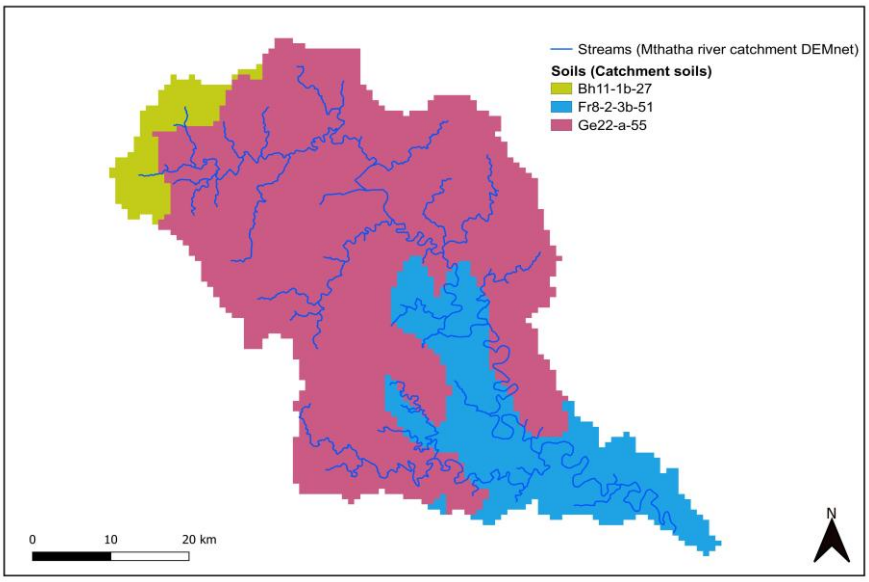

Figure 2: Mthatha River Catchment soil classification

The soil type codes Bh11-1b-27, Fr8-2-3b-51, and Ge22-a-55 stand for the sandy loam, loam, and sandy clayed loam classification labels for the area. Although they seem to have different filtering capacity distributions, a greater extent suggests water holding capacity has dropped in favour of an increasing direct runoff. This particularly holds for loamy soils. In the middle reaches, lies the Mthatha urban settlements with numerous ends of sewer pipe carrying effluents to be discharged into the Mthatha River. Many of the underground drainage system networks carry sewage and direct runoff which flows off the low-lying areas (such as roads, adjacent residential areas, allotments, and green spaces) after heavy rainfalls, and this usually occurs from time to time. The nature of the catchment streamflow network and distribution orders play a key role in transporting the action of water through their drainage discharge. Features such as size, area, shape, slope, and perimeter of the stream network continue to alter the quantification of its water balance.

3. Methodology

3.1 Model Selection and Working Techniques

The study employed an offline coupling of the QSWAT model with the SWMM tool in populating the socio-hydrological approach framework. These models were selected for their robustness flexibility, data availability, urban focus and accessibility. The QSWAT was used to model the streamflow and delineate the catchment into stream network and sub-catchments for water balance evaluation while the SWMM was used to model the drainage network and to determine the amount of water to be collected from each sub-catchment of the Mthatha urban areas. The model was used to simulate the urban flow quantity, the water storage balance in-built was used for the flow from the land surface and the equations of continuity and motion were used for channel flow prediction [42]. The socio-hydrological approach views the urban water balance configuration as a combination of societal urbanization and ecosystem sustainability [43].

3.2 Data Acquisition

Field data such as meteorological, land use change, soil type, societal, economic, and demographic changes for the Mthatha catchment, was collected from past documentation (2000-2020). Hydrological drainage network characteristics such as size, area, shape, slope, and stream network distribution orders that are useful in estimating surface flow discharge and quantifying the runoff were obtained from the catchment delineation in the QSWAT model. Other required data regarding the effects of topography terrain and related features such as soil type, slope, aspect, grain size, groundwater level, and the different degrees of land use/cover change, indices for soil wetness on the hydrologic processes, were evaluated from the compiled soil and land digital elevation model data process in QGIS for the area.

3.3 Data Quality and Validation

Data sources from the Google Earth as base map were refined and processed to the required resolution, by cross-referencing the Google Earth imagery with field surveys while other global source data were compared against local meteorological stations for reliability. We used a 30 m DEM resolution from the SRTM and a 2,000-ha drainage area threshold to define the stream network. At the same time, the rate of changes for different land cover types was generated through Google Earth ground-truth data for historical image classifications (2000, 2005, 2010, 2015, and 2020). Also, because the study lacks detailed sewer infrastructure data, like malfunctioning or pipeline leakages, we assumed constant leakage rates for all pipeline conditions. Moreover, the function of the sewer system (that accelerates the drainage of the land parcels by collecting precipitation and runoff water directly in the river) is estimated according to the land use classes which are included in the QSWAT model via the in-built parameters menu for surface runoff, evapotranspiration, percolation and lateral flow. Also, each land parcel area's soil texture distribution and vegetation in the catchment area were assumed to be uniformly distributed. Table 1 gives an overview of some of the various assumptions made in the QSWAT and SWMM models.

Table 1: Summary of assumptions parameters made in the QSWAT and SWMM

Symbol	Parameter	Description	Domain
CN	SCN	Service Curve Number for land use, soil, vegetation,	(0.3, 0.6)
Sp	Seepage	up_seepage_ flux and down_seepage_flux	(0, 3)
Cw	Cw	Runoff coefficients	(0.3, 0.7)
deep_gw	deep_gw	deep groundwater	(2, 23)
Ns	N-sewerconduit	Manning's n for sewer conduits	(0.002, 0.026)
Dc	Decay-constant	Infiltration coefficient(h-1)	(1, 6)
Min-r	Minrate	Minimum infiltration rate	(18,120)
Max-r	Maxrate	Maximum axfiltration rate	(1,11)
Zi	Zero-impervious	Percent pf impervios area without depression storage (%)	(4, 75)
Dp	Destore-perv	Depression storage for pervious area (mm)	(1,11)
Di	Destore-imperv	Depression storage for impervious area (mm)	(0.1, 0.11)
Np	N-pervious	Manning's n for previous area	(0.01, 0.08)
Ni	N-impervious	Manning's n for impervious area	(0.011, 0.05)

3.4 Data processing, QSWAT model and SWMM drainage network setup

Figure 3 depicts the workflow diagram showing data flow from GIS to SWMM and SWAT for modelling the water resources of the catchment. The data requirements for the SWMM model setup include rainfall data, slope and elevation, land use data, stormwater pipe system, and discharge data while the QSWAT model was set up with processed DEM, soil, and land processed raster data in a QGIS environment. Figure 3 Workflow diagram for water balance estimation from the SWAT and SWMM models

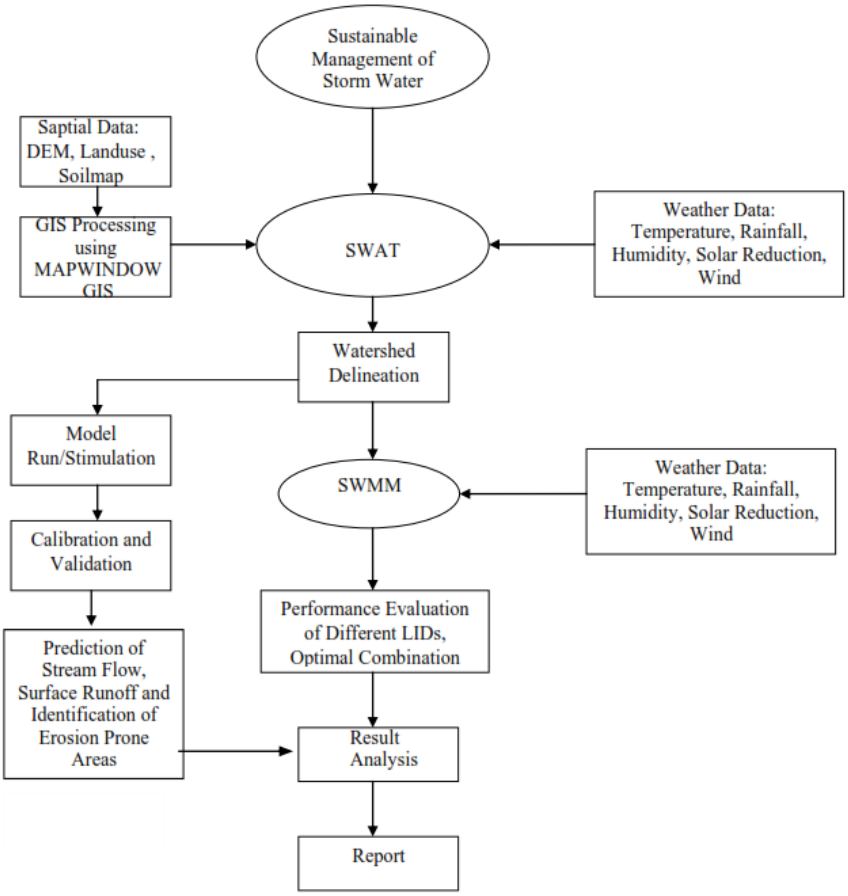

Figure 3: Workflow diagram for water balance estimation from the SWAT and SWMM models

The QGIS hydro statistic tool has been used for Digital Elevation Data (DEM), soil, and land use raster image processed and re-projected to Universal Transverse Mercator Zone 34 South. Before rigorous analysis in QSWAT for the catchment delineated into sub-catchments, consisting of stream network, slope lengths, and other aspect ratio to capture the street drainage network and interconnectivity. Since urbanization meant the growth of new impervious land and built-up areas around the urban periphery, information on soil grain size, and field capacity for each land parcel was assessed through QSWAT land use and soil texture distribution on the catchment area while the regional climate data collected from South Africa Weather Service (SAWs) for the period (2000-2020) for precipitation and evaporation were fed into the used models (QSWAT, SWMM). The temporal changes in the catchment hydrologic water balance were assessed using the modified socio-hydrological urban water balance formula in which water enters the system via precipitation (P), converted into evaporation (E) and runoff (R), and the associated storage (S) or change in storage (ΔS) for the period under investigation (2000-2020). To assess the effect of urbanization, the SWMM model was set up to quantify the urban area runoff, water held up in sewer, re-use, and discharge back to manholes which were computed using spatial analyst tools in a QGIS environment [44] while the socio-hydrological framework approach was used to quantify man use and ecosystem water use in arriving the urban water balance formula.

Due to its simplicity, the open-source EPA-SWMM, developed under the support of the US-EPA, was selected to model the drainage network and to determine the amount of water to be collected from each sub-catchment of the Mthatha urban areas. The model was set up with processed soil, and land raster data, processed in a QGIS environment. The model simulates the drainage system network by (i) rainfall-runoff transformation, (ii) 1D flow routing on a street network, (iii) flow interception at street inlets, and (iv) flow interaction between surface water on the streets and the underground storm-water system.

The hydrologic model (first module) transforms rainfall to runoff using the kinematic wave approximation and simulates the infiltration process with the Green-Ampt method. The street network is based on a finite-volume shock-capturing scheme that solves the fully conservative Saint-Venant equations to model both subcritical and supercritical flows. Flow interaction between surface water on the streets and underground storm-water systems was achieved by interfacing the QGIS model with EPA-SWMM. This interaction allows the flow to enter from streets to the underground storm-water system and vice versa. The proposed model has several potential applications such as the identification of critical zones for flooding (zones with high water depths and flow velocities) in urban development and can be used to take appropriate measures for drainage control (to increase the number and/or size of inlets), to determine the consequences of different degrees of inlet clogging, and to assess flooding hazards through the application of suitable hazard criteria.

4. Results and Discussion

4.1. Model sensitivity, Calibration and Validation Fit

Most model predictions inherit much error and uncertainty by the underlying Empirical Risk Minimization (ERM) principle usage. Hence, before calibration and validation of the QSWAT model, a sensitivity analysis was examined as part of the modelling process to determine which parameters influence the model structure and output most. It is also used to understand the influence of input on model structure and the model outputs. The modelling approach presented several simulations that have been carried out using a range of different input values for the most sensitive model parameters. The calibration and validation technique employed for the models was through comparing the model simulated drainage system network discharge with observed data in rainfall-runoff transformation. Most parameters employed are assumed to be uniformly distributed in the models. We achieved an acceptable fit between predicted and observed flow during calibration and validation for most parameters at the outlet gauge. Suggesting the model was suitable for predicting the discharge flow and reliable over the different hydro-climatic periods. Figures 4 and 5 depict the calibration and validation results for the flow discharge.

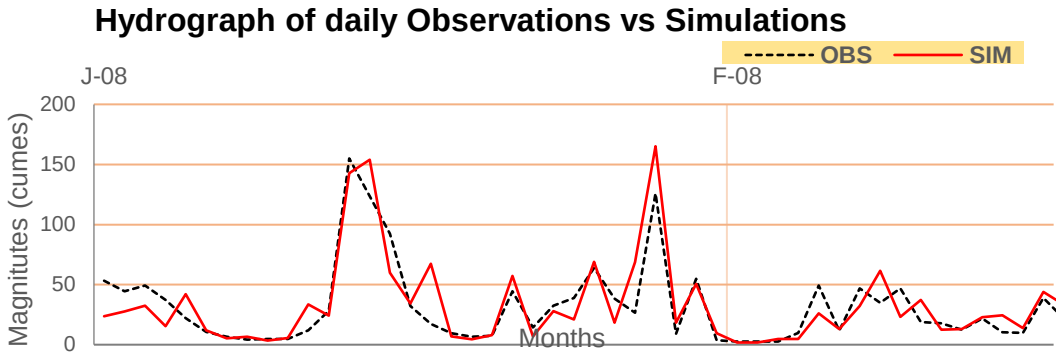

Figure 4: Observed and simulated discharge during the calibration period 2010-2014

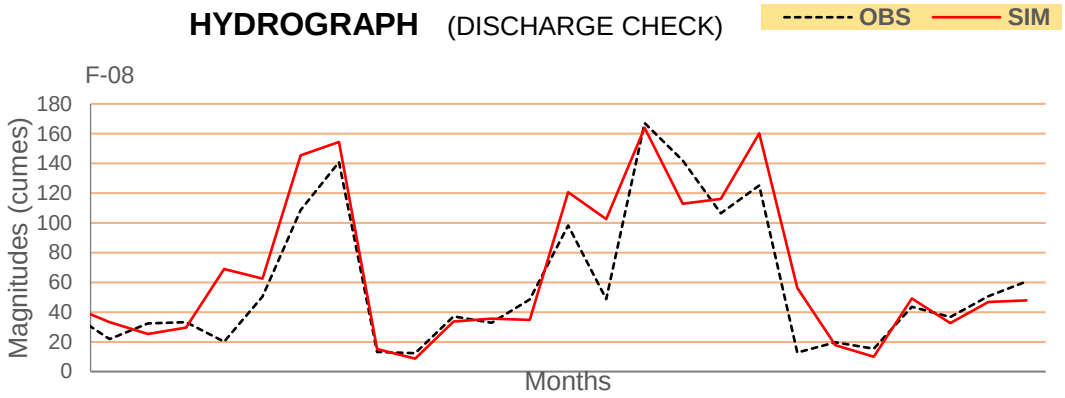

Figure 5: Observed and simulated discharge during the validation period 2015-2020

The most sensitive parameters for the hydrological modelling of MRB watershed are CN2.mgt; ALPHA_BF.gw; GW_DELAY.gw; A__RCHRG_DP. gw. Thus, The CN2.mgt parameter is the most sensitive parameter with best fitting values of less than -0.01 at relative change (r__). [45] also confirmed that these four parameters are the crucial sensitive parameters for water balance and stream flow. Therefore, the goodness-of-fit of the QSWAT model estimates of runoff should be viewed in the context of the goodness-of-fit of the available observed sample data used as inputs. The calibration and validation values for goodness-of-fit (NSE, and R^2), obtained during the calibration and validation period, are all acceptable(values greater than 0.5). For instance, the NSE and R^2 are about 0.84 and 0.79 respectively at validation for daily discharge simulation. Table 2 shows the simulated monthly discharge for MRC for the period.

Table 2: Goodness-of-fit for simulated monthly discharge.

	Calibration	Validation
	(2010-2014)	(2015-2020)
NSE	0.65(g)	0.84(vg)
R^2	0.63	0.79

Where g= good; vg= very good

Both the meteorological data and land use changes have a considerable impact on the water balance of a catchment and sub-catchments. The influence of climatic variables on various parameters such as water yield, surface runoff, and evapotranspiration (ET) transcend land

cover as shaped by land use practices which in turn affects the concentration of greenhouse gas emission and transpiration processes. land use change is sensitive to the soil curve number, soil type and distribution. All these parameters are important drivers of the environment and contributors to prevailing weather conditions in an area. A change in land use and land cover invariably affects runoff and available groundwater resources. A decline in groundwater levels may be attributed to increased extraction rates or the intrusion of saltwater in coastal areas. All these interchangeable factors affect and contribute to water scarcity that poses a threat to some part of the country's overall water security. Below are the results of assessing the impacts of Land Use and Land Cover Changes (LULCC) on the water quantity degradation.

4.2 Land use and cover change result

The land use maps were reclassified using detailed land cover types from the prevailing land uses in the area. Much of the land cover was characterized by different grassland and savannah vegetation. As shown in Figure 3, the map codes classified AGRL, PAST, FESC, BARR, URBN, WATR, RNGE, and UCOM to represent Agriculture, Pastures, Forest, Barren, Urban Settlements, Water occupied, Residential, and Urban commercial areas respectively, with varying percentages as the main land use activity in the area. Figure 3 depicts the land use and cover type for the study area.

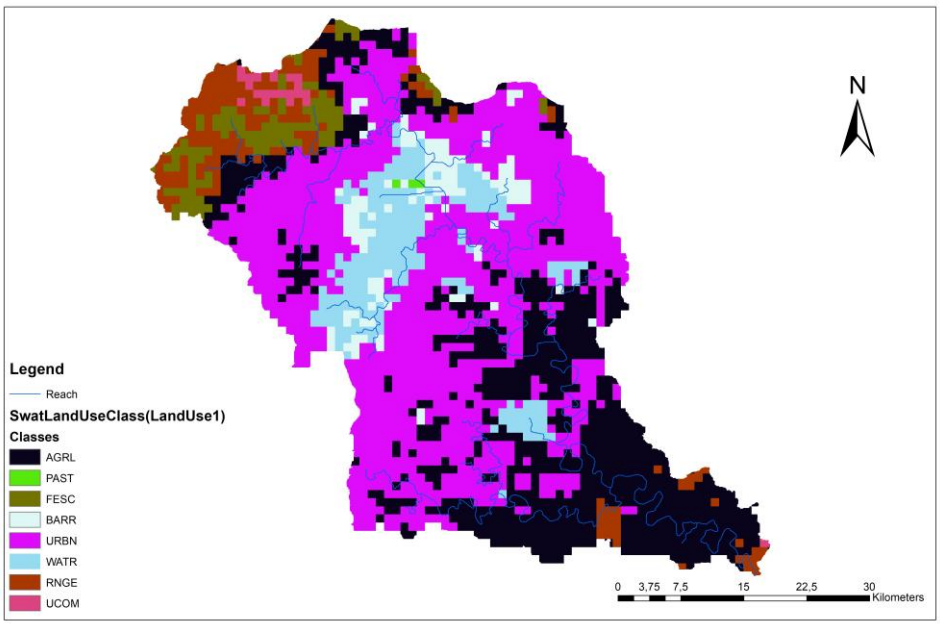

Figure 3: SWAT-based land uses and land cover classification at MRC

4.3 Urban growth and sprawling land consumption result

Table 3 depicts the derived LULC change area composition variation per decade year for the MRC. Urban sprawling land consumption and its effect on water availability within 2000-2020 reflected a long-term increase in bare land by 11.72% with a negative 3.65% in water bodies and a marginal increase in built-up areas (0.52%). The period (2000 – 2010) had the biggest

change in bare lands (13.09%) followed by a major decline in agriculture, vegetation, and water bodies. The built-up area covered the smallest area in comparison with/to other land cover types. The results also demonstrated that the area occupied by water decreased from 14152 ha in 2000 to 4758 ha in 2020, representing a -3.65% change in the overall composition of water bodies in response to LULC change. The built-up areas had the least changes overall.

Table 3: Derived LULC change area composition variation per decade year for the MRC

Class name	Area (ha)			% composition			% change		
	2000	2010	2019	2000	2010	2019	2000 - 2010	2010-2019	2000-2019
Agriculture	71 118	38 432	63 181	27,61	14.92	24,53	-12,69	9,61	-3,08
Bare land	128678	162468	158 943	49,98	63,07	61,70	13,09	-1,37	11,72
Built up areas	2 365	2 845	3 701	0,92	1,10	1,44	0,19	0,33	0,52
Vegetation	41 344	26 645	26 918	16,05	10,34	10,45	-5,71	0,11	-5,60
Water bodies	14 152	4 914	4 758	5,49	1,91	1,85	-3,59	-0,06	-3,65
Total area mapped (ha)	257609	257609	257 609	---	---	---	---	---	---

Figure 7 shows the map for the satellite-derived LULC changes for the MRC. There has been a declining trend in water bodies within the catchment since the year 2000, which is also attributed to the observed increase in bare lands.

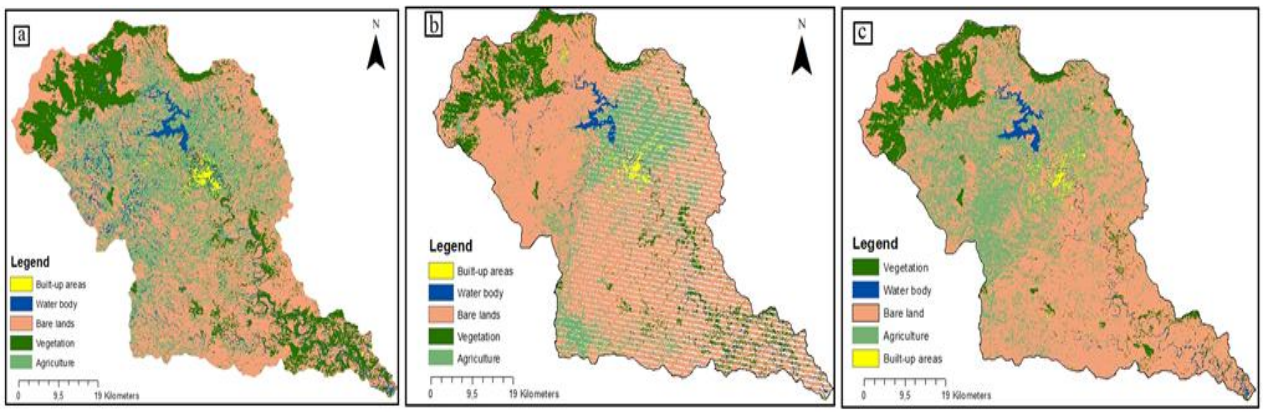

Figure 7: Satellite-derived Land use and Land cover changes for the MRC (2000-2020).

Water bodies were the only land cover type with a persistent decrease throughout the period. Also, land emittance of greenhouse gases leads to global warming and climate change. The world is now warming faster than at any point in recorded history. Warmer temperatures over time are changing weather patterns and disrupting the usual balance of nature.

4.4 Results of Urban Water Balance Components

4.4.1 SWMM simulation results

Figure 8 shows the 3D digital elevation model of the Mthatha case study area. The elevation data is provided in a different file format called *.bed file. The DEM's resolution was set at 4m, which is useful for the pictorial view and demarcation of the sub-catchment area.

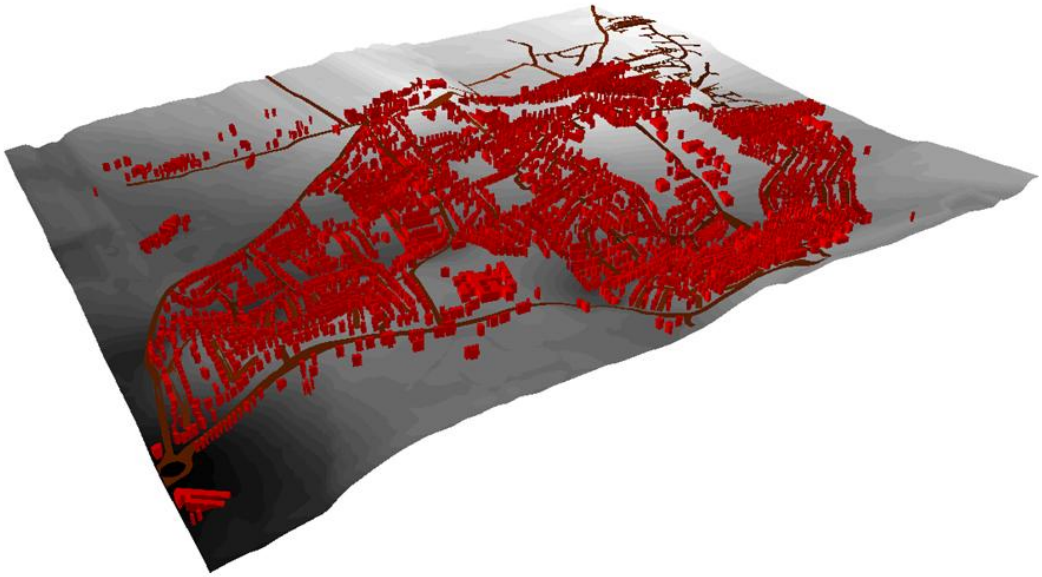

Figure 8: 3D DEM of Mthatha township, attributed with roads and buildings.

4.4.2 SWMM and QSWAT Hydrological Routing

Roughness data was needed for the topographical terrain of the study area in SWMM routing. A uniform value of 0.02 was adopted and Manning's formula was used for the computation of the conveyance friction terms in the shallow water equations. The surcharge flow occurred at separate times depending on the given discharge flow time series from the SWMM simulation. The surcharge flow is contributed by 28 nodes and the total volume from collected street and impervious layer is estimated to be 4,915 m^3. A summary of the model result is presented in Table 4. The run-time of 5hr - simulation is quite an acceptable computational speed especially when considering a quick prediction of urban street flow scenario analysis. The mass balance error of the simulation result is also quite insignificant, and this may be attributed to the finite volume scheme used for the solution of the model equations.
Arising from the street network studies, the interconnecting drains listed in Table 5 were selected based on their capacity to control flow.

Table 4: Summary of the model results for the case study area

Model Results	**Value**
Total simulation time(h)	5
Model run-time (min)	70
Mass balance error (%)	7.6 x10^{-9}
Total Inundated area range (Sqm)	65-554

Table 5: Expected Discharge for the Drains

Road / Drain	**Area, Km^2**	**Discharge, Q m^3/s**
1-3dR	0.078	2.651
1-3R	0.037	1.248
1-4R	0.038	1.278
1-5R	0.039	1.339
1-6R	0.039	1.309
1-6aR	0.036	1.218
1-7R	0.038	1.278
1-7aR	0.037	1.248
1-8R	0.032	1.098
1-9R	0.039	1.309
1-10R	0.035	1.188
1-11R	0.036	1.218

Since drains were attached to each side of the roads, the conveyor capacity using the rational formula Qmax = (CIA)/36 - in metric units. Where "A" is the area in hectares; "λ" is the catchment factor governed by the losses and other conditions of the catchment; "I0" is the maximum intensity of rainfall in cm/hr. Catchment factor, C = 2 f P/(tc+1); Where "f" is the speed factor of the depending on its uniformity in a given basin. For basin areas up to 100km2, "f" is taken as 1.0; P is the Permeability factor (coefficient of runoff); "tc" is the time of concentration in hours given by; tc = 0.88 (L^3/F)0.385. Where "L" is the length of the drainage basin in km; F is the fall in elevation in meters in the length "L" of the catchment. The values of the permeability factor, "P", for Steep, bare, rocky, and city pavements (0.9) and for Clayey soil, stiff and bare (0.6) as contained in [46,47]. Figure 9 illustrates the QSWAT rainfall-runoff transformation.

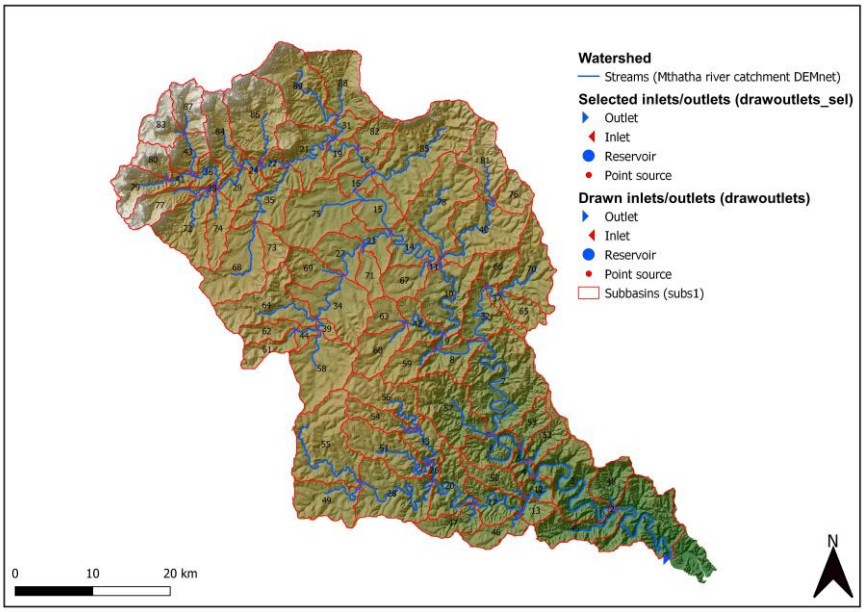

Figure 9: Streamflow network and sub-drainage pattern formation at MRC

Likewise, considering the assumption made on soil grain size and field capacity, these affect the drainage capacities and runoff pathways. The nature of the catchment streamflow network and distribution orders play an important role in the transportation of wastes through their surface flow discharge. The catchment transforms precipitation into runoff patterns, which in consequence affects the surface flow, replenishes the groundwater, and the overall equilibrium of water within the catchment. Also, it's worth noting the portion of water that flows into/through combined sewers, or even direct water that flows into the channel drainage and those collecting network that flows as runoff through the impervious road layout were all detailed in the SWMM manual [25]. In all, the modified SCS method is used for runoff quantification. This method is based on the area's hydrologic soil group, land use, treatment and hydrologic curve number (CN) condition. Although the method is designed for a single storm event, it can be scaled to find average annual runoff values. Depending on the settlement type (urban versus peri-urban areas), this could influence water balance depending on hydrologic curve number (CN) condition. Figure 9 depicts the streamflow network and sub-drainage pattern of the MRC. Most sub-drainage formation patterns and the catchment drainage network were characterized by radial drainage forms where water flows downward from a hill or mountain to a wheel circular network of parallel channels flowing away from a central high point.

4.4.3 Estimation of Precipitation Component

The average monthly precipitation data for the period under study has been estimated from Precipitation records from 2000-2020 and were used as presented in Figure 10.

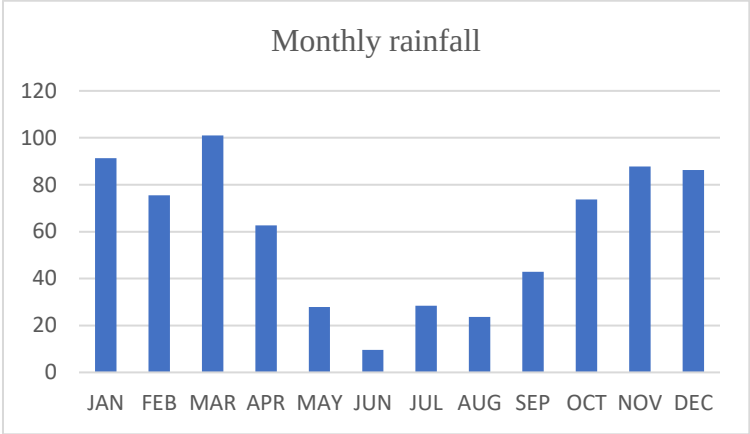

Figure 10: Monthly Rainfall depth in MRC (mm) (2000-2020)

In this study, the mean monthly (11-22 mm) and mean annual precipitation range from 489 to 959 mm of the study area was calculated from data obtained from the South Africa Agriculture Meteorological Agency (ARC), for the Mthatha catchment area.

4.4.4 Estimation of Evapotranspiration (ET) Component

The collected potential evapotranspiration, ET data from ARC is presented in Figure 11. In this study, the mean monthly and mean annual evapotranspiration of the study area was obtained from the South Africa Agriculture Meteorological Agency (ARC), for the Mthatha catchment area. It was noticed no available records were available for the years 2000 and 2001, this was extrapolated from free water surfaces estimated by the Modified Penman method.

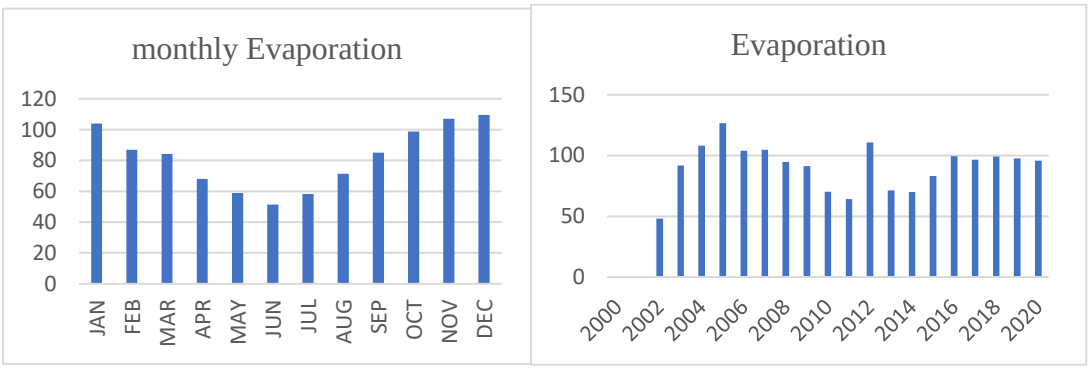

Figure 11: Monthly and yearly Evapotranspiration data from ARC

Even though the evaporation from free water surfaces could be estimated by several methods such as Blaney Criddle, Modified Penman, Thorntwaite, and others. The modified Pennman method provides a reasonable estimate where sophisticated measurement equipment is not available. The mean monthly estimated for the area is 109.426 mm.

4.4.5 Estimation of Catchment Runoff Component

The direct runoff is the result of the immediate response of a catchment to the input rainfall. The catchment runoff was estimated using the rational method by multiplying the volume of rain that falls on that surface by its "runoff coefficient"- (P*Cw). The runoff coefficient ranges from 0.30-0.50 for different land use/land cover with clay and silty loam for both urban and Agricultural areas [48]. Using a coefficient of 0.35, the predicted monthly runoff depth is summarized in Figure 12.

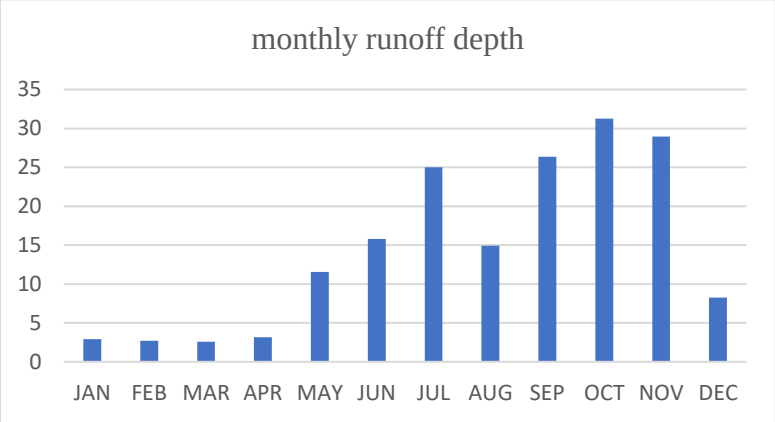

Figure 12: Predicted monthly runoff depth (mm) for MRC (2000 - 2020)

In this study, the mean monthly runoff of the study area was calculated from data obtained from the South Africa Agriculture Meteorological Agency (ARC), for the Mthatha catchment area. The mean monthly runoff ranges from 2.58 to 28.97 mm.

4.4.6 Groundwater Recharge Component

The amount of percolation in the area was to be assumed 20% of sewer collection accrued to percolation due to leakage, malfunction of pipe, and during repair. Thus, 0.20 of 4,915=983 m^3. This is the total permeable leakage and percolation for the area. The average flow per street length equals the total discharge divided by the area (Q=VA). When area occupied =0.038 Km^2. Therefore, the volume of water occupied by each street length was estimated as 37.354 m^3.

4.4.7 Ecosystem and Environment Flow Component

The environmental flow was calculated by subtracting surface water diversion and outflows into the sea from surface runoff or better still, by assuming 20% of the 75% dependable flows in each of the wet months or using 15% of the average monthly flows in different months for the dry months. Thus, using 15% of the average monthly flows in different months for the dry months equals 0.15 of 14.93 = 2.23 mm.

4.5 Urban Monthly Water Balance Configuration Result

The mean monthly hydrologic budget value for 2000 – 2020 using the different computed components from Equation 5 is presented in Figure 13. The change in storage (ΔS) was based on Equation 3: (P - (ET + RO) = ±ΔS), substitution with an appropriate monthly value. Where: P = precipitation, ET = evapotranspiration, R = surface runoff, and ΔS = change in storage.

The analysis shows a surplus in water balance from January to April (a total of 91.86 mm), while the remaining eight months (May till Dec) exhibit a negative balance with a total of 174.248 mm annually. Therefore, there is a need for groundwater inflow of 91.859 mm annually to balance the deficit.

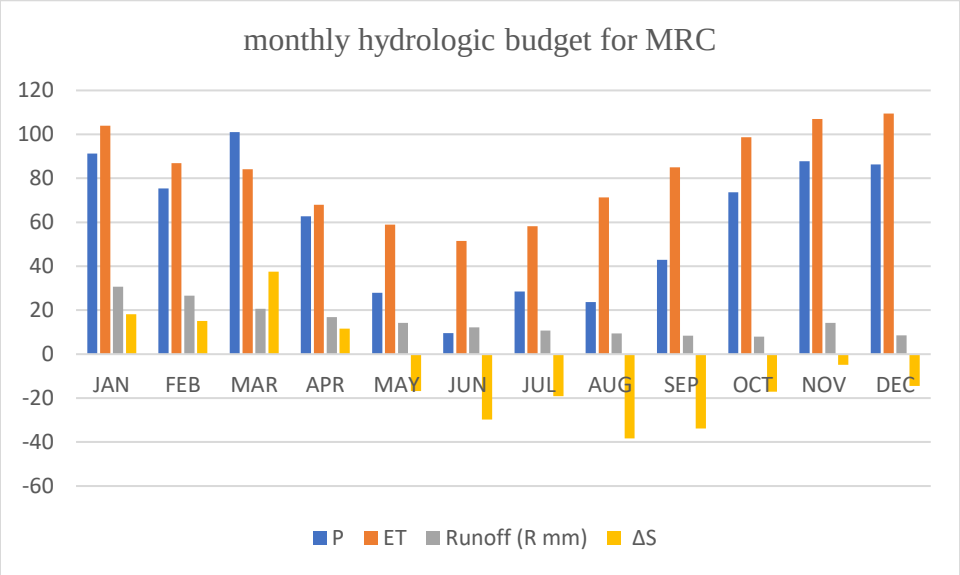

Figure 13:Monthly hydrologic budget for Mthatha River Catchment

4.6 The Mean Annual Hydrologic Budgets

Substituting the appropriate value in Equation 8. The annual average water balance is tabulated in Table 10. Where n = number of years of record = 20 years; P = Mean annual Precipitation = 1225mm; R_{in} = Mean Annual Runoff of MRC at downstream=443mm; $ET_s = 123$ mm; $ET_e = 204$ mm; $R_{out} = 143$ mm; $^{dG}/_{dt} = 534$; The net annual hydrologic budgets indicate a negative budget, the value ranging from -624.955 mm to -19.40 mm. However, this negative budget suggests that for the hydrologic budget to balance, -624.955 mm to -19.40 mm of water must enter the system from some source. The balance has an error margin of 2.22 mm/year. This is small compared to the complexity of the estimation of each of the water budget components.

Figure 15 presents the annual variation of water balance for MRC. However, since the primary input to the watersheds is precipitation, the catchments could be affected by numerous factors including longer dry seasons, topography, soil types, with intense population activities which may have resulted in a negative balance.

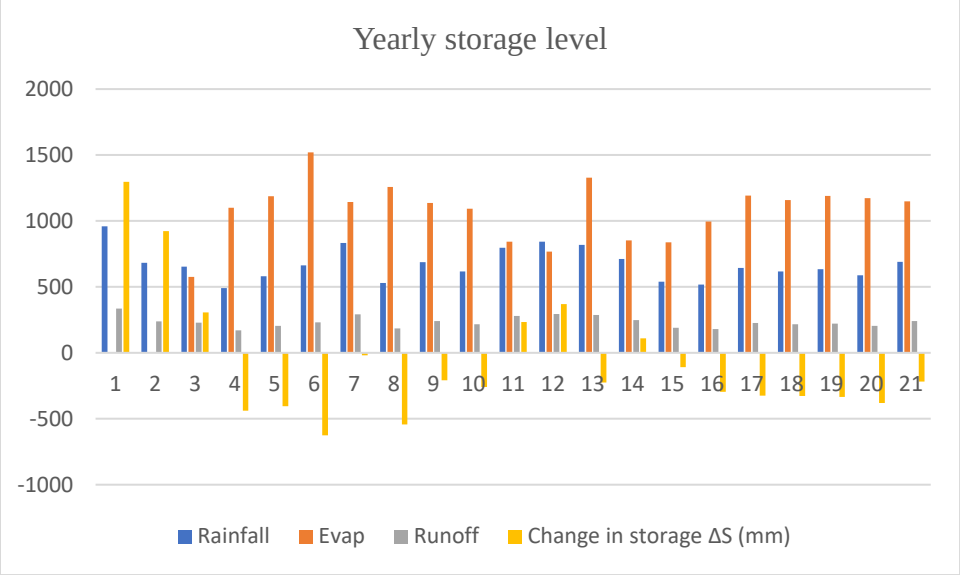

Figure 15: Annual variation of water balance for MRC

The reported negative annual water balances (-624.96 mm) imply insufficient water to meet the population density, forestry, and industrial development needs - such as mining activities, and farming practices, thus hindering industrial growth and many economic activities that may be useful to the city development and urban growth planning. This indicates a total water surplus of 3238.86 mm and a total water deficit of 4707.84 mm annually for the period under investigation. The water balance results reveal time-varying hydrologic-meteorological datasets to evaluate the monthly and annual extrapolation while additional characterization of depletive and consumptive sewer uses would result in wide differences regarding the rate of infiltration and runoff/recharge. Hence, water must enter the system from other sources to maintain hydrological water balance.

4.7 Implication of results

Conversely, the adverse effect of water depletion witnessed in the area has resulted in the extinction of certain species of animals and aquatics preservation in the catchment. Mthatha's socio-economic and ecological conditions had suffered drastically due to the negative annual water. Thus, raises the growing concern that policies for sustainable water use, environmental quality and efficient allocation of the available water resources should be implemented, particularly in the study area. The severe drought and its attendant problems have contributed to the severe consequences on the status of the Mthatha River and its tributaries, biodiversity, landscapes, key habitats, and floodplains. This has caused considerable pressure on the ecosystem, resulting in conflicts over water resource allocation among riparian users.

Most of the converted forests to grazing lands and agricultural lands have resulted in reduced soil infiltration and reduced groundwater recharge in most of MRC's lowlands. The changes in land cover/use have been most rapid on the foot slopes of the mountain where large commercial

afforestation has been established. This has adversely affected the downstream and ecological systems leading to conflict over water demand, which calls for careful planning to alleviate the growing water challenges. The diverse uses and demands have resulted in water stress situations particularly in times of drought, which has characterized the South African environment in recent times, The aggregated effect of LULC may have also contributed to the water deficit due to almost impermeable layer and thereby contributed to the continuous flooding volumes.

4.8 Findings Summary

The paper analyzes how urbanization and land cover changes impact water availability in Mthatha, South Africa. Using hydrological models, it finds that increased impervious surfaces and climate variability lead to a consistent water deficit, underscoring the need for sustainable water management in growing urban areas. The study has contributed to and enhanced our understanding of the current land use and land cover as it impacts urban water balance configuration. Accordingly, assesses the impacts of human-ecosystem water relationship over the catchment and before investigating the effect of urbanization on water balance configuration.

From the results, there is a notable change noticed in the shift in land cover between 2010 to 2019, this has a direct bearing on reducing the water bodies area makeup. From 2000 to 2010, there is a negative 3.59% change in water bodies. From 2010, there was a negative 0.06% change in water bodies, while in 2019, there was a negative 3.65% change. Also, in terms of vegetation, there was a negative 5.71% change by 2000, and this was reduced to a positive 0.11 in 2010 before a further reduction of 5.60 in 2019 representing a 76% reduction from the total area mapped (257,609). The correlation coefficient results of negative 3.08 in 2019 suggest built-up area contributes largely to characterize the impervious layer, even though agricultural land use contributes (-12.69) in reduction to (-3.08) in 2019, but the proportion is minimal. This implies that the catchment witnesses geometric man-made land use and land cover for urbanizing areas. Hence, the rate of urbanization is quite different. The water budget developed through this study was based on estimated HRUs within a catchment and then aggregated to the sub-catchment level.

The SCS runoff equation was selected for this study, because it uses daily precipitation data, whereas the Green & Ampt method requires sub-daily precipitation data, which were not available for the study area. Also, the most sensitive parameters for the hydrological modelling of MRC are CN2.mgt; ALPHA_BF.gw; GW_DELAY.gw; A__RCHRG_DP. gw. The CN2.mgt parameter is the most sensitive parameter with best fitting values of less than -0.01 at relative change (r__). The effect of close pavement with runoff, (Table 3) suggests a direct link from substantial conversion in precipitation into runoff patterns, which consequently affect the surface flow, the replenishment of groundwater, and the overall equilibrium of water within the catchment.

Further research on how the different soil types with their soil moisture content help in detecting anomalies in the soil filtration capacity and could be used to respond to both emissivity and resistivity impact on the catchment. The catchment's response to impervious layer implies a reduction of water bodies through evaporation and built-up area, thereby making the area

susceptible to losing water content. The study has equally helped to show how human activities impact and could modify the natural flow of water and help to maintain an ecological water balance system. The findings show a simple, but effective water balance component estimation.

The study has maintained that the earth's water is constantly changing form although other components of urban water balance may suggest not. These changes in water form tend to justify more analyses that could require sophisticated models at the sub-catchment scale. The study did not perform any sensitivity analysis on climate parameters, such as varying precipitation and evapotranspiration rates, to observe impacts on water balance as this is beyond the study scope.

Further research concerning urban water balance could focus on varying climatic variables, land use, and soil parameters to observe their impacts on water balance. Also. the effect of sub-division of impervious layers against the assumed broad constructed land surface, air temperature emissivity, and resistivity in land use can be further investigated. The study assumes a mean uniform runoff coefficient based on land use/land cover at the detriment of the area's heterogeneity. Further research on how sensitive this parameter could affect the overall water balance would be beneficial for future studies.

5. Conclusion and Recommendations

Our results contribute to understanding the role of precipitation, infiltration/recharge, runoff, and evapotranspiration in water-related ecosystem services. The study area had witnessed urban water deficits. Hence dependable water uses with land uses recovering in an integrated system that fits with growing urban land development issues was recommended. Also, sustainable integrated management approaches from a catchment perspective in contrast to a fragmented approach that artificially separates land management from water management is suggested as a viable option for policymakers, and the catchment management area board. In short, water management practitioners would find the study useful in formulating laws and practices for controlling or preventing catchment water deficit.

It is crystal clear that of the urbanization impacted soil sealing, hence catchment water balance would benefit by using global big data for improvement in hydraulic conveyance and hydrological model monitoring data, and application of isotopic analysis for groundwater. Likewise, the study of LULC has provided actionable insights for water resources managers to advance environmental conservation initiatives. The study suggests that both the adaptative catchment management and the legislative provincial initiatives approaches are viable ways to ensure water conservation and maintained urban water balance.

Adaptive catchment management is designed to restore or protect water quality conditions in catchments through best management practice (BMP) operation. At the same time, legislative provincial initiatives address the various formulated laws and practices for integrated catchment management. The utilized water balance framework could serve as a suitable decision support system in evaluating available water and provide a comprehensive scientific assessment

methodology for the peril of water scarcity experienced in the region. The outputs of this study could also serve as baseline information for water balance management in the MRC.

Acknowledgments

The authors acknowledge and thank the WRC, ARC-ISSC, SAWS, and DWA for providing the data and those who participated in the survey field data. We are also grateful to grant No. C2019/2020-00166 for sponsoring part of this study and the Walter Sisulu University, Mthatha, for providing the enabling environment. We also thank the financial support from the Department of Science, Technology and Innovation and the National Research Foundation through the Centre for Global Change. We are indeed grateful for the constructive comments and suggestions from the two anonymous reviewers which have improved the presentation of the paper.

Conflicts of Interest: The authors declare no conflict of interest.

References

[1] Astuti, I. S., Sahoo, K., Milewski, A., & Mishra, D. R. (2019). Impact of land use land cover (LULC) change on surface runoff in an increasingly urbanized tropical watershed. *Water Resources Management*, *33*(12), 4087-4103.

[2] McGrane, S.J., 2016. Impacts of urbanisation on hydrological and water quality dynamics, and urban water management: a review. *Hydrological Sciences Journal*, *61*(13), pp.2295-2311.

[3] Haase, D., 2009. Effects of urbanization on the water balance–A long-term trajectory. *Environmental Impact Assessment Review*, *29*(4), pp.211-219.

[4] Aspinall, R. and Pearson, D., 2000. Integrated geographical assessment of environmental condition in water catchments: Linking landscape ecology, environmental modelling and GIS. *Journal of Environmental Management*, *59*(4), pp.299-319.

[5] Melloul, A.J. and Collin, M.L., 2003. Harmonizing water management and social needs: a necessary condition for sustainable development. The case of Israel's coastal aquifer. *Journal of Environmental Management*, *67*(4), pp.385-394.

[6] Akram, M. and Hamid, A., 2013. A comprehensive review on water balance. *Biomedicine & Preventive Nutrition*, *3*(2), pp.193-195.

[7] Huang, X., Wang, H. and Xiao, F., 2022. Simulating urban growth affected by national and regional land use policies: Case study from Wuhan, China. *Land Use Policy*, *112*, p.105850.

[8] Fletcher, T.D., Andrieu, H. and Hamel, P., 2013. Understanding, management, and modeling of urban hydrology and its consequences for receiving waters: A state of the art. *Advances in water resources*, *51*, pp.261-279.

[9] Kleemann, J., Inkoom, J.N., Thiel, M., Shankar, S., Lautenbach, S. and Fürst, C., 2017. Peri-urban land use pattern and its relation to land use planning in Ghana, West Africa. *Landscape and urban planning*, *165*, pp.280-294.

[10] Enoguanbhor, E.C., Gollnow, F., Walker, B.B., Nielsen, J.O. and Lakes, T., 2022. Simulating urban land expansion in the context of land use planning in the Abuja City-Region, Nigeria. *GeoJournal*, pp.1-19.

[11] Haase D., 2003. Holocene floodplains and their distribution in urban areas – functionality indicators for their retention potentials. Landsc Urban Plan ; 66: 5-18.

[12] Herczeg, A.L. and Leaney, F.W., 2011. Environmental tracers in arid-zone hydrology. *Hydrogeology Journal*, *19*(1), p.17.

[13] Bam, E.K. and Ireson, A.M., 2019. Quantifying the wetland water balance: a new isotope-based approach that includes precipitation and infiltration. *Journal of Hydrology*, *570*, pp.185-200.

[14] Birkel, C., Duvert, C., Correa, A., Munksgaard, N.C., Maher, D.T. and Hutley, L.B., 2020. Tracer-aided modeling in the low-relief, wet-dry tropics suggests water ages and DOC export are driven by seasonal wetlands and deep groundwater. *Water Resources Research*, *56*(4), p.e2019WR026175.

[15] Mook, W. and Rozanski, K., 2000. Environmental isotopes in the hydrological cycle. *IAEA Publish*, *39*(1), p.2.

[16] Tondu, J.M.E., Turner, K.W., Wolfe, B.B., Hall, R.I., Edwards, T.W.D. and McDonald, I., 2013. Using water isotope tracers to develop the hydrological component of a long-term aquatic ecosystem monitoring program for a northern lake-rich landscape. *Arctic, antarctic, and alpine research*, *45*(4), pp.594-614.

[17] Mohammed, A.A., Sule, B.F., Salami, A.W., Adeogun, A.G., Ayanshola, A.M. and Oladeji, A.S., 2022. Prediction and Simulation of Kainji Hydropower Reservoir Operation in Nigeria. *Nigerian Journal of Engineering*, *29*(1), pp.29-29.

[18] Jain, G.V., Agrawal, R., Bhanderi, R.J., Jayaprasad, P., Patel, J.N., Agnihotri, P.G. and Samtani, B.M., 2016. Estimation of sub-catchment area parameters for Storm Water Management Model (SWMM) using geo-informatics. *Geocarto International*, *31*(4), pp.462-476.

[19] Amoo, T.O., 2018. Integrated hydrological modelling for sustainable water allocation planning: Mkomazi Basin, South Africa case study (Doctoral dissertation).

[20] Borah, D. K., Ahmadisharaf, E., Padmanabhan, G., Imen, S., & Mohamoud, Y. M. (2019). Watershed models for development and implementation of total maximum daily loads. *Journal of Hydrologic Engineering*, *24*(1), 03118001.

[21] Ballinas-González, H.; Alcocer-Yamanaka, V.; Canto-Rios, J.; Simuta-Champo, R. **2020.** Sensitivity Analysis of the Rainfall–Runoff Modeling Parameters in Data-Scarce Urban Catchment. *Hydrology*, *7*, 73.

[22] Hussain, S.N.; Zwain, H.M.; Nile, B.K. 2021. Modeling the effects of land-use and climate change on the performance of stormwater sewer system using SWMM simulation: Case study. *J. Water Clim. Chang. 13*, 125–138.

[23] Duarte, A. C., Ferreira, C., & Vitali, G. (2022). Use of simulation models to aid soil and water conservation actions for sustainable agro-forested systems. In *Natural resources conservation and advances for sustainability* (pp. 389-412). Elsevier.

[24] Lin, Z. (2011). Estimating Water Budgets and Vertical Leakages for Karst Lakes in North-Central Florida (United States) Via Hydrological Modeling 1. *JAWRA Journal of the American Water Resources Association*, *47*(2), 287-302.

[25] Arjenaki, M.O., Sanayei, H.R.Z., Heidarzadeh, H. and Mahabadi, N.A., 2021. Modeling and investigating the effect of the LID methods on collection network of urban runoff using the SWMM model (case study: Shahrekord City). *Modeling Earth Systems and Environment*, *7*(1), pp.1-16.

[26] Branger, F., Kermadi, S., Jacqueminet, C., Michel, K., Labbas, M., Krause, P., ... & Braud, I. (2013). Assessment of the influence of land use data on the water balance components of a peri-urban catchment using a distributed modelling approach. *Journal of Hydrology*, *505*, 312-325.

[27] Clark, G.E., Ahn, K.H. and Palmer, R.N., 2017. Assessing a regression-based regionalization approach to ungauged sites with various hydrologic models in a forested catchment in the northeastern United States. *Journal of Hydrologic Engineering*, *22*(12), p.05017027.

[28] Duarte, A. C., Ferreira, C., & Vitali, G. (2022). Use of simulation models to aid soil and water conservation actions for sustainable agro-forested systems. In *Natural resources conservation and advances for sustainability* (pp. 389-412). Elsevier.

[29] Daniel, E. B., Camp, J. V., LeBoeuf, E. J., Penrod, J. R., Dobbins, J. P., & Abkowitz, M. D. (2011). Watershed modeling and its applications: A state-of-the-art review. *The Open Hydrology Journal*, *5*(1).Krebs, G., Kokkonen, T., Valtanen, M., Setälä, H., & Koivusalo, H. (2014). Spatial resolution considerations for urban hydrological modelling. *Journal of hydrology*, *512*, 482-497.

[30] Pandi, D., Kothandaraman, S., & Kuppusamy, M. (2021). Hydrological models: a review. *International Journal of Hydrology Science and Technology*, *12*(3), 223-242.

[31] Krebs, G., Kokkonen, T., Valtanen, M., Setälä, H., & Koivusalo, H. (2014). Spatial resolution considerations for urban hydrological modelling. *Journal of hydrology*, *512*, 482-497.

[32] Akoko, G., Le, T.H., Gomi, T. and Kato, T., 2021. A review of SWAT model application in Africa. *Water*, *13*(9), p.1313.

[33] Fu, B., Merritt, W. S., Croke, B. F., Weber, T. R., & Jakeman, A. J. (2019). A review of catchment-scale water quality and erosion models and a synthesis of future prospects. *Environmental modelling & software*, *114*, 75-97.

[34] Arnold, J. G., Moriasi, D. N., Gassman, P. W., Abbaspour, K. C., White, M. J., Srinivasan, R., Santhi, C., Harmel, R., Van Griensven, A. and Van Liew, M. W. 2012. SWAT: Model use, calibration, and validation. *Transactions of the ASABE*, 55 (4): 1491-1508.

[35] Tetsoane, S. T., Woyessa, Y. E., & Welderufael, W. A. (2013). Evaluation of the SWAT model in simulating catchment hydrology: case study of the Modder River Basin. *Interim: Interdisciplinary Journal*, *12*(3), 73-85.

[36] Lee, S., Yeo, I.Y., Lang, M.W., Sadeghi, A.M., McCarty, G.W., Moglen, G.E. and Evenson, G.R., 2018. Assessing the cumulative impacts of geographically isolated wetlands on watershed hydrology using the SWAT model coupled with improved wetland modules. *Journal of Environmental Management*, *223*, pp.37-48.

[37] Tufa, F.G. and Sime, C.H., 2021. Stream flow modeling using SWAT model and the model performance evaluation in Toba sub-watershed, Ethiopia. *Modeling Earth Systems and Environment*, *7*, pp.2653-2665.

[38] Blair, P., & Buytaert, W. (2016). Socio-hydrological modelling: a review asking "why, what and how?". *Hydrology and Earth System Sciences*, *20*(1), 443-478.

[39] Zhou, S., Huang, Y., Wei, Y. and Wang, G., 2015. Socio-hydrological water balance for water allocation between human and environmental purposes in catchments. *Hydrology and Earth System Sciences*, *19*(8), pp.3715-3726.

[40] Sivapalan, M., Savenije, H.H. and Blöschl, G., 2012. Socio-hydrology: A new science of people and water. *Hydrol. Process*, *26*(8), pp.1270-1276.

[41] Vika, V., Ndhleve, S., Mbandzi, N., & Nakin, M. D. V. (2023). Assessment of Physico-Chemical and Microbiological Parameters of Mthatha River in Eastern Cape, South Africa. Environmental Forensics, 1-14.

[42] Rattanaviwatpong, P., 2001. Comparison of Water Quality Models-HSPF, SWMM, and WASP and TMDL applications. *University of Washington, Department of Chemical Engineering*.

[43] Kumar, P., Avtar, R., Dasgupta, R., Johnson, B. A., Mukherjee, A., Ahsan, M. N., ... & Mishra, B. K. (2020). Socio-hydrology: A key approach for adaptation to water scarcity and achieving human well-being in large riverine islands. *Progress in Disaster Science*, *8*, 100134.

[44] Sivapalan, M., 2015. Debates—Perspectives on socio-hydrology: Changing water systems and the "tyranny of small problems"—Socio-hydrology. *Water Resources Research*, *51*(6), pp.4795-4805.

[45] Neitsch, S. L., Arnold, J. G., Kiniry, J. R. and Williams, J. R. 2011. *Soil and water assessment tool theoretical documentation version 2009*. Texas Water Resources Institute.

[46] Horne, D., 1997. FHWA study of South African pavement and other highway technologies and practices. Federal Highway Administration.

[47] Hainin, M.R., Cooley Jr, L.A. and Prowell, B.D., 2003. An investigation of factors influencing permeability of Superpave mixes. *International Journal of Pavements*, *2*(2), pp.41-52.

[48] Wolski, P., Conradie, S., Jack, C. and Tadross, M., 2021. Spatio-temporal patterns of rainfall trends and the 2015–2017 drought over the winter rainfall region of South Africa. *International Journal of Climatology*, *41*, pp.E1303-E1319.

DOI: 10.2478/sspjce-2024-0020

A Simplified 3D Model for Tunnel Pile Interaction

Bousbia Nawel

Faculty of Technology, Department of Civil Engineering, LMGHU Laboratory, University of 20 August 1955, Skikda, Algeria
e-mail: bousbia1101@yahoo.com/ n.bousbia@univ-skikda.dz

Abstract

Due to the development of communication routes (metro, railways), it is frequently necessary to build underground structures in order to improve traffic flow, which is a key factor in the metropolitan areas' regeneration. Taking in account of the interaction between tunnel-soil-piles is a significant topic and a vital factor in the analysis the total solutions of these underground projects. The significance of the impacts communicated depends on a number of factors, including the genre of structure, and the soil type. The main purpose of the present paper is to study numerically the immediate influences that will result from the new tunnels construction near existed piles (micropiles), this model will be employed to an existent case of an Algerian East-West highway tunnel section, while using the code of calculation Plaxis3D tunnel. A detailed parametric survey that will be made to put in evidence influences it of the different parameters geometric and mechanical on the interaction between shallow tunnel and an existing piles and security objectives. And for understand furthermore the problem of interaction mechanism between micropiles and tunnel, principally when piles are positioned in close proximity to tunnels. The obtained findings show that the tunneling may affect in nearby piles a considerable bending moments, lateral deflection, compressive forces, and axial forces.

Key words: interaction, tunnel, pile, three dimensional simulations, Plaxis3

1 Introduction

In Algeria, the rapid development of land has indirectly increased the congestion situation of the traffic in cities. As a result, network of highways, railroads... known significant development in recent years, and might have to be constructed to accommodate the transportation system, communication and utility networks such as highway East-West 7000 km of length. This project imposes often the difficult crossing of the relief, as the mounts, which request underground works (construction of tunnels). An evaluation of the effect of tunneling on the stability and integrity of existing piles is sometimes required prior to the construction of the shallow tunnels. Tunneling may cause critical axial stresses and bending moments in nearby piles, particularly when piles are installed in fragile soils, according to laboratory research by Morton and King and centrifuge experiments by [1]. Therefore, it is very important to understand in detail the interaction mechanism between tunnel and pile

during their construction processes. Several works of research studied the interaction between tunneling and groups piles at different position of the pile tip concerning the horizontal axis of the tunnel; the numerical analyses were used to study this problem as well.
The tunnel T4 comes within the framework of the realization of the Maghreb Unit Highway which is about 7000 kilometers. The tunnel is part of section 4 of this highway. The highway tunnel T4 comprises two substantially parallel tubes of a total length of 2500 m; this case includes evaluating the underground and ground movement (settlements), the internal forces in the existing piles (constructs in first) before and after interaction with newly adjacent tunnel (to construct in second) using the finite element method [2].
In this work, we suggest using completely three-dimensional finite element modeling to investigate the micropiles reactions to tunneling at the kilometer point (231+220), which is in a zone of weak cover (shallow tunnel).
It ducts to search for suitable solutions adapted to this type of ground. The recent research moves toward the reinforcement of soil by the micropiles, in this part we are going to pass to the numerical modeling for a calculation model that is dedicated by the interaction between tunnel-pile. The interaction mechanism between tunnel - soil- piles is a difficult problem. It is divided into two major categories:

- The impact of tunneling on existing piles.
- The impact of pile building and loading on already-existing tunnels.

An overview of the impact of tunnel building on already-existing neighboring pile foundations was provided by [3-4]. They gave two instances where pile movements related to building tunnels had been measured

2 Problematic

For several reasons, we construct the shallow tunnels (weak cover zone). The excavating of the shallow tunnels can induce movements of ground that are susceptible to provoke some distortions and in extreme cases the important damages and can conclude the collapses, the slips to the level of the ground surface, therefore. For resolving the problems results to the excavation of the underground works at weak cover. We start in the first place with the reinforcement of this zone by bored piles, after the reinforcement, we pass by the excavation of tunnel to double tubes. The right tube of the tunnel is excavated in first, the one of left in continuation, in accordance with the exposed method. This operation creates a problem of the interaction between piles and tunnels [5-6]. For analyzing and resolving the tunneling-piles interaction problem. We can achieve some analyses by finite element to study the displacement; axial forces; bending moment and the lateral deflection in the micropiles resulting from tunneling located close proximity to them.

3 Site of Tunnel “T4”

The tunnel “T4”is located to the North - East of Constantine. It crosses from South to North Jebel El Cantor over a total length of 2500m. The tunnel is characterized by a zone of low

coverage above which extends over a very significant length. The tracing of the tunnel is raised on the geological card of S'mendou at 1/50.000th [7].

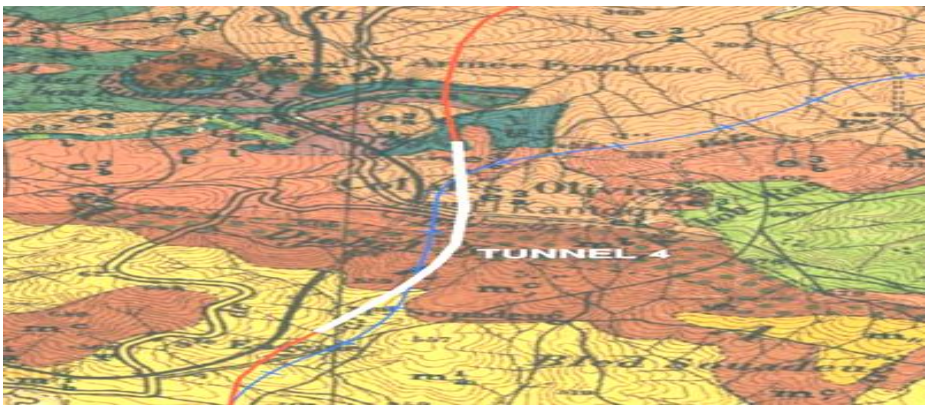

Figure 1: Location of the tunnel T4 on the geological map of Smendou

4 Simulation model (Tunnel-Micropile interaction)

4.1 Terrain to be treated using micropiles

Micropiles are generally used when there are difficult ground conditions, such as natural or man-made obstructions, sensitive ground with adjacent excavations, are also an option for use as in-situ reinforcements to provide stabilization of excavations. Micropiles are high-performance drilled deep foundation elements typically between 5–12 inches in diameter that can extend to depths of 200 feet depending on the design requirements and site condition.

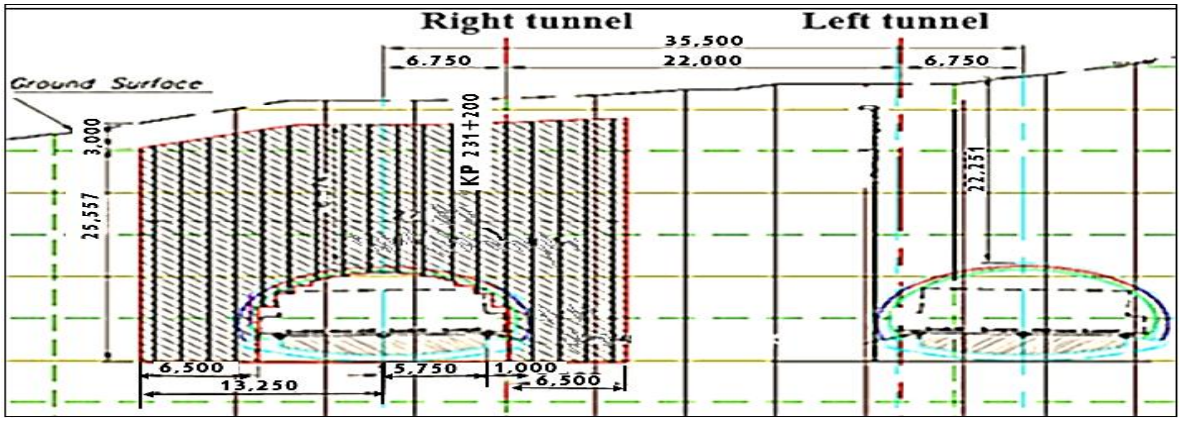

Figure 2: The extended of the section to trea*t*

4.2 Section model to stabilize

The soil will be treated up to the bottom of the tunnel for maximum efficiency. Width of the terrain to be treated: an enlarged excavation zone of 5m on all sides. Improving and reducing

the ground movements induced by excavation of tunnel T4 using micropiling is an appropriate solution for the present study in the most critical section (PK 231+220) corresponds to the lowest coverage of the tunnel, which is 22,5m [7].
The micropiles are modeled by plate element, in reality a micropile is made up of a T32 steel bar and a cement grout, finally the diameter is 10 cm and the length is 40 m. (Figure 4)

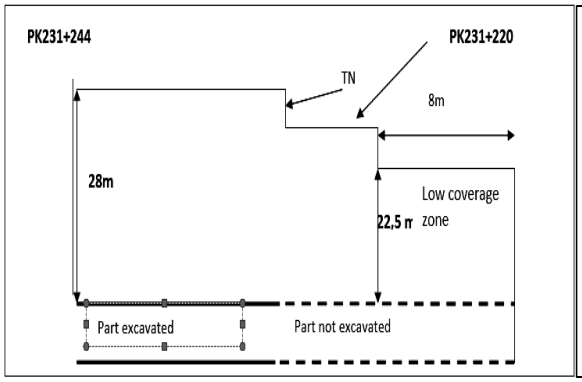

Figure 3: Parts of the T4 tunnel concerned

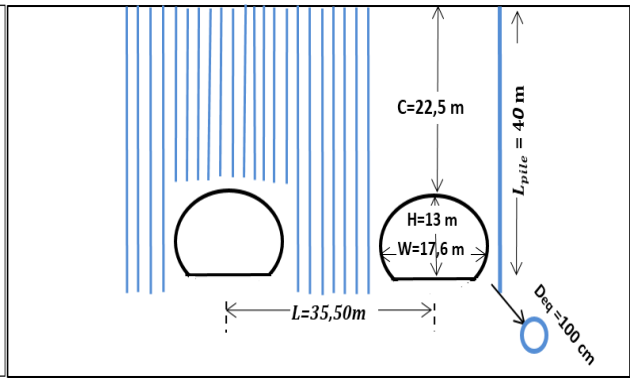

Figure 4: Relative location of tunnels and micro-piles

Figure 4 presents the relative location of tunnels and the micropiles. Mohr coulomb model (MMC) has been applied in this analysis. This model is appropriate to simulate the behavior of soil below the conditions of excavation, with the introduction of group's micropiles.

5 Mechanical characteristics of the chosen section

We take a model section at kilometer point (231+220) that is in a weak coverage zone = 22,5m. The parametric mechanical of the soil that is located at this zone is adopted in the table 1, according to the Mohr Coulomb model.

Table 1. Mechanical and geotechnical characteristics of soil used the Mohr Coulomb Model

Soil	γ (kN/m^3)	E (kpa)	ν	C (kPa)	ø (°)
Marly clay	17,50	30000	0.30	5	27

The lining of the tunnel is composed of a reinforced concrete ring. The tunnel lining properties are given in table 2.

Table 2: Properties of lining tunnel's thickness (40cm)

	E (MPa)	A (m^2)	I (m^4)	d	EA_{eq} (kN/m)	EI_{eq} ($kN.m^2/m$)	ν	$d_{equival}$ (m)
Shotcrete	$1x10^4$	0,4	$5.33*10^{-3}$	1	$5,18x10^6$	$6,9x10^4$	0,20	0,4
Steel H200*200	$2x10^5$	$78.1x10^{-4}$	$0.569x10^{-4}$	1				

6 Model calculation

The tunnel is consisting of two tubes that practically parallel. The right tube is excavated in first, the left tube in continuation, in accordance with the method pro0posed. We excavate the totality of the section of the tunnel (in order to simplify the studied model, we take a simplified equivalent model (Figure 5). In the present analysis, the two tubes are circular in equivalent cross-section with 15.25 m outer diameter and 0.40 m of concrete lining thickness. The centers of the tunnels are to 1,97D below the surface of soil (coverage + radius), the distance between the centers of the two tubes is to 35.5m. For micropiles, the length and width are equal to L_p = 40 m and D_{eq} = 10 cm. The pile has an axial stiffness and a bending stiffness EA=3 E7 kN/m/m and EI=3 E4 $kN.m^2/m$, respectively.
Numerical simulation has been carried out for this investigation using the PLAXIS3D finite element approach. The modeled domain has dimensions of 100 m, 60 m, and 50 m in depth.
The two tubes and micropiles are supposed constructed in a homogeneous soil.

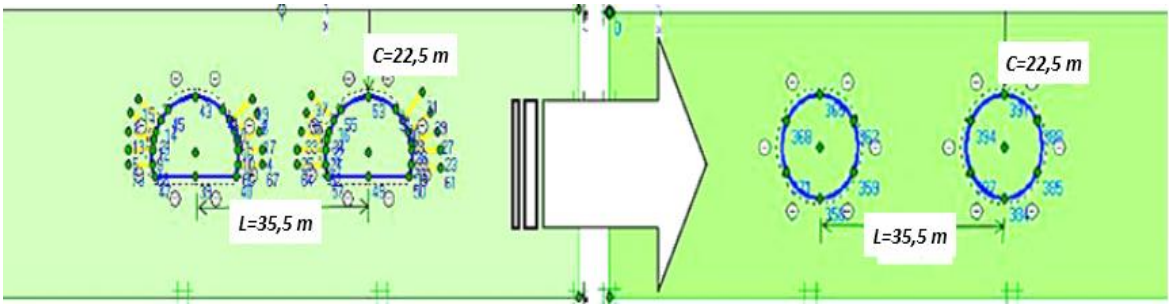

Figure 5: The equivalent model simplified

7 Calculation model according to bored tunnel method

Convergence confinement method is used as an approach simplified of the analysis of the interaction between tunnel-soil [8.9].; and the shape of the tunnel plays a vital function in the lining tunnel convergence.
The micropiles have been localized enough distant that tunnels; this rapprochement of the tunnels gives some effects on the answer of the micro-piles, which could be studied. Due to the symmetry and the simplicity, we take simply the group from four micro-piles that have been simulated with the two tunnels (right and left). The distances between the axis of the micro-piles and the centers of tunnels T1 and T2 are shown in the figure 6. Following the

results of auscultation done to this zone of the weak cover = 22,5m that has given a settlement of 15 cm after 10m excavation, we take only a section longitudinally equal to 10m. Figure 7 displays the finite element mesh used in the numerical modeling; the horizontal (x), vertical (y) and longitudinal (z) is respectively 100, 60 and 10 m. Given that the bottom boundary is outside of the tunnel excavation's influence, it is assumed that there has been no horizontal or vertical displacement there.

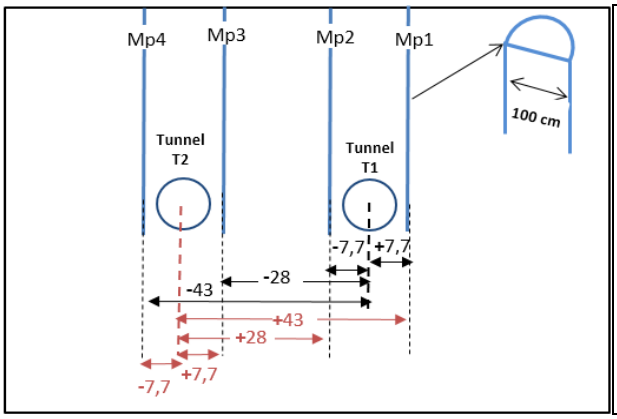

Figure 6: Emplacement of micropiles relative to T1 and T2

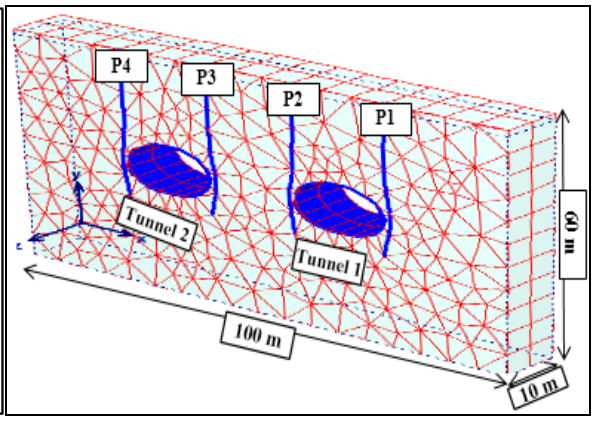

Figure 7: Deformed Mesh 3D

Convergence confinement approach is one of the various similar approaches that enables control of the deconfinement process. The convergence confinement method is used as an approach simplified of the analysis of the interaction between tunnel-soil [8.9]; and the shape of the tunnel plays a vital function in the lining tunnel convergence.

8 Results analysis of interaction between tunnels and micropiles

8.1 Settlement at surface soil Result of analyses

A comparison between the results gotten as the curves, settlements at surface soil measured before and after the presence of the micropiles and the two tubes T1 and T2, therefore we present considered three cases (Micropile in virgin ground, micropile with single right tunnel excavation, and micropile with both tunnels). The curves give variable values in relation to the distinguished cases. It can be viewed from this figure that the settlement is negligible if there are only micropiles. However, the two cases remnant, we note that the values of settlement are more important in the both tunnels case with the presence of the piles, the value max is to the level of the vertical axis (Y) of the left tunnel (T2). It has been observed that, in comparison to building tunnel T1 alone, the two tunnels together construction resulted in a settlement of more than 50%. This is due to that soil after the first excavation already entered in state of instability, once we dig the tunnel T2, reproduces a more important state.

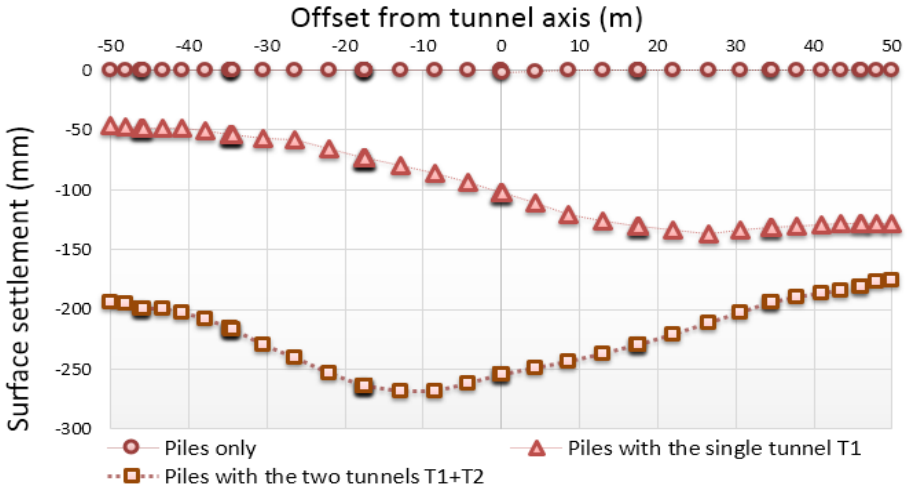

Figure 8 Settlements at surface soil induced by tunneling

8.2 Lateral deflection of mircopiles

Figure 8 presents the lateral displacements profiles in the four micropiles (P1, P2, P3 and P4) before and after the tunnels excavation; the investigation of the pile's movement in a lateral section shows a negligible deflection (practically zero) before the tunneling. Once the tunnel T1 is excavated, the lateral deflections are produced in the four micropiles P1, P2, P3 and P4 and move in either a positive or negative direction toward the tunnel T1 according to the pile-tunnel position, these lateral deflections of the micropile due to the tunnel T1's construction, which is the cause of the ground movement. This behavior is different compared with each pile where the lateral deflection is greater (until the 250 mm) for P2 nearest to the tunnel T1, per contrary this value decreased to 18% when the micropile P4 is distant to the tunnel T1, and can be explained by their relative distance of the tunnel T1. (-7.7; - 28 and - 43.1). We dig the second tunnel T2, the lateral displacements for each micropile are modified either from point of view aspect or from the value. The second excavation modifies the piles' behavior, causing each micropile to move in the direction of the nearby tunnel. Following the opening of the 1st tunnel T1 and the opening of the two tunnels together T1+T2, figure 8 combines the profiles of the lateral displacements obtained in the four (4) micropiles into one illustration.

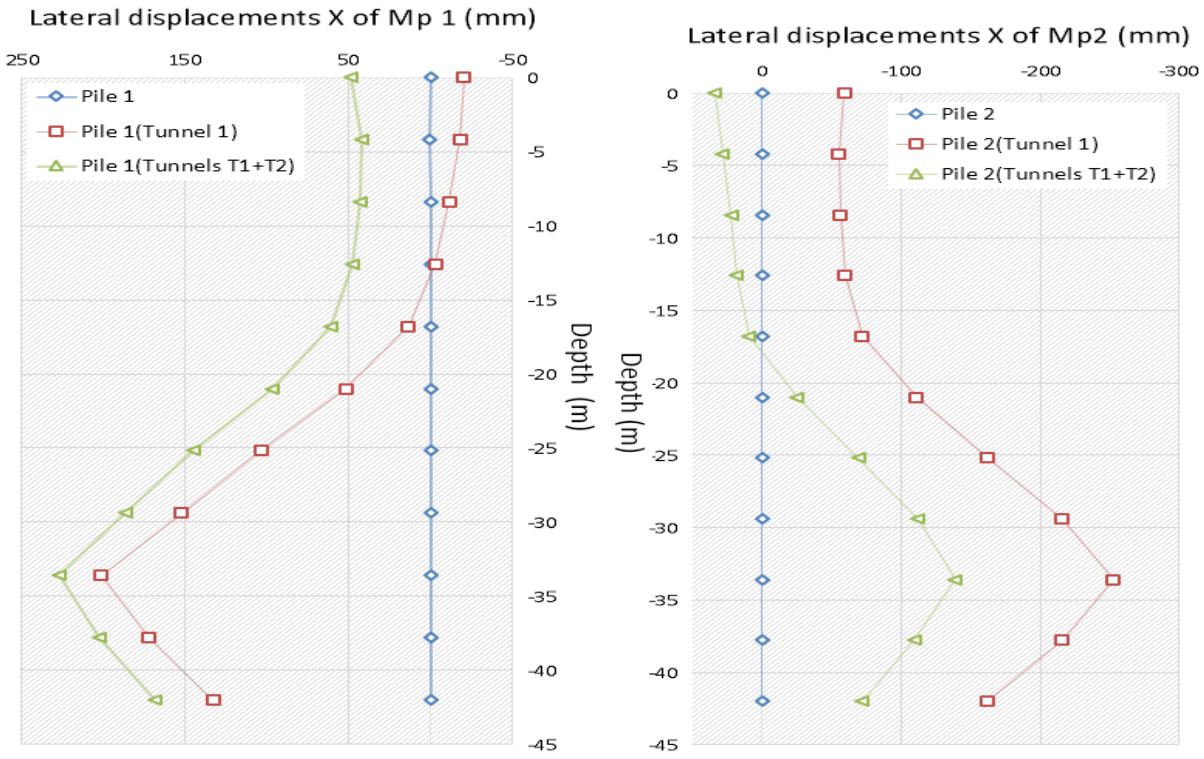

Figure 9.a: Variation lateral displacement in the micropiles P1 and P2 with the passage of the tunnels

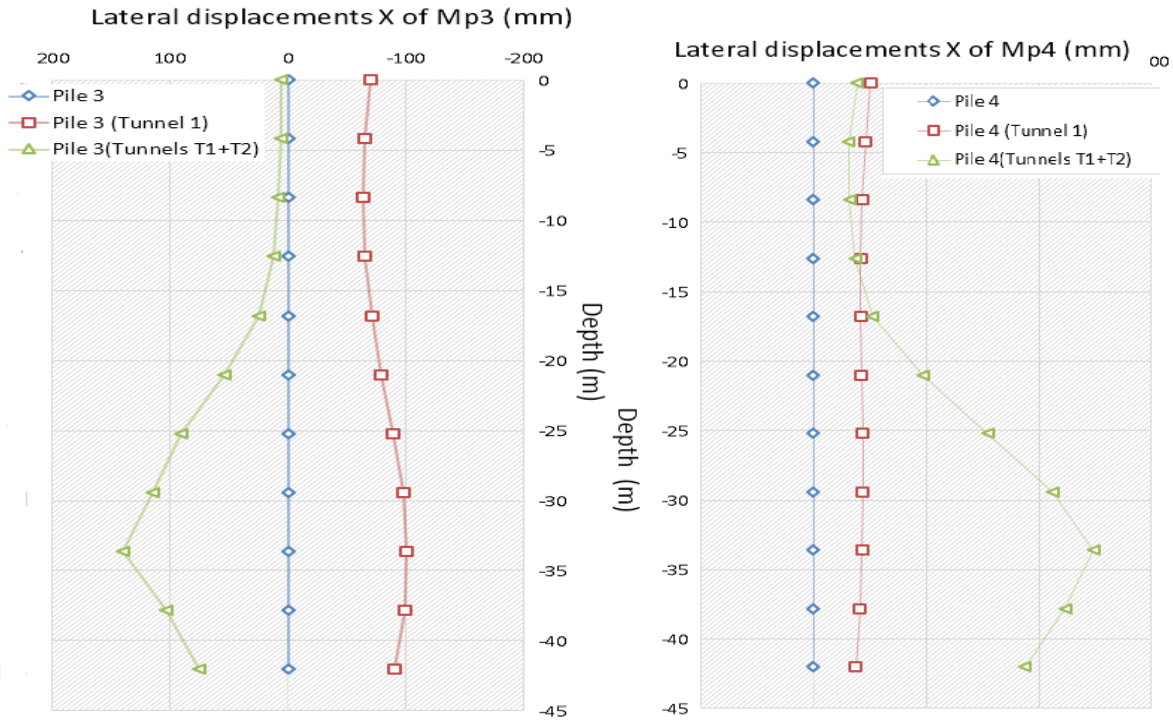

Figure 9.b: Variation lateral displacement in the micropiles P3 and P4 with the passage of the tunnels

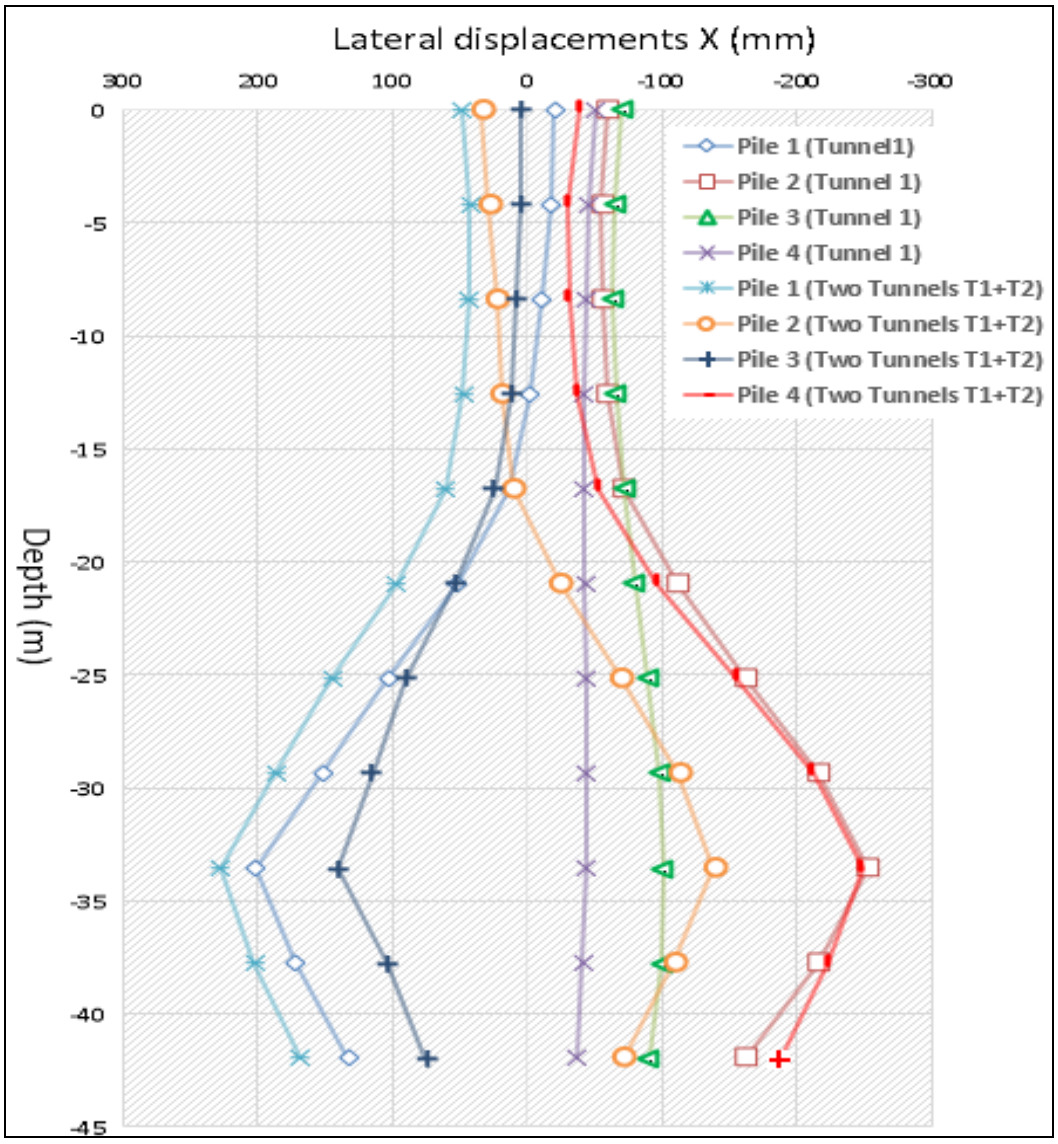

Figure 10: Variation of lateral displacement induced in the four micropiles with the passage of the tunnel T1 alone, and the two tunnels together T1+T2

8.3 Axial forces in mircopiles

We determine the fields of the axial force in the four micropiles according to the three distinguished cases, before and after the excavation of two tunnels; the axial forces of micropiles are negligible before tunnel excavation, nevertheless, they rapidly grow if a tunnel is dug, reaching a maximum value of 17650 KN in the micropile P1 closest to the tunnel, this value is observed in a section localized to the depth (X_p=0, 8Lp) and a minimum value until the 1570 kN in the micropile P4 is distant to tunnel T1. Once the left tunnel T2 was in existence, Two tunnels together (T1+T2), the axial profiles are changed, becoming more significant than in the first tunnel T1. It has been found that the internal axial force generated in the micropiles is significantly increased by the excavating of second tunnel T2.

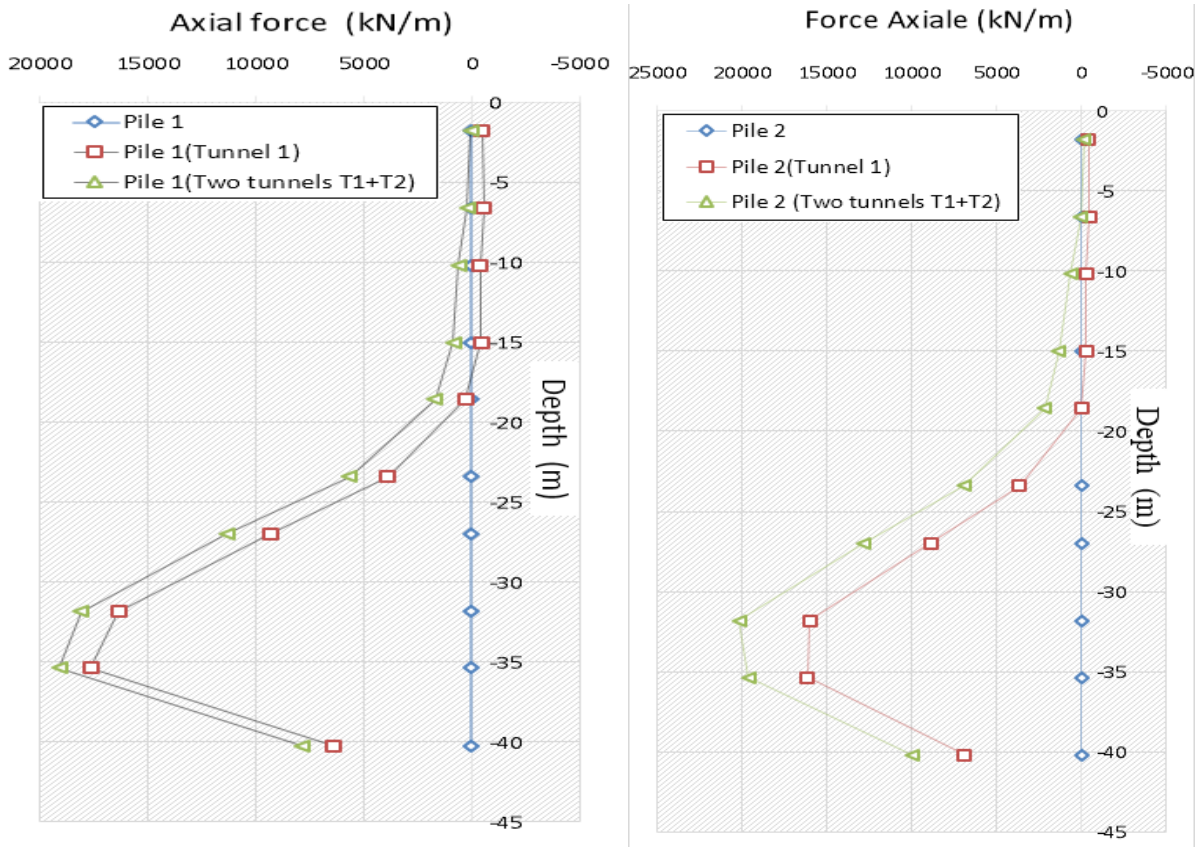

Figure 11a: Variation of Axial Force induced in the micropiles P1, P2 with the passage of the tunnels

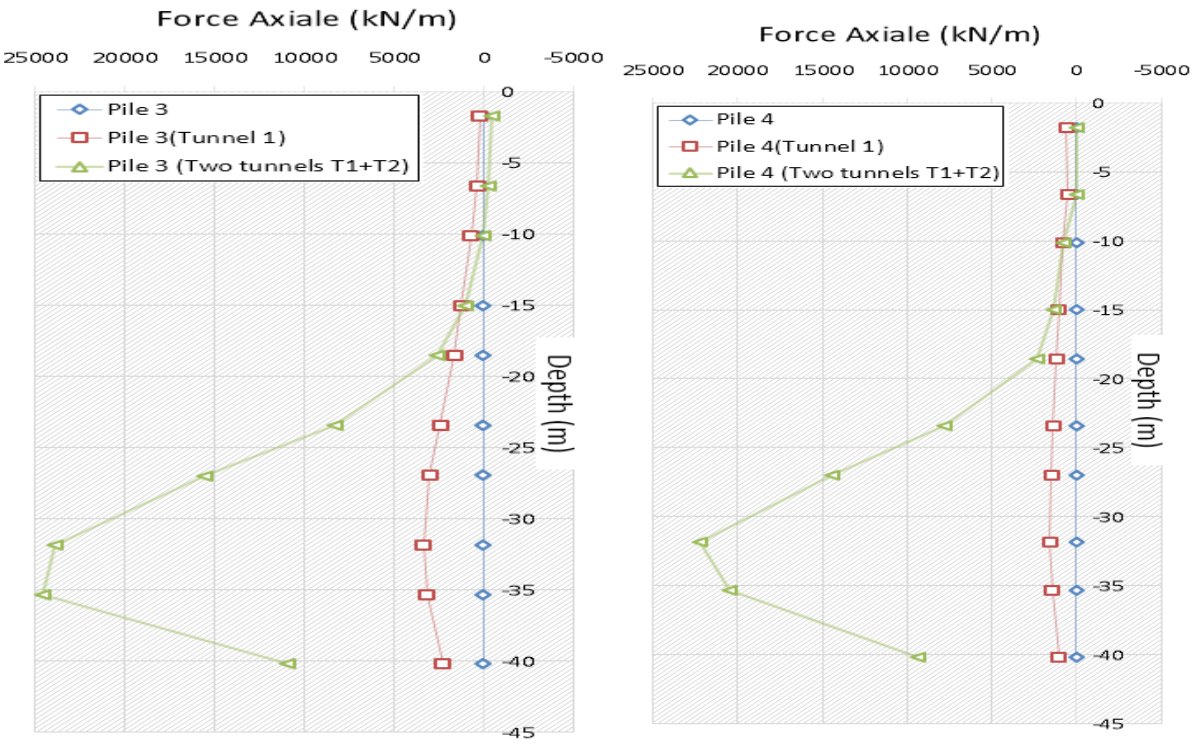

Figure 11b: Variation of Axial Force induced in the micropiles P3, P4 with the passage of the tunnels

8.4 Bending moment in mircopiles

We determine the fields of moments bending in the micropiles in the three distinguished cases. In an unperturbed ground without digging, with tunnel T1's construction and with the two tunnels together (T1+T2). The moments bending in the micropiles are negligible before the tunneling, after the digging, these moments will have maximum values in the micropiles P1 and P2 that are nearest to tunnel T1 that attain to 24 kN.m (interaction between pile-tunnel). In contrary, the farther micropiles P3 and P4, where we have the relatively modest values, are unaffected by digging. The moments of P1 and P2 practically remain the same after we construct the second left tunnel T2, changing only (increase) in the micropiles P3 and P4

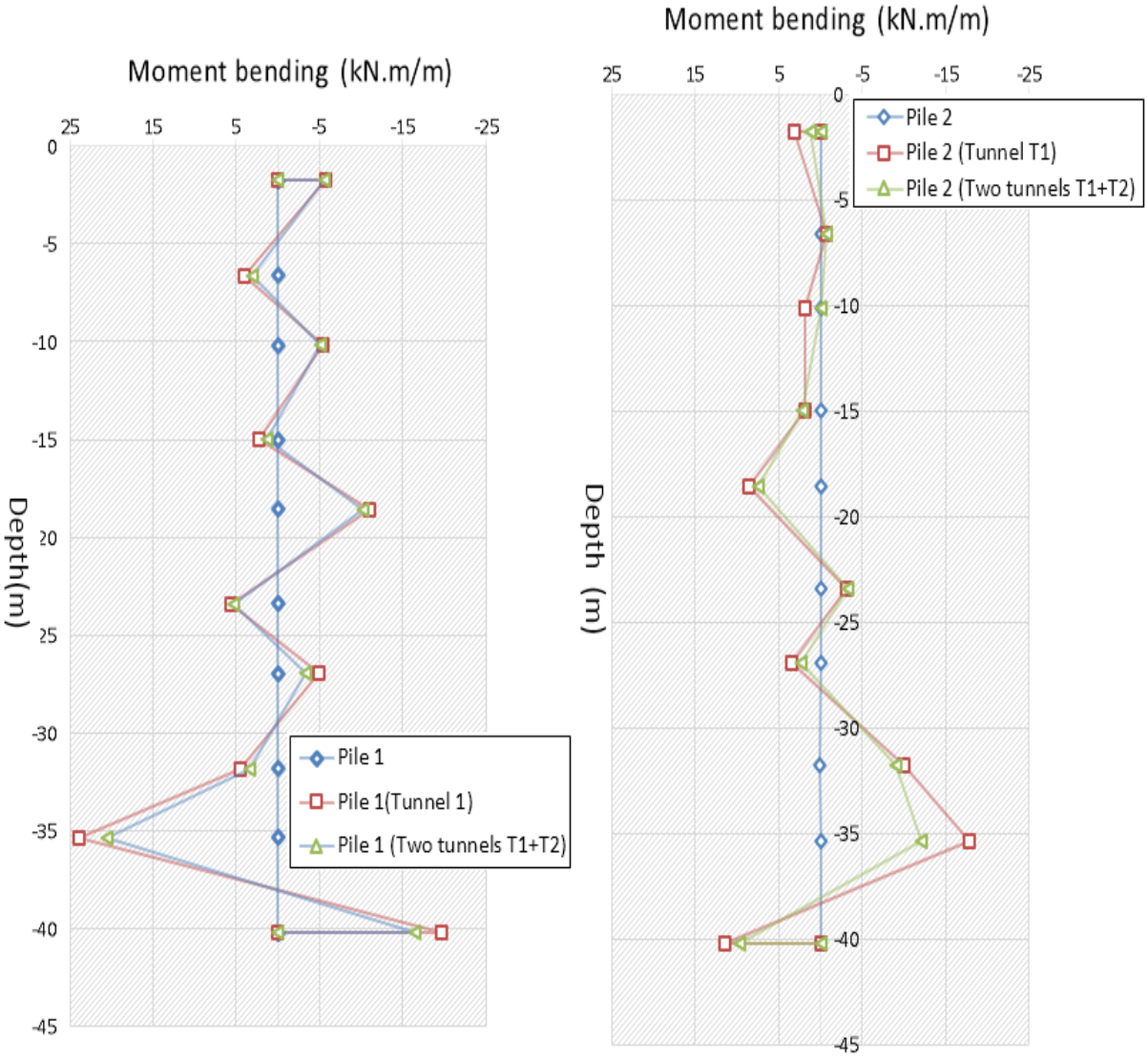

Figure 12 a: Variation of moment bending induced in micropiles P1 and P2 with the passage of the tunnels

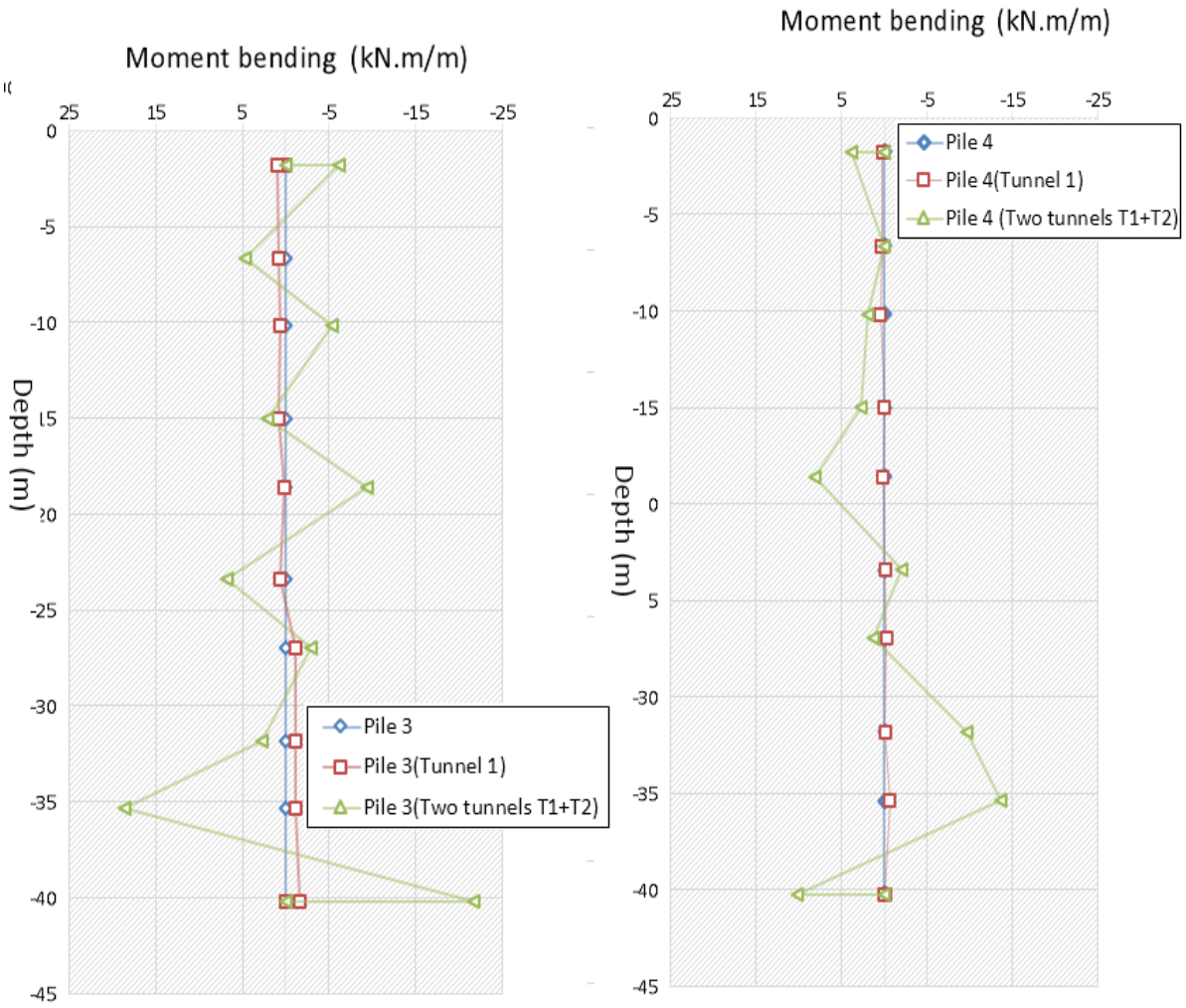

Figure 12 b: Variation of moment bending induced in micropiles P3 and P4 with the passage of the tunnels

9 Investigating the effect of micropiles depth on the interaction

9.1 Zone of influence and pile location effect

According to Yang Min et al. [10], we used four different lengths of micropile to investigate the impact of pile length on the interaction between pile and tunnel, and the stability of this micropile; therefore, the length of micropile relative to tunnel is examined. L_{pile}/H_{tunnel} of 0.5; 0.7; 1 and 1.4. In order to cover the zones of influence delineated by the lines that projecting 45° from the tunnel. The depth tunnel ($H_{tunnel)}$ and the length of the micropile ($L_{pile)}$ are 30 and 40 meters, respectively.

Figure 13 illustrates the micropile- tunnel configuration at different positions of L_{pile}/H_{tunnel} and constant X_{pile}/D_{tunnel} values of 1.0.

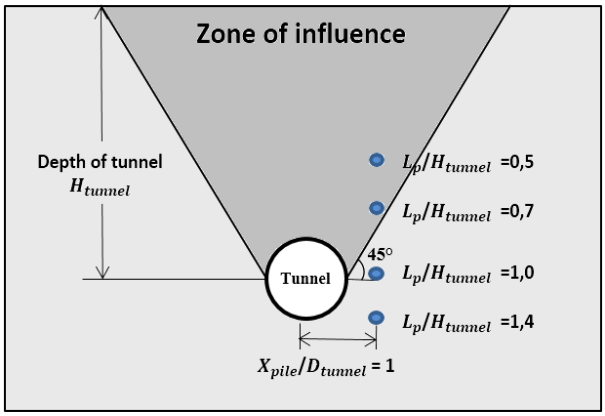

Figure 13: Micropile-tunnel configuration

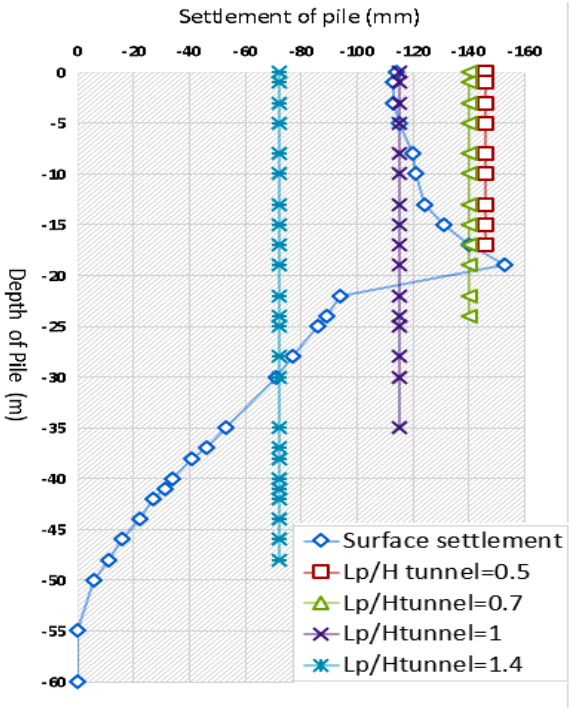

Fig. 14 Pile settlement profile at various L_{pile} /H $_{tunnel}$

It is evident that the micropile settlement in the zone of influence, measured by L_{pile}/H_{tunnel} values of 0.5 and 0.7, is greater than the Greenfield surface settlement. When the length of the micropile is increased (i.e., L_{pile}/H_{tunnel} of 1 and 1.4), the micropile settlement is drastically reduced. It can be concluded that the line differentiates the two behaviors is projected at an angle of 45° from the tunnel spring-line in this instance because the pile head settlement becomes less than the greenfield surface settlement due to support from the "toe effect" (i.e. Pile length prolonging outside the zone of influence) [11]; (Figure 14). The zone of influence appears to emanate from nearby the tunnel spring-lines, initially at an angle of approximately 45°. The zone on influence can be sub-divided based on the amount of settlement that the micropiles had undergone at a volume loss of 1.5% comparative to that of the surface.

9.2 Influence the passage of tunneling on micropile

Many authors [5-11-10] suggested investigating the interaction between the tunnel and piles foundations. H. Mroueh et al. [5] studied a considerable influence passage of tunneling on piles and their answers. Figure 15 shows the longitudinal section of the passage of tunneling and adjacent micropile, in order to study the interaction problem between tunnel-pile. The micropile lateral deflection due to tunneling in the lateral section is shown in the figure 16.
Analysis of the soil movement in the lateral section shows that tunneling induces a minimum translation of the micropile while the passage of the tunnel faces on the same vertical plan with micropile ($\Omega_{Ft\text{-}Micopile}$ =0),

These lateral deviations increase when the distance of the tunnel face from the micropile becomes superior than a slice that equal 10 m ($\Omega_{Tf\text{-}Mictopile}$ > +1 slice). The maximum value of the lateral deflection is about 100 mm at X_{Mp}/L_{Mp}=0.8.

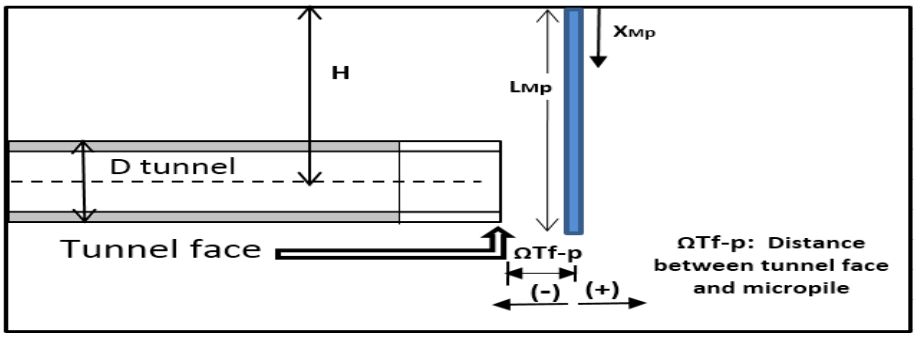

Figure 15: Longitudinal section of tunneling and adjacent micropile

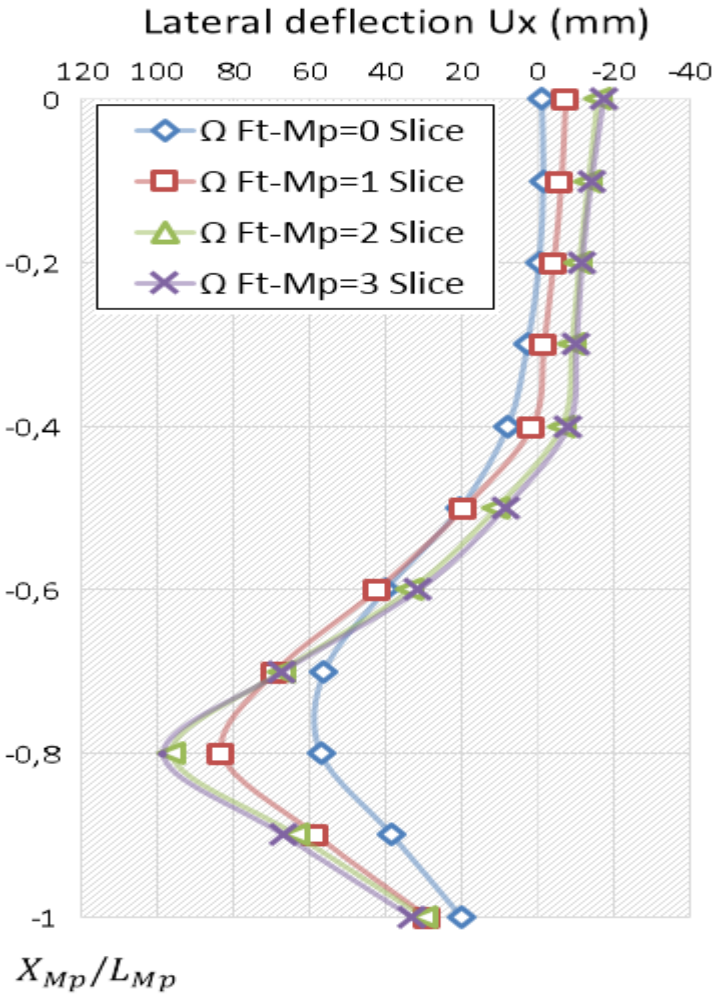

Figure 16: Micropile deflection due to tunneling in the lateral section

10 Investigating the effect of the tunnel position on the interaction

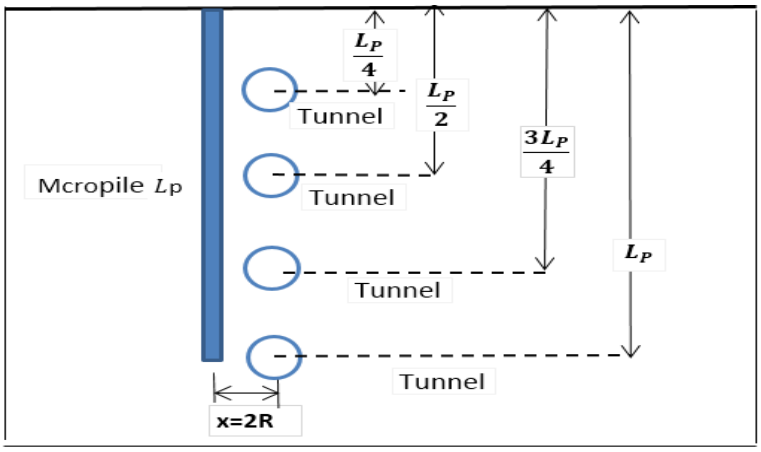

Figure 17: Tunnel positions relative to micropile

In this part, we present the effect of new tunnel position relative to micropile length on the existing micropile, this study was performed to examine the effect of the vertical locations of a new tunnel relative to an existing micropile, the distance x between the new tunnel and micropile was kept constant at two times the tunnel radius (x=2R).

The stability of this micropile has been investigated, we use four different locations of tunnel (0.25 L_p; 0.5L_p; 0.75L_p; L_p); therefore, the tunnel locations investigated as shown in the figure 17. Length micropile L_p is equal 40m, the tunnel's locations are equal 10 m; 20m; 30m and 40m respectively.

Figure 18 shows the interaction problem between tunnel to be excavated and the an existing micropiles. It presents the lateral displacements profiles in the micropile after the tunneling at different positions. These curves give different values in relation to the distinguished locations. It has been noted a negligible deflection in the micropile (practically zero) before tunneling, After the tunnel is dug, this micropile endures lateral displacement. This is because once the tunnel was dug, the ground became unstable, which was brought on by ground movement.

Prior to excavation, the value of lateral displacement is 1 mm, almost negligible.

After to excavating tunnel T4, we note that the values of lateral displacement in the micropile begin to increase, and by changing the vertical level of excavating tunnel location following to the micropile length, the esteemed maximum values of lateral displacements in the micropile, when excavating tunnel T4 at a height of: Quarter length, half length, two-thirds length and whole length are 25,6 mm/ 13,7 mm/ 17.8 mm and 22 mm respectively.

We recommended digging the new tunnel at a location half the length of the existing micropiles to reduce the impact of tunneling on them.

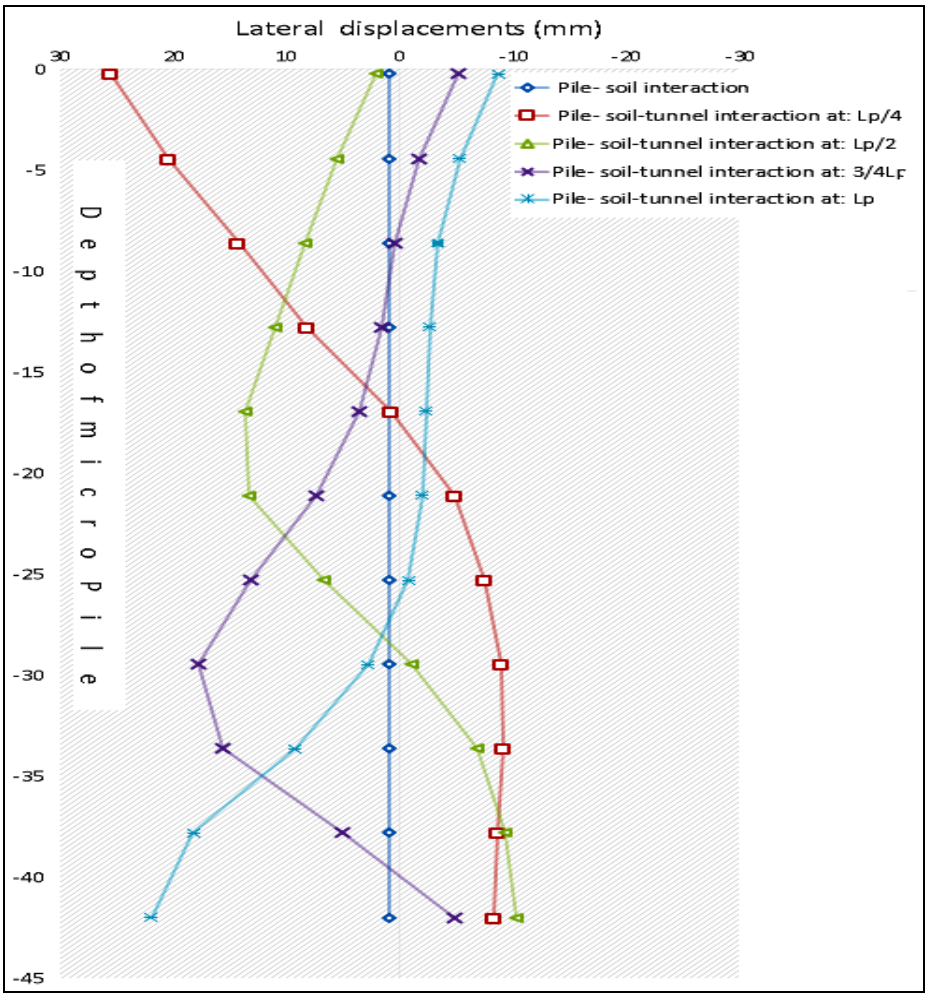

Figure 28: Lateral displacements profiles in the micropile after the excavating tunnel at different positions

11 Conclusion

In this study, it will be required to reinforce the soil with micropiles to enable tunnel excavation in order to increase the stability of the ground from the shallow tunnels excavation (weak cover zone), however this technique often necessitates research into the interaction between shallow tunnel and an adjacent micropiles.

- This study includes a numerical analysis of the interaction between the initially constructed micropiles and the future designed tunnels; the gotten results illustrate the effect of tunneling on the pre-existing micropiles. The analysis of the data demonstrates that the evolution of the axial force, the moment bending, and the lateral deflection in the nearby micropiles are always significantly impacted by the excavation of a single tunnel T1, excavating the two tunnels together (T1+T2) intensifies these affects. In this case, each micropile deviates in the direction of the tunnel next to it.

- The micropile settlement value must be greater than or equal to the surface soil settlement value to be considered within the influence zone; otherwise, the micropile settlement must be less than the settlement of the surface soil outside of the influence zone. The stability of these micropiles is affected when they are positioned in a zone of influence.
- Investigating how the length of the micropile relative to depth tunnel impact on the interaction between shallow tunnel and an adjacent micropiles. As a result, when the length of the micropile is increased, the settlement of the micropile is drastically reduced.
- The passage of the tunneling face affects how tunnels and micropiles interact.
- Investigating how the tunnel position relative to length tunnel impact on the interaction between tunnel and adjacent micropiles. As a result, we recommended digging the new tunnel at a location half the length of the existing micropiles
- The obtained findings show that the tunneling may affect in nearby micropiles a considerable lateral deflection, bending moments, compressive forces, and axial forces.

Tunnelling in densely populated areas is generally associated with undesirable ground movement and subsequent damage to adjacent piles (Micropiles). This work can provide a practical experience in the field for the constructing new tunnels in close proximity to existing piles (Micropiles). It has been shown that the tunneling process significantly affects current micropiles, which calls for more research.

References

[1] Loganathan, N., Poulos, H.G., Stewart, D.P. (2000). Centrifuge Model Testing of Tunnelling-Induced Ground and Pile Deformations." *In Geotechnique* 50 (3), 283–94.

[2] Bousbia Nawel, Messast Salah. (2015): Numerical modeling of two parallel tunnels interaction using Three-dimensional Finite Elements Method. *Geomechanics and Engineering*. 9 (6) ,775-791.

[3] Mair RJ, Taylor RN, Burland JB (1996): *Prediction of ground movements and assessment of risk building damage due to bored tunneling*. Proceedings, Geotechnical Aspect of Underground Construction in soft Ground, Balkema: Rotterdam

[4] Bousbia Nawel, Messast Salah, Houssou Noura (2021).: A simplified 3D model for existing tunnel response to piles construction. *Journal of civil engineering SSP*. 16 (2) ,87-103.

[5] H. Mroueh and I. Shahrour (2002). Three-dimensional finite element analysis of the interaction between tunneling and pile foundations. *International journal for numerical and analytical methods in geomechanics*. Vol 26, 217-230

[6] Yang Min, Sun Qing, LI Wei-chao, MA Kang (2011): Three-dimensional finite element analysis on effects of tunnel construction on nearby pile foundation, *J. Cent. South Univ, Technol.* Vol.8, 909−916

[7] Dar Al-Handasah (Shair and Partners) (2009). *Documents d'autoroute Est Oust Lot Unique Est*", Consortium Japonais pour L'autoroute Algérienne COJAAL

[8] Panet, M. and Guenot, A (1982): *Analysis of convergence behind the face of a tunnel*. Proceedings of the 3rd International Symposium, Brighton, UK, June

[9] Pierpaolo Oreste (2009): The Convergence-Confinement Method: Roles and Limits in Modern Geomechanical Tunnel Design, *American Journal of Applied Sciences*. 6(4), 757-771

[10] Felix Christian Schroeder (2002): *The influence of bored piles on existing tunnels.* Ph.D. Dissertation, Department of Civil and Environmental Engineering, London

[11] Bousbia Nawel (2021): Effects of different processes of tunneling on displacements soil using

3D Finite Element Method. *Journal of civil engineering SSP*. 16 (2) ,203-217

[12] Mair RJ, Taylor RN, Burland JB (1996): *Prediction of ground movements and assessment of risk building damage due to bored tunneling*. Proceedings, Geotechnical Aspect of Underground Construction in soft Ground, Balkema: Rotterdam

[13] C.H. Pang, K.Y. Yong & Y.K. Chow (2005): Three-dimensional numerical simulation of tunnel advancement adjacent pile foundation. *Underground Space Use*

[14] Afifipour, M., Sharifzadeh, M., Shahriar, K. and Jamshidi, H (2011): Interaction of twin tunnels and shallow foundation at Zand underpass, Shiraz metro, Iran. *Tunnelling and Underground Space Technology*. 26(2), 356-363

[15] Alec M. Marshall, Twana Haji (2015): An analytical study of tunnel–pile interaction. *Tunneling and Underground Space Technology*,45, 43–51

[16] Andrea Franza, Alec M. Marshall, Twana Haji, Amged O (2017). Abdelatif, Sandro Carbonari, Michele Morici.: A simplified elastic analysis of tunnel-piled structure interaction. *Tunnelling and Underground Space Technology*. 61, 104– 121

[17] C.J. Lee (2012): Three-dimensional numerical analyses of the response of a single pile and pile groups to tunneling in weak weathered rock. *Tunneling and Underground Space Technology*.

[18] Chen, L.T., Poulos H.G. and Loganathan (1999): Pile responses caused by tunneling. *J. Geotechnical and Geoenvironmental Engineering*, ASCE. 125(3), 207-215

[19] C.Y. Cheng, G.R. Dasari, Y.K. Chow, C.F. Leung (2007): Finite element analysis of tunnel–soil–pile interaction using displacement-controlled model. *Tunnelling and Underground Space Technology*. 22, 450–466

[20] F. Hage Chehade, I. Shahrour (2007): Numerical analysis of the interaction between twin-tunnels: Influence of the relative position and construction procedure. *Tunneling and Underground Space Technology*. 23(2), 210-214

[21] Francesco Basile (2014): Effects of tunneling on pile foundations, *Soils and Foundations*. 54(3), 280–295

[22] G.A. Torres-Alves, C.M.P. 't Hart, O. Morales-Nápoles, S.N. Jonkman (2022): Structural reliability analysis of a submerged floating tunnel under copula-based traffic load simulations. *Engineering Structure*s. 269, 1147521

[23] Giorgia Giardina, Matthew J. DeJong, Robert J. Mair (2015): Interaction between surface structures and tunnelling in sand: Centrifuge and computational modeling. *Tunnelling and Underground Space Technology*. 50(2),465-478

[24] Jiao-Long Zhang, Christoffer Vida, Yong Yuan, Christian Hellmich, Herbert A. Mang, Bernhard Pichler (2017): A hybrid analysis method for displacement-monitored segmented circular tunnel rings. *Engineering Structures*.148, 839–856

[25] H. Mroueh, I. Shahrour (2008). A simplified 3D model for tunnel construction using tunnel boring machines. *Tunneling and Underground Space Technology*. 23, 38-45

[26] Hassan Obaid Abbas (2020): Influence of Tunnel Excavation on Tower Foundation Settlement Constructed on Sandy Soil. *Transportation Infrastructure Geotechnology*.7, 651–663

[27] Hergarden H.J.A.M., Van der POEL J.T. & Van der SCHRIER J.S (1996): *Ground movements due to tunneling: Influence on pile foundations*. Proceedings, Geotechnical Aspects of Underground construction in Soft Ground, Mair & Taylor, Rotterdam

[28] Khadija Nejjar, Daniel Dias, Fahd Guira, Gilles Chapron, Hervé Le Bissonnais (2022) : Numerical modelling of a 32 m deep excavation in the suburbs of Paris. *Journal of Engineering structures*. 268

[29] M. Wasif Naqvi, M. F. Akhtar, Mohammad Zaid (2021) : Effect of Superstructure on the Stability of Underground Tunnels. *Transportation Infrastructure Geotechnology*. 8, 142-161